ABSTRACT

Title of Document: DIRECT FUSION DRIVE BASED ON CENTRIFUGAL MIRROR CONFINEMENT

Jerry Lee Carson
Doctor of Philosophy, 2023

Directed By: Professor Raymond J. Sedwick
Department of Aerospace Engineering

A concept for direct fusion drive based on centrifugal mirror confinement of thermonuclear plasmas (DFD-CM) is described. In centrifugal mirrors, electric and magnetic fields are combined to confine the plasma within a rapidly rotating annulus of burning plasma fixed between two mirror magnets. High-energy fusion products leave the reactor core at a rate determined by the velocity of plasma rotation and the strength of the mirrors. Those departing through the aft jet-side mirror deposit their energy in a "warm plasma" which then expands through a magnetic nozzle to deliver jet power in the 100-1000 kW range. Fusion products departing through the forward, power-side mirror are converted to electricity to power the reactor. Moderate thrusts at attractive specific impulses (15000+ seconds) are possible. Findings are presented on centrifugal mirror reactor dynamics in propulsion applications, to include new insights into the relationship between mirror and centrifugal components of plasma confinement. Additionally, analysis is presented on reactor operability limits and characterization of viable configurations based on power density, technology constraints, and the ability to self-power. Physics of the warm plasma are discussed, to include

estimates for fusion energy deposition. Finally, considerations for Alfvén's "frozen-in" theorem relative to fusion plasmas and magnetic nozzle performance will be outlined.

Analysis indicates the DFD-CM system can self-power, and would be relatively compact. For the 200 kW delivered jet power system, the volume of burning plasma in the CM fusion reactor is estimated to be on the order of 1 m^3. Self-powering in propulsion applications requires DFD-CM reactor operation at $M_\theta > 9$. This in turn requires electric fields ranging from 40-90 MV/m, and mirror strengths up to 15T. The main losses in the propulsion system are due to heating and ionizing the propellant. These losses decrease with increasing specific impulse.

This work has resulted in four contributions. To start, it is the first analysis of the end-to-end performance of direct fusion drive based on centrifugal mirror confinement of the burning plasma. It demonstrates that the concept is thermodynamically feasible with nominal cycle efficiencies of 50 percent based on fusion energy entering the propulsion system. The second contribution is characterization of CM fusion reactor performance and operability. A particular finding is that self-powering DFD-CM reactors in propulsion applications may need to operate at centrifugal Mach numbers greater than 9, as previously mentioned. The third contribution is the development and preliminary application of a set of engineering models of the reactor, warm plasma, and plasma acceleration and expansion. These models are considered moderate fidelity in that they account for first order effects, as well as salient second order effects. The fourth contribution is identifying the possibility that the burning plasma in the reactor and the warm plasma may be electrically coupled. The nature and implications of any coupling are uncertain, and the current research proceeds assuming that the coupling does not occur. However, the question indicates the need for further research.

DIRECT FUSION DRIVE BASED ON CENTRIFUGAL MIRROR CONFINEMENT

by

Jerry Lee Carson

Dissertation submitted to the Faculty of the Graduate School of the
University of Maryland, College Park, in partial fulfillment
of the requirements for the degree of
Doctor of Philosophy
2023

Advisory Committee:
Professor Raymond Sedwick, Chair
Professor Kenneth Yu
Professor James Baeder
Professor David Akin
Dr. Ian Abel
Professor Thomas Antonsen

Dedication

To my wife, Cecilia, the love of my life.

Acknowledgements

"…your old men will dream dreams"

Acts 2:17

Many, many thanks to my advisor, Dr. Raymond Sedwick, for his guidance, encouragement, and patience. Early on, he recognized the potential for DFD-CM, and I am grateful that he asked me to take on this problem. I would also like to thank Dr. Adil Hassam of University of Maryland's Institute for Research in Advanced Electronics and Physics. Dr. Hassam was generous with his time and always available for questions, which he answered with characteristic quiet, good humor.

I wish to thank Dr. Sonny White and the Limitless Space Institute for funding a large part of the present work, as well as work going forward. LSI has a unique charter to sponsor forward leaning research, and its support has allowed me to focus on advancing the DFD-CM concept.

Thanks to the Advisory Committee for their engagement and support, and for the time they spent in meetings and with the manuscript. Their feedback and inputs strengthened the dissertation, and their questions made me think more deeply on key parts of the problem.

DFD-CM is a complex technical challenge. The present work addresses DFD-CM as a system, but that is only one part of the problem, and in many ways, the easiest. My team mates in the Space Power and Propulsion Laboratory (SPPL) have each undertaken significant research related to DFD-CM. They provided early feedback on my research that was invaluable in shaping the work going forward. I have truly enjoyed being part of this energetic team and appreciate the opportunity to work with them. I am likewise indebted to the Centrifugal Mirror Fusion Experiment (CMFX)

team for their ongoing collaboration with SPPL and for sharing what they learn as their work advances.

Finally, I remember Professors David Tomlinson, Vladimir Sergeyvich Tolstoy, and Dennis “Doc” Hasson, late faculty of the United States Naval Academy. They gave me my first lessons in critical thinking and passed on their lifelong love of learning and intellectual adventure.

Table of Contents

List of Figures

List of Tables

This page blank

1 The Research Problem

1.1 Concept Overview

This research assesses the feasibility of Direct Fusion Drive based on Centrifugal Mirror Confinement (DFD-CM). Viable space commerce and future space exploration will require advanced power and propulsion technologies capable of multi-megawatt power generation with high specific impulse, moderate thrust levels, and low system specific mass. Conventional rockets and nuclear thermal propulsion will be sufficient for low Earth orbit (LEO) and Cis-Lunar applications, but cost-effective travel to Mars and asteroid mining will require much higher specific jet power. Direct fusion propulsion would provide thrust through the energy of high-velocity products of thermonuclear reactions. A viable system must: 1) maintain the high temperature plasma for a stable, self-sustaining reactor; 2) contain the plasma; 3) integrate the reactor with a magnetic nozzle; 4) ensure the plasma plume detaches from the magnetic nozzle. Centrifugal confinement in mirror devices have potential for meeting these requirements. The plasma in a conventional mirror device is contained by a cylindrical magnetic field with strong magnets, the mirrors, at either end. The magnetic field lines in mirror devices are longitudinal. Each charged particle in the plasma is bound to an individual magnetic line of force about which it gyrates millions of times per second. The particles also move along the lines of force, but are reflected back and forth by the mirror magnets at each end, hence their name. However, mirrors are leaky, and particles entering the characteristic loss cone will escape. As shown in Figure 1-1, in a centrifugally confined plasma, a radial electric field imposed from the center of a mirror device will work with the longitudinal magnetic field to force the charged particles to take on an azimuthal drift velocity

$$u_\theta = \frac{E \times B}{B^2}. \qquad 1.1$$

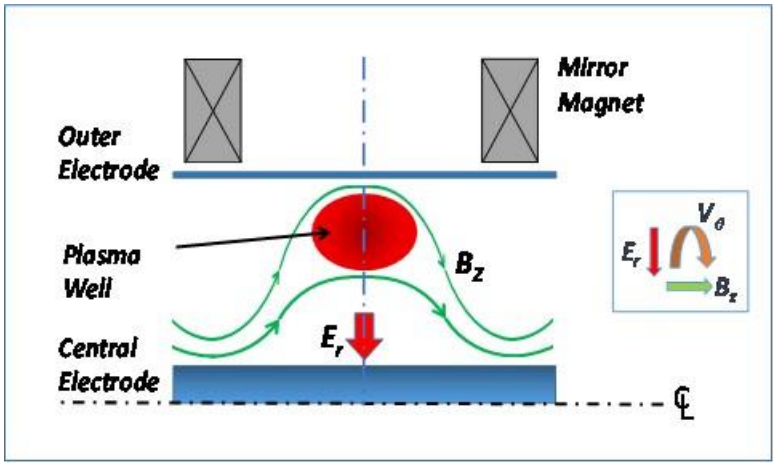

Figure 1-1 - Centrifugally confined plasma

Centrifugal confinement has been successfully demonstrated in the US by the Ixion device in the 1950s and 1960s, and the Maryland Centrifugal Experiment (MCX) in the 2000s. [Baker, *et al*, 1961][Ellis, *et al*, 2001] MCX achieved 100 eV plasma temperatures. [Reid, *et al*, 2014] The University of Maryland (UMD) Institute for Research in Electronics and Applied Physics (IREAP) is currently developing a follow-on to MCX with funding from ARPA-E, the Centrifugal Mirror Fusion Experiment (CMFX). The goals of CMFX include: 1) $T > 0.5\ keV$; and 2) a triple product of $nT\tau > 10^{17}$ with H-H and D-D plasmas. [Hassam, 2020]

The drift velocity u_θ has an associated Mach number $M = u_\theta/(k_B T/m_i)^{1/2}$. In addition to compressing the plasma radially, the azimuthal velocity also results in a force component parallel to the B field that confines the plasma axially. When integrated with a magnetic nozzle, a centrifugal containment scheme could be used for deep space propulsion.

Thermonuclear plasmas are highly energetic but inherently low thrust, because of the small mass flow from the reactor. However, mixing high-energy fusion products with higher density, low temperature, i.e., "warm," plasmas could increase thrust, but at the expense of specific impulse. In this scheme, high-energy fusion products would pass out of the reactor, i.e., the mirror device, and into a downstream energy transfer zone containing the warm plasma. The warm plasma is also contained in a magnetic confinement scheme. The fusion products would deposit energy into the cold plasma, heating the plasma as they did. The higher energy warm, dense plasma flows through a downstream magnetic nozzle producing thrust. Figure 1-2 shows the schematic of a direct fusion drive incorporating a warm plasma. The α and θ species are prompt and thermal fusion products from the reactor depositing energy into the warm plasma made up of β propellant species. Warm plasmas flows – within limits – may vary, suggesting a tradeoff between specific impulse and thrust as suggested by [Clauser, 1958]. The forward mirror can be configured to allow the flow of fusion products into a power conversion system to power the reactor. The baseline concept in the current research envisions a standing wave direct energy conversion (SWDEC) system as proposed by [Chap and Sedwick, 2015].

Effective integration of magnetic nozzles is a core research problem for direct fusion drive. Transport processes play critical role in plasma detachment from the magnetic nozzle, and detachment is necessary for the nozzle to produce thrust. The warm plasma serves a second intended purpose in the direct fusion drive system by converting fusion energy into a lower temperature, collisional plasma that can detach from the magnetic field.

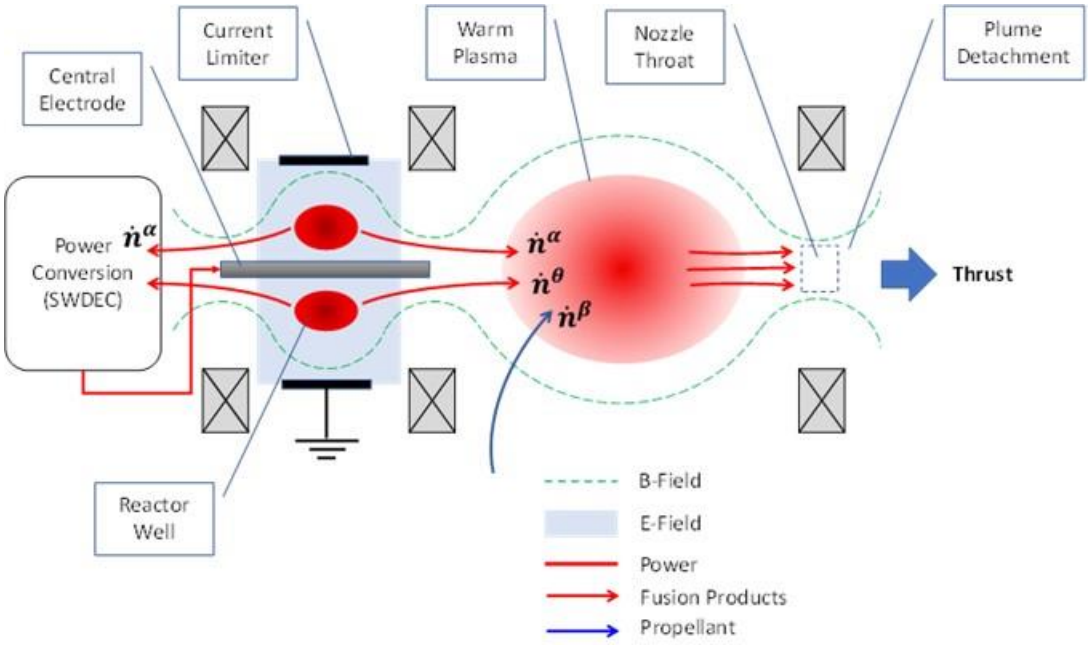

Figure 1-2 - Direct fusion drive propulsion system

1.2 CM Reactor Dynamics

1.2.1 Thermonuclear Reactions

The deuterium-tritium (D-T) reaction is technologically the most accessible approach for controlled nuclear fusion. Nuclear fusion can also occur through the D-D and deuterium-helium-3 (D-^{3}He) reactions, but the D-T reaction occurs at rates 100 times faster than the other two below temperatures of 100 keV. [Huba, 2013] Therefore the present work focuses on DFD-CM powered through the D-T reaction

$$ {}_1^2D + {}_1^3T \rightarrow {}_2^4He + {}_0^1n + 17.6\ MeV \qquad 1.2 $$

The alpha and neutron have energies of 3.5 MeV and 14.1 MeV, respectively.

In order for thermonuclear fusion to occur, the reaction kinetics must be sufficiently fast, and the heat balance of the reaction must be self-sustaining. Reaction kinetics are a function of particle density of participating species and reaction cross-sections. Nuclei must collide and in so doing, overcome mutually repulsive coulomb forces. The conditions necessary for this are that the particles be of sufficient velocity, and that there is a sufficient probability of collision. The first of these conditions implies a high temperature. The second implies both a sufficient concentration of particles and reaction cross-section. The reaction cross-section in turn is a function of temperature and the properties of the participating nuclei. The rate of alpha production in the D-T reaction is

$$\dot{n}^{\alpha} = n_0^2 x_D x_T \langle \sigma v \rangle_{DT} \qquad 1.3$$

n_0 is the plasma number density. x_D and x_T are the mole fractions for deuterium and tritium. $\langle \sigma v \rangle_{DT}$ is the reaction cross-section. At 10 keV, the D-T reaction $\langle \sigma v \rangle_{DT}$ is on the order of 10^{-16} cm^3-s^{-1}. By comparison, the D-D reaction at the same temperature is approximately 10^{-18} cm^3-s^{-1}. To determine the power of fusion from alphas, it is necessary to multiply reaction rate by E^{α}, the energy of a single fusion reaction alpha particle. The total energy of fusion is 17.6 MeV, but only 3.5 MeV comes from the alpha particles released in the reaction. The rest of the energy, 14.1 MeV, is released with the neutron. [Huba, 2013]

1.2.2 Reactor Power Balance

Figure 1-3 shows the qualitative power balance a D-T reactor, which must account for losses due to bremsstrahlung and cyclotron radiation. Additionally, losses of thermal species and primary

alphas must be captured. Neutrons do not contribute to the power balance in the plasma, and so are not shown. The confinement time for charged species, relevant to conventional mirror, scales by a factor of $(M^2/4)exp(M^2/4)$ for centrifugal mirrors. [Ellis, *et al*, 2001]. This scaling follows from [Pastukhov,1974] who developed a rigorous expression relating electron confinement times in mirror devices to collisional frequencies based on the electrostatic potential of the plasma within the mirror.

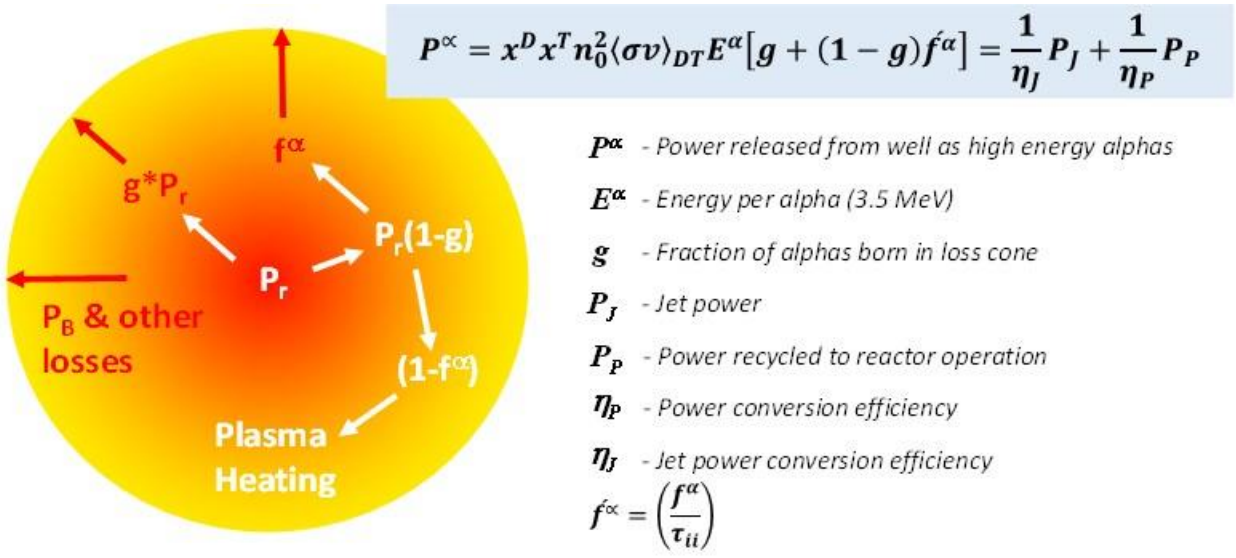

Figure 1-3– Power balance reactor well – prompt species

In Figure 1-3, g is the fraction of fusion products born in the loss cone, and it has components for jet-side and power-side, i.e., $g = g_J + g_P$. Fusion products are thermalized at a rate of $\dot{n}^{\alpha}(1-g)$. The thermal species ultimately leave the well based on their energy relative to the well potential and the ion-ion collision rate, $\nu_{ii} = 1/\tau_{ii}$, the rate at which they diffuse into the loss cone. More

precisely, thermal species will leave the well at a rate of $(f^{\alpha}/\tau_{ii})n_0$, where f^{α} represents the high-end tail of the energy distribution.

1.2.3 Centrifugal Mirror Confinement

As discussed in [Ellis, *et al*, 2001], the system is strongly magnetized, so that Larmor radii are small, and particle dynamics can be expressed as velocity drifts. The resulting drift Hamiltonian is

$$H = \tfrac{1}{2}m_i u_{\parallel}^2 + \mu B - \tfrac{1}{2}m_i r^2 \Omega^2, \tag{1.4}$$

where μ is the magnetic moment, and $u_{\parallel}$ is the particle velocity parallel to the magnetic field. For the system described in cylindrical coordinates (r, θ, z), r is the radius of the trajectory described by the drift velocity u_θ, and Ω is the associated angular velocity such that $u_\theta = r\Omega$. The magnetic field *B* is expressed

$$B = \nabla\theta \times \nabla\psi = \frac{1}{r}\left(\frac{\partial\psi}{\partial z}\hat{r} + r\frac{\partial\psi}{\partial r}\hat{z}\right), \tag{1.5}$$

where ψ is the magnetic flux. The angular velocity of a particle on any given flux surface is related to the electric field at that surface. Equation (1.6) is a form of the generalized Ohm's law.

$$E + u \times B = \eta J, \tag{1.6}$$

where η is the plasma resistivity, and *J* is the current density. For ideal magnetohydrodynamics, conductivity is assumed to be infinite, so Equation (1.6) can be expressed

$$\nabla\varphi = u \times B. \tag{1.7}$$

Evaluating Equation (1.7) at the plasma midplane

$$\frac{u_\theta}{r}\frac{\partial\psi}{\partial r}\hat{r} = u \times B. \tag{1.8}$$

Combining Equations (1.7) and (1.8), substituting $r\Omega$ for u_θ, and rearranging these term results in the following identity for Ω

$$\Omega = \frac{d\varphi}{d\psi}. \tag{1.9}$$

The electric potential φ is approximately constant on any given flux surface, and therefore, according to Equation (1.9), Ω is also constant. This suggests that field lines along the flux surface rotate like a rigid rotor, and that magnetized particles with parallel velocity $u_\parallel$ along the field lines behave like a "bead on a wire." [Ellis, *et al*, 2001] This is consistent with the observation that magnetic moment term in the Hamiltonian is much smaller than the centrifugal force potential in Equation (1.4). One can see qualitatively from Figure 1-1 that flux surfaces with larger radii near the midplane will rotate faster, which will tend to confine the plasma in that region. A more rigorous perspective can be obtained starting with the momentum equation for MHD.

$$n_i m_i u \cdot \nabla u = -\nabla P + J \times B. \tag{1.10}$$

Considering the system at the midplane, $u \cdot \nabla \mathrm{u} = -\frac{u_\theta^2}{r}\hat{r} = -\frac{1}{2}\nabla(r^2\Omega^2)$. Substituting this expression into Equation (1.10) and taking the scalar product with $\hat{b} = B/B$

$$\hat{b} \cdot \nabla \mathrm{P} = \frac{1}{2} n_i m_i \hat{b} \cdot \nabla (r^2 \Omega^2) + \hat{b} \cdot (J \times B), \tag{1.11}$$

which describes the variation of state properties along the field lines. Taking $\hat{b} \cdot (J \times B) = J \cdot \left(\hat{b} \times B\right) = 0$, and applying the equation of state, Equation (1.11) becomes

$$\frac{\partial P}{\partial s} = \frac{1}{4} \frac{P}{C_s^2} \frac{\partial}{\partial s} (r^2 \Omega^2), \tag{1.12}$$

where C_s is the acoustic velocity. Equation (1.12) is derived based on the assumption of constant temperature over a flux surface, which is a reasonable approximation given the high mobility of the electrons. Finally, integrating Equation (1.12) provides the following relation for pressure variation in the plasma well

$$P(z, \psi) = P_0(\psi) exp\left(\frac{r^2(z, \psi)\Omega^2}{4C_s^2}\right) \tag{1.13}$$

For $z = 0$ at the midplane, $r(z, \psi)$ decreases with increasing *z*. On a given flux surface with constant C_s and constant Ω, pressure decreases exponentially with decreasing $r(z, \psi)$. Note that the exponential value in Equation (1.13) is equal to $M^2/4$. The preceding discussion, following a similar development in [Ellis, *et al*, 2001] demonstrates how the centrifugal potential confines the plasma axially. As also pointed out in [Ellis, *et al*, 2001], the azimuthal velocity u_θ must conform with the inequality $C_s \ll u_\theta < V_A$. The Alfvén velocity $V_A = B/\sqrt{n_i m_i \mu_0}$ is the speed at which ions oscillate in a magnetic field in response to force imbalances. Rotational velocities in excess of the Alfvén speed will distort the magnetic field, so the Kármán number, u_θ/V_A must be approximately unity or less. [Teoderescu, *et al*, 2010] This constraint gives rise to a useful

relationship between M and β, the magnetic pressure ratio where a single charge state Z_i for the fuel has been assumed

$$\beta = \frac{n_i k_B (T_i + Z_i T_e)}{\frac{B^2}{2\mu_0}}. \quad 1.14$$

The form of Equation (1.14) shown assumes that ion and electron temperatures are equal. Under these conditions, and noting that β can also be expressed as C_s^2/V_A^2, the Mach number in a rotating plasma is limited to

$$M \leq K\sqrt{\frac{2(Z_i + 1)}{\beta}}. \quad 1.15$$

1.3 Propulsion System

1.3.1 The Warm Plasma

Propulsion performance is determined by fusion species energies (prompt and thermal), and the propellant "bypass" flow ratio ξ^β, i.e., the ratio of propellant flow (#/s) to the rate at which prompt fusion species arrive at the warm plasma, $\dot{n}^\alpha g_J V_r$. The corresponding value for fusion thermal species ξ^θ is the rate of thermal fusion products arriving at the warm plasma normalized by that of the prompt species, i.e., $\xi^\theta \approx \frac{g_J}{g}\left(\frac{f^\theta}{\tau_{ii}}\right)\left(\frac{n_0}{\dot{n}^\alpha}\right)$. These definitions allow the power balance for the warm plasma to be expressed in terms of the prompt fusion product generation rate, and they fix the proportions in which fusion power is converted to thrust and exhaust velocity, i.e., specific impulse.

Energy deposition in the warm plasma is a collisional process. Collisions between fusion products and electrons in the warm plasma are much faster than those with warm plasma ions. This can be approximated by a two-step mechanism where the overall thermalization time for the alphas, in the case of a D-T system, the relation is approximated $\tau^{\alpha} = \tau^{\alpha/e} + \tau^{e/\beta}$ where $\tau^{\alpha/e}$ is the characteristic power deposition time for alphas to electrons, and $\tau^{e/\beta}$ is the rate for electrons to propellant ions. The time for the fusion energy deposition should be much shorter than the residence time of the warm plasma. The residence time of the warm plasma is determined by its volume, the ratio of the nozzle magnetic field to that of the warm plasma, and the warm plasma electron temperature.

1.3.2 Magnetic Nozzle

The warm plasma, heated by the reactor products, flows into the magnetic nozzle and is accelerated by electrostatic forces in the nozzle to produce thrust. Electrostatic acceleration of the plasma through a magnetic nozzle was proposed by [Kuriki and Osaka, 1970]. The electrostatic field is created by the segregation of charged species that results from the greater mobility of the electrons. This creates the "current-free" layer, or structure, similar to the sheath between a plasma and a physical wall. The current-free structure follows from the requirement that electron and ion fluxes be equal as they leave the sheath. Based on this requirement, the resulting ideal potential of the accelerated plasma is

$$\phi = -\frac{k_B T_e}{2e}\left[1 + ln\left(\frac{m_i}{2\pi m_e}\right)\right]. \qquad 1.16$$

The temperature T_e is the bulk electron temperature of the warm plasma. At potential φ, the fluxes of the ions and electrons are the same, consistent with a current-free layer. The ions are denser,

but slower than the electrons. Equation (1.16) is derived from the continuity equation and requires that the fluxes of ions and electrons be equal to maintain zero-current across the flow. The masses of the ions and electrons enter Equation (1.16) through expressions for ion acoustic speed and thermal speed of the electrons, respectively. [Chen, 2006]

In order to function effectively as a propulsion system, the plasma passing through the magnetic nozzle must detach from the magnetic field. For the ions, this occurs mainly through inertial processes, but for the lighter electrons, it is necessary that the plasma be sufficiently collisional in the nozzle to enable cross-field transport of the electrons, so that ambipolar forces can allow them to detach with the ions. [Olson, *et al*, 2015] argue that anomalous diffusion processes are necessary in the magnetic nozzle to achieve the necessary flow rates. At a macroscopic scale, the criterion for inertial detachment of ions is that the Cowling number, the square of the ratio of the Alfvén velocity to flow velocity, is greater than unity, i.e., the flow is super-Alfvénic.

1.3.3 Reactor-Propulsion System Interface

The simplest model of the interface between the reactor well and the warm plasma is expressed in terms of the jet-side mirror ratio R_{mJ} and considers only the high-energy fusion products that depart the well through the loss cone at birth. For a D-T system, the energy of the prompt alphas passing from the reactor to the warm plasma is $\dot{n}^{\alpha}E^{\alpha}g_J V_r$, where E^{α} is 3.5 MeV, the energy of the alphas, V_r is the volume of burning plasma in the reactor, and $g_J = f(R_{mj})$. The energy of thermal species arriving at the warm plasma is $\dot{n}^{\alpha}g_J\xi^{\theta}E^{\theta}V_r$ and in the keV range, far less than that of the prompt alphas. From Section 1.3.1, ξ^{θ} is the ratio of thermal species to prompt alphas leaving the well. Thermal species could provide over 10 percent additional jet power. Therefore, it is important to know the energy of the thermal species when they arrive at the warm plasma.

1.4 Powering the Reactor

As stated in [Ellis, *et al*, 2001], to the first order, specific power needed to operate the reactor is

$$\overline{IV}_0 = \frac{n_i m_i u_\theta^2}{\tau_{mom}}, \tag{1.17}$$

where $\overline{IV}_0$ is the power (W/m^3) in terms of potential bias and input current, and τ_{mom} is the momentum confinement time. Equation (1.17) represents the power necessary to offset the loss of angular momentum due to the departure of ions from the centrifugal well. For a D-T system, the power from charged products available to operate the reactor is $\eta_P \overline{P_r^\alpha} g_P$, where η_P is the power conversion efficiency, $\overline{P_r^\alpha}$ is the rate of fusion power generated as alphas per volume of burning plasma. Momentum confinement time is equal to ion collision time scaled by the Pastukhov factor, as discussed in Section 1.2.2, so that $\tau_{mom} \sim \tau_{ii} \frac{M^2}{4} exp\left(\frac{M^2}{4}\right)$. With this in mind, Equations (1.3) and (1.17) can be used to characterize a plasma that will allow the reactor to power itself with the SWDEC using charged fusion products. And since $u_\theta^2 = M^2 \frac{k_B T_e}{m_i}$, it can be shown that

$$g_P \eta_P \left(\frac{1}{4 k_B T_e}\right) n_0 \tau_{ii} exp\left(\frac{M^2}{4}\right) x_D x_T \langle \sigma v \rangle_{DT} E^\alpha \approx Q^\alpha \geq 1, \tag{1.18}$$

where Q^α is introduced as the breakeven figure of merit for alphas in a D-T reactor.

1.5 Analysis Plan

1.5.1 Technical Objectives

The objective of this research is to assess the viability and performance of D-T fusion reactor using CM confinement applied to deep space propulsion. Central to the idea of viability is that the reactor

be self-powering. Viability is also a matter of DFD-CM performance in terms of specific jet power, thrust and specific impulse. The value of Q^{α} as defined in Equation (1.18) is strictly concerned with what is necessary to power the reactor and need not be more than 1.0. This differs from traditional definitions of Q for terrestrial power plants, where Q must be large enough to cover both breakeven and economic requirements. Ideal specific jet power (kW/m^3) is defined $\bar{P}_{J0} = \eta_J g_J \overline{P_r^{\alpha}}$, which relates jet power delivered to the warm plasma to the volume of burning plasma, a major factor in the size and mass of the power plant.

The problem is broken down into two parts. The first is to characterize the performance of the CM reactor and to demonstrate whether $Q \sim 1$ can be achieved. The second part is to evaluate the propulsion performance of the overall system. Given the power provided to the warm plasma by the reactor, it is necessary to quantify system losses in order to estimate the efficiency of the warm plasma propulsion system. An important part of propulsion performance is the operability of the warm plasma propulsion system relative to plume detachment.

1.5.2 Thesis Development

The research problem is addressed through the following stages of development, which build on the overview provided in this chapter. A review of relevant literature and prior art is provided in Chapter 2. The review is divided into two parts, the first related to centrifugal confinement of plasmas, and the second on plasma propulsion. Literature on centrifugal plasmas includes early theoretical work, and descriptions of centrifugal confinement experiments, including the MCX campaign in the 2000s. It also includes recent analytic treatments based on MCX. These papers are discussed in chronological order. Literature on propulsion systems presents two main themes relative to magnetic nozzles: plasma detachment and plasma acceleration. Some papers address

only one of these, several address both. This part of the literature review is organized by theme and by whether the paper is theoretical or experimental.

Chapter 3 describes centrifugal mirror reactor dynamics. This includes simplified solutions of the momentum equation at the reactor midplane, elaboration on the Alfvén velocity limit, derivation of the loss cone factor g, and development of the reactor heat balance model. The various terms in the reactor power balance are presented. The chapter then describes the code which models the 0D reactor power balance. "0D" refers to the fact that the reactor is modeled with constant, isotropic state and transport properties. The 0D code is capable of evaluating single use cases, and batch use cases with randomized inputs. Results from batch runs are analyzed to characterize viable domains of the reactor operating space.

Chapter 5 describes the propulsion system and associated modeling. It starts with the reactor-warm plasma interface This includes analysis of the well potential of the thermal ion species leaving the reactor in order to estimate their energy state as they arrive at the warm plasma. The second section of Chapter 5 describes physics related to the warm plasma, including energy deposition by fusion products, as well as transport, radiation and momentum losses within the warm plasma. Based on these considerations, a 1D model of the warm plasma is derived that estimates the state of the plasma as a function of radial distance from the centerline.

Plasma acceleration and expansion are also discussed Chapter 5. This section includes discussion of plume detachment, in particular, engineering criteria for plume detachment, e.g., the Cowling number for ion detachment. The magnetic nozzle is modeled in two parts, first the electrostatic acceleration of the warm plasma through the current-free structure, and then calculation of the plasma velocity and state properties as the plasma passes through the diverging part of the nozzle.

The second part of Chapter 5 describes the code resulting from integrating the models of the warm plasma and magnetic nozzle.

Chapter 6 provides analysis of the integrated system performance. A run matrix is developed for various reactor and warm plasma configurations. Post-processing and analysis of run data from respective cases characterize performance of various system configurations, as well as trends related to design choices, such as nozzle magnetic field configuration.

Chapter 7 summarizes key findings and contributions to the research, and it outlines future work.

1.6 Research Contributions

This work has resulted in four contributions. To start, it is the first analysis of the end-to-end performance of direct fusion drive based on centrifugal mirror confinement of the burning plasma. It demonstrates that the concept is thermodynamically feasible with nominal cycle efficiencies up to 50 percent based on fusion energy entering the propulsion system. The viability of the concept is indicated based on analysis showing the reactor is self-powering and that volumes of burning plasma are on the order of 1 m^3 for delivered jet power up to 500 kW.

The second contribution is characterization of CM fusion reactor performance and operability. A particular finding is that self-powering DFD-CM reactors may need to operate at Mach numbers greater than 9 for plasmas relevant to propulsion systems. The work also identifies and describes a novel behavior of the reactor CM plasma, a critical Mach number characterized by a minimum jet-side mirror ratio. Additionally, the research shows that operating regimes of self-powering CM

fusion reactors are significantly constrained by desirable operating parameters and nominal limits for magnetic and electric fields.

The third contribution is the development and preliminary application of a set of engineering models of the reactor, warm plasma, and plasma acceleration and expansion. These models are considered moderate fidelity in that they account for first order effects, as well as salient second order effects. For example, the 0D CM reactor model allows the specification of different mirror ratios for jet-side and power-side mirrors. The 1D warm plasma model accounts for radial variation of transport properties. The research developed engineering relations based on experimental data from the literature to assess likelihood of plume detachment as the plasma expands in the diverging section of the magnetic nozzle. These relations are incorporated into the plasma acceleration and expansion model.

The fourth contribution is identifying the possibility that the burning plasma in the reactor and the warm plasma may be electrically coupled. The nature of this coupling is uncertain, and the current research proceeds assuming that the coupling does not occur. However, the question indicates the need for further research.

References – Chapter 1

1. Baker, D.A., Hammel, J.E., Ribe, F.L., ”Rotating Plasma Experiments. I. Hydromagnetic Properties,” The Physics of Fluids 4, 1534 (1961);doi:10.1063/1.1706312
2. Ellis, R.F., A.B. Hassam, S. Messer and B.R. Osborn, “An experiment to test centrifugal confinement for fusion,” Physics of Plasmas, 8, 2057 (2001)

3. Reid, R.R., Romero-Talámas, C.A., Young, W.C., Ellis, R.F., and Hassam, A.B., "100 eV electron temperatures in the Maryland centrifugal experiment observed using electron Bernstein emission," Physics of Plasmas 21, 063305 (2014)
4. Personal communication with Dr. Adil Hassam, University of Maryland, June 2020
5. Clauser, T.M., "The Feasibility of Thermonuclear Propulsion," 1958, Proceedings of the Conference on Extremely High Temperatures, John Wiley & Sons, Inc.
6. Andrew M. Chap, Raymond J. Sedwick, "One-Dimensional Semianalytical Model for Optimizing the Standing-Wave Direct Energy Converter," JOURNAL OF PROPULSION AND POWER Vol. 31, No. 5, September–October 2015
7. Huba, J.D., Naval Research Laboratory Plasma Formulary, 2013
8. Pastukhov, V.P., Nucl Fusion 14 3, 1974
9. Teodorescu, C.; Clary, R.F.; Ellis, A.B.; Hassam, A.B.; Lunsford, R.; Uzun-Kaymak, I.; Young, W.C.; "Experimental study on velocity limits of magnetized plasmas," Phys. Plasmas 15, 042504 (2008)
10. Kuriki, K., and Okada, O., "Experimental Study of a Plasma Flow in a Magnetic Nozzle," The Physics of Fluids, Volume 13, Number 9, September 1970
11. Chen, F.R., "Physical mechanism of current-free double layers," Physics of Plasmas 13, 034502 (2006)
12. Olsen, C.S., Ballenger, M.G., Carter, M.D., Chang Diaz, F.R., Giambusso, M. Glover, T.W., Ilin, A.V., Squire, J.P., Longmier, B.W., Bering III, E.A., Cloutier, P.A., "Investigation of Plasma Detachment From a Magnetic Nozzle in the Plume of the VX-200 Magnetoplasma Thruster," IEEE Transactions on Plasma Science, Vol 43, No. 1, January 2015

2 Literature Review

2.1 Centrifugal Confinement and Thermonuclear Reactors

This section surveys research on centrifugal confinement starting with early theoretical development and experiments which took place from the 1950s through the 1990s. There follows a summary of selected papers that came out of the Maryland Centrifugal Experiment (MCX) in the 2000s and early 2010s. The objective is to provide an overview of key theoretical insights and to benchmark the current state of centrifugal confinement technology.

2.1.1 Centrifugal Mirror Theory

The motivation for early research into centrifugal confinement of plasmas was its potential for enabling thermonuclear fusion reactors by reducing end losses of ions and electrons in mirror devices. [Lehnert, 1974] and [Bekhtenev, *et al*, 1980] in particular were notable for their analyses of rotating plasmas specifically in the context of fusion reactors.

Lehnert considered a poloidal magnetic field scheme where rotating plasma speeds exceeded the critical ion velocity (CIV). CIV was set by ion-neutral interactions at the insulators, and its value calculated as $v_c = (2e\phi/m_i)^{\frac{1}{2}}$, and $(v_0)_{max} = v_c(r_0/r_w)$, where *0* and *w* refer to plasma radii at the outer equatorial plane and the wall. These relations follow from the "iso-rotation law" that assumed constant angular momentum on each field line. Lehnert proposed a momentum balance expressed in terms of C_w, the ratio of plasma density at the insulators to that at the equatorial plane: $C_w \sim exp(-m_i v_0^2/4k_B T) * (1 - r_w^2/r_0^2)$. This expression is based on the iso-rotation law and the assumption of constant temperature along the field lines. The exponential nature of $C_w$suggests

that mirror losses can be limited through centrifugal confinement. Given these results, Lehnert developed breakeven power balances for thermonuclear D-D and D-T plasmas. As an illustration, the case for D-T at 10^8 K (~ 8 keV) had a number density n_0 of 1.3×10^{20} #/m^3, β of 0.08, B_0 of 5 T, v_0 of 4.1×10^6m/s, and C_w of 10^{-5}. [Lehnert, 1974]

[Bekhtenev, *et al,*1980] outlined the major theoretical features of the thermonuclear plasma based on centrifugal confinement, including considerations for static equilibrium, reactor efficiency, and plasma stability. Azimuthal velocity is imparted by the $E \times B$ drift, where $E(r)$ is imposed by a system of concentric ring electrodes nested within the mirror region, and the potentials of the respective rings are graduated. Evaluating a D-T plasma, they posed a system with an electric field of 100 kV/cm, $n_0 = 3 \times 10^{13}$ #/cm^3, *β=0.25*, B_0*=15-25* kG, and mirror ratios varying from 2-7. The quantity of $n\tau$ achievable with centrifugal mirror confinement is characterized by requiring that electrons and ions depart at the same rate, and assuming that these rates follow from collision frequency. The development arrives the result that $n\tau$ is proportional to $exp(\Xi_i/k_B T_i)$, where Ξ_i is the potential energy of the ions determined by kinetic energy due to azimuthal velocity and electric potential. The work also develops estimates for $n\tau$ in an "ideal" plasma based on solving a one-dimensional Fokker-Planck (F-P) equation without a collision term, and assuming a square well. For mirror ratios of 2-7, $n\tau$ for the centrifugally confined plasma ranged from $2 - 10 \times 10^{10}$ #-s/cm^3. Various concepts for reactor design are presented, including the recovery of charged particles that escaped the well and their reinjection into the reactor. [Bekhtenev, *et al*, 1980]

[Hamieri, 1983] provides an analysis of equilibrium of rotating plasmas and finds that the velocity field in a rotating plasma is defined by the magnetic flux surfaces, a consequence of the frozen-in condition. Starting with ideal MHD equations, an expression is derived that describes the $\nabla\psi$

component of the momentum equation in cylindrical coordinates for static equilibrium of the plasma

$$\nabla \cdot \left(\frac{1}{r^2}\nabla\psi\right) + r\rho u_\theta \frac{d\Omega}{d\psi} + \frac{dP}{d\psi} = 0. \qquad 2.1$$

This relation is described as being the analog of the Grad-Shafranov equation for centrifugal confinement and shows the force balance across the flux surfaces. [Hamieri, 1983] The form shown in Equation (2.1) assumes that $B_\theta = 0$, and so associated arbitrary functions provided in the general form are not included, consistent with a similar expression provided in [Ellis, *et al*, 2001]

Contemporary with these efforts, Pastukhov formalized the description of electron confinement in the electrostatic well of a mirror device. Starting with the F-P equation, and including the collision term, he developed a relation for the case of collisional scattering into the loss cone. Based on the assumptions of a square well, where f does not change much in the axial direction, and that mirror bounce time is much less than collision time, Pastukhov reduced the F-P equation to $\frac{\partial f_0}{\partial t} = St[f_0]$, where f_0 is taken at the center of the well. St is the change in the distribution f caused by collisions and has a diffusional form in velocity space. Following the observation that f for most of the electrons differs only slightly from Maxwellian, because of the high positive potential in the well, it is asserted that change in characteristic time for f scales by $exp(e\phi/k_B\,T)$. This scaling appears again in the expression for electron loss that is ultimately derived

$$\frac{dn}{dt} \sim -\frac{2}{\sqrt{\pi}}\frac{n}{\tau_0}\frac{2R_m}{2R_m+1}\frac{\exp(-e\phi/k_BT)}{ln(4R_m+2)}. \qquad 2.2$$

Equation (2.2) says that the loss of electrons from an electrostatic well, or "trap," is reduced exponentially by the potential of that well, suggesting the idea of the Pastukhov factor mentioned in [Ellis, *et al*, 2001]. The factor R_m is the mirror ratio of the machine, and τ_0 is the relevant collision time. [Pastukhov, 1974]

[Catto and Bernstein, 1981] extend Pastukhov's work to include loss rates for ion species in a mirror confinement scheme. In this, they use a variational method, i.e., a trial function, to solve the collisional F-P equation, and so obtain an analytic function for the loss rate of charged species from an electrostatic well. It is assumed that $Ze\phi_0/k_BT > 1$, where ϕ_0 is the maximum potential relative to that at the center of the well, where $\phi = 0$. The constraint allows the confined species to be treated as a Maxwellian distribution, and that this portion of the population in the high-energy tail does not affect the rest of the distribution. This condition permits the collision operator to be linearized. Assuming the bounce frequency is much higher than other characteristic frequencies, e.g., ion-ion collisions, the F-P equation is reduced to $\oint \frac{ds}{u_\parallel} C_f = 0$, where $u_\parallel$ is the parallel speed, and C_f is the F-P collision operator. The variational method allows solution of the F-P equation without knowledge of the distribution function for f, and it results in the following expression for losses for charged species

$$\frac{d\langle n\rangle}{dt} = -\left(\frac{2n\Sigma\exp(-Ze\phi_0/k_BT)}{\sqrt{\pi}\tau(Ze\phi_0/k_BT)ln(R_m\Sigma)}\right)\Gamma_B, \qquad 2.3$$

where $\Sigma = Z_i + 1$ for electrons, and one for ions. The time τ is the characteristic collision time, and Γ_B is a function of the magnetic field configuration and is equal to one, given the square well approximation. [Catto and Bernstein, 1981]

Collectively, these papers present several important ideas related to centrifugal confinement. The first is the iso-rotation law, which requires that azimuthal velocity Ω remain constant on a given flux surface and the corollary that ϕ also is a constant. [Lehnert, 1974][Bekhtenev, *et al*,1980]

As pointed out in [Ellis, *et al*, 2001], these results indicate that ϕ and ψ and Ω are related by $\frac{d\phi}{d\psi} = \Omega$. A second, related idea is that for a rotating plasma confined by a magnetic field, the hydrostatic equilibrium velocity field must lie within the flux surfaces of the magnetic field, due to frozen-in requirements. Additionally, the hydrostatic equilibrium can be expressed in terms of momentum forces evaluated at any given flux surface, as shown by Equation (2.1). [Hameiri, 1983] One consequence of the frozen-in condition is that in ideal rotating plasmas, there is no mass flow across flux surfaces, i.e., $u \cdot \hat{r} = 0$.

[Pastukhov, 1974] derived the exponential scaling for confinement time of electrons in an electrostatic well confined by a mirror scheme. [Catto and Bernstein, 1981] extended this relationship to include ions. Additionally, [Lehnert, 1974] explicitly demonstrated the potential of rotating plasmas for confining thermonuclear plasmas, by showing the exponential drop-off in plasma density from the center of the well. Finally, the hydrostatic equilibrium of the plasma, described in Equation (2.1) shows the relationship between $(\phi, \psi, \Omega)$and the pressure gradient $\frac{dP}{d\psi}$. At the midplane for a given B_z and constant ψ on a flux surface, Equation (2.1) reduces to $\frac{dP}{d\psi} = -r\rho u_\theta \frac{d\Omega}{d\psi} + C(z_o, \psi)$, where $C(z_0, \psi)$ is a function of ψ only. Since $\hat{r}$ lies on $\nabla\psi$ at the midplane,

this shows that a negative pressure gradient in the radial direction can be sustained as long as $\left|r\rho u_\theta \frac{d\Omega}{d\psi}\right| > C(z_0, \psi)$. These results for radial equilibrium complement those for axial confinement shown in Equations (1.12) and (1.13).

2.1.2 Early Centrifugal Mirror Experiments

Centrifugal mirror confinement was demonstrated in the US with Ixion in the late 1950s, in Sweden during the 1960s and 1970s with the F I and F III machines, and in the Soviet Union with PSP-2 in the 1980s.

The Ixion consisted of a vacuum chamber 85 cm in length and 24 cm in diameter, and which served as the system anode. At each end was a Pyrex insulator with a separation of 61 cm between them. The cathode was implemented as a beam of electrons along the axis. Power was supplied through a capacitor bank that could provide a 20 kV potential. The fill gas was deuterium, and the active plasma was 2 liters in volume and occupied the annular region around $r = 9.5\ cm$. The magnetic field at midplane was 9.5 kG, and typical electric field was 740 V/cm, implying rotation velocities up to 8×10^6 cm/s. During operation, the investigators reported an initial ionization phase with 7.5 kV potential. The potential dropped as current was drawn and the plasma started rotation. At steady-state, a typical run drew a current of 2 kamp, and rotation and was sustained for approximately 300 μs. Rotational velocities of 4×10^6 cm/s were observed at $r = 11\ cm$, based on Doppler shift of spectral lines of carbon impurity ions. The electric field was small at the outer wall, possibly due to plasma-wall interactions. Figure 2-1 shows measurements of the electric

field. The circular and square symbols are from different instruments at the midplane; the triangles are taken 19 cm from the midplane. [Baker, *et al*, 1961]

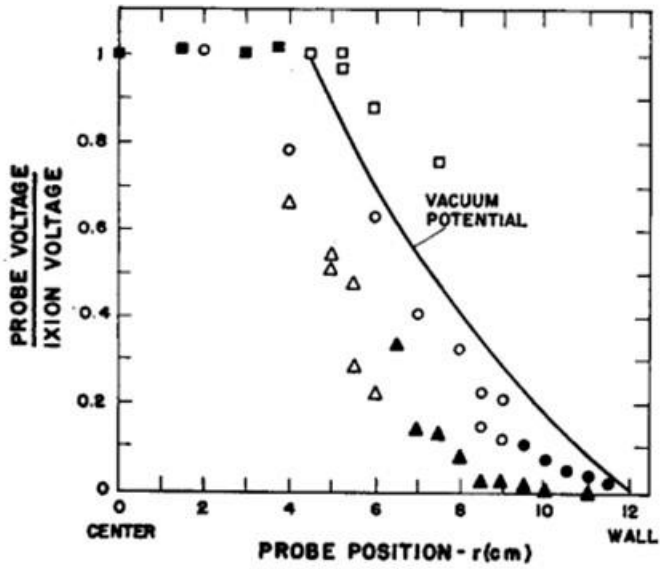

Figure 2-1 - Ixion electric field measurements [Baker, et al, 1961]

One set of experiments with Ixion consisted of measuring the potential drop after cutting power from the capacitor banks. The magnetic field was 7.5 kG and the initial potential 7 kV. Based on the transient response, the resistance and capacitance for the plasma were estimated, with the resistance increasing by 3 orders of magnitude and the capacitance decreasing by a like amount. In the same experiments, estimated rotational energy from the drift velocity decreased from 100 J to 0.01 J in 800 μs. The investigators reported observing voltage limiting above 7.5 kV, when resistance dropped and back emf approached zero. The losses were initially attributed to the velocity limit of ions passing through neutrals in the end regions, as predicted by Alfvén. Subsequent measurements of radiation losses indicated that the limit was likely due to ultraviolet emissions. [Baker and Hammel, 1961]

In a paper discussing velocity and β limits in centrifugal mirror plasmas, Lehnert describes the FI and FIII machines operated in Sweden. The FI was a dipole configuration and had been used in many experiments by the time of that writing. It had demonstrated the critical ion velocity limit predicted by Alfvén for neutral-ion interactions. The more recent FIII was built with the objective of investigating plasmas with higher rotational velocities. Plasma rotation was induced by discharging current from a capacitor bank across a poloidal magnetic field, which resulted in the $E \times B$ drift. The anode was at an inner annulus surrounding the field magnets, and cathode plates were located so as to set the last good flux surface (LGFS). The FIII demonstrated a limit in β related to a "centrifugal expansion instability," i.e., an outward distending of the plasma and flux surfaces due to increased angular momentum related to the higher β. [Lehnert, 1974]

The PSP-2 was a magnetic mirror device with a radial electric field imposed by a system of concentric ring electrodes. The concept for the device had been previously described by [Bekhtenev, *et al*, 1980]. PSP-2 experiments achieved radial electric fields of 0.5 MV and highly ionized rotating plasmas in a "quasi-stationary mode." At 20-30 keV, ions were highly energetic, while electrons demonstrated energies on the 1 keV range. The machine operated with hydrogen fed through neutral gas puffs. System parameters were *B* field of 9-10 kG, mirror ratio of 2.4, 450 kV potential bias, and number density of 4×10^{11} #/cm^3. Active plasma volume was 0.1 m^3, and ion confinement times in the 100 μs range. The MHD stable plasmas achieved by PSP-2 were attributed in part to the consequences of the iso-rotation law. [Adrashitov, *et al*, 1991]

The respective experiments demonstrated centrifugal mirror confinement with supersonic flows, as well as various architectures. For example, in the Ixion, an electron beam served as the central electrode, while the PSP-2 employed ring electrodes. The experiments varied in scale, with the

PSP-2 operating at extremely high ion temperatures, e.g., 20-30 keV, and electric fields approaching the threshold for thermonuclear operation, i.e., 0.5 MV/m. The FI and FIII machines appear to have verified the existence of the critical ion velocity limit.

2.1.3 The Maryland Centrifugal Experiment (MCX)

[Ellis, *et al*, 2001], referenced earlier, provides a comprehensive prospectus of the Maryland Centrifugal Experiment (MCX) that at the time was in development at the University of Maryland. The paper provides an overview of the underlying principles related to magnetized particle motion, MHD equilibrium, plasma transport, and stability. It also describes the components of the MCX system, including the axial magnetic field, the vacuum vessel, the central core for biasing the plasma, the capacitor discharge system, and insulating end assemblies. Anticipated operational characteristics were projected, including B-field of 0.2 to 2 T, mirror ratios of 3-10, potential less than 20 kV, number densities of 10^{19} to 10^{20} #/m^3, $T_e \sim T_i \sim$ 10-100 eV, and rotational Mach numbers of 3-6.

Published in the same timeframe, [Huang and Hassam, 2001] describes a simulation of viscous shear and its effects on flute instabilities in a generic centrifugal mirror plasma. Flute instabilities are inherent in mirror confinement schemes, and they result from particle exchange between field lines heavily populated with highly energetic particles and those populated less energetic particles. The dynamics of the instability are analogous to the Rayleigh-Taylor instability in gravitational fields. The MHD simulation suggests that shears may disrupt and disperse convection cells responsible for the flute instability. A 2D simulation first demonstrated the expected hydrostatic equilibrium, with outboard localization of plasma pressure and density at the midplane. The velocity field produced by the simulation was consistent with magnetic flux surfaces, an expected outcome. In a 3D simulation, random noise was introduced into the steady-state plasma, but with

finite viscosity included in the model there was no indication of the flute instability over a period of 60 Alfvén time scales (L_{char}/V_A). Based on these findings it is asserted that the velocity shear rendered the flow field laminar.

A later simulation evaluated time dependent MHD and transport equations in the (r, z) plane of an (r, z, θ) system. The geometry consisted of an electrode in center with a poloidal magnetic field. The electrode was fed by an insulated conductor extending to one wall. Viscosity and resistivity were isotropic, while perpendicular and parallel thermal conductivity were specified. It was assumed that Ohmic heating was small relative to viscous heating. The model included a no-slip condition where field lines intersected solid surfaces. Transient start-up simulations show the electric field penetrating the plasma and then the achievement of steady-state. In the steady-state, the velocity field conforms to the magnetic flux surface. The pressure is localized to the outboard side of the electrode, and detachment of the plasma from the walls is observed, as the centrifugal motion confines the plasma. The pressure ratio of the confined plasma to that at the walls is 40 to one. In steady-state, viscous losses impose an $F \times B$ drift and an accompanying radial current that counters the applied electric field. This condition necessitates the replenishment of the current from external sources in order to maintain the electric field. [Osborn, *et al*, 2003] In assessing the MCX, [Aydemir, 2004] proposed that centrifugal confinement of the plasma at midplane was feasible, but also flagged concerns about rapid heat conduction along magnetic field lines. The work also suggested a potential sub-Alfvén upper limit to rotational speed related to the square of the ratio of acoustic and Alfvén velocities.

An early MCX experiment characterized its momentum confinement time by measuring transient voltages and currents through the system and then applying the measurands to an electrical model of the system. In this manner, data gathered over 43 shots allowed for a rough estimate of

$\tau_{mom} \sim O(10^2 \mu s)$, that was much longer than characteristic MHD instability growth. The work discussed the possibility that τ_{mom} might be dominated by ion-neutral collisions. [Messer, *et al*, 2005] In early spectrographic measurements of the MCX, [Ghosh, *et al*, 2004] measured N^+ and neutral hydrogen temperatures using Doppler shift and Doppler broadening methods. The temperature of neutral hydrogen atoms was estimated to be 5-10 eV with 10km/s rotation velocity. Electron temperature was inferred to be ~15eV, based on line intensities relative to those of trace C ions. [Ghosh, *et al*, 2006] obtained radially resolved velocity profiles in the MCX using a five channel fiber-optic collection system in tandem with a high-resolution spectrograph. Figure 2-2 shows rotational velocities for trace C^+ ions (open symbols), which are in good agreement with analytic estimates (closed symbols.)

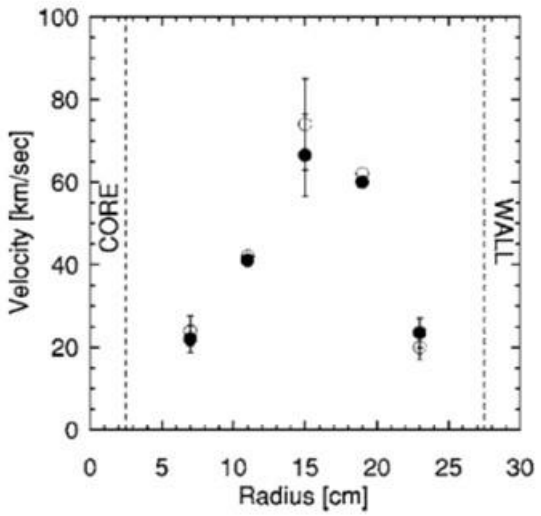

Figure 2-2 - MCX radial velocity measurements [Ghosh, et al, 2006]

[Uzun-Kaymak, *et al*, 2008] investigated residual fluctuations in the MCX at the edge of the plasma region through varying levels of imposed shear. Frequency spectra obtained from 16 azimuthal magnetic pickup coils were analyzed and found to exhibit predominantly low

interchange modes. Further testing with higher resolution spectral analyzers uncovered indications of non-linear mode coupling.

[Teodorescu, *et al*, 2008] reported on theoretical and experimental treatments of Alfvénic velocity limits in rotating plasmas. The MHD equations were used to develop a relation between changes in magnetic flux and the Alfvén Mach number (M_A), also known as the Kármán number (K) previously discussed,

$$\frac{\Delta B_z(r)}{B_z(r)} = \beta + \int_r^{r_2} M_A^2 \frac{dr}{r}. \qquad 2.4$$

For finite values of M_A radially averaged values cannot exceed 1 without severely distorting the magnetic field within the control volume. The limit was experimentally demonstrated in MCX by increasing n_0 at varying magnetic fields. Figure 2-3 shows the data for bias of 17 kV, $B = 0.11T$ (filled symbols) and $B = 0.23T$ (open symbols).

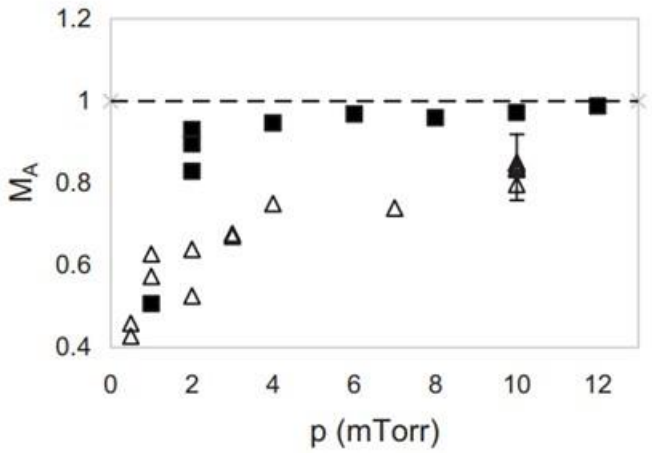

Figure 2-3 – Alfvén velocity limits [Teodorescu, et al, 2008]

[Teodorescu, *et al*, 2010(1)] using interferometric density measurements in a Mach 2 experiment demonstrated axial confinement over many 1000s of flute instability times, with midplane

densities ~ 5×10^{20} vs. end densities $< 1 \times 10^{20}$ at $R_m = 8$. [Teodorescu, et al, 2010 (2)] investigated the possibility of sub-Alfvénic velocity limits related to the critical ionization velocity predicted by Alfvén. This limit would be expected to manifest itself at the insulators where concentrations of neutrals are higher. As higher values of Ω were approached in experiments, externally applied torques to the plasma appeared to result in increased plasma density or lower values of momentum confinement time, instead of higher rotation velocities. Various methods were attempted to exceed the limit, including increasing voltage and moving insulators further apart.

[Young, *et al*, 2011] reported on the measurement of diamagnetic flux in MCX. The diamagnetic flux was shown to peak at the midplane, indicating higher pressure there, and thus demonstrating effective confinement. Theoretical estimates for diamagnetic flux were in good agreement with experimental values. Additionally, both theoretical and experimental data show that for centrifugally confined plasmas with high mirror ratios ($R_m > 5$), the magnetic field peaks at midplane and exceeds predicted values for non-rotating plasmas.

[Romero-Talámas, *et al*, 2012] reported on high-frequency voltage fluctuations in MCX run data and attribute them to changes in magnetic inductance at the inner flux surfaces. These changes result from localized deformations in the B-field, which expand and then snap back by merging or reconnecting with field lines in the affected region. The result is that iso-rotation is not a uniform condition in the plasma for the inner flux surfaces where differences in angular velocity between midplane and ends were observed to be in the $3 - 4 \times 10^5$ rad/s. Additionally, data in this work appears to show MCX exceeding critical ion velocity for the first time. This occurred over a 0.5 ms time segment during which time iso-rotation was also uniform across the flux field.

[Reid, *et al*, 2014] evaluated electron temperatures in an MCX plasma by measuring electron Bernstein waves (EBW) coupled to an electromagnetic mode. This mode was detected by an antenna within the MCX pressure vessel, but outside of the plasma. Measurements indicated an average electron temperature of 20eV, but based on the prediction of 20 percent effective coupling, a maximum of 100eV with a 500μs confinement time was inferred.

[White, *et al*, 2018] offered an analysis of centrifugal confinement that included higher fidelity treatment of particle kinematics, vis-à-vis cyclotron motion about $\boldsymbol{B}$ field lines. The analysis considered finite Larmor motion in highly magnetized plasmas, and combined this motion in the lab frame with Ω. One result of the analysis was the prediction of electron losses from low rotation near the plasma edge, due to wall effects.

The MCX successfully demonstrated supersonic azimuthal flow up to Mach 2.5, as well as axial confinement of the plasma, evidenced by an order of magnitude density drop from the midplane to the insulators. Additionally, plasma confinement times of more than 200 μs were achieved. Typical plasmas were between 10^{20} and 10^{21} $\#/\mathrm{m}^3$ number density with ion temperatures of 40eV, and they were almost completely ionized. Viscous control of stabilities was demonstrated as the plasma could be maintained for thousands of flute instability times. The Alfvén velocity limit was demonstrated, i.e., $K \leq 1$. MCX potentially exceeded the critical ion velocity, but that result and the general applicability of the limit remain inconclusive. [Ellis, *et al*, 2012]

2.2 Propulsion Performance

The research question in this section is motivated by the frozen-in condition which predicts that for ideal MHD, particles should not be able to detach from the magnetic field lines. This is a critical

consideration for propulsion performance and for which there does not appear to be a technical consensus. Other factors related to propulsion, including plasma acceleration in the magnetic nozzle, are also addressed in the surveyed literature.

2.2.1 Theoretical Work and Simulations

[Hooper, 1970] was among the first to address the specific question of plasma detachment from a magnetic nozzle. He developed a kinematic criterion that balances kinetic energy of the charged species with the energy of the magnetic field. Beginning with a description of electron drift velocity in the frame of the local magnetic flux surface, he derived an expression that includes a "hybrid" Larmor radius, i.e., the geometric mean of the ion and electron Larmour radii. This equation is reduced to an algebraic expression with a family of solutions indicating detachment will preferentially occur near the centerline of a coaxial plasma. For a heavy ion, e.g., argon, only 4 percent of the axial aperture would allow plasma to escape the nozzle. Cross-field currents and dissipative processes are not addressed in the model.

The interplay between the externally generated magnetic field of the nozzle and the plasma magnetic field is considered by [Briezman, *et al*, 2007]. Briezman and his colleagues addressed high-energy ions and cold electrons flowing from a helicon-ion cyclotron heating (ICH) source. Starting with the Vlasov equation and assuming a collisionless plasma, an expression for azimuthal current is derived. This expression is further reduced to paraxial ideal MHD equations. A relation for the external magnetic field based on Ampere's law is then developed. These two sets of equations are coupled by determining self-consistent, steady-state solutions for the plasma boundary using a numerical scheme formulated in a Lagrangian frame. The solutions indicate that

the external magnetic field stretches, and that the resulting ion stream tubes depart from the vacuum external field as the plasma transitions to super-Alfvénic velocities. The analysis is based on two key assumptions: 1) initial flow conditions are supersonic downstream of the nozzle throat; 2) the nozzle itself is slowly diverging. It should be noted that experimental investigators, e.g., [Deline, *et al*, 2009] and [Takhashi, 2017] attribute detachment in their respective experiments to stretching of the external magnetic field "to infinity," in theory obviating the frozen-in condition for charged species.

[Ilin, *et al*, 2002] report on simulation of detachment of a deuterium plasma in the VF-24 Variable Specific Impulse Magneto Rocket (VASIMR) then being developed by the Advanced Space Propulsion Laboratory. A central consideration in detachment is the increase of the magnetic pressure ratio β in the far-field, such that when $\beta > 1$, the plasma has "enough energy to stretch the magnetic field lines along the flow and thereby detach from the thruster." They note that this condition also implies that the flow velocity is greater than the Alfvén velocity. The simulation is solved in steady-state and includes modules for the external field, ion motion, the electric field, and the plasma magnetic field. Ion energy is adiabatic at 100 eV, and a constant electron temperature of 5 eV is assumed. The Larmor radius for ions is shown to exceed the plasma radius near the nozzle exit, while that of the electrons remains much smaller than the plasma radius into the far-field. Consistent with the increase in the Larmor radius, the magnetic moment of the ions increases with plasma expansion, indicating a loss of adiabaticity in the system.

[Ahedo and Merino, 2014 and 2017] provide different perspectives on detachment, and in particular emphasize that mechanisms related to detachment are intimately related to thrust. From a phenomenological view, ion detachment is characterized kinematically through the following relation

$$\kappa_i R \sim \frac{1}{M^2} + \frac{\omega_{i0}^2 (B/B_0)}{M^2} \qquad 2.5a$$

Here, $\kappa_i R$ is the curvature of the ion stream tube in the meridional plane, M is the Mach number, ω_{i0} is the ion cyclotron frequency, and B/B_0 is the ratio of the magnetic field to that at the nozzle throat. The numerator in the second term of Equations (2.5a) will decrease in the far-field, as M^2 increases, so that the trajectory of the ions becomes more shallow in the meridional plane and depart from the magnetic field lines. The ions are assumed to be cold, so that the energy of the plasma is carried entirely by the electrons

$$T_{e0} \ln(n/n_0) - e\phi = H_e(\psi), \qquad 2.5b$$

and

$$-eu_{\theta e} = \nabla H_e(\psi). \qquad 2.5c$$

The value $H_e(\psi)$ is invariant along a given stream tube and can be calculated from initial conditions in the throat. A negative gradient in density number, i.e., pressure, results in the diamagnetic current eu_θ that produces a magnetic force repulsive to the external magnetic field and so generates thrust. This thrust would be additive to that produced by the electrostatic acceleration. The high-energy tail of the electron population moves downstream faster than the ions, the respective values for $u_e n_e e = u_i n_i e$ so that globally net current is zero, even while local currents in the meridional plane follow from the ambipolar potential.

[Araya, *et al*, 2011] performed a parametric analysis of a normalized casting of the Boltzmann equation, where plasmas within the magnetic nozzle were characterized according to the relative contributions of terms for effects related to the electric field, magnetic field, or collisions. For

practical systems, and for the Ad Astra VX-200 in particular, plasma flows move through regions that are dominated by either magnetic forces or electric forces. In the nozzle throat, where the Larmor radii of both ions and electrons are smaller than the characteristic length, both species are dominated by the magnetic field, and perpendicular motion is restricted. In the electromagnetic region, the ion Larmor radius becomes larger than the characteristic length, and ion motion is dominated by the electric field, while the electrons remain magnetized. In the electric region, Larmor radii of both ions and electrons are larger than the characteristic length, and both species are dominated by electrical forces. In this model, collisional processes tend to decrease as the Larmor radii decrease.

Theories for mitigating the frozen-in condition relative to plume detachment can be divided roughly into: 1) the notion of stretching of magnetic field lines; and 2) kinematic or inertial mechanisms. Several investigators, including those who proposed infinite magnetic field stretching, assert that detachment is related to super-Alfvénic velocities, and the loss of adiabaticity, i.e., the increase in μ, the magnetic moment. However, these two considerations appear to favor the inertial model. The Alfvén velocity is inversely proportional to the square root of the ion mass, and the magnetic moment reflects the ion kinetic energy relative to that of the magnetic field. [Araya, *et al*, 2011] describe the contributions of collisions and transport properties which provide insight into how the much lighter electrons might also detach with the ions.

2.2.2 Experiments in Plasma Detachment

Early work by [Kuriki and Okada, 1970] demonstrated the effect of electrostatic acceleration. These investigators observed an axial potential gradient downstream of the magnetic nozzle throat and correlated the resulting electric field with ion convective velocity. The argon plasma was low temperature and had a low ionization level. The resulting velocity profile peaks just downstream

of the nozzle, possibly because of the preponderance of neutrals. They show that the radial electric field – aligned with the magnetic field lines upstream of the throat – serve to compress the charged species; while the axial electric field downstream accelerate them.

[York, *et al*, 1992] produced a deuterium plasma in a theta-pinch device with $T_e \sim 20$ eV. Flow velocities reached a maximum of 80 km/s just downstream of the nozzle exit and then decreased. Observed values for the external magnetic field relative to those of the plasma magnetic field increased downstream, which the investigators cited as evidence that the external field was self-collimating.

Similar to the criterion for ion detachment provided by {Ahedo and Merino], [Deline, *et al*, 2009] propose the parameter

$$\beta_k = \frac{\mu_0 n_i m_i U^2}{B^2} = \left(\frac{U}{U_A}\right)^2 > 1, \qquad 2.6$$

where U_A is the Alfvén velocity, the corollary being that detachment requires super-Alfvénic velocities as a condition for detachment. The investigators show where this condition is achieved in their experimental results, and its location is qualitatively similar to that suggested by Ahedo and Merino. Flow velocities for both hydrogen (17.5 km/s) and helium (15.5 km/s) plasmas are both relatively constant along the expansion zone. At the same time, measurements for T_e for the hydrogen plasma also remain constant at 1.2 eV over the expansion region, as well. There were no measurements of ion temperatures. Note that β_k as defined by Deline is the inverse of the Cowling number. The investigators suggest that internal, local currents in the plasma stretch the external magnetic field lines facilitating detachment. They state that the ion current departs from expected values for frozen flow in the expansion region, and that they remain fairly constant at ~ 275 A.

This is described as evidence of detachment. They cite [Breizman, *et al*, 2008] as describing the mechanism of detachment from stretched magnetic field lines.

[Longmier, *et al*, 2011] reported on ambipolar ion acceleration in the VX-200i. This experiment was performed with the helicon only, i.e., without operating the ICH second stage. They note the absence of a current-free double layer (CFDL) in their experiment, but observe instead the presence of a "large potential structure," i.e., a potential drop of 12V along the expansion zone.

[Olsen, *et al*, 2015] provided an extensive dataset and detailed analysis based on experiments with the VX-200. They discount mechanisms such as magnetic field line stretching. Their explanation is that the ions demagnetize as their Larmor radii increase in the expansion zone, but that the overall process of plume detachment derives from non-adiabatic processes such as cross-field diffusion of electrons, Coulomb interactions, anomalous transport, and force balance. These factors are related, e.g., anomalous transport facilitating electron cross-field diffusion. Coulomb interactions and force balance are evidenced by the occurrence of high-frequency electric fields observed along the edges of the plume. The investigators report Hall parameters for $e-i$ and $e-e$ interactions falling below unity toward the end of the expansion zone. Collectively, this model and the specific, supporting data make a convincing case for a valid detachment mechanism. Finally, while the investigators state that they observed no change in the external magnetic field, they did observe a self-collimation of the plume. The scale of the experiment is important, as well, as the far-field in the test cell is well away from the nozzle exit.

[Takahashi, *et al*, 2016] offer a macroscopic analysis of magnetic nozzle performance with argon. B is 0.28T, T_e is 3 eV. A parametric performance model was developed that estimated T_e, n_0, and

F_t as functions of a loss parameter designated α. Data from the experiment were compared with the parametric values and loss parameter of 10% to the walls was inferred.

[Zhang, *et al*, 2016] provides experimental evidence indicating polytropic processes in magnetic nozzle flow for argon from a helicon plasma source. Electron density and temperature were measured over the expansion region and then used to calculate an effective ratio of specific heats, $\gamma_{eff} = 1.17$, vs. ideal of 1.67 expected for argon. The investigators infer the presence of a CFDL based on observations consistent with those in experiments by other investigators. They go on to discuss its possible role in plasma acceleration, noting that a higher population of energetic electrons downstream of the CFDL would neutralize currents in the ion beam. The investigators use measurements of plasma potential to estimate the electron energy probability functions (EEPFs). They describe these results in connection with the high-energy electron population produced downstream. A short development near the end of the paper analytically links the increase in ion kinetic energy with a decrease in electron enthalpy over the expansion zone.

[Takahashi, *et al*, 2017] reported on observations of changes in the external magnetic field in magnetic nozzles. Their results show that the magnetic field is distended over the expansion zone and into the far-field. Specifically, the field is reduced in the expansion zone, and then increases in the far field before returning to baseline field behavior.

Although the mechanisms for plume detachment do not appear to be a fully settled matter, both theoretical considerations and experimental data appear to favor the inertial detachment model. In particular, [Olsen, *et al*, 2015] provide experimental results that ion detachment occurs primarily through inertial mechanisms, and that the necessary ambipolar electron detachment is facilitated by collisional processes in the nozzle. This model underpins the “warm plasma” concept outlined

in Chapter 1, i.e., the energies of the fusion products – essentially collisionless - are deposited into the propellant, which then flows through the nozzle at temperatures low enough to allow collisions necessary for detachment. The mechanism for plasma electrostatic acceleration through the nozzle throat are discussed in [Kuriki and Okada, 1970], [Longmier, *et al*, 2011],[Olsen, et al, 2015], and [Zhang, *et al*, 2016]. Based on these investigations, it appears that initial plasma acceleration occurs over a relatively short distance across a current-free "structure" in the vicinity of the nozzle throat.

References – Chapter 2

1. Lehnert, B. "On the Possibilities of Plasmas Rotating at Supercritical Velocities," 1974 Phys. Scr. 9 189
2. Bekhtenev, A.A., *et al*, "Problems of a thermonuclear reactor with a rotating plasma," 1980 Nucl. Fusion 20 579
3. Hameiri, Eliezer, "The equilibrium and stability of rotating plasmas," The Physics of Fluids 26, 230 (1983); doi: 10.1063/1.864012
4. Ellis, R.F., A.B. Hassam, S. Messer and B.R. Osborn, "An experiment to test centrifugal confinement for fusion," Physics of Plasmas, 8, 2057 (2001)
5. Pastukhov, V.P., Nucl Fusion 14 3, 1974
6. Catto, P.J., Bernstein, Ira B., "Collisional end losses from conventional tandem mirrors," Phys. Fluids 24 (10), October 1981
7. Baker, D.A., Hammel, J.E., Ribe, F.L., "Rotating Plasma Experiments. I. Hydromagnetic Properties," The Physics of Fluids 4, 1534 (1961);doi:10.1063/1.1706312

8. Baker, D.A., and Hammel, J.E., “Energy Measurements and Velocity Limiting Effects,” The Physics of Fluids 4, 1549 (1961);doi:10.1063/1.1706313
9. Lehnert, B., “On the Equilibrium and Stability of Rotating High-beta Plasmas,” Phys. Scr. 9 229, 1974
10. Abdrashitov, G.F., Beloborodov, V.I., Volosov, V.I., Kubarov, V.V., Popov, Y.S., Yuda, Y.S., “Hot Rotating Plasma in the PSP-2 Experiment,” Nucl. Fusion 31 1275 1991
11. Huang, Y., “Velocity Shear Stabilization of Centrifugally Confined Plasma,” Physical Review Letters, Volume 87, Number 23, 3 December 2001
12. Osborn, B. R., Ellis, R. F., and Hassam, A. B., “Numerical simulation of the equilibrium and transport of a centrifugally confined plasma,” Physics of Plasmas 10, 2389 (2003); doi: 10.1063/1.1571543
13. Aydemir, A.Y., “Magnetohydrodynamic equilibrium and stability of rotating plasmas in a mirror geometry,” Physics of Plasmas 11, 5065 (2004); doi: 10.1063/1.1799352
14. Messer, S, Ellis, R., Case, A., Gupta, D., Hassam, A., Lunsford, R., and Teodorescu, C., “Observation of momentum confinement time scalings in a rotating plasma,” Physics of Plasmas 12, 062509 (2005); doi: 10.1063/1.1931981
15. Ghosh, J., Elton, R.C., Griem, H.R., Case, A., Ellis, R., Hassam, A.B., Messer, S., and Teodorescu, C., “Spectroscopic measurements of plasma rotation and ion and neutral atom temperatures in the Maryland Centrifugal Experiment,” Physics of Plasmas 11, 3813 (2004); doi: 10.1063/1.1765132
16. Ghosh, J., Elton, R.C., Griem, H.R., Case, A., DeSilva, A.W., Ellis, R.F., Hassam, A., Lunsford, R., and Teodorescu, C., “Radially resolved measurements of plasma rotation and

flow-velocity shear in the Maryland Centrifugal Experiment," Physics of Plasmas 13, 022503 (2006); doi: 10.1063/1.2167915

17. Uzun-Kaymak, I.U., Guzdar, P.N., Clary, R., Ellis, R.F., Hassam, A.B., and Teodorescu, C., "Analysis and modeling of edge fluctuations and transport mechanism in the Maryland Centrifugal Experiment," Physics of Plasmas 15, 112308 (2008)
18. Teodorescu, C., Young, W.C., Swan, G.W.S., Ellis, R.F., Hassam, A.B., and Romero-Talámas, C.A., "Confinement of Plasma along Shaped Open Magnetic Fields from the Centrifugal Force of Supersonic Plasma Rotation," PRL 105, 085003 (2010) PHYSICAL REVIEW LETTERS, 20 August 2010
19. Teodorescu, C., Clary, R., Ellis, R.F., Hassam, A.B., Romero-Talámas, C.A., and Young, W.C., "Sub-Alfvénic velocity limits in magnetohydrodynamic rotating plasmas," Physics of Plasmas 17 052503 (2010)
20. Young, W.C., Hassam, A.B., Romero-Talámas, C.A., Ellis R.F., and Teodorescu, C., "Diamagnetism of rotating plasma," Physics of Plasmas 18, 112505 (2011)
21. Romero-Talámas, C.A., Elton, R.C., Young, W.C., *et al*, "Isorotation and differential rotation in a magnetic mirror with imposed E×B rotation," Phys. Plasmas 19, 072501 (2012); doi:10.1063/1.4731729
22. Reid, R.R., Romero-Talámas, C.A., Young, W.C., Ellis, R.F., and Hassam, A.B., "100 eV electron temperatures in the Maryland centrifugal experiment observed using electron Bernstein emission," Physics of Plasmas 21, 063305 (2014)
23. White, Roscoe, Hassam, Adil, and Brizard, Alain, "Centrifugal particle confinement in mirror geometry," Physics of Plasmas 25, 012514 (2018); doi: 10.1063/1.5003359

24. Ellis, R.F., Hassam, A.B., *et al*, 2012, "Final Technical Report 2012, The Maryland Centrifugal Experiment (MCX): Centrifugal Confinement and Velocity Shear Stabilization of Plasmas in Shaped Open Magnetic Systems," DOE Grant Number DEFG0200ER54605, 2012

25. Hooper, E.B., "Plasma Detachment from a Magnetic Nozzle," Journal of Propulsion and Power, Vol.9, No.5, Sept-Oct. 1993

26. Breizman, B.N., Tushentsov, M.R., Arefiev, A.V., "Magnetic nozzle and plasma detachment model for a steady-state flow," Phys. Plasmas 15, 057103 (2008)

27. Deline, C.A., Bengston, R.D., Breizman, B.N., Tushentsov, M.R., Jones, J.E., Chavers, D.G., Dobson, C.C., Schuettpelz, B.M., "Plume detachment from a magnetic nozzle," Physics of Plasmas 16, 033502 (2009)

28. Takahashi, K., Ando A., "Laboratory Observation of a Plasma-Flow-State Transition from Diverging to Stretching a Magnetic Nozzle," Physical Review Letters 118, 225002 (2017)

29. Ilin, A.V., Chang-Diaz, F.R., Squire, J.P., Tarditi, A.G., Breizman, B.N., Carter, M.D., "Simulation of Plasma Detachment in VASIMR," AIAA 2002-0346

30. Merino, M., Ahedo, E., "Space Plasma Thrusters: Magnetic Nozzles for," Encyclopedia of Plasma Technology DOI 10.108/E-EPLT-120053936, 2017

31. Merino, M., Ahedo, E., "Plasma detachment in a propulsive magnetic nozzle via ion demagnetization," Plasma Sources Sci. Technol. 23 (2014) 032001

32. Araya, Daniel B., Girimaji, Sharath, Carter, Mark D., Olsen, Christopher S., "Parameterization of magnetic nozzle flow physics for an in-space propulsion application," 42nd AIAA Plasmadynamics and Lasers Conferences, 27-30 June 2011 (AIAA 2011-4010)

33. Kuriki, Kyoichi and Okada, Osami, "Experimental Study of a Plasma Flow in a Magnetic Nozzle," The Physics of Fluids, Volume 12, Number 9, September 1970

34. York, T.M., Jacoby, B.A., Mikellides, P., “Plasma Flow Processes Within Magnetic Nozzle Configurations,” Journal of Propulsion and Power, Vol.8, No.5, Sept-Oct. 1992
35. Longmier, B.W., et al, “Ambipolar ion acceleration in an expanding magnetic nozzle,” 2011 Plasma Sources Sci. Technol. 20 015007
36. Olsen, C.S., Ballenger, M.G., Carter, M.D., Chang-Diaz, F.R., Giambusso, M., Glover, T.W., Ilin, A.V., Squire, J.P., Longmier, B.W., Bering, E.A., Cloutier, P.A., “Investigation of Plasma Detachment From a Magnetic Nozzle in the Plume of the VX-200 Magnetoplasma Thruster,” IEEE Transactions on Plasma Science, Vol. 43, No.1, January 2015
37. Takahashi, K., Komuro, A., Ando, A., “Operating a magnetic nozzle helicon thruster with strong magnetic field,” Phys. Plasmas 23, 033505 (2016)
38. Zhang, Y., Charles, C., Boswell, R., “Thermodynamic Study on Plasma Expansion along a Divergent Magnetic Field,” Physical Review Letters 116, 025001 (2016)

3 The Centrifugal Mirror Reactor

3.1 Reactor Dynamics

3.1.1 The Power Balance Calculation

The centrifugal mirror reactor requires power input IV_0 to maintain the azimuthal velocity u_θ in the well. The power going into the well must offset viscous shear losses P_{SH} and fueling losses related to ionizing and "spinning up" incoming fuel, P_F. Equation (3.1) describes this in terms of power per unit volume of burning plasma V_r. This form will be the convention throughout the calculation.

$$\overline{IV}_0 = \bar{P}_{SH} + \bar{P}_F. \tag{3.1}$$

Shear losses are calculated by taking the scalar product of the shear force with the velocity of the plasma. Equation (3.2) shows this relation, where μ_1^i is the appropriate viscosity component taken from [Braginskii, 1965].

$$\bar{P}_{SH} = \mu_1^i \frac{\partial^2 u_\theta}{\partial r^2} \cdot u. \tag{3.2}$$

Equation (3.3) shows the calculation of the power for reactor fueling, P_F. Plasma must be replenished at the rate that it leaves the system, so P_F is proportional to momentum losses incurred by thermal species departing the well through the loss cone, the value $\dot{n}_i$.

$$\bar{P}_F = (2g\dot{n}^\alpha + \dot{n}_i)\left(m_i u_\theta^2 + e\varphi_{ion}\right), \tag{3.3}$$

where φ_{ion} is the ionization potential of the fuel. Note that the factor of 2 applied to departing "prompt" alphas follows from the fusion reaction. Equations (3.1)-(3.3) describe the power balance

as it relates to the rotational energy in the well. In a steady-state system, there is no net change in stored rotational energy, which would otherwise appear in Equation (3.1).

Equation (3.4) provides the specific thermal balance (W/m^3) in the well. The first two terms on the left-hand side include gains from fusion power P^{α} and P^{n} from alphas and neutrons. Note as well that P_{SH} shows up as a power gain due to viscous heating.

$$\bar{P}_r^{\alpha} + \bar{P}_r^{n} + \bar{P}_{SH} = \bar{P}_B + \bar{P}_C + \bar{P}_{TH} + \bar{Q}_{\perp} + \bar{P}_r^{\alpha}\left(g_J + g_P\right) + \bar{P}_r^{n} + \overline{PV}_{\parallel}. \qquad 3.4$$

The first four terms on the right-hand side are losses due to bremsstrahlung, cyclotron radiation, thermal species leaving the well, and heat conduction perpendicular to the field lines. Alphas born in the loss cone depart immediately taking 3.5 MeV per alpha with them to either the jet-side mirror or power-side mirror; this loss is proportional to $g_J + g_P$. Neutrons, being 14.1 MeV and uncharged, depart the well without interacting with the plasma. The last term on right-hand side is the loss of potential energy of the thermal species as they traverse the centrifugal and potential gradient leaving the well.

Summing Equations (3.1) and (3.4) results in the form implemented in the 0D reactor model, shown in Equation (3.5). Note that $\bar{P}_{SH}$ and $\bar{P}^{n}$ do not appear in the equation. $\bar{P}^{n}$ cancels out in equation (3.5) and does not contribute to the power balance in the well. $\bar{P}_{SH}$ is included in the $\overline{IV_0}$ term and so does contribute.

$$\bar{P}_r^{\alpha}\left[1 - \left(g_J + g_P\right)\right] + \overline{IV}_0 = \bar{P}_F + \bar{P}_B + \bar{P}_C + \bar{P}_{TH} + \bar{Q}_{\perp} + \overline{PV}_{\parallel}. \qquad 3.5$$

For a D-T system, the specific fusion power $\bar{P}_r^{\alpha}$ for charged species is $\dot{n^{\alpha}}E^{\alpha}$, where $\dot{n^{\alpha}}$ is given by Equation (1.3), and E^{α} is the energy per alpha created in the D-T reaction.

It can be shown that the kinetic energy terms in Equations (3.2) and (3.3) arise from the momentum equation

$$\rho \frac{du}{dt} = -\nabla \mathrm{P} + \nabla \cdot \bar{\pi} + J \times B + \dot{n} p. \tag{3.6}$$

The last term on the right-hand side of Equation (3.6) is a source term representing the change in momentum p resulting from the rate of addition or loss of particles n. In general, this loss is related to the momentum confinement time τ_{mom}. At the midplane, the divergence of the stress tensor $\bar{\pi}$ is evaluated in the θ direction

$$(\nabla \cdot \bar{\pi})_\theta = \frac{1}{r}\frac{\partial}{\partial r} r \pi_{r\theta} = \mu \frac{\partial^2 u}{\partial r^2}\hat{\theta}, \tag{3.7}$$

where the viscosity μ is assumed constant. Further, in steady-state at the midplane, the azimuthal component of the total derivative on the left-hand side of Equation (3.6) is zero, as is the azimuthal component of the pressure gradient on the right-hand side. The momentum p is $m_i u_\theta \hat{\theta}$. Substituting these values and Equation (3.7) into Equation (3.6) results in the expression

$$J_c \times B = -\left(\mu \frac{\partial^2 u_\theta}{\partial r^2} + \dot{n}_i m_i u_\theta\right)\hat{\theta}. \tag{3.8}$$

Considering again the midplane constraint, for $B = B_z \hat{z}$, it is clear that for Equation (3.8) to hold, it must be true that $J_c = J_c \hat{r}$, so that

$$J_c = -\frac{1}{B_z}\left(\mu \frac{\partial^2 u_\theta}{\partial r^2} + \dot{n}_i m_i u_\theta\right)\hat{r}. \tag{3.9}$$

This defines the radial current J_c that evolves because of transport and momentum losses in the well. The specific power losses associated with Equation (3.9) are found by taking the scalar product of the electric field with the radial current, i.e., $\bar{P}_s = E \cdot J_c$. Ohm's law for ideal MHD

assumes $\sigma \to \infty$, so that $E = -u \times B$. Invoking the midplane condition a final time, Equation (3.1) becomes

$$\bar{P}_s = \overline{IV}_0 = u_\theta \mu \frac{\partial^2 u_\theta}{\partial r^2} + \dot{n}_i m_i u_\theta^2. \tag{3.10}$$

The first term on the right-hand side is equal to $\bar{P}_{SH}$ defined in Equation (3.2), and the second term is the kinetic component of $\bar{P}_F$ defined in Equation (3.3). In general, $\dot{n} = u \cdot \nabla \mathrm{n} \approx \dot{n}_\parallel + D_\perp \nabla^2 n$. However, perpendicular momentum loss is neglected in this work, so that $\dot{n}_i \approx \dot{n}_\parallel$.

Losses due to bremsstrahlung and cyclotron radiation are given in Equations (3.11) and (3.12), respectively

$$\bar{P}_B = 1.69 \times 10^{-32} n_e T_e^{1/2} \sum [Z^2 n(Z)] \;\; W/cm^3, \tag{3.11}$$

and

$$\bar{P}_C = 6.21 \times 10^{-28} B^2 n_e T_e \;\; W/cm^3. \tag{3.12}$$

Equations (3.11) and (3.12) are for "hydrogen-like plasmas" and functionalized in cgs units, and with T_e in eV. [Huba, 2013]

Energy losses due to departure of thermal species from the well are calculated

$$\bar{P}_{TH} = \dot{n}_i \frac{3}{2} k_B (T_i + Z_i T_e), \tag{3.13}$$

where $\dot{n}_i$ as before is the loss rate of ions due to the momentum confinement time τ_{mom}.

Heat loss across the field lines $\bar{Q}_\perp$ is evaluated

$$\bar{Q}_{\perp} = \nabla \cdot q_H = \nabla \cdot \left(\kappa_{i,\perp} \nabla_{\perp} k_B T_i\right). \quad 3.14$$

The perpendicular heat transfer coefficient $\kappa_{i,\perp}$ is taken from [Braginskii, 1965] and [Huba, 2013] and has units of $m^{-1}s^{-1}$

$$\kappa_{i,\perp} = \frac{2n_0 k_B T_i}{m_i \omega_{ci}^2 \tau_i}. \quad 3.15$$

The last term in Equation (3.5) represents the potential energy that is given up as the thermal species depart the well

$$\bar{P} V_{\parallel} = \dot{n}_i \left(\Xi_i + Z_i \Xi_e\right), \quad 3.16$$

where Ξ_j is the centrifugal mirror potential energy of species *j*. Its occurrence in the power balance implies that the loss of this potential energy contributes to the heating of the plasma, or that potential energy is fungible with thermal energy. This is consistent with [Abel, *at al*, 2013] which suggests an exchange between thermal and potential energy that contributes to plasma heating for relevant plasmas.

Charge exchange losses result from the neutralization of high-energy ions from collisions with lower energy neutrals, the latter becoming ionized in the process. Assuming elastic collisions, the neutralized ions leave the system along with their energies. The effect on the heat balance in Equation (3.5) is that the $\bar{P}_F$ term will increase to offset losses due to the charge exchange, i.e., there is a loss component $\dot{n}_{CX} = n_0/\tau_{CX}$, where $\tau_{CX}$is the charge exchange time scale.

3.1.2 The Centrifugal Mirror Potential

Up to this point, losses from the well have been discussed in terms of confinement times. However, the confinement time itself is a consequence of the loss rate, i.e., $\tau_{mom} = n_o/\left(\frac{dn}{dt}\right)$. As shown in Equation (2.3), for a conventional mirror, $\frac{dn}{dt}$ is a function of the electrostatic potential energy of the species. The centrifugal mirror potential of the species *s* is given by Equation (3.17), with contributions from the electrostatic potential and the centrifugal energy.

$$\Xi_s = Z_i e\varphi - \frac{m_s}{2}\omega^2 r^2. \tag{3.17}$$

Equations (3.18) and (3.19) below show how the centrifugal potentials of electrons and ions determine the rates they depart the well. These relations were adapted from Equation (2.3) by [Abel, 2021], where the centrifugal potential is added to the electrostatic potential in the exponential. As in Equation (2.3), the factor Γ is related to the configuration of the magnetic field, and for this analysis is taken as unity for a square well configuration.

$$\dot{n}_i = \frac{-2n_0 exp(-\Xi_i/T_i)}{\sqrt{\pi}\tau_{ii}(\Xi_i/T_i)ln(R_m)}\Gamma. \tag{3.18}$$

$$\dot{n}_e = \frac{-2n_0 exp(-\Xi_e/T_e)(Z_i+1)}{\sqrt{\pi}\tau_{ie}(\Xi_e/T_e)ln[R_m(Z_i+1)]}\Gamma. \tag{3.19}$$

The rates for ions and electrons must conform to the ambipolar constraint that that $\dot{n}_e = Z_i\dot{n}_i$ for a given R_m and M. Additionally, Equations (3.18) and (3.19) are for losses through both mirrors, assuming that the mirror ratios are equal. However, in DFD-CM, this may not be the case. Accordingly, these equations are solved for each mirror separately, with the resulting loss rates for each mirror halved. Total system losses are the sum of the two mirror losses. This is assumed to

be valid, based on the convention that Ξ_i and Ξ_e are zero at the center of the well, and more rigorously when $R_{mJ} \approx R_{mP}$.

3.1.3 Approximate 1D and 2-D Solutions to the Momentum Equation for the Reactor Well

The model presented in Section 3.1.1 is a 0D representation of the reactor for power balance and is suitable for purposes of the current analysis, which is concerned with an engineering estimate of the performance of the DFD-CM concept. Additional insights can be obtained from a simple 1D solution of the momentum equation. Evaluation of Equation (3.6) at the midplane in the radial direction provides a characterization of the electric field, the azimuthal velocity profile, and other system parameters. The solution starts with Equation (3.6) and the generalized Ohm's law, Equation (1.6). Perpendicular conductivity across the field lines and viscosity and are calculated based on [Braginskii, 1965] relations for nominal plasma temperature and number density, and they are assumed to be constant. The annulus is divided into *n=20* elements bounded by the vacuum wall (r_w) and the inner cathode (r_i). The potential and velocity expressed as Taylor expansions of three terms each are used to evaluate the generalized Ohm's law. The electric field at each value of r is calculated $E_r = u(r) * B_z - \frac{J_2(r)}{\sigma_\perp}$, where $J_c(r) = J_1(r) + J_2(r)$. $J_1(r)$ is the current density resulting from momentum losses per Equation (3.9). $J_2(r)$ is the current density predicted by generalized Ohm's law. This model differs from the 0D model with the inclusion of $J_2(r)$. $J_2(r)$ about the same magnitude of the viscous loss term in $J_1(r)$, so it is much smaller than the current density resulting from particle losses. Because its magnitude is comparable to the

viscous term, it allows a simplification in the calculation of u'', i.e. $u'' = \frac{-J_2(r)*B_z}{\mu}$. This approximation is discussed in Appendix B.

It is necessary to specify boundary conditions for u and ϕ. From [Ghosh, et al, 2006], a parabolic velocity profile is expected. Since B_z is constant at the midplane, this implies that the electric field must also be parabolic. In a manner similar to [White, *et al*, 2018], the potential is modeled

$$\phi = \frac{\phi_0}{2}\left[cos\left(\pi\frac{r - r_i}{r_w - r_i}\right) + 1\right], \qquad 3.20a$$

where ϕ_0 is the specified bias at the cathode. Equation (3.20a) is provided as a means to obtain the Neumann boundary condition for ϕ

$$\left(\frac{d\phi}{dr}\right)_{ri} = -\frac{\phi_0}{2}\left[sin\left(\pi\frac{k_1 r_i}{r_w - r_i}\right)\right]\left(\frac{\pi}{r_w - r_i}\right), \qquad 3.20b$$

where the proportional factor $k_1 r_i$ is introduced to ensure that $\phi(r) = 0$ at $r = r_i$. The Neumann boundary condition for u_θ follows from a scaling of the iso-rotation law

$$\left(\frac{du_\theta}{dr}\right)_{ri} \sim \frac{k_2}{B_z}\left(\frac{d\phi}{dr}\right)_{ri}, \qquad 3.20c$$

where k_2 is a factor to ensure that the Dirichlet boundary conditions for u_θ are satisfied. For this model, the no-slip condition is applied, so that $u_\theta(r_i) = 0$ and $u_\theta(r_w) = 0$. For purposes of benchmarking, the model was applied to a case generated by MCTrans++, a code the CMFX team is using for experiment design. The parameters of that case are provided in Table 3-1.

Table 3-1 – MCTrans++ benchmark case characteristics

Parameter		Units	Value
n0	Number density	#/m3	2×10^{20}
Te	Electron temperature	keV	10.9
Bz	Magnetic field intensity	T	4.5
Rm	Mirror ratio		3.33
I	Current	A	0.232
M	Mach number		6.53
u_θ	Azimuthal velocity	m/s	4.17×10^6
ϕ_0	Cathode bias	V	-7.5×10^6
IV0	Input power	MW	1.74 MW
ri	Cathode radius	m	0.05
rw	Vacuum wall radius	m	0.8
a	Plasma column width	m	0.2
L	Plasma column length	m	2

Figures 3-1 through 3-4 show the plasma potential, the electric field, the angular speed, and azimuthal velocity for the benchmark case, with k_1 and k_2 appropriately specified for the boundary conditions.

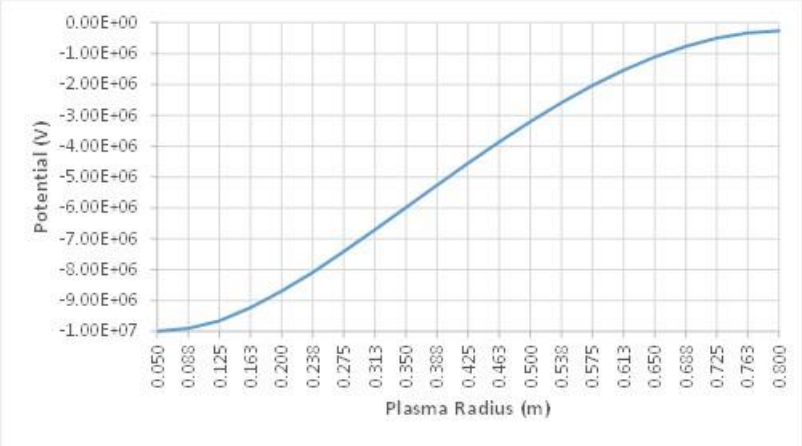

Figure 3-1 – Benchmark case plasma potential

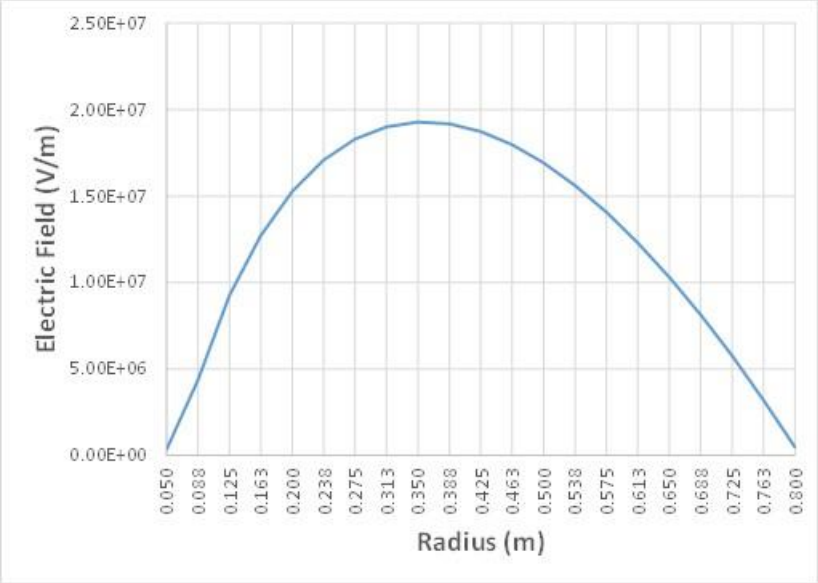

Figure 3-2 – Benchmark case electric field

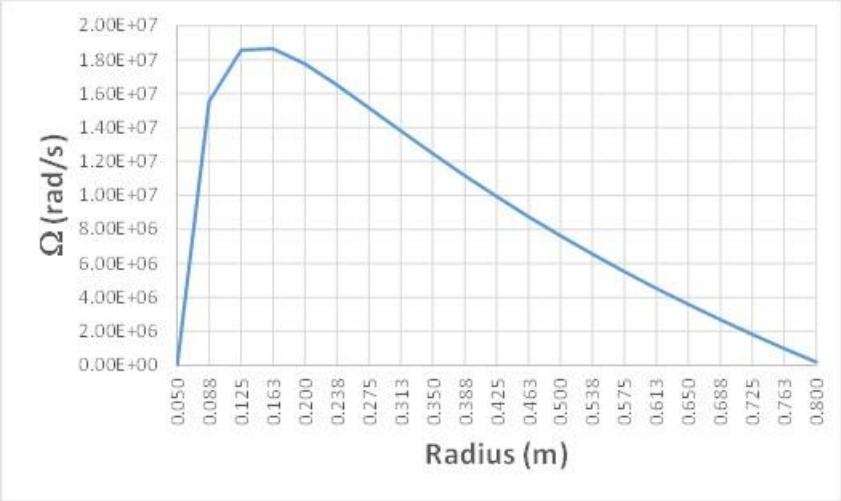

Figure 3-3 – Benchmark case angular speed

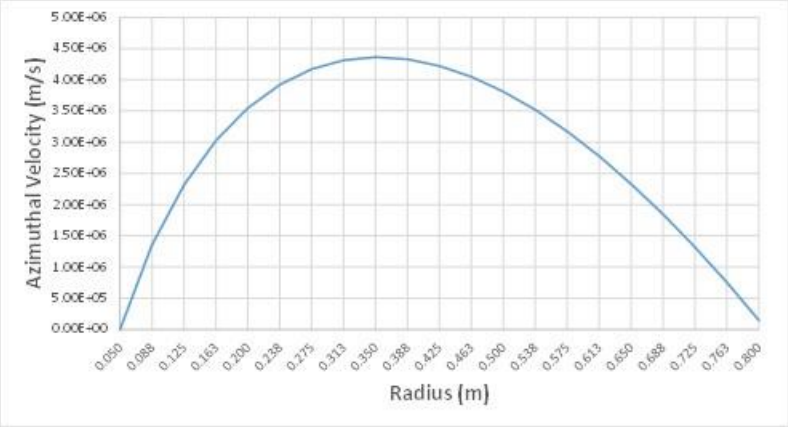

Figure 3-4 – Benchmark case azimuthal velocity

From Figure 3-1, it can be seen that the bias at the cathode is -10 MV, compared to -7.5 MV from the benchmark case. The difference may be because the latter was calculated assuming the presence of current limiters in the reactor, electrodes that stand off from the vacuum wall and so provide an alternate path for the current. In that case, the distance the current would have to travel in the plasma is limited and could explain the lower potential. Qualitatively, the potential and electric field shown in Figures 3-1 and 3-2 appear in school with results from MCX, and for Ixion, as well, per Figure 2-1. Although the expected inflection in the curve for ϕ is not obvious in Figure 3-1, it is apparent in Figure 3-2. The maximum azimuthal velocity shown in Figure 3-4 is in good agreement with the benchmark value. Integrating $\overline{IV}_0$ over the 1D solution results in a value of 1.76 MW, compared to 1.75 MW from the benchmark case. Similarly, the total current predicted by the 1D model is 0.183 A, compared to 0.232 A in the benchmark case. It should be noted that the benchmark value results from application of the plasma volume defined by *a*, the plasma column width, while the 1D approximation is an integration over the whole reactor volume.

The 1D approximation can be extended to a 2D by the introduction of a specified magnetic field that allows evaluation of the Mach number and state properties in the $(r-z)$ plane. The generating function for the magnetic flux is

$$r(\psi,z)=\frac{2\psi_0(r)}{[B_0 f(z)]^{1/2}}, \tag{3.21a}$$

where $\psi_0=\frac{1}{2}B_0 r_0^2$ at the point of maximum azimuthal velocity at the midplane, and, as adapted from [White, *et al*, 2018]

$$f(z)=\frac{a}{\left(\frac{2z}{L}+1\right)^2-w_1}+\frac{b}{\left(\frac{2z}{L}-1\right)^2-w_2}. \tag{3.21b}$$

The factors a, b, w_1, and w_2 are chosen to provide the desired magnetic field, and L is overall length between mirrors. Given $r(\psi,z)$ from Equation (3.21a), $u_\theta(r,z)=\Omega(r)r(\psi,z)$ and $M(r,z)$ can be calculated directly. The pressure field is then calculated $P(r,z)=2n_0k_BTexp\left[\frac{M(r,z)^2}{4}-\frac{M(r_0,0)^2}{4}\right]$, where $M(r_0,0)$ and n_0 are the maximum for both Mach number and number density respectively at the midplane. The results of this analysis for the benchmark case $M(r,z)$ and $P(r,z)$ are provided in Figures 3-5 and 3-6. These figures are generated by extracting $[r,\Omega,T]$ from the previously described 1D solution and then, in a MATLAB script file, applying the flux generation function in conjunction with the iso-rotation law. A datum number density at the insulators is chosen so that the desired number density at the center of the plasma is the same as in the 1D solution.

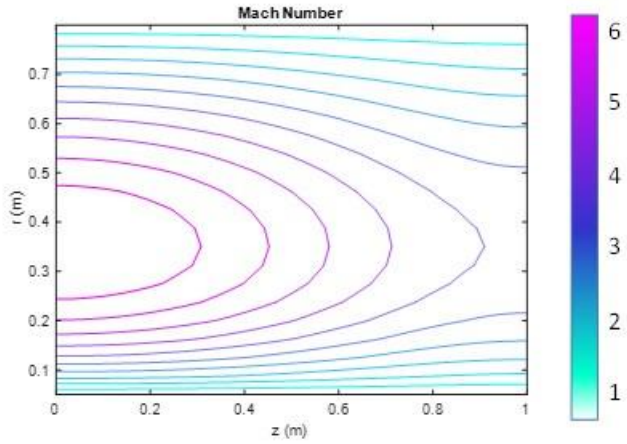

Figure 3-5 – Benchmark case Mach number field

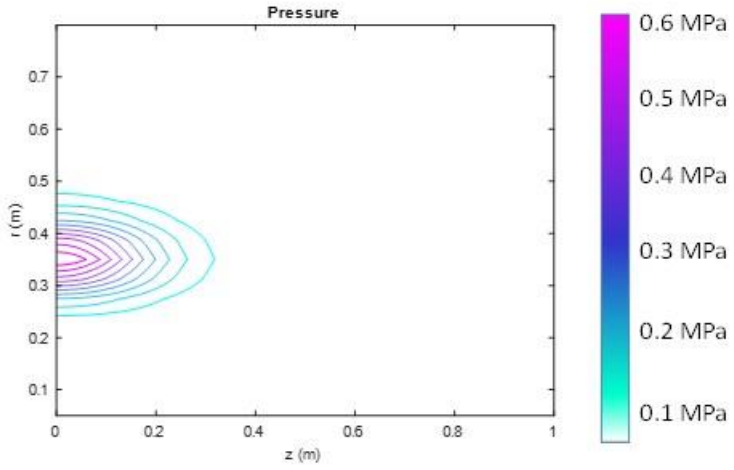

Figure 3-6 – Benchmark case pressure field

Figures 3-5 and 3-6 show the plasma confinement to an annulus region centered on the point of maximum azimuthal velocity, and its radial extent is in general conformance with the benchmark case plasma column width $a = 0.2\ m$. However, because a physical magnetic field is specified, the axial confinement is smaller than the length assumed with the square well approximation in the benchmark case.

3.1.4 Powering the Reactor

Equation (1.18) provides an estimate for the breakeven figure of merit. As discussed previously, the required value for Q differs from that in terrestrial applications where it is necessary that $Q \gg 1$ for economic reasons. It also differs in that Q for DFD-CM, as defined, does not include the jet power delivered by the system. Rather it is based only on the power extracted from the reactor that is used to power the reactor. Accordingly, for a viable DFD-CM, it is necessary that $Q \approx 1$. Since the main losses are due to momentum losses, an approximate, analytic expression for Q can be derived based on momentum losses, the reactor specific power, and mirror ratio on the power-side. Modifying Equation (3.10) to include shear losses as a margin relative to momentum losses:

$$\overline{IV}_0 = (1+x)\dot{n}_{\parallel} m_i u_\theta^2 = (1+x)\dot{n}_{\parallel} k_B T_e M^2. \tag{3.22}$$

The margin x accounts for the shear losses, which may be 10 to 20 percent of the momentum losses. Approximating the potential energy for the ions as $\Xi_i \approx \frac{M^2}{4} k_B T_i$, Equation (3.18) can be written:

$$\dot{n}_{\parallel} \approx \frac{-2n_0}{\sqrt{\pi}\tau_{ii} ln(R_m) \frac{M^2}{4} exp\left(\frac{M^2}{4}\right)}. \tag{3.23}$$

The approximation for Ξ_i neglects the electrostatic potential term. Additionally, it drops a factor of $\left(1 - \frac{1}{R_m}\right)$, which essentially results in a square well approximation, i.e., $R_m \to \infty$. Note as well that Γ from Equation (3.18) is taken as unity, which is also an expression of the square well approximation. These are all important second order effects, so the resulting calculation must be

understood to be a first order estimate. Given these considerations, substituting Equation (3.23) into Equation (3.22) results in an expression for reactor power requirements

$$\overline{IV}_0 = (1+x)\frac{8n_0 k_B T_e}{\sqrt{\pi}\tau_{ii} ln(R_m) exp\left(\frac{M^2}{4}\right)}. \quad 3.24$$

The negative sign in Equation (3.23) is dropped, since Equation (3.24) now represents power going back into the system. The power that is available from charged species leaving the reactor is

$$\bar{P}_r^{\alpha} = g_P \eta_c x_D x_T n_0^2 \langle \sigma v \rangle_{DT} E^{\alpha}. \quad 3.25$$

As usual, $\bar{P}_r^{\alpha}$ is the specific power due to alphas per volume of burning plasma in the reactor. The power conversion efficiency is η_c. Defining Q^{α} as $\overline{P}_r^{\alpha}/\overline{IV}_0$, the value is calculated by dividing Equation (3.25) by Equation (3.24)

$$\frac{P_P^{\alpha}}{IV_0} = Q^{\alpha} = \frac{g_P \eta_c}{(1+x)}\left(\frac{\sqrt{\pi}}{8k_B T_e}\right) n_0 \tau_{ii} exp\left(\frac{M^2}{4}\right) \ln (Rm) x_D x_T \langle \sigma v \rangle_{DT} E^{\alpha}. \quad 3.26$$

A similar expression can be derived for power availability from neutrons

$$\frac{P_P^{n}}{IV_0} = Q^{n} = \frac{(1-f)\eta_c}{(1+x)}\left(\frac{\sqrt{\pi}}{8k_B T_e}\right) n_0 \tau_{ii} exp\left(\frac{M^2}{4}\right) \ln (Rm) x_D x_T \langle \sigma v \rangle_{DT} E^{n}. \quad 3.27$$

Neutron energy $E^n$is 14 MeV. The loss cone factor g_P is not relevant to the neutrons, since they are not charged, but there is a factor $(1-f)$, where f is the blanket leakage.

Equations (3.26) and (3.27) provide an analytic, first order estimate of the ability of the reactor to power itself. They were developed assuming $R_{mJ} = R_{mP}$. From equation (1.15), $\frac{M^2}{4}$ can be replaced by $\frac{K^2}{\beta}$ in the exponential, so both Mach number or alternately β have significant effect on

Q. Equation (3.26) is evaluated at varying mirror ratios for a representative thermonuclear plasma in Figure 3-7. The plasma temperature is 10 keV, number density 5×10^{20}, and τ_{ii} is taken as 15 ms. The margin x is 0.20 and η_c is 0.80.

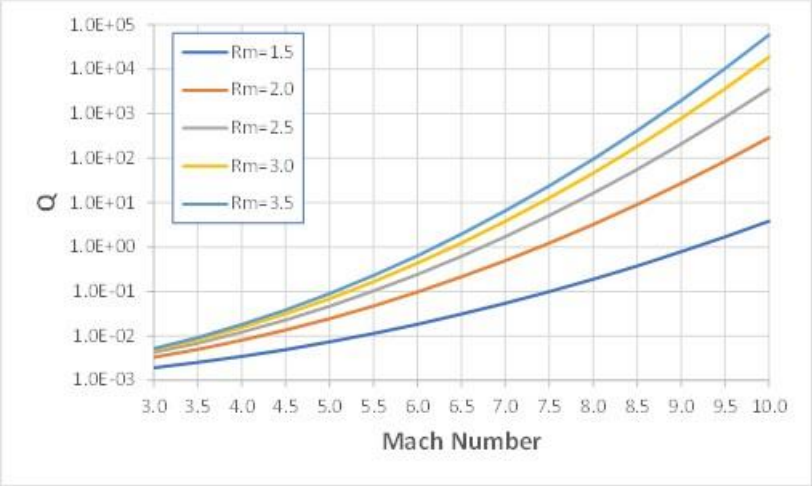

Figure 3-7 – Breakeven figure of merit Q vs. centrifugal Mach number

The curves in Figure 3-7 indicate that for a mirror ratio of 3.5, the reactor can self-power at Mach 6, while for a mirror ratio of 2, Mach 8.5 is required. These solutions correspond with values for β of 0.11 and 0.055, respectively. In general, it is better from a propulsion standpoint to have a lower mirror ratio, since that increases specific jet power. This suggests a tradeoff between propulsion performance and recycled power. However, the mirror ratios must be chosen so that the reactor power balance is met, per Equation (3.5). This is a highly non-linear problem for which the 0D reactor model can be used to study.

3.2 Implementing the 0D Reactor Model

3.2.1 Model Overview

The 0D model was developed as a moderate fidelity representation suitable for ongoing system-level investigations into the feasibility and viability of DFD-CM. Primarily it performs a power balance calculation for a specified set of operating conditions. Each use case is specified by the following quantities:

n_0 – number density (#/m^3)

T_i, T_e – ion and electron temperature (keV)

K- Kármán number (Alfvén Mach number)

β - magnetic pressure ratio

R_{mP} – mirror ratio on forward or power-side of the reactor

Characteristics of the reactor and energy conversion system, e.g., plasma length L and annular width a, must also be entered. The principal value that the model returns is R_{mJ}, the mirror ratio on the jet-side, required to satisfy the reactor power balance. The quantities n_0, T_t, and T_e are basic properties of the plasma. Once these are set, specific fusion power and bremsstrahlung radiation can be calculated. With K constrained to approximately unity, and when β is specified, these two values set the Mach number M and the magnetic field strength B. As shown in Equation (1.15), M, β, and K are related

$$M = K\left[\frac{2(Z_i + 1)}{\beta}\right]^{\frac{1}{2}}. \qquad 1.15$$

The magnetic field strength B in the reactor well is calculated from the given state properties. With these quantities known, the azimuthal velocity $u_\theta = M \cdot C_s$ is calculated. With these results from

the use case specification, the simulation first calculates transport and state properties of the system that are independent of R_{mJ}. Additionally, it calculates momentum, thermal and prompt alpha losses related to the forward or power mirror based on specified R_{mP}. With these data available, the simulation calculates momentum, thermal, and prompt alpha losses through the jet-side mirror for a range of R_{mJ} values. For each value of R_{mJ}, each term in Equation (3.5) is calculated. A value Q_{net} is then found for each value of R_{mJ}. Q_{net} is the difference between the power gains and the power losses, normalized by the losses. The code then finds the point at which the curve (R_{mJ}, Q_{net}) crosses the zero-axis for Q_{net} which is the value for R_{mJ} where the reactor well thermal balance meets the reactor power balance. The representative solution in Figure 3-8 is for $n_0 = 10^{20}$ *#/m*^{3}; $T_e = 10.9$ *keV*; $T_i = 10.6$; β*=0.087*; *K=0.95*; R_{mP}*=3.55*. The simulation returns the solution $M = 6.44$; $B = 4.46\ T$; $R_{mJ} = 3.55$. In this case, $R_{mJ} = R_{mP}$

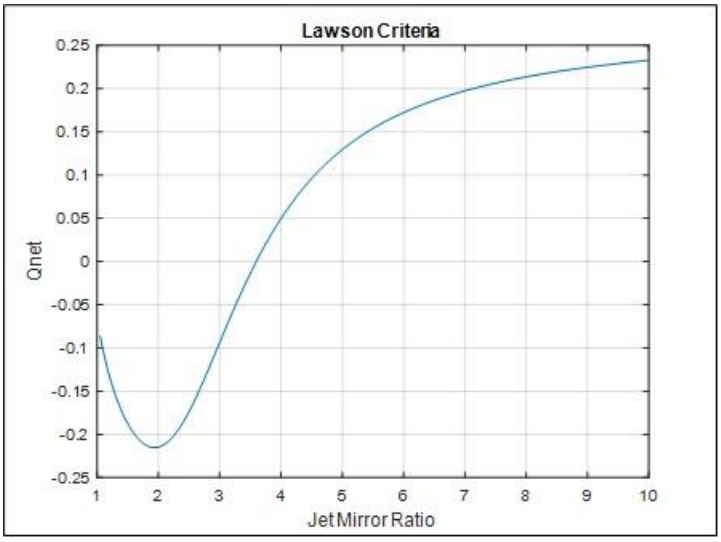

Figure 3-8 – Representative 0D reactor model solution

3.2.2 Organization of the Code

The 0D model named *dfdcm_r5a.m* is implemented in MATLAB as a collection of instruction blocks, script files and function files. Figures 3-9 and 3-10 provide a graphical representation of its organization, and Tables 3-2 and 3-3 provide details on the individual functions and types of calculations. The various auxiliary calculations performed in the code, but not specifically referenced in these tables are detailed in Section 3.2.3. Additionally, the calculations for ion and electron loss are described on Section 3.2.4. This latter calculation is performed by the function file *parallel_r1.m*.

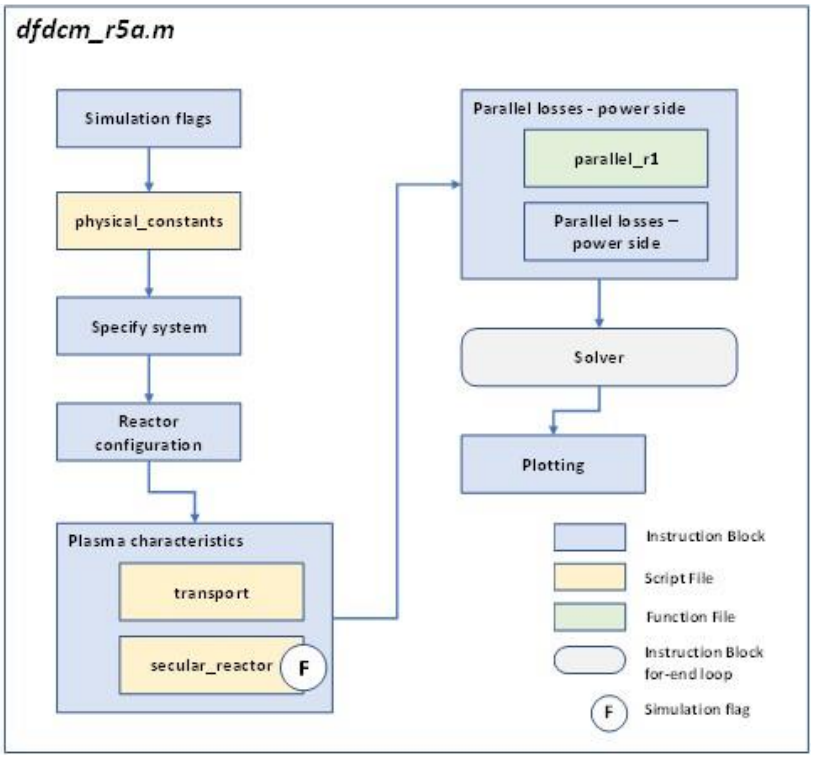

Figure 3-9 – Main code organization

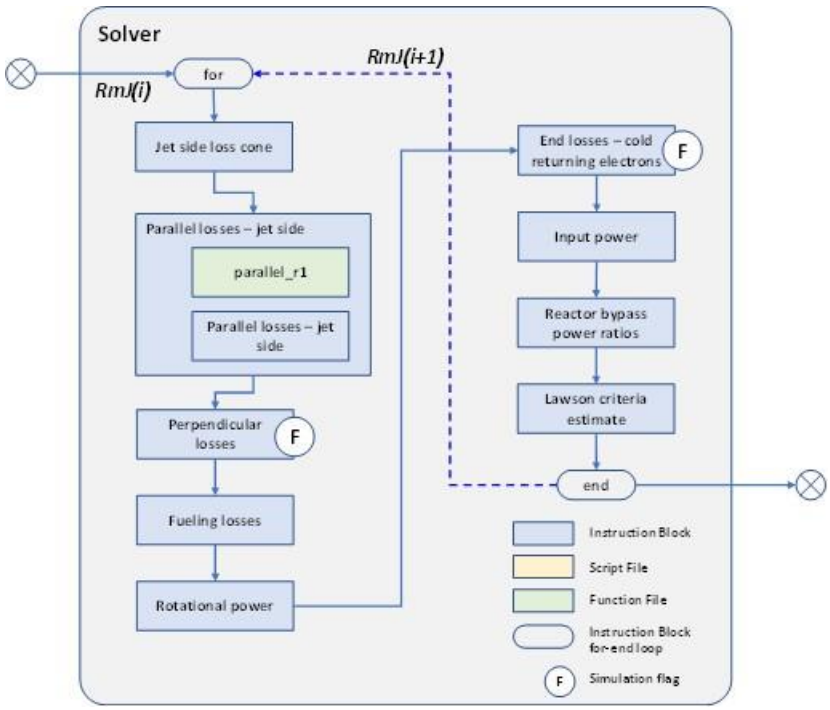

Figure 3-10 – Simulation solver

Table 3-2 – Main code functional description

Element	Type	Function	References
Flags	Instruction Block	Allows selection of simulation flags	Section 3.2.2
physical_constants	Script File	Defines physical constants	
Specify system	Instruction Block	User inputs to enter use case vector (n_D, T_e, T_i, K, β, R_{mP})	
Reactor configuration	Instruction Block	User inputs for key dimensions and other characteristics	
Simulation specification	Instruction Block	Domain ranges, numbers of iterations, size of increments, etc.	
Calculate plasma characteristics	Instruction Block		
transport	Script File	Calculates transport properties of the plasma	Braginskii, 1965; Huba, 2013
secular_reactor	Script File	Calculates plasma characteristics and losses that remain constant during simulation.	Huba, 2013; Section 3.2.3
Parallel losses - power side	Instruction Block		
parallel_r1	Function File	Calculates parallel ion and electron losses	Section 3.2.4
Parallel losses - power side	Instruction Block	Calculates potential energy losses through power side mirror	Section 3.2.4
Solver	Instruction Block	Performs power balance calculation	Section 3.2.3 and 3.2.4
Output	Instruction Block	Plots solution vector	

The flags shown in Figures 3-9 and 3-10 allow the simulation to be modified to include four types of losses. The first is that of perpendicular thermal losses due to diffusional losses of ions and electrons. The second is end loss due to cold returning electrons. Since DFD-CM is an open system, these losses are generally not included in the simulation. The derivation of both of these losses is provided in Section 3.2.3. The third flag allows bremsstrahlung to be parametrically varied. The fourth flag is to specify how charge exchange losses are calculated.

Table 3-3 – Solver functional description

Element	Type	Function	References
for-end loop	Instruction Block	Advances simulation by increment of dR_{mJ}	
Jet-side loss cone	Instruction Block	Calculates $g(R_{mJ})$ and g	Section 3.2.3
Parallel losses - jet side	Instruction Block		
parallel_r1	Function File	Calculates parallel ion and electron losses	Section 3.2.4
Parallel losses - jet side	Instruction Block	Calculates: 1) thermal losses, and 2) potential energy losses through jet side mirror	Section 3.2.3
Perpendicular losses	Instruction Block	Calculates perpendicular thermal losses due to cross-field diffusion. Flag allows inclusion or exclusion; default is exclusion	Section 3.2.3
Fueling losses	Instruction Block	Calculates power required to ionize and to accelerate incoming fuel	Section 3.1.1
Rotational power	Instruction Block	Calculates power required to offset fueling losses and shear losses	Section 3.1.1
End losses - cold returning electrons	Instruction Block	Calculates losses due to cold returning electrons based on bounce frequency. Flag allows inclusion or exclusion; default is exclusion	Section 3.2.3
Input power	Instruction Block	Calculates IV_0/Vr	Section 3.1.1
Reactor bypass power ratios	Instruction Block	Calculates Q for alphas and neutrons	Sections 3.2.3 and 3.2.4
Power balance	Instruction Block	Calculates Q_net and other parameters as a function of RmJ	Equation (3.5)

3.2.3 Auxiliary Relations

Many of the calculations described in Section 3.2.2 require side calculations, the value for effective Z in the equation bremsstrahlung, Equation (3.11), for example. This section summarizes these auxiliary calculations.

The M-K-β Relation

For any arbitrary ionization state, Equation (1.14) is modified

$$\beta = \frac{(1 + Z_i) n_i k_B T}{\frac{B^2}{2\mu_0}}. \tag{3.28}$$

At the same time

$$\frac{C_s^2}{V_A^2} = \frac{k_B T_e}{m_i} \frac{n_i m_i \mu_0}{B^2} = \frac{n_i k_B T_e \mu_0}{B^2}. \tag{3.29a}$$

The right-hand side of Equation (3.29a) can be expressed as $\frac{\beta}{2(1+Z_i)}$, and this value is equal to $\frac{C_s^2}{V_A^2}$.

Since $MC_s = KV_A$

$$M^2 = K^2 \frac{V_A^2}{C_s^2} = \frac{2K^2(1 + Z_i)}{\beta}, \tag{3.29b}$$

which results in Equation (1.15), $M = K \left[\frac{2(1+Z_i)}{\beta}\right]^{\frac{1}{2}}$, where $K \leq 1$. A general form of the relation applicable to multiple species, charge states, and temperatures is provided in Appendix B.

Loss Cone Calculations

Figure 3-11 shows the reactor loss cone in phase space. It is assumed that the mirror ratios on the jet and power-sides are equal, so that the critical angles θ_c are also equal. For fusion alphas born in the reactor, the kinetic distribution is taken as $f(u) = A\delta(u - a)$, where a is the thermal velocity at 3.5 MeV.

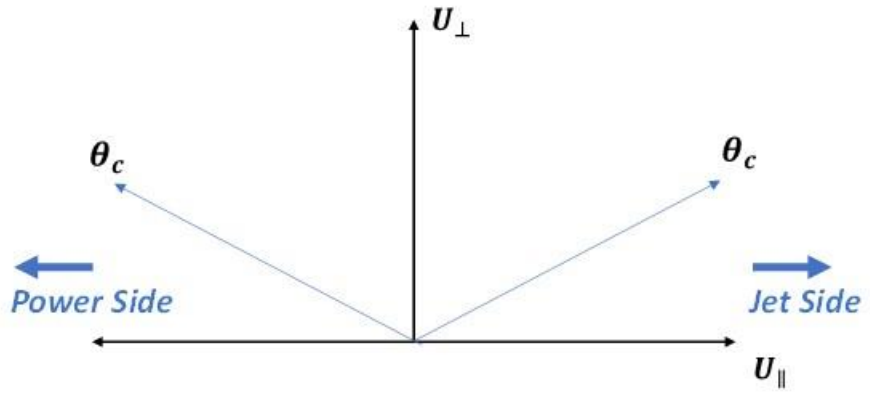

Figure 3-11 – Reactor loss cone in phase space

In spherical coordinates, $du = u^2 sin\theta d\varphi du$. Setting $\int_{-\infty}^{\infty}\int_0^{2\pi}\int_0^{2\pi} f(u)du = 1$, it is found that $A = \frac{1}{4\pi u^2(a)}$, and now g can be solved for

$$g = \frac{1}{4\pi u^2(a)}\int_{-\infty}^{\infty}\int_0^{2\pi}\int_0^{\theta_c} f(u)du = \tfrac{1}{2}[1 - cos\theta_c]. \qquad 3.30a$$

Since $\theta_c = arcsin\left(\frac{1}{R_m}\right)^{\frac{1}{2}}$, it follows that $\cos\left[arcsin\left(\frac{1}{R_m}\right)^{\frac{1}{2}}\right] = \sqrt{1 - \frac{1}{R_m}}$, and that

$$g = \frac{1}{2}\left[1 - \sqrt{1 - \frac{1}{R_m}}\right]. \qquad 3.30b$$

The upper limit on the inner integral in Equation (3.30a) applies only to a given half plane in phase space. Therefore, Equation (3.30b) can be used to evaluate g for the either side based on the mirror ratio of that side and independently of the other mirror ratio.

Bremsstrahlung

For a system with ${}_1^2D$, ${}_1^3T$ and ${}_2^4He$ species, given specification of x_D and x_T, the mole fraction of ${}_2^4He$ is $1 - (x_D + x_T)$. The expression under the summation sign in Equation (3.11) can be written

$$Z_\alpha^2 n^\alpha + Z_D^2 n^D + Z_T^2 n^T = n_0(Z_\alpha^2 x_\alpha + Z_D^2 x_D + Z_T^2 x_T). \qquad 3.31a$$

At the same time, $n_e = n_0(Z_\alpha x_\alpha + Z_D x_D + Z_T x_T)$, so that Equation (3.11) is implemented

$$\bar{P}_B = 1.69 \times 10^{-32} n_0^2 T_e^{1/2}(Z_\alpha x_\alpha + Z_D x_D + Z_T x_T)\left(Z_\alpha^2 x_\alpha + Z_D^2 x_D + Z_T^2 x_T\right). \qquad 3.31b$$

In the code, Equation (3.21b) is calculated using cgs units and the result converted to mks.

Perpendicular Diffusion

This calculation is performed, so that perpendicular diffusional losses can be included in the simulation, if needed. Normally, this loss is not included, with the appropriate simulation flag set to zero. From [Chen, 1974], the cross-field diffusion coefficient is $D_\perp = \frac{k_B T \nu}{m\omega_c^2}$, and the rate of diffusion is governed by $(\mathrm{v} \cdot \nabla n_s) = D_\perp \nabla^2 n_s$. [Bird, *et al*, 1960] Taking $k_B T = \frac{1}{2} m v_{th}^2$ and

$r_L^2\omega_c^2 = v_{th}^2$, the cross-field diffusion coefficient can be written: $D_\perp = \frac{r_L^2}{2}\nu_{ii}$. Approximating $\nabla^2 n_s$ with $\frac{n_0}{a^2}$, the perpendicular losses are given

$$\dot{n}_{i,\perp} \approx \frac{r_L^2}{2}\nu_{ii}\frac{n_0}{a^2} \tag{3.32}$$

Fueling

The particles leaving the well must be replenished by refueling. Since this analysis works with an average particle mass of 2.5 amu, it is possible to balance only the charged particle flow rates, instead of the more complicated calculation of balancing the mass flow rates for the well. The losses specific to the prompt alphas are through the loss cones at birth, $\left(g_P + g_J\right)\dot{n}^\alpha$, and these must be replenished at twice the rate at which they leave by deuterons and tritons, as required by Equation (1.2), the D-T fusion reaction. The parallel losses defined by Equations (3.18) and (3.19) represent the main momentum losses. Perpendicular losses can be included in the calculation, but as mentioned previously, these diffusional losses are not included in the simulation unless the appropriate flag is set. Given these considerations, the fueling requirement can be written

$$\dot{n}_F = 2g\dot{n}^\alpha + flag * \dot{n}_{i\perp} + \dot{n}_{i\parallel} \tag{3.33}$$

Viscous Losses

In the 0D representation, the second derivative in Equation (3.2) is approximated as $\frac{u_\theta}{a^2}$, so that relation is implemented as:

$$\bar{P}_{SH} = \mu_1^i \frac{u_\theta^2}{a^2}. \tag{3.34}$$

The viscosity is taken from [Braginskii, 1965][Huba, 2013] and is calculated: $\mu_1^i = \frac{3n_0 k_B T_i}{10\omega_{ci}^2 \tau_{ii}}$.

End Losses – Cold Returning Electrons

Since electrons are highly mobile on a flux surface, there is a possibility that energetic electrons may reach the insulators of the reactor, deposit their energy, and then return cold to the well. Since DFD-CM is open at the mirrors, this may be less of a concern. Nonetheless, the 0D model includes a calculation for these losses which can be included in the simulation based on setting a flag. This calculation is based on estimating a bounce frequency in the mirror and then multiplying that frequency by the energy of the electrons. In a mirror device, the portion of energy for a charged particle stored in velocity parallel or perpendicular to the field lines is

$$\tfrac{1}{2} m v_\parallel^2 + \mu B = constant, \tag{3.35a}$$

where the magnetic moment $\mu = \frac{1}{2}\frac{m v_{\perp 0}^2}{B_0}$ is invariant. Parallel velocity $v_\parallel$ is zero for trapped particles at $B = R_m B_0$, where B_0 is the midplane field strength, so that the constant can be evaluated $C_1 = \mu R_m B_0$, and

$$v_{\parallel e} = \left[\left(\frac{2}{m_e}\right)(\mu R_m B_0 - \mu B)\right]^{\frac{1}{2}}. \tag{3.35b}$$

Moving the expression $\mu R_m B_0$ out of the parenthesis on the right results in the quantity $\left(1 - \frac{\mu B}{\mu R_m B_0}\right) = \left(1 - \frac{1}{R}\right)$, where R is the local ratio of $B/R_m B_0$, so that

$$v_{\parallel e} = \left[\left(\frac{2\mu R_m B_0}{m_e}\right)\left(\frac{R-1}{R}\right)\right]^{\frac{1}{2}}. \qquad 3.35c$$

Taking the bounce time to be $\tau_B = 2\int_0^L \frac{dz}{V_\parallel}$ for $dz \approx ds$

$$\tau_B = \sqrt{2}\left(\frac{m_e}{\mu R_m B_0}\right)^{\frac{1}{2}} \int_0^L \left(\frac{R(z)}{R(z)-1}\right)^{\frac{1}{2}} dz. \qquad 3.35d$$

The usual coordinate system applies: $z = 0$ at the midplane and $z = (-L, L)$ at the mirrors. Assuming the test function $R(z) = az^n + 1,\ a = (R_m - 1)L^{-n}$. Substituting a into the test function allows Equation (3.35d) to be written

$$\tau_B = \sqrt{2}\left(\frac{m_e}{\mu R_m B_0}\right)^{\frac{1}{2}} R_m^{\left(\frac{n-1}{n}\right)} \frac{L}{n} \int_0^{Rm} (R(z)-1)^{\left(\frac{1-n}{n}\right)} \left(\frac{R(z)}{R(z)-1}\right)^{\frac{1}{2}} dR. \qquad 3.35e$$

Arbitrarily setting $n = \frac{2}{3}$ and solving the integral in Equation (3.48e), for $v_\perp = v_{th}/\sqrt{2}$ the relation for bounce time becomes

$$\tau_B = 2\sqrt{2}\left(\frac{L}{v_{th}}\right)\left(\frac{1}{R_m B_0}\right)^{\frac{1}{2}} \left(R_m^{\frac{3}{2}} - 1\right). \qquad 3.35f$$

The population of electrons energetic enough to reach the insulators is proportional to $\exp(-\Xi_e)$, the energy losses due to cold returning electrons is

$$\overline{PH}_e = \left(\frac{y}{\tau_B}\right)\frac{3}{2} n_0 k_B T_e \exp(-\Xi_e). \qquad 3.35g$$

The quantity y is a design factor describing the proportion of the electrons that contact the insulators. For a completely open system, it might be zero, which is the default value in the simulation. For a terrestrial system with conventional insulators, it would be 1. For practical propulsion systems, $0 \leq y \ll 1$.

Charge Exchange Losses

The charge exchange time scale is

$$\tau_{CX} = \frac{1}{n_0(1-\alpha)\sigma_{CX}u_\theta}, \tag{3.36}$$

where α is the specified degree of ionization, and σ_{CX} is the charge exchange cross-section. The simulation can also be set not to include charge exchange losses. These calculations are performed in *secular_reactor.m*. If charge exchange losses are included, a marginal factor $f_{CX} = \dot{n}_{CX}/\dot{n}$ is calculated and the values for $\dot{n}$ in Equations (3.3) and (3.13) are multiplied by a factor of $(1 + f_{CX})$ in the code.

3.2.4 Parallel Loss Calculations

This section describes how the function file *parallel_r1.m* calculates ion and electron losses. As discussed in Section 3.1.2, this calculation is done independently for each mirror. The results of each calculation are halved to reflect losses from only one mirror. To obtain the total system losses, the values for the power and jet mirror are summed. This is valid, because the loss cone relation for g is derived assuming symmetry in phase space as shown in Section 3.2.3.

The Potential Offset

[Abel, 2021] defines a potential offset φ_0, such that $\Xi_i = \Xi_e = 0$ at $z = 0$ and $B = B_0$. Starting with the Boltzmann relation $n_s = n_s(\psi) exp\left(-\frac{\Xi_s}{k_B T_s}\right)$, assuming quasi-neutrality so that $Z_i n_i = n_e$, and taking $m_e \ll m_i$, an expression for potential can be written

$$\varphi = \left(\frac{Z_i e}{k_B T_i} + \frac{e}{k_B T_e}\right)^{-1} \frac{m_i}{2T_i} r^2 \Omega^2. \tag{3.37a}$$

For any value of r

$$\frac{e\varphi}{k_B T_e} = \left(\frac{Z_i}{\tau} + 1\right)^{-1} \frac{m_i}{2k_B T_e} r_0^2 \Omega^2 \left(\frac{r^2}{r_0^2} - 1\right) + O(1), \tag{3.37b}$$

where $\tau = T_i/T_e$. Recognizing that $r_0^2 \Omega^2 = u_\theta^2$

$$\frac{e\varphi}{k_B T_e} = \left(\frac{Z_i}{\tau} + 1\right)^{-1} \frac{M^2}{2} \left(\frac{r^2}{r_0^2} - 1\right). \tag{3.37c}$$

For electrons, the centrifugal potential is $\Xi_e = -e(\varphi + \varphi_0)$, or

$$\Xi_e = \left(\frac{Z_i}{\tau} + 1\right)^{-1} \frac{M^2}{2} k_B T_e \left(1 - \frac{r^2}{r_0^2}\right) - e\varphi_0. \tag{3.37d}$$

By similar development

$$\Xi_i = Z_i \left[\left(\frac{Z_i}{\tau} + 1\right)^{-1} \frac{M^2}{2\tau} k_B T_i \left(\frac{1}{R_m} - 1\right) + e\varphi_0\right] - \frac{M^2}{2\tau} k_B T_i \left(\frac{r^2}{r_0^2} - 1\right), \tag{3.37e}$$

where the expression inside the brackets is the potential with offset applied. Factoring out $\left(\frac{r^2}{r_0^2} - 1\right)$ and simplifying

$$\Xi_i = \left(\frac{Z_i}{\tau} + 1\right)^{-1} \frac{M^2}{2\tau} k_B T_i \left(1 - \frac{r^2}{r_0^2}\right) + Z_i e \varphi_0. \quad 3.37f$$

Equations (3.37d) and (3.37f) are implemented in the code to calculate respective values of Ξ_s.

Calculating Parallel Losses for Ions and Electrons

This section describes the method for calculating φ_0 and then solving Equations (3.18) and (3.19) for ion and electron loss rates. The solution requires finding φ_0 so that Equation (3.45) below is satisfied. For ambipolar flow, $\dot{n}_{\parallel e} = Z_i \dot{n}_{\parallel i}$. Substituting Equations (3.19) and Equation (3.18) into this relation and grouping expressions for Ξ on one side

$$\left(\frac{n_e}{n_i}\right)\left(\frac{Z_i + 1}{Z_i}\right)\left(\frac{\nu_e}{\nu_i}\right)\frac{ln(R_m)}{ln[(Z_i + 1)R_m]} = \frac{(\Xi_e / k_B T_e)}{(\Xi_i / k_B T_i)} exp(\Xi_e / k_B T_e - \Xi_i / k_B T_i). \quad 3.38$$

The respective collision frequencies are chosen as those most operative relative to moving the respective species into the loss cone, so for ions it would be ν_{ii}. Similarly, electron-ion collisions are more likely to edge electrons into the loss cone. Given these considerations, from [Braginskii, 1965]

$$\left(\frac{\nu_{ei}}{\nu_{ii}}\right) = \sqrt{2}\left(\frac{m_i}{m_e}\right)^{\frac{1}{2}}\left(\frac{T_i}{T_e}\right)^{\frac{3}{2}}\frac{1}{Z_i^2}\left(\frac{ln\Lambda_e}{ln\Lambda_i}\right) \quad 3.39$$

Substituting Equation (3.39) into the left-hand side of Equation (3.38) and defining this as Y:

$$Y \equiv \sqrt{2}\left(\frac{Z_i + 1}{{Z_i}^2}\right)\left(\frac{m_i}{m_e}\right)^{\frac{1}{2}}\left(\frac{T_i}{T_e}\right)^{\frac{3}{2}}\frac{ln(R_m)}{ln[(Z_i + 1)R_m]}\left(\frac{ln\Lambda_e}{ln\Lambda_i}\right). \quad 3.40$$

Note that the lead factor in Equation (3.40) $\left(\frac{1}{Z_i}\frac{n_e}{n_i}\right) = 1$ because of quasi-neutrality.

Moving on to the right-hand side of Equation (3.38), define X such that

$$X \equiv \frac{1}{K}\frac{M^2}{2}\left(1 - \frac{1}{R_m}\right), \qquad K = \left(\frac{Z_i}{\tau} + 1\right). \tag{3.41}$$

And then setting $y = \frac{e\varphi_0}{k_B T_e}$, the potential energy terms are written

$$\Xi_e / k_B T_e = X - \frac{e\varphi_0}{k_B T_e} = X - y. \tag{3.42a}$$

$$\Xi_i / k_B T_i = X + \frac{Z_i e\varphi_0}{k_B T_i} = X + (K-1)y. \tag{3.42b}$$

$$\frac{\Xi_e / k_B T_e}{\Xi_i / k_B T_i} = \frac{X - y}{X + (K-1)y}. \tag{3.42c}$$

$$\Xi_e / k_B T_e - \Xi_i / k_B T_i = -Ky. \tag{3.42d}$$

Substituting Equations (3.42) into the right-hand side of Equation (3.38) and Equation (3.40) into the left-hand side

$$Y = \frac{X - y}{X + (K-1)y} \exp(-Ky). \tag{3.43}$$

For a given use case $[n_0, T_i, T_e, K, \beta, R_{mP}]$, values for K, X and Y are determined. (Note that K in the use case specification is the Kármán number.) A range for y is traversed, and the value satisfying Equation (3.43) is found. The offset potential is then calculated: $\varphi_0 = \frac{y k_B T_e}{e}$. This value for φ_0 is substituted into Equations (3.37d) and (3.37f); and those results are then used with Equations (3.18) and (3.19) to calculate ion and electron loss rates.

3.2.5 Random Variable Input Batch Simulations

The *dfdcm_r5a.m* code was implemented within a framework that allows an arbitrary number of trials with randomized input vectors $[n_0, T_i, T_e, K, \beta, R_{mP}]$. The code is named *dfdcm_r5a_dotland.m*. To set up a run, ranges for the input vector are entered, $0.7 \leq K \leq 1.1$, for example. Additionally, the number of trials m is entered. As with the basic *dfdcm_r5a.m* code, physical characteristics of the reactor and SWDEC must be entered. These values are not varied in a run, so the output of a simulation is particular to the specified configuration.

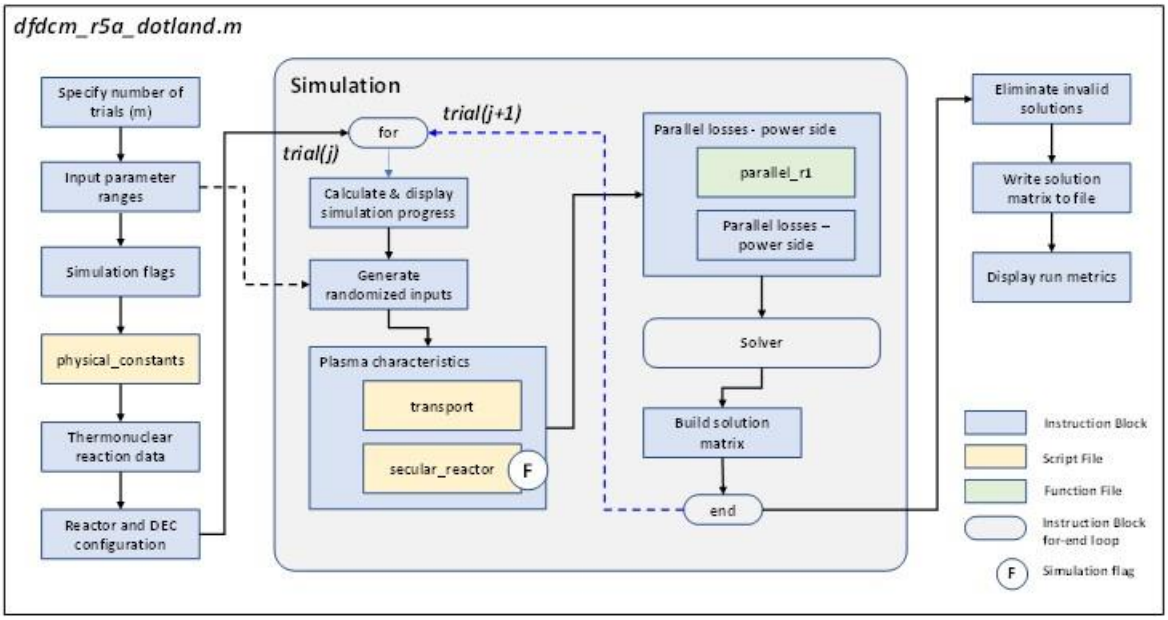

Figure 3-12 – Random variable batch simulation code organization

The solution matrix is an array of solution vectors $[R_{mJ}, R_{mP}, n_0, T_e, T_i, \beta, K, M, B_z, \overline{Q_r^{\alpha}}, \overline{Q_r^{n}}, \overline{P_r^{\alpha}}, \overline{P_r^{n}}, \tau_{mom}]$ for m' trials, where m' is the number of successful trials.

Figure 3-12 shows the organization of the code and how the basic model is implemented in a loop running m specified trials. Table 3-4 summarizes functions of respective simulation elements that differ from or are added on to the basic code.

Table 3-4 - Random variable batch simulation functional description

Element	Type	Function
Specify number of trials	Instruction Block	Number of trials m
Input parameter range	Instruction Block	User inputs to enter max/min for use case vector (n_0, T_e, T_i, K, β, R_{mP})
Thermonuclear reaction data	Instruction Block	Product energies, partial pressures, ionization states and average particle mass
Reactor and DEC configuration	Instruction Block	User inputs for key dimensions, conversion efficiencies, and other characteristics
Calculate and display simulation progress	Instruction Block	Tracks number of trials and displays as percent complete in increments of 100 trials
Generate randomized inputs	Instruction Block	Tophat distribution, random draw from input parameter ranges
Build solution matrix	Instruction Block	Saves solution vector for each trial in a matrix
Eliminate invalid solutions	Instruction Block	Removes invalid solution vectors from solution matrix
Write solution matrix to file	Instruction Block	Writes updated solution matrix to output file
Display run metrics	Instruction Block	Displays percentage of successful solutions

The instruction block removing invalid solutions identifies those solutions by the value of R_{mJ} returned by the simulation. As discussed in Section 3.2.1, the solver works by traversing a range of values for R_{mJ} to balance Equation (3.5). If the solver cannot find a solution that balances Equation (3.5), the solver defaults to $R_{mJ} = R_{mJ\,min}$. These results are invalid, and they are removed from the solution matrix.

References – Chapter 3

1. Braginskii, S.I., “Transport Processes in a Plasma,” Rev. Plasma Physics I, p205 (1965)
2. Huba, J.D., Naval Research Laboratory Plasma Formulary, 2013
3. Abel, I.G., Plunk, G.G., Wang, E., Barnes, M., Cowley, S.C., Dorland, W., Schekochihin, A.A., “Multiscale gyrokinetics for rotating tokamak plasmas: fluctuations, transport and energy flows,” Rep. Prog. Phys. 76 (2013) 116201 (69pp), doi:10.1088/0034-4885/76/11/116201
4. Abel, I.G., “MCTrans++ Reference Manual, version dated 21 August 2021
5. Ghosh, J., Elton, R.C., Griem, H.R., Case, A., DeSilva, A.W., Ellis, R.F., Hassam, A., Lunsford R., and Teodorescu, C., “Radially resolved measurements of plasma rotation and flow-velocity shear in the Maryland Centrifugal Experiment,” Physics of Plasmas 13, 022503 (2006); doi: 10.1063/1.2167915
6. White, Roscoe, Hassam, Adil, and Brizard, Alain, “Centrifugal particle confinement in mirror geometry,” Physics of Plasmas 25, 012514 (2018); doi: 10.1063/1.5003359
7. Chen, Francis F., “Introduction to Plasma Physics,” New York, 1974, p151

4 Reactor Operation and Performance

4.1 Scope and Approach

4.1.1 Scope

The objectives of efforts described in this chapter are: 1) gain insights into the operability and performance of CM fusion reactors in propulsion applications; 2) characterize viable reactor configurations; 3) specify model reactor configurations.

Operability is the ability of the reactor to operate within constraints for technology and system safety, magnetic field strength or plasma temperatures, as examples. An operationally viable system should be self-powering and comport with near-to-midterm technologies for system components and characteristics. Performance for propulsion systems is described in terms of jet power, and more particularly, jet power per volume of burning plasma. An important objective of the chapter is to define model CM reactor configurations as a basis for analysis of the propulsion system. The model configurations are point solutions that specify performance and operating characteristics.

4.1.2 Approach

The initial task is a parametric analysis of the domain for the plasma characteristics $[n_0, T_i, T_e, K, \beta, R_{mP}]$. Using tools and methods described in Chapter 3, these quantities are varied randomly and the results are screened in order to determine the number of viable results. Viability is defined in terms of limits for system characteristics, e.g., mirror magnet strength less than 15 T.

Following the initial screening, subsets of the larger domain are examined in greater detail with the goal of isolating solutions balanced for performance and operability. With the data generated from the screenings, an analysis of CM reactor behavior can be performed.

4.2 Parametric Analysis

4.2.1 The Operational Domain

Table 4-1 provides the ranges of plasma parameters considered in the parametric analysis. These are the same quantities used to specify use cases for the 0D CM reactor model. The lower values for number density n_0 and plasma temperature T_i, T_e follow from reactivity curves for D-T reactions, which translates to power density for the burning plasma. The upper values are based on considerations for likely technology and design limits for magnetic field strength for a given magnetic pressure ratio.

The range for mirror ratio for the power-side of the reactor R_{mP} reflects the desire to evaluate the largest space possible. In early cases run with the 0D reactor, R_{mP} was relatively low for some viable solutions, hence the minimum value of 1.05, set to provide a robust traverse of this parameter. Mirror ratios above 5, given midplane values of B_z, could drive magnetic mirror field strengths to unreasonably high values. Lower values of R_{mP} provide more power to run the reactor with charged species, but also result in more losses and higher power requirements. At the same time, for reactors powered by neutrons, possibly with a blanket and shielding assembly (BSA), it might be desirable to limit losses of charged species through the forward mirror, and a high R_{mP} might be specified as a result.

The value for K is limited on the high side to approximately unity, in order to minimize distortion of the magnetic field. The lower limit is set to 0.65 based on the desire to keep Mach numbers above 5 or 6. As shown in Equation (1.15), the Mach number is directly proportional to K.

Table 4-1 – CM plasma characteristics

Parameter	Units	min	max
n0	#/m^3	10^{19}	10^{22}
β		0.005	0.05
K		0.65	1.05
Te	keV	7.5	15
Ti	keV	7.5	15
RmP		1.05	5

Cases for evaluation are calculated using the 0D model (*dfdcm_r5a_dotland.m*) in batches varying in size from a few hundred to 2000. The resulting cases are then assessed relative to likely technological constraints for E and B fields shown in Table 4-2. An initial canvass, Case 0 with 4000 trials, was performed taking in the entire domain described in Table 4-1. Of the 4000 trials, 2900 returned solutions for which the 0D reactor power balanced, and that met constraints in Table 4-2.

Table 4-2 – Assumed technology constraints for E and B fields

Field	Units	Risk			Basis of Assessment
		Low	Moderate	High	
B	T	<10	10-20	>20	SCM critical current density 10^8 A/m^2
E	MV/m	1-10	10-100	>100	Notional

In the case of the magnetic field, the proposed values for B are along the centerline in the midplane. A representative critical superconducting magnetic current density of 10^8 A/m^2 was applied to

likely reactor geometries on the scale of 1m aperture at the mirrors, and assuming a 50 percent fill factor for the superconducting material. These constraints did not take into account structural loading of magnets providing such fields. Proposed limits for the electric field are based partly on values for confinement observed in early exploratory analysis. Otherwise, these limits are notional. Practically speaking electric field limits will be limited by technologies for power conversion, and particularly the ability to generate biasing potentials in the MV range. For purposes of evaluating the viability of specific solutions, those with values for E or B falling within the "high risk" range in Table 4-2 were excluded from the analysis.

Table 4-3 defines reactor configurations considered in assessing the cases. Configuration 1 is the baseline and is used in most cases. The volume for burning plasma is consistent with a 500-1000 kW class reactor, while Configurations 2 and 3 scale up to 5 MW. The respective radii factor into calculations for radial transport as discussed in Chapter 3.

Table 4-3 – Reactor configurations

Reactor Configuration	ri (m)	r0 (m)	a(m)	L (m)	V (m^3)	Ar (m^2)
1	0.1	0.5	0.2	2	1.51	3.77
2	0.1	0.5	0.2	5	3.77	9.42
3	0.2	1	0.4	2	6.03	7.54

Table 4-4 summarizes initial performance goals for DFD-CM in terms of reactor breakeven and burning plasma power densities. The breakeven parameter for charged species $Q^{\alpha}\sim 1$ accounts for a power conversion efficiency of 0.8 based on estimated performance of the SWDEC [Chap and Sedwick, 2015]. The breakeven parameter for neutrons Q^{n} is expressed as a range of 1-4, however, because of uncertainties related to potential conversion methods. This range must account for leakage of any BSA, the view factor from the burning plasma to the BSA; and the actual conversion

efficiency. In theory, this range could accommodate a configuration characterized by a low leakage factor, high view factor, and a Carnot limited power conversion scheme. Alternately, it could represent a moderate leakage factor and a highly efficient power conversion scheme. The initial minimum values for fusion power densities $\bar{P}_r^{\alpha}$ and $\bar{P}_r^{n}$ are set at 100 kW/m^3 and 400 kW/m^3, respectively. These are low thresholds, but they are carried to include a large domain and otherwise viable solutions.

Table 4-4 – Preliminary reactor performance criteria

Performance		Units	Value
Q^{α}	Breakeven - charged species		0.95-1.05
Q^{n}	Breakeven - neutrons		1-4
Pr^{α}	Specific power density - charged species	kW/m^3	100
Pr^{n}	Specific power density - neutrons	kW/m^3	400

=

4.2.2 Case Specification and Preliminary Analysis

In preparing the run matrix shown in Table 4-5, variations of the input vector $[n_0, T_i, T_e, K, \beta, R_{mP}]$ within the domain specified in Table 4-1 were defined. Three levels were set for number density (n_0) and electron temperature (T_e). It was assumed that ion temperature and electron temperature were the same. Values for β, K, and R_{mP} were blocked to cover their respective ranges from Table 4-1. This analysis design allowed more focus on variations in power density and transport properties that follow from number density and temperature. Repeatability runs were conducted for most cases, in order to ensure that the model was providing consistent results. Since the batch inputs are generated randomly, the number of viable cases should vary, but only slightly, from the base runs.

The analysis design results in 9 cases of 2000 trials each to be run in the 0D reactor model (*dfdcm_r5a_dotland.m*). Reactor configuration 1 was run for this baseline raft of cases. Based on the criteria specified in Tables 4-2 and 4-4, the number of viable solutions for each case was determined. Note that viable solutions are a subset of successful solutions generated by the 0D model, i.e., the code was able to find a value of R_{mJ} that allowed that solution point to meet the reactor power balance. For the most part, successful solutions were not viable relative to system constraints, e.g., $B > B_{max}$.

Cases 2-6 show relatively high incidences of viable solutions for neutron self-powering reactors, with the highest density of viable solutions occurring in Case 3 $[n_0(10^{19} - 10^{20}\ \#/m^3), T_e(12.5 - 15\ keV)]$. By comparison, there is only one viable solution for alpha self-powering that occurs in Case 6 $[n_0(10^{20} - 10^{21}\ \#/m^3), T_e(12.5 - 15\ keV)]$. No viable solutions were identified for number densities above $10^{21}\ \#/m^3$ (Cases 7-9), for either neutron or alpha self-powering configurations.

Based on characteristics of the single viable solution for charged species self-powering in Case 6, as well as those solutions marginally approaching viability criteria, Case 11 was derived. Values for n_0 and T_e were narrowed from Case 6, as were values for β, K, and R_{mP}. Case 11 was run with 2000 trials, with the result of 92 viable solutions for neutron self-powering configurations, and 40 for alpha self-powering. The higher density of viable solutions within the reduced domain suggests that there is a preferred operational region, especially for systems self-powered by charged species.

Case 13 is identical to Case 6, except that Reactor Configuration 3 is used instead of Configuration 1 used in Cases 1-9. The results show a smaller number of viable neutron self-powering solution

points, but the limitations of the experiment design preclude any assertion of a difference associated with reactor configuration. The underlying relations suggest that at least to the first order, there should be no difference in performance of the respective configurations. Specifically, values for r_0, r_i, and a are included in factors related to perpendicular transport losses, which are not enabled within the model for these runs. However, a does factor into the estimate for the second derivative of the radial velocity gradient. The larger value relative to Configuration 1 would result in a smaller value for plasma heating due to shear, and may have played a marginal role in reducing the number of successful solutions, vis-à-vis the reactor power balance.

Cases 14-16 were run to evaluate the effects of a "strong mirror" for configurations self-powered by neutrons. The upper value for the magnetic pressure ratio range was increased to 0.10. This was done with the thought that the higher mirror ratio might allow for denser plasmas. As the case turned out, however, solutions for B_z and R_{mJ} resulted in many of the solutions exceeding the limit for magnetic field strength in Table 4-2. The majority of points that are excluded from Case 14 are because the maximum *B* in the system exceeded 20T. As a result, Case 14, which was otherwise the same as Case 4, produced 79 viable solutions for neutron self-powering, versus 235 in Case 4. Cases 10 and 12 are repeats of Cases 6 and 11, respectively, but with seeding of the plasma modeled as a gain of 3 applied to the bremsstrahlung radiation. The experiment was motivated by the hypothesis that momentum losses could be traded with losses not associated with momentum, e.g., radiation losses. This hypothesis and the results of Cases 10 and 12 will be addressed in Section 4.3 on reactor operability.

Table 4-5 – Analysis matrix and preliminary metrics

Case	Reactor Configuration	N	beta	K	RmP	Te (keV)	x3	n0 (#/m^3)	Viable Solutions		Repeatability Run	
									Neutrons	Alphas	Neutrons	Alphas
0	1	4000	0.0025-0.075	0.65-1.05	1.05-5.0	7.5-17.5	1	10^{19}-10^{22}	181	0		
1	1	2000	0.005-0.05	0.65-1.05	1.05-5.0	7.5-10.0	1	10^{19}-10^{20}	4	0		
2	1	2000	0.005-0.05	0.65-1.05	1.05-5.0	10.0-12.5	1	10^{19}-10^{20}	246	0	224	0
3	1	2000	0.005-0.05	0.65-1.05	1.05-5.0	12.5-15.0	1	10^{19}-10^{20}	397	0	477	0
4	1	2000	0.005-0.05	0.65-1.05	1.05-5.0	7.5-10.0	1	10^{20}-10^{21}	235	0	290	0
5	1	2000	0.005-0.05	0.65-1.05	1.05-5.0	10.0-12.5	1	10^{20}-10^{21}	224	0	214	1
6	1	2000	0.005-0.05	0.65-1.05	1.05-5.0	12.5-15.0	1	10^{20}-10^{21}	180	1	166	1
7	1	2000	0.005-0.05	0.65-1.05	1.05-5.0	7.5-10.0	1	10^{21}-10^{22}	0	0	0	0
8	1	2000	0.005-0.05	0.65-1.05	1.05-5.0	10.0-12.5	1	10^{21}-10^{22}	0	0	0	0
9	1	2000	0.005-0.05	0.65-1.05	1.05-5.0	12.5-15.0	1	10^{21}-10^{22}	0	0	0	0
10	1	2000	0.005-0.05	0.65-1.05	1.05-5.0	10.0-12.5	3	10^{20}-10^{21}	213	1	176	0
11	1	2000	0.0125-0.025	0.85-1.05	1.25-1.65	11.5-15.5	1	1.25×10^{20} - 2.75×10^{20}	92	40	90	40
12	1	2000	0.0125-0.025	0.85-1.05	1.25-1.65	11.5-15.5	3	1.25×10^{20} - 2.75×10^{20}	4	77	4	69
13	3	2000	0.005-0.05	0.65-1.05	1.05-5.0	12.5-15.0	1	10^{20}-10^{21}	136	0		
14	1	2000	0.005-0.10	0.65-1.05	5.0	7.5-10.0	1	10^{20}-10^{21}	79		79	
15	1	2000	0.005-0.10	0.65-1.05	5.0	10.0-12.5	1	10^{20}-10^{21}	52			
16	1	2000	0.005-0.10	0.65-1.05	5.0	12.5-15.0	1	10^{20}-10^{21}	27			

4.3 Operability

4.3.1 The Well-Depth Potential

The well-depth potential is the main determinant of confinement time for both simple mirror devices and centrifugal mirrors. Figure 4-1a from Case 0 data suggests that the relative contributions of centrifugal and mirror confinement are reciprocal, and that is true up to a certain Mach number. However, Case 0 is an unrestricted sampling of the domain, and even though the data present a clear front, there is inherent confounding present. Figure 4-1b from the narrower domain of Case 6 shows a similar front at lower Mach numbers, but at higher Mach numbers, the mirror ratio appears to be increasing.

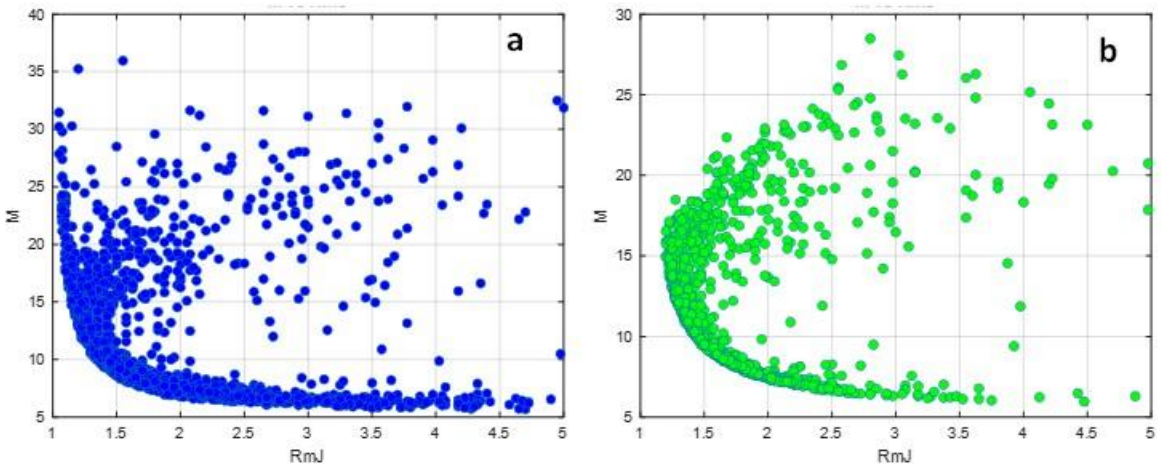

Figure 4-1 – Mach vs. mirror ratio – Cases 0 (a) and 6 (b)

Figure 4-2 shows a traverse of the Mach number for a 12.5 keV plasma with number density of 2.5×10^{20} #/m^3. The power-side mirror ratio is held constant at 1.5. Below a certain Mach

number, as Mach number increases, mirror ratio decreases, which seems intuitive. However, above a certain Mach number, the mirror ratio starts to increase with increasing Mach number.

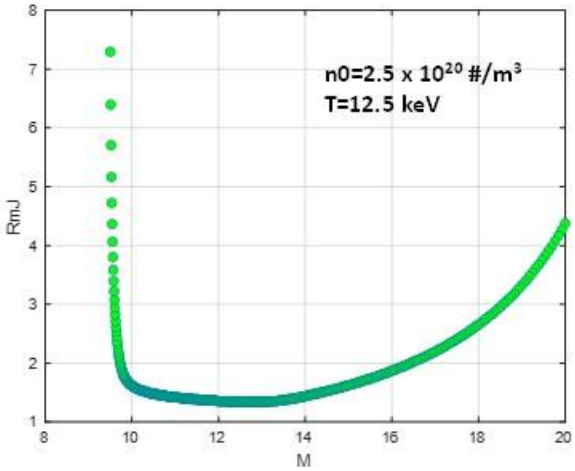

Figure 4-2 – M-β traverse for Case 6 solution

As a hypothesis, this happens because the loss of prompt species becomes dominant over that of thermal species at higher Mach numbers. The loss of thermals is diminished by several orders of magnitude in this regime. The prompt species are only mirror confined, but the cost of replacing the them increases with square of the Mach number. The system compensates accordingly by increasing the mirror ratio to maintain thermal balance in the well. Equation (3.37f) is the ion well potential defined in terms of the offset potential φ_0 which is set so that $\Xi_i = 0$ at the center of the well. In the special case where mirror ratios are equal, the total differential of the well potential for ions is

$$d\left(\frac{\Xi_i}{k_B T_i}\right) = \frac{\partial}{\partial M}\left(\frac{\Xi_i}{k_B T_i}\right) dM + \frac{\partial}{\partial R_m}\left(\frac{\Xi_i}{k_B T_i}\right) dR_m + \frac{\partial}{\partial \varphi_0}\left(\frac{\Xi_i}{k_B T_i}\right) d\varphi_0. \qquad 4.1$$

Solutions to Equation (4.1) are unique to each operating point in the (M, R_m, φ_0) domain, each having a particular, constant value for Ξ_i at that point. Accordingly the total differential is equal

to zero. Evaluating the partial derivatives in Equation (4.1), dividing by dR_m and collecting terms for M^2 and M results in the expression

$$M^2 + 2R_m^2 \frac{dM}{dR_m} M + 4(R_m^2 - R_m)\left\{\frac{Z_i e}{k_B T_i}\frac{d\varphi_0}{dR_m}\right\} = 0. \tag{4.2}$$

Equation (4.2) is quadratic in form, so that M can be found

$$M = -\lambda_1 \pm \frac{1}{2}\sqrt{\lambda_1^2 - 4\lambda_2} \tag{4.3a}$$

$$\lambda_1 = R_m^2 \frac{dM}{dR_m} \tag{4.3b}$$

$$\lambda_2 = 4(R_m^2 - R_m)\left\{\frac{Z_i e}{k_B T_i}\frac{d\varphi_0}{dR_m}\right\} \tag{4.3c}$$

The factors λ_1 and λ_2 are unique to specific solutions for the reactor power balance. Therefore, the locus of solutions in the (R_{mJ}, M) domain represent different systems, not variation within a system. Given the limited objective of verifying the general shape of the (R_{mJ}, M) curve in Figure 4-2, the λ_1 factor is of primary interest, because it contains an explicit expression for $\frac{dM}{dR_m}$. As an initial observation, it has two roots, consistent with the respective branches of the (M, R_{mJ}) curve in Figure 4-2. In the (M, R_{mJ}) domain, Equation (4.3b) is a differential equation with the apparent form $\frac{dy}{dx} = -\frac{Q(x,y)}{P(x,y)}$, which suggests λ_1 could be found by separation of variables. However, $\frac{dM}{dR_m}$ is multivariate with non-linear dependencies, so it cannot be evaluated analytically. In order to characterize λ_1, it is necessary is to consider the physics relevant to the proposed hypothesis, the reactor power balance in Equation (3.5). Consistency with the hypothesis proposed at the start of this section requires that below a particular, critical Mach number, $\frac{dM}{dR_m}$ is negative, and above, positive. It also requires accounting for the relative contributions of thermal and prompt losses.

Substituting definitions for $\bar{P}_F$, $\overline{PV}_{\parallel}$, and $\bar{P}_{TH}$ into Equation (3.5) and grouping terms that are multiplied by thermal losses $\dot{n}_{\parallel}$ results in

$$\bar{P}_r^{\alpha}(1-g)+\overline{IV}_0=\dot{n}_{\parallel}\left\{m_i u_\theta^2+\tfrac{3}{2}k_B(T_i+Z_iT_e)+\Xi_i+Z_i\Xi_e\right\}+2\dot{n}^{\alpha}gm_iu_\theta^2+\bar{P}_R+\bar{Q}_{\perp}. \quad 4.4$$

The radiation term $\bar{P}_R$ includes both bremsstrahlung and cyclotron losses. Taking $Z_i=1, T_i=T_e$, and recalling that $m_iu_\theta^2=k_BT_eM^2$, and that $g=1-\sqrt{1-\frac{1}{R_m}}$, Equation (4.4) can be written

$$\dot{n}^{\alpha}E^{\alpha}\left(1-\frac{1}{R_m}\right)^{\frac{1}{2}}+\bar{IV}_0=\dot{n}_{\parallel}k_BT_eF_1+\dot{n}^{\alpha}k_BT_eF_2+\bar{P}_R+\bar{Q}_{\perp}, \quad 4.5a$$

$$F_1=3+\frac{M^2}{2}\left(3-\frac{1}{R_m}\right), \quad 4.5b$$

$$F_2=2M^2\left[1-\left(1-\frac{1}{R_m}\right)^{\frac{1}{2}}\right]. \quad 4.5c$$

The factor F_1 fixes the thermal energy cost of the thermal species, and F_2, the thermal energy cost of replacing prompt alphas. Note that F_2 does not include losses in fusion energy due to the prompt species. Those losses are accounted for in the first term on the LHS. In order to generate a term for $\frac{dM}{dR_m}$, it is necessary to take the derivative of Equations (4.5) with respect to R_m

$$\frac{\dot{n}^{\alpha}E^{\alpha}}{2R_m^2}\left(1-\frac{1}{R_m}\right)^{-\frac{1}{2}}=k_BT_e\left(\frac{d\dot{n}_{\parallel}}{dR_m}F_1+\dot{n}_{\parallel}\frac{dF_1}{dR_m}+\dot{n}^{\alpha}\frac{dF_2}{dR_m}\right), \quad 4.6a$$

$$\frac{dF_1}{dR_m}=M\left(3-\frac{1}{R_m}\right)\frac{dM}{dR_m}+\tfrac{1}{2}\left(3-\frac{1}{R_m}\right)^{-1}\frac{M^2}{R_m^2}, \quad 4.6b$$

$$\frac{dF_2}{dR_m}=4M\left[1-\left(1-\frac{1}{R_m}\right)^{\frac{1}{2}}\right]\frac{dM}{dR_m}-\left(1-\frac{1}{R_m}\right)^{-\frac{1}{2}}\frac{M^2}{R_m^2}. \quad 4.6c$$

The $\overline{IV}_0$ term is independent, and the radiation and parallel loss terms are not dependent upon R_m, so their derivatives are zero. Additionally, $\dot{n}^{\alpha}$ is calculated using Equation (1.3), so $\frac{d\dot{n}^{\alpha}}{dR_m} \approx 0$. Grouping like terms and dividing by $k_B T_e$ and $\dot{n}^{\alpha}$, Equations (4.6) become

$$\frac{E^{\alpha}}{2k_B T_e R_m^2}\left(1-\frac{1}{R_m}\right)^{-\frac{1}{2}} - \frac{1}{\dot{n}^{\alpha}}\frac{d\dot{n}_{\parallel}}{dR_m}F_1 = G_1\frac{dM}{dR_m} + G_2\frac{M^2}{R_m^2}, \tag{4.7a}$$

$$G_1 = M\left\{\left(\frac{\dot{n}_{\parallel}}{\dot{n}^{\alpha}}\right)\left(3-\frac{1}{R_m}\right) + 4\left[1-\left(1-\frac{1}{R_m}\right)^{\frac{1}{2}}\right]\right\}, \tag{4.7b}$$

$$G_2 = \frac{1}{2}\left(\frac{\dot{n}_{\parallel}}{\dot{n}^{\alpha}}\right)\left(3-\frac{1}{R_m}\right)^{-1} - \left(1-\frac{1}{R_m}\right)^{-\frac{1}{2}}. \tag{4.7c}$$

Equations (4.7) can be rewritten to find $\lambda_1 = R_m^2\frac{dM}{dR_m}$

$$R_m^2\frac{dM}{dR_m} = \frac{E^{\alpha}}{2G_1 k_B T_e}\left(1-\frac{1}{R_m}\right)^{-\frac{1}{2}} - \left(\frac{R_m^2}{\dot{n}^{\alpha}}\frac{d\dot{n}_{\parallel}}{dR_m}\frac{F_1}{G_1} + \frac{G_2}{G_1}M^2\right). \tag{4.8}$$

Equation (4.8) describes the changes in system performance relative to the changes in the mirror ratio. The equation is normalized by $\dot{n}^{\alpha}$, so that it is dimensionless and can be scaled to plasmas of varying power densities. The lead term on the right-hand side, which will be called J_1, represents the ratio of fusion power generation to the rate of change in power loss due to thermal species. Provisionally, the first term in the second set of parentheses is the ratio thermal losses due to changes in $\dot{n}_{\parallel}$ to that due to losses in the prompt species. The second term in the parentheses is the ratio of the rate of change in thermal losses to the change due to losses for replacing the prompt alphas leaving the system.

Returning to the hypothesis attending Figure 4-2, for systems with equal mirror ratios, R_m will exceed 2 only fractionally, because of power balance limits. For the 12 keV Case 6 plasma, $\frac{\dot{n}_\parallel}{\dot{n}^\alpha}$ will be *O(10)* below the critical Mach number and much less than unity at higher Mach numbers, as shown in Figure 4-3 for varying plasma temperatures.

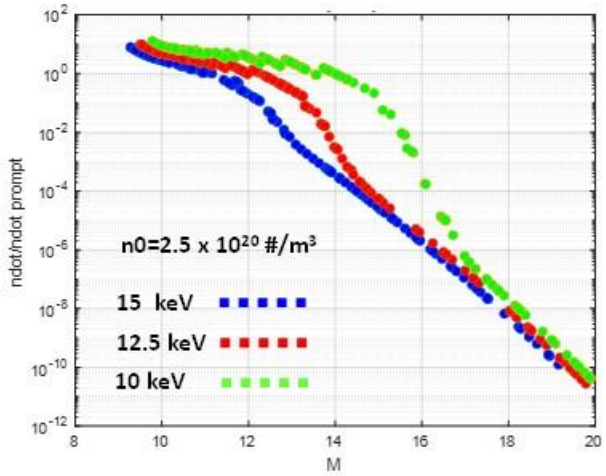

Figure 4-3 – Ratio of thermal to prompt losses – Case 6

The value $\frac{d\dot{n}_\parallel}{dR_m}$ is on the order of n_o/τ_i where τ_i is *O(10¹)* below the critical Mach number based on model results, and *O(10²)+* above it. Depending on values of *F₁*, *G₁*, and *G₂*, these trends suggest that for a given *Rm*, at higher Mach numbers, with lower values of $\frac{\dot{n}_\parallel}{\dot{n}^\alpha}$ and $\frac{d\dot{n}_\parallel}{dR_m}$, that the second term on the right-hand side of Equation (4.8) will tend to be smaller than the first term $\frac{E^\alpha}{2G_1 k_B T_e}\left(1-\frac{1}{R_m}\right)^{-\frac{1}{2}}$, and so $R_m^2\frac{dM}{dR_m}$ would be positive. Conversely, the values of these respective parameters below the critical Mach number would tend to result in $R_m^2\frac{dM}{dR_m}$ being negative.

The 0D reactor model does not support direct calculation of cases for equal mirror ratios, but inputs can be defined so that the model generates a locus of solutions for the traversal of one variable, β

for example. Since $M = 2K/\sqrt{\beta}$ for $Z_i = 1$, a β traversal is also a Mach number traversal for constant K. These traversals can be produced for varying values of R_{mP}, which is held constant for each run. Within each successive run, the solutions where $R_{mJ} \cong R_{mP}$ can be extracted. In this manner, a case for equal mirror ratios can be built, and Equations (4.6)-(4.8) can be evaluated. Case s1, with plasma temperature of 12.5 keV and number density of 2.5×10^{20} #/m^3 includes 14 solutions with mirror ratios ranging from 1.4 to 1.8. Figure 4-4 shows the locus of solutions in the (R_{mJ}, M) domain, where $R_{mJ} = R_{mP}$ The critical Mach number is seen to be between 12 and 13, and the critical mirror ratio ~1.4. Figure 4-5 shows λ_1 for Case s1 calculated from Equation (4.8). As expected, there are two branches in the solution, one positive and one negative. One point of the lower branch in the critical region is excluded, because coarse discretization resulted in apparently invalid values G_1 and G_2. Figures 4-5a and 4-5b show λ_1 and $\frac{dM}{dR_{mJ}}$ for Case s1, the latter which can be calculated directly from λ_1, per Equation (4.8). Since Case s1 was built with a fixed discretization, it is also possible to estimate $\frac{dM}{dR_{mJ}}$ from adjacent solutions. This is overlaid on the curve in Figure (4.5b) and has reasonable agreement with the curve calculated from λ_1. It should be mentioned that the datasets generated from the 0D model are random solutions for the thermonuclear power balance, and there is no uniform discretization among any of the parameters in the respective solutions. As a result, it is not possible to calculate spatial derivatives from the cases generated by the 0D model.

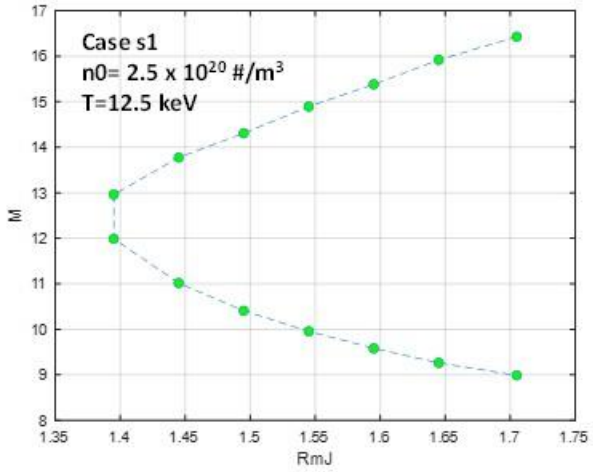

Figure 4-4 – Mach number vs. RmJ – Case s1

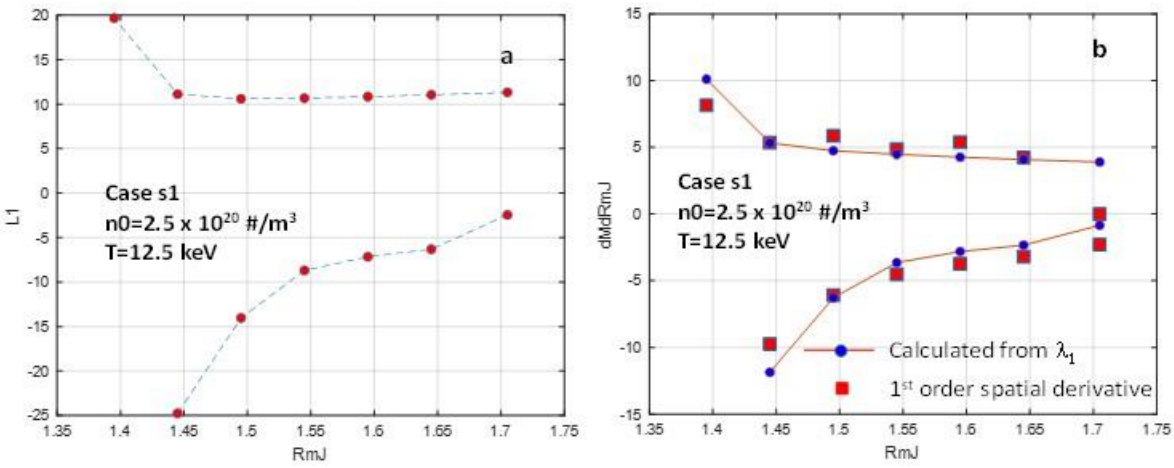

Figure 4-5- λ_1 and dM/dRmJ curves – Case s1

For the general case in a propulsion system, mirror ratios may not be equal. The $\bar{P}_r^{\alpha}$ term and the prompt species replacement term of $\bar{P}_F$ in Equation (3.5) are dependent upon the loss cone factor g, and $g = g_P + g_J$. The development of Equations (4.8) could be performed in terms of g, instead of R_m, and these terms would be unaffected by differences in mirror ratios. However, the $\overline{PV}_{\parallel}$ term is affected by differing mirror ratios. In the 0D code, $\dot{n}_{\parallel}$ and $\overline{PV}_{\parallel}$ losses for the respective

mirrors are calculated separately using numerical methods and then added together to obtain the total system losses

$$\overline{PV_{\parallel}} = (\Xi_i + Z_i\Xi_e)_J \dot{n}_{\parallel J} + (\Xi_i + Z_i\Xi_e)_P \dot{n}_{\parallel P}, \tag{4.9}$$

where $\dot{n}_{\parallel J} + \dot{n}_{\parallel P} = \dot{n}_{\parallel}$. For purposes of this analysis, a simple model provides additional insight into the effects of different mirror ratios. Defining

$$\chi \equiv (\Xi_i + Z_i\Xi_e)_P - (\Xi_i + Z_i\Xi_e)_J, \tag{4.10}$$

Equation (4.9) can be rewritten

$$\overline{PV_{\parallel}} = (\Xi_i + Z_i\Xi_e)_J \dot{n}_{\parallel J} + \left[(\Xi_i + Z_i\Xi_e)_J + \chi\right]\dot{n}_{\parallel P}. \tag{4.11}$$

Grouping terms and defining the quantity $\kappa = \dot{n}_{\parallel P}/\dot{n}_{\parallel}$

$$\overline{PV_{\parallel}} = \left[(\Xi_i + Z_i\Xi_e)_J + \kappa\chi\right]\dot{n}_{\parallel}. \tag{4.12}$$

Expanding Equation (4.10),

$$\chi = \left(\frac{Z_i}{\tau} + 1\right)^{-1} \frac{M^2}{2} k_B T_e \left[\left(1 - \frac{1}{R_{mP}}\right)\tau - \left(1 - \frac{1}{R_{mJ}}\right)\tau + Z_i\left(1 - \frac{1}{R_{mP}}\right) - Z_i\left(1 - \frac{1}{R_{mJ}}\right)\right] + Z_i e(\varphi_{0P} - \varphi_{0J}) + e(\varphi_{0P} - \varphi_{0J}), \tag{4.13}$$

where $\tau = T_i/T_e$. Equation (4.13) can be simplified to

$$\chi = \left(\frac{Z_i}{\tau} + 1\right)^{-1} \frac{M^2}{2} k_B T_e (\tau + Z_i)\left(\frac{1}{R_{mJ}} - \frac{1}{R_{mP}}\right) + (Z_i + 1)e(\varphi_{0P} - \varphi_{0J}). \tag{4.14}$$

Equation (4.14) represents an additional term that would be included in calculating F_1, the grouping of losses proportional to $\dot{n}_{\parallel}$. Including χ in Equation (4.5b) for F_1 results in

$$F_1 = 3 + \frac{M^2}{2}\left(3 - \frac{1}{R_{mP}}\right) + \frac{\kappa\chi}{k_B T_e}. \qquad 4.15$$

Taking $Z_i = 1\,, \tau = 1$ and expanding χ

$$F_1 = M^2 + 3 + \frac{M^2}{2}\left(1 - \frac{1}{R_{mP}}\right) + \frac{M^2}{2}\left(\frac{1}{R_{mJ}} - \frac{1}{R_{mP}}\right)\kappa + \frac{2e}{k_B T_e}(\varphi_{0P} - \varphi_{0J})\kappa. \qquad 4.16$$

Grouping terms

$$F_1 = 3 + \frac{M^2}{2}\left[3 - \frac{1+\kappa}{R_{mP}} + \frac{\kappa}{R_{mJ}}\right] + \frac{2e}{k_B T_e}(\varphi_{0P} - \varphi_{0J})\kappa. \qquad 4.17$$

For $R_{mJ} = R_{mP} = R_m$, $\kappa = \frac{1}{2}$, and $\varphi_{0P} = \varphi_{0J}$, Equation (4.5b) is recovered. For $R_{mJ} \neq R_{mP}$, however, there are now three new factors, R_{mP}, $\Phi_0 = \varphi_{0P} - \varphi_{0J}$ and κ.

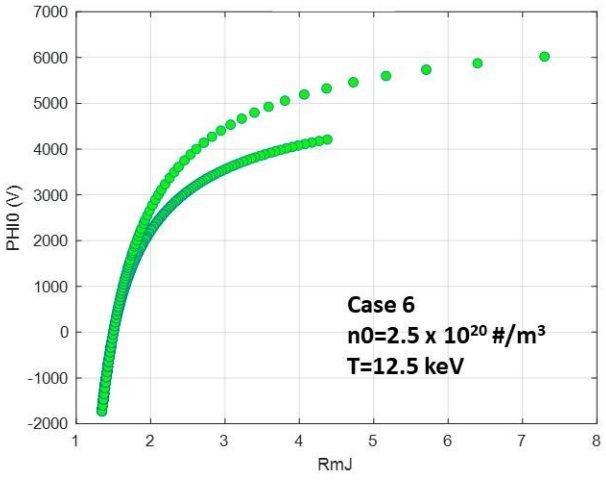

Figure 4-6 - Φ_0 vs. R_{mJ} – Case 6

Figure 4-6 shows Φ_0 vs.R_{mJ} for $R_{mP} = 1.45$, which, given the scale of $\frac{2e}{k_B T_e}$, will affect F_1 to a non-negligible extent. Values for κ and R_{mP} would likely have similarly appreciable effects.

Recalling that F_I is related to the amount of energy that the system loses for thermal ions leaving, these factors ultimately affect R_{mJ} as a matter of the thermal balance of the well.

Figure 4-7 shows the $M\ vs. R_{mJ}$ curves for Case s1 (blue squares) and a representative Case 6 solution (green circles). The most obvious difference is the limited range for $R_{mJ} = R_{mP}$ in Case s1. For a given g for asymmetric mirrors at which a solution is balanced, a low R_m on one mirror may be offset by a higher one on the other. However, if both mirrors are constrained to be equal, the resulting R_m will be relatively small. The other feature is that the Case s1 curve is symmetric above and below the critical Mach number.

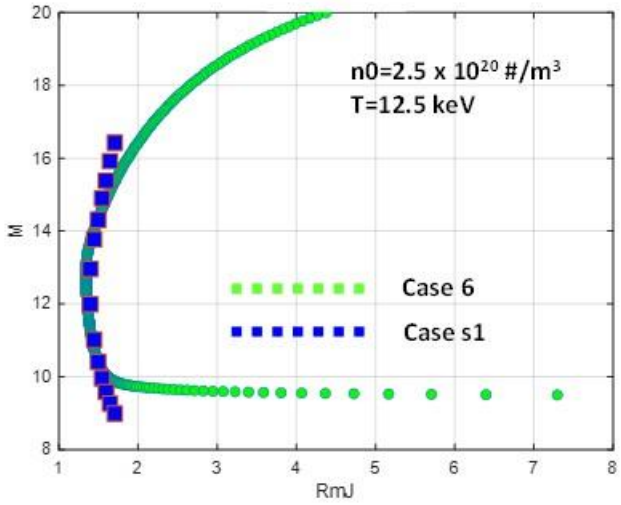

Figure 4-7 – Mach vs. RmJ – Cases 6 and s1

Figure 4-8 shows the well potentials vs. Mach number for jet-side and power-side mirrors for a representative Case 6 solution. The Case s1 data is overlaid (blue squares). The Case 6 power-side mirror ratio is fixed at 1.5, and its potential $\frac{\Xi_{iP}}{k_B T_i}$ increases monotonically with *M*, as does the Case

s1 potential. The potential for the Case 6 jet-side mirror has a minimum in the vicinity of the critical Mach number.

Figure 4-9 is the plot of J_1 *vs. M* for a Case 6 solution. The value of J_1 increases up to the critical Mach number, because $\dot{n}_{\parallel}/\dot{n}^{\alpha}$ is decreasing, and with it, the value of G_1. Above the critical Mach number, $\dot{n}_{\parallel}/\dot{n}^{\alpha}$ is small and does not affect G_1. In this regime, both R_m and M increase to limit losses of prompt species, now dominant because M is high, and along with it, the cost to replace prompt losses. Accordingly, both G_1 and the R_m^2 factors in the denominator of J_1 become larger, and J_1 then decreases. As R_m increases in the super-critical region, J_1 exhibits a minimum and starts to increase again, but slowly. J_1 for Case s1 is overlaid on the Case 6 curve and there appears to be good agreement between the two cases, even over the critical region of $M = 10 - 14$.

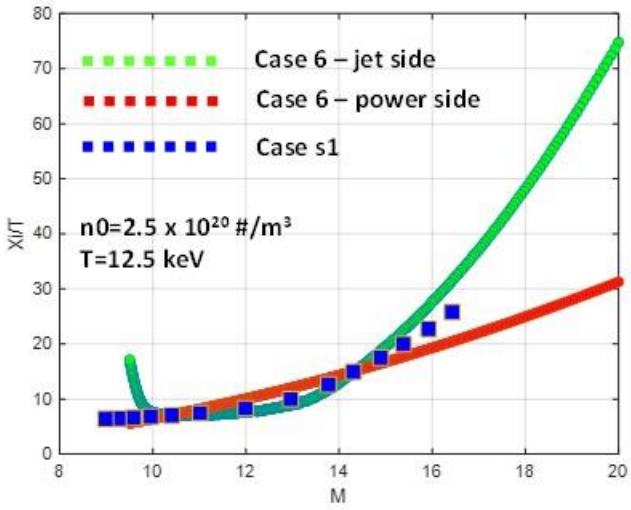

Figure 4-8 – Well potentials vs. Mach number – Cases 6 and s1

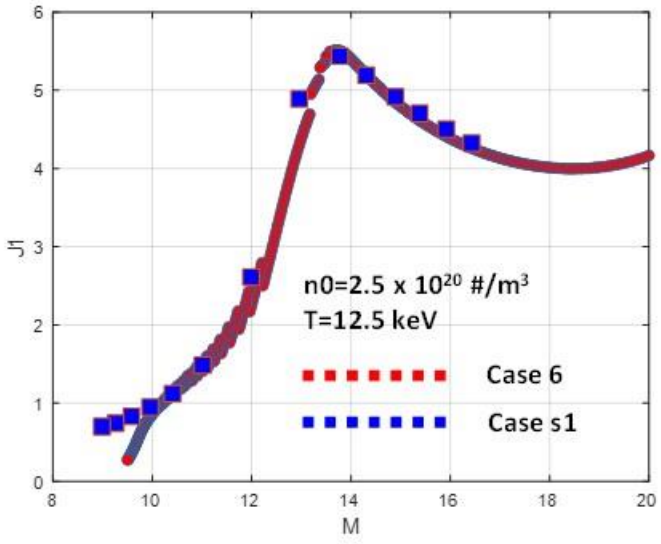

Figure 4-9 – J1 vs. Mach number – Cases 6 and s1

Figure 4-10a and 4-10b show curves for G_2/G_1 and F_1/G_1, respectively. These ratios appear in Equation (4.8). G_2/G_1 is the ratio of the rate of change of energy due to fueling to the rate of change of thermal species. F_1/G_1 is the ratio of energy losses due to thermal species to its own rate of change.

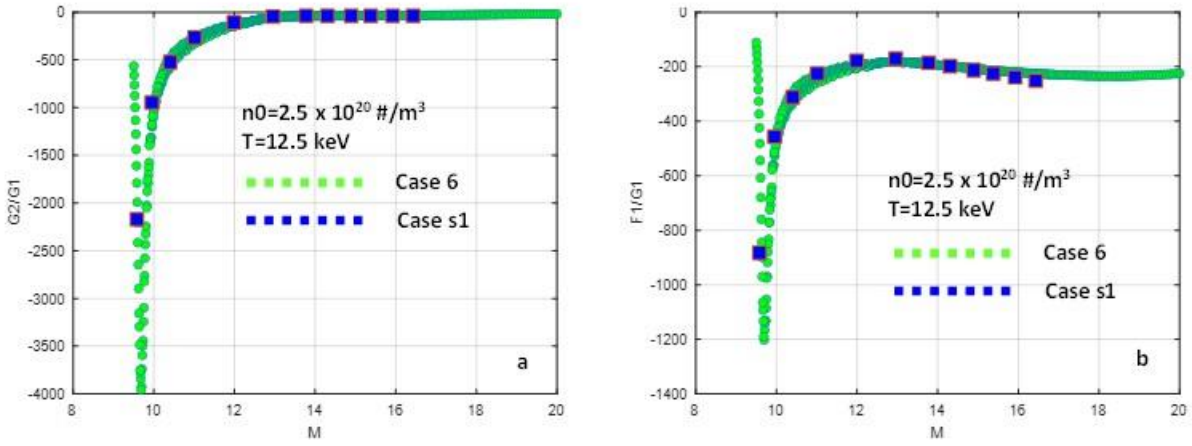

Figure 4-10 – G2/G1 and F1/G1 curves for Cases 6 and s1

As with previous figures, Case s1 data is overlaid, and the results appear consistent between Case 6 with its non-symmetrical mirrors and Case s1 with its symmetrical mirrors. However, as shown in Figure 4-7, the region of overlap is limited to small mirror ratios. Given that, Case s1 demonstrates comparable Mach numbers with Case 6, albeit at lower mirror ratios.

Figures 4-11a and 4-11b show curves for λ_1 and $\frac{dM}{dR_m}$ vs.R_{mJ} for Case 6 that are corollary to those shown for Case s1 in Figures 4-5a and 4-5b. Note that the minimum and maximum values for β correspond to the respective maximum and minimum values for M, respectively. Away from the critical region, the curves are similar qualitatively and to an extent, quantitatively. The curve above the critical Mach number is positive, while below the critical Mach number, it is negative and has a small magnitude, consistent with the relatively shallow (R_{mJ}, M) curve in that region. Within the critical region, Figure 4-11b shows a high rate of change for M, which is consistent with the nearly vertical curve in that region in the (R_{mJ}, M) domain. The curve for λ_1 shows similar behavior. There is a zero crossing for the Case 6 data in the vicinity of $\chi = 0$. And based on the shape of the (R_{mJ}, M) curve for both symmetric and asymmetric mirrors, there should be a singularity in curves for both λ_1 and $\frac{dM}{dR_{mJ}}$ in the vicinity of the minimum R_{mJ}.

The critical Mach number is provisionally defined as the Mach number occurring at the minimum value of R_m, the latter which is also provisionally defined as the critical mirror ratio. From a physical standpoint, these values correspond to the maximum value of J_1, the ratio of fusion power generation (charged species) to thermal losses. It also corresponds to the point where $G2/G1$ goes from negative to approaching zero, and to the maximum value for λ_1.

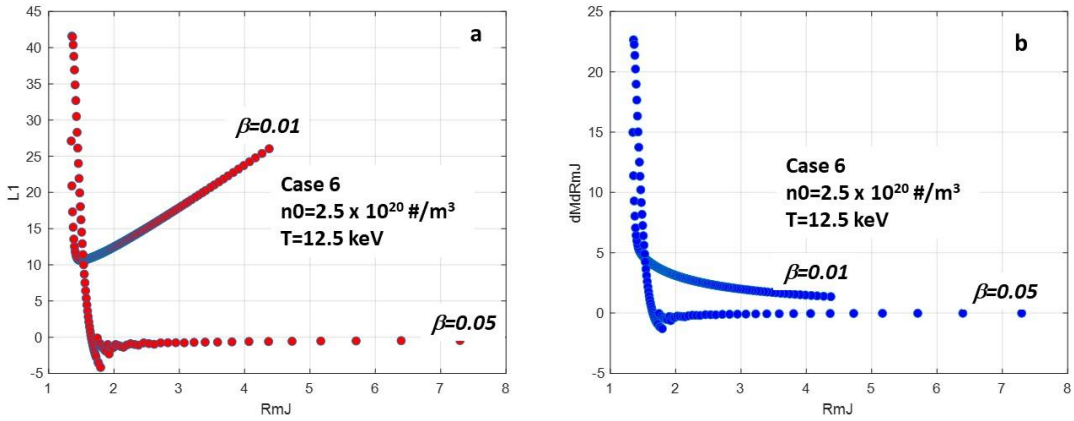

Figure 4-11 - λ_1 and dM/dRmJ curves – Case 6

Figures 4-12a and 4-12b are plots of χ vs. M and R_{mJ} for Case 0. For most solutions, it appears that $\chi > 0$, indicating higher power-side potentials. In general, the range of $|\chi|$ tends to increase with M. However, this observation is qualified in the same way that trends in Figure 4-1 were. The most likely solutions are for small values of $|\chi|$. The reason is provided in Equation (4-15). Thermal losses to the well are directly proportional to F_1. The model will find solutions for $[Rm_J, M, \chi]$ that minimize losses, and this tends to minimize $|\chi|$. An expected consequence of this tendency is that the solution for R_{mJ} will be close to the specified input for R_{mP}, an outcome which is consistently observed in results of the 0D model for viable system solutions.

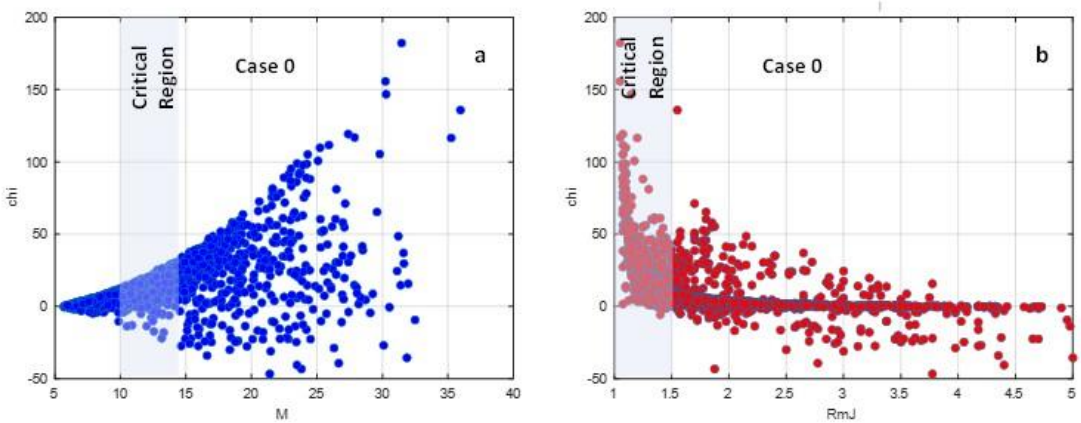

Figure 4-12 - χ vs. M and RmJ – Case 0

The preceding section affords a preliminary exploration of the thermal balance of the CM reactor well derived from the well potential Equation (3.37f). The results shown in Figures 4-2 and 4-3 provide a specific finding, i.e. the relative contributions of thermal losses from thermal and prompt species with increasing Mach number. Finally, it is important to remember that there may be practical limits to the Mach number in the super-critical region not captured in this development.

4.3.2 Magnetic Pressure Ratio

The magnetic pressure ratio affects the performance and operability of the reactor in multiple ways. First, for any given temperature or number density, the magnetic field strength is directly proportional to the inverse of β. Since β is typically a small number, i.e., less than 0.1, this has a significant effect on B_z. In order to minimize B_z, then, a relatively large β would be desirable. Higher values for β also support higher power densities for the plasma. However, M is inversely proportional to the square root of β, and the momentum confinement time for ions increases exponentially with M^2, or put another way, exponentially with $1/\beta$. Additionally, β has an important impact on the ability of the reactor to self-power. This is illustrated for a representative plasma in Figure 4-13. The blue curve for $\beta = 0.025$ shows that a plasma thermally balanced at $R_{mJ} = 1.4$ can power itself with charged species, i.e., $Q^{\alpha} \sim 1$. The same plasma with $\beta = 0.04$ and $R_{mJ} = 1.55$ can provide only 20 percent of the necessary power.

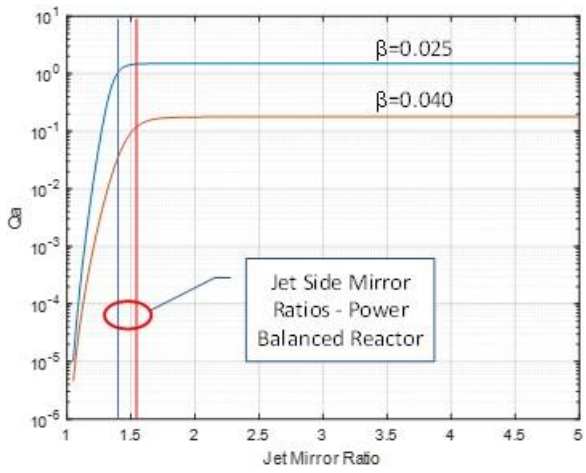

Figure 4-13 – Effect of magnetic pressure ratio on reactor self-powering for charged species

Figure 4-14 is a plot of the electric field for Case 6 solutions at varying values of β. The radial electric field at the midplane can be expressed $E_r = u_\theta / B_z$ based on Equation (1.1) for drift velocity. Taking $u_\theta = MC_s$ and finding B_z as a function of β from the magnetic pressure ratio, the electric field at the midplane can be expressed

$$E_r = \frac{2(Z_i + 1)K}{\beta} C_s^2 \sqrt{n_0 m_i \mu_0}. \qquad 4.18$$

The expression $2(Z_i + 1)K/\beta$ enters into Equation (4.18) through Equation (3.29b) relating the Mach number to K and β. The data presented in Figure 4-14 comport with Equation (4.18), and since E_r is determined by u_θ, it follows once again that β is an important parameter in the effectiveness of centrifugal confinement.

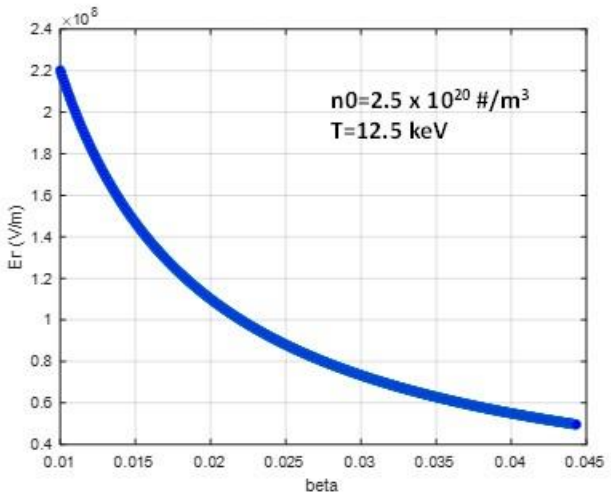

Figure 4-14 – Electric field vs. magnetic pressure ratio in CM reactors – Case 6

4.3.3 The Electric Field

In Section 3.1.1, the power requirements to drive the rotating plasma were calculated from the momentum equation and the current-potential relation. This assumed that the power deposition into the plasma from the *E* field is equivalent to the power required. The power deposition rate, however, is a function of the electrical properties of the plasma. Equation (1.1) shows that the electric field is a critical parameter for centrifugal confinement. In the operation of a CM reactor, the electric potential will be the independent variable, and for a given plasma, it determines the electric field. The power balance is satisfied in the 0D model with solutions that specify mirror ratio and Mach number, thus fixing the well potential for each solution. For each solution, there is also a unique electric field. Figure 4-8 shows the well potential for both mirrors for the representative Case 6 solution. Given a notional technological limit of 100 MV/m, the well potential $\frac{\Xi_i}{k_B T_i}$ would be limited to ~10 for this plasma.

Anticipating discussions of reactor performance, Figures 4-15 and 4-16 for Case 0 show the relationship between breakeven parameters Q^{α} and Q^{n} and electric field as indicated by the solution front on the upper left of each figure. The notch to the right in the figures is the result of limits of parameter sampling. These solutions show that a neutron powered system would require electric fields significantly lower than those needed for self-powering with charged species.

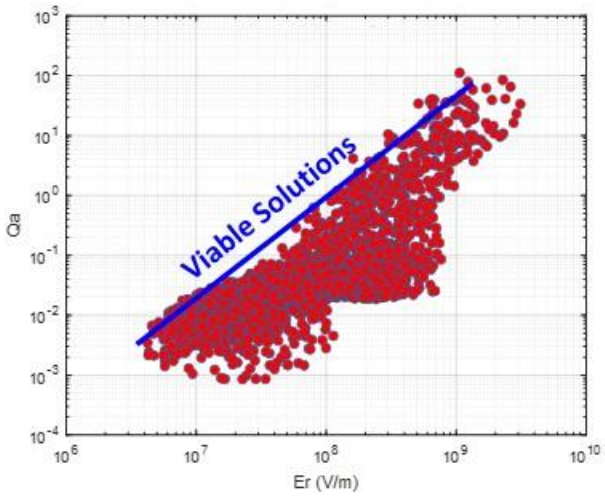

Figure 4-15 - Charged species breakeven Qa vs. Er – Case 0

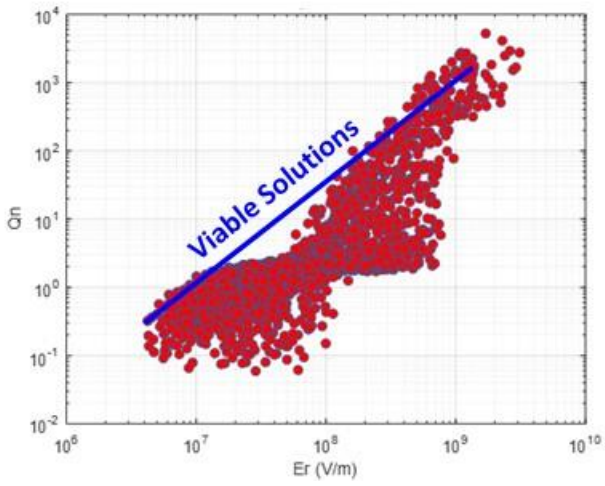

Figure 4-16 - Neutron breakeven Qn vs. Er – Case 0

4.3.4 Magnetic Field Configuration Γ

Relations for calculating ion losses from the well are provided in Equations (2.3) and (3.18). Equation (2.3) is developed in [Catto and Bernstein, 1981] and Equation (3.18) is an adaptation of Equation (2.3) developed by [Abel, 2021]. Both relations include the factor Γ that characterizes the contribution of the magnetic field to momentum loss. Both assumed a square well approximation that results in Γ being unity. Per [Catto and Bernstein, 1981], the magnetic configuration factor is calculated

$$\Gamma = \left(\oint \frac{ds}{B}\right)^{-1} \left(\oint \frac{ds\, exp(-\Xi_s/k_B\, T)}{B[1-(\varphi/\varphi_0)]}\right). \tag{4.19}$$

The denominator of Equation (4.19) is the contour integral over the last good flux surface (LGFS) of the magnetic field. The numerator is the contour integral of the product of the same surface scaled by the well potential. It is apparent that the numerator of the second contour integral will decrease with increasing well potential. At the same time, φ along each flux surface will vary from φ_0 at the mirror to zero at the midplane, with the further result that the magnitude of the integral will be reduced from the baseline. For any real, non-idealized magnetic field then, Γ will be less than unity.

The model magnetic field in Figure 4-17 adapted from [White, et al, 2018] has a mirror ratio of 10, and the value of the flux at the LGSF is 47.6 webers. Equation (4.19) was evaluated numerically for this configuration and its value was estimated $\Gamma = 0.43$. The value is calculated for the contour *a-b-c-d* in Figure 4-17 and by symmetry, the resulting value is equivalent to that of the field as a whole. The longitudinal magnetic intensity B_z was calculated from the analytic model provided in [White, et al, 2018] with a maximum of 10 T at the mirrors and 1 T at the

midplane. Equation (3.21b) is the relation for the model magnetic field. The radial field B_r was taken to be a small constant value, and the two were combined to form B as a function of s in the traverse of *a-b-c-d* shown in Figure 4-17. Further, given a 10 keV D-T plasma and a radial electric field of 6 MV/m, u_θ and M are found to be 4.2 $\times$ 10^6 m/s and 6.8, respectively. In addition to the radial electric field, an electric field along the flux surfaces of 1000 V/m is specified. These values together with the nominal $\varphi_0 = -20\ kV$ allow for the calculation of $\Xi_i/k_B\,T_i$ as a function of $R_m(s)$ and $\varphi(s)$ over the same traverse of *a-b-c-d* using Equation (3.37f). In keeping with the convention provided in [Abel, 2021], φ_0 is the offset value of potential at the mirror, chosen so that in the well $\varphi = 0$. The nominal value for φ_0 is representative of values observed in cases for thermonuclear plasmas run in the 0D reactor model.

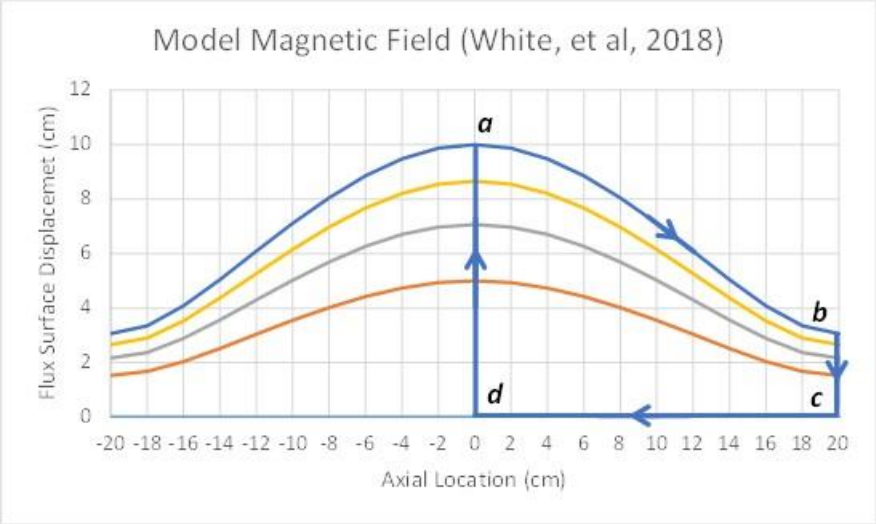

Figure 4-17 - Evaluation of Γ_B for model magnetic field

These values associated with any given $s_{n+1} = s_n + \Delta s$ are summed over *a-b-c-d:*

$$\Gamma_B \approx \left(\sum \frac{ds}{B}\right)^{-1} \left(\sum \frac{ds\ exp(-\Xi_s/k_B\,T)}{B[1-(\varphi/\varphi_0)]}\right). \qquad 4.20$$

The offset potential along segments *b*-*c* and *d*-*a* are taken as constants, φ_0 and 0, respectively. Additionally, $B = B_z(r)$ is taken as approximately constant for constant R_m along *b*-*c* and *d*-*a*, where $z = constant$. Accordingly these segments of the contour do not contribute to the calculation. As a result of the approximation of constant potentials along these two segments, the value of Γ in this estimate is a function of segments *a*-*b* and *c*-*d* only. The constant values for *B* and R_m along segments *b*-*c* and *d*-*a* are expected, but the assumption of constant potential offset φ_0 introduces some error, which is assumed to be small.

It is important to keep in mind that the radial electric field does in fact impose varying potentials along these segments in the *r*-direction with respect to the central electrode. However, φ and φ_0 in Equations (2.3) and (3.17) refer to potentials along the flux surfaces ds. While potential relative to the central electrode will vary from one flux surface to the next, the potential for a given flux surface is more or less constant.

A simple reading of Equations (2.3) and (3.18) suggests that it might be possible to scale momentum losses by judicious design of the magnetic field. In order to test this idea, the 0D reactor model was run for the case detailed in Table 3-1 for Γ of 0.4, 0.6, 0.8, and 1.0. This range of values for Γ is considered representative of a practical system based on the foregoing calculation.

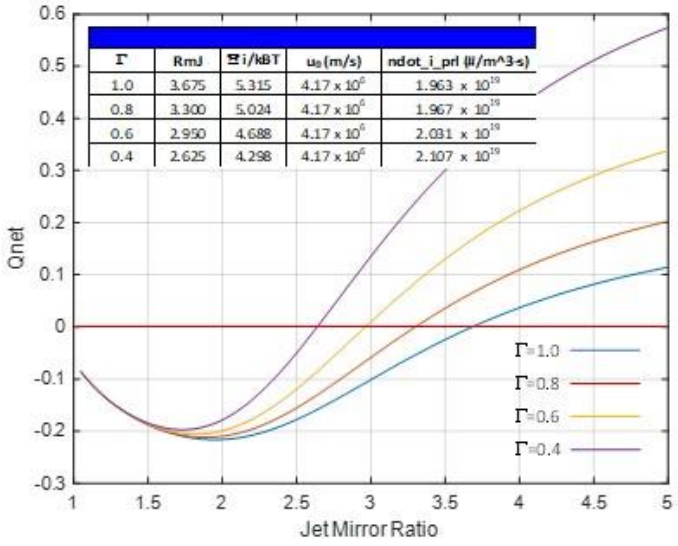

Figure 4-18 – The effect of magnetic field configuration on momentum loss

Figure 4-18 shows the results of the analysis. The red line at $Q_{net} = 0$ indicates a thermally balanced system. Instead of decreasing momentum losses with decreasing Γ, however, the rate of ion loss remains approximately the same, and in fact, increases slightly. But the jet-side mirror ratio decreases, as do the normalized potential energies. Additionally, values remained constant for midplane magnetic field, Mach number, and azimuthal velocity for each run. The variance in $\Xi_i / k_B T_i$ then is due entirely to changes in R_{mJ} needed to balance the respective cases thermally. Note that the power-side mirror ratio is held constant at 3.55.

In order to assess this observation and its validity, the reactor power balance in Equation (3.5) is revisited. The goal is to isolate terms related to momentum loss and possibly to understand better how they might be related to the mirror ratio. Grouping loss terms for radiation and heat transfer into a new term $\sum_j \bar{P}_{Hj}$, the power balance can be written

$$\bar{P}_r^{\alpha}(1-g) + \overline{IV}_0 - \sum_j \bar{P}_{Hj} = \bar{P}_F + \bar{P}_{TH} + \overline{PV}_{\parallel}. \tag{4.21}$$

The terms on the right-hand side of Equation (4.21) are defined in Equations (3.3), (3.13) and (3.16)

$$\bar{P}_F \approx \dot{n}_i\left(m_i u_\theta^2 + e\varphi_{ion}\right), \tag{3.3}$$

$$\bar{P}_{TH} = \dot{n}_i \tfrac{3}{2} k_B (T_i + Z_i T_e), \tag{3.13}$$

$$\overline{PV}_{\parallel} = \dot{n}_i\left(\Xi_i + Z_i \Xi_e\right). \tag{3.16}$$

Note that for Equation (3.3) as shown here, $\dot{n}_i \gg 2g_J\dot{n}^{\alpha}$ which is more likely in systems self-powered with charged species. Assuming $R_{mP} = R_{mJ}$, the terms for well potential in Equation (3.16) can be expanded

$$\Xi_i + Z_i\Xi_e = \frac{M^2}{4} k_B (T_i + Z_i T_e)\left(1 - \frac{1}{R_m}\right) + (Z_i - 1)e\varphi_0. \tag{4.22a}$$

Substituting Equations (3.3), (3.13),(3.16), and (4.22a) into Equation (4.21) and solving for $\dot{n}_i$

$$\dot{n}_i = \frac{\overline{IV}_0 + \bar{P}_r^{\alpha}\sqrt{1 - \frac{1}{Rm}} - \sum_j \bar{P}_{Hj}}{k_B T_e M^2 + k_B(T_i + Z_i T_e)\left[\frac{3}{2} + \frac{M^2}{4}\left(1 - \frac{1}{Rm}\right)\right] + (Z_i - 1)e\varphi_0}. \tag{4.22b}$$

$(1-g)$ from Equation (4.21) has been replaced by $\sqrt{1 - \frac{1}{Rm}}$, and that ionization losses in Equation (3.3) are neglected. For any given plasma specified by $[n_0\ T_i\ T_e\ \beta\ K]$, Equation (4.22b) indicates that for singly charged ions, associated momentum losses are affected only by R_m, since under these conditions, every other term in Equation (4.22b) except for $\overline{IV}_0$ is fixed. Note that fixing K and β also fixes M. $\overline{IV}_0$ is specified in Equation (3.1) and is an independent variable.

Although it is related to momentum losses, for a balanced system, its value will be self-consistent with $\dot{n}_i$. If this observation holds generally, it means that momentum losses cannot be reduced by reducing Γ in Equations (2.3) or (3.18), because the mirror ratio and the resulting well potential will relax to ensure the power balance in Equation (3.5) is maintained. And as R_m is reduced, the denominator in Equation (4.22b) decreases at a slightly faster rate than the numerator, which could explain the slightly higher values of $\dot{n}_i$ observed in Figure 4-18 at lower R_m.

One interesting possibility implied by Equation (4.22b) is reducing momentum losses by increasing radiation losses, i.e., losses not related to momentum. Such reduction could theoretically reduce $\dot{n}_i$, which would also tend to reduce $\overline{IV}_0$. Keeping in mind that the latter is also dependent upon shear losses, the relationship is not linear. As discussed at the end of section 4.2.2, such a scheme might be realized through seeding the plasma with a high-Z ion such as boron in order to amplify radiation losses. [Bekefi, 1966] gives the increase in bremsstrahlung due to impurities as

$$G_j = x_j Z_j \left(1 + Z_j + x_j Z_j^2\right), \qquad 4.23$$

where G_j is the gain related to the impurity j, x_j is the molar fraction of the impurity, and Z_j is its ionization state. A one percent molar fraction of fully ionized boron would result in a gain of 1.4531 over the plasma without impurities. Complicating this, however, are ionization and charge exchange losses that would result from such seeding. In Case 10 and 12, the gain in the model – designated $x3$ – was set to 3. Case 10 is the same as Case 6 in the base run matrix, and its results show no significant difference in the number of viable solutions over Case 6.

Case 11 is a subset of the Case 6, more focused on a nominally more viable operation space. As with Case 6, the gain for radiation losses is the baseline value of 1. Case 12 applies $x3 = 3$ to Case 11. The results were that viable solutions for alpha-powering nearly doubled over Case 11, 77

versus 40, but neutron-powered solutions were greatly reduced. The repeatability runs for Cases 11 and 12 showed similar results. These results suggest that within the appropriate operational regime, it might be possible to reduce momentum losses through amplified radiation losses.

4.3.5 Operability Regions for Q^a and Q^n

The parametric analysis summarized in Table 4-5 provides some insight into viable reactor configurations. The most promising cases are Cases 6 and 11. Case 6 produced a single solution for a self-powering reactor using charged species, and 180 using neutrons. Case 11, a more focused survey of a sub-domain of Case 6, produced 40 solutions for charged species and 92 for neutrons. However, these results represent a coarse sort on the domain, and in many cases, the specific solutions may not be viable. First, the minimum power density criterion was set low in order to retain more solutions as part of the initial sort. Similarly, values for the electric field were set high. Additionally, the summary results in Table 4-5 provide only limited insight on the relationships among various parameters.

This section examines the operability of the reactor in more detail, with more realistic values for various parameters, with the intent of understanding better relationships among operational parameters and constraints. Table 4-6 is a revised set of performance parameters and constraints that are applied in analyses presented in this section. The values for Q^{α} and Q^{n} are defined as $Q^{x} = \bar{P}_P^x / \overline{IV}_0$, where $\bar{P}_P^x$ is the power extracted from the reactor for self-power. In the case of Q^{n}, leakage factor f and view factor F_{12} are included in a pre-factor to η_c, so that Q^{n} is set at 2 based on the assumption that $\eta_c(1-f)F_{12} = 0.5$. (Note that these quantities are not the same as Q_{net} defined in Chapter 3 as the sum of power inputs, e.g., IV_0, and losses.)

System parameters presented in Table 4-6 represent moderate to high technical risk, but they are balanced with concomitant risk at the system-level. For example, choosing Q^n assuming values for η_c based on Carnot limits would incur low technical risk at the component, i.e., reactor, level, but at the expense of higher system-level risk: a larger and potentially impractical thermal management system.

Table 4-6 – Updated DFD-CM target operational parameters

Parameter		Units	Value	Type
Q^{α}	Breakeven - charged species		1	
Q^{n}	Breakeven - neutrons		2	
Pr^{a}	Specific power density - charged species	kW/m^3	500	minimum
Pr^{n}	Specific power density - neutrons	kW/m^3	2000	minimum
Bm	Mirror magnet field intensity	T	15	maximum
Er	Radial electric field	MV/m	40	maximum

Power densities were chosen based on the number density range in Case 11 and a 10 keV plasma. These properties result in a representative power density of 0.5 MW/m^3 for alphas, and four times that for neutrons. For a nominal mirror ratio of 2, this also enables jet power of 100s of kW for a cubic meter of burning plasma. The maximum mirror magnet field appears to be a reasonable target, given current technology. The target electric field is ambitious by any standard. The 40 MV/m is a "not to exceed" number, and as shown in Figure 4-15, solutions for alpha self-powered reactors can exceed the limit.

The analysis incorporates 5 levels each for β and plasma temperatures. The ranges are shown in Table 4-7. There are two levels for number density, one in the mid-range for Case 11 $(2.5 \times 10^{20}\ \#/m^3)$, and one for mid-range of Case 6 $(5 \times 10^{20}\ \#/m^3)$. The Kármán number is

maintained at unity. The mirror ratios for jet-side and power-side are assumed to be the same, both equal to 2, except for one case where they are set to 1.5. The values for K and R_m are representative for Cases 6 and 11 solutions.

Table 4-7 – Ranges for β and plasma temperature

Parameter	Units	min	max
β		0.02	0.1
Te	keV	5	15
Ti	keV	5	15

The analysis incorporates these values into an assessment of Q^n and Q^α as functions of electric field. For each value of β and T, both Q^x and E_r are calculated. The result is an $n \times m$ matrix of paired values for $E_r(\beta, T)$ and $Q^x(\beta, T)$ which are presented in a series of carpet plots. Limits for $\bar{P}_r^x$ and B_z in Table 4-6 are plotted as parametric functions of E_r.

In order to express E_r as a function of β and T, start with the drift velocity, i.e., $u_\theta = (E \times B)/B^2$. At the midplane

$$E_r = u_\theta B_z = K V_A B_z = \frac{K B_z^2}{\sqrt{\rho \mu_0}}, \tag{4.24}$$

From the definition of magnetic pressure in Equation (1.14), and taking $T_e \approx T_i$

$$B_z^2 = \frac{2(Z_i + 1) n_0 m_i \mu_0}{\beta} \left(\frac{k_B T_e}{m_i} \right) = \frac{2(Z_i + 1) \rho \mu_0}{\beta} C_s^2. \tag{4.25}$$

Substituting Equation (4.25) into (4.24)

$$E_r(\beta, T_e) = \frac{2K(Z_i + 1)C_s^2\sqrt{\rho\mu_0}}{\beta}, \quad 4.26$$

where C_s is a function of T_e, and ρ is fixed, because n_0 is specified. Note that Equation (4.26) is equivalent to Equation (4.18).

The values for Q^n and Q^α are calculated using Equations (3.26) and (3.27). For purposes of this analysis, viscous losses are neglected, i.e., x in Equations (3.26) and (3.27) is set to zero. Additionally, instead of using only $M^2/4$ to represent the well potential, Equations (3.37d) and (3.37f) are evaluated and then normalized by $k_B T$ to obtain $\Xi_i/k_B T_i$. The Mach number can be found as a function of K and β per Equation (3.29b). Ion collision time τ_{ii} is calculated as a function of n_0 and T. The offset potential φ_0 is approximated as $k_1 E_r$, where k_1 is chosen to provide representative values of φ_0 obtained from more detailed calculations. The result of this calculation is the $n \times m$ array of $E_r(\beta, T)$ and $Q^x(\beta, T)$. The respective arrays are converted to log10 values and then plotted as (E_r, Q^x) and $(E_r', Q^{x\prime})$, which results in a carpet plot in the $E_r - Q^x$ domain.

Curves for constraints are constructed as follows. By Equation (4.18), it can be seen that E_r is related to B_z through β. Since *K* is constrained to unity, there is an electric field E_r that corresponds to the maximum B_z, such that $B_{z\,max} = B_{m\,max}/R_m$. The curve representing the minimum specific power is constructed by finding the corresponding plasma temperature, based on specified values for n_0, x_D, and x_T. Instead of using parametric β as is done for the carpet plot, β is calculated from parametric E_r using Equation (4.18). The calculation of the curve representing Q^x based on $\bar{P}_r^x$ then follows procedure described above for the base plot.

Figure 4-19 is the resulting plot for $n_0 = 2.5 \times 10^{20}$ #/m^3. The vectors for T and β above the figure show the levels of the two parameters represented in the carpet plot.

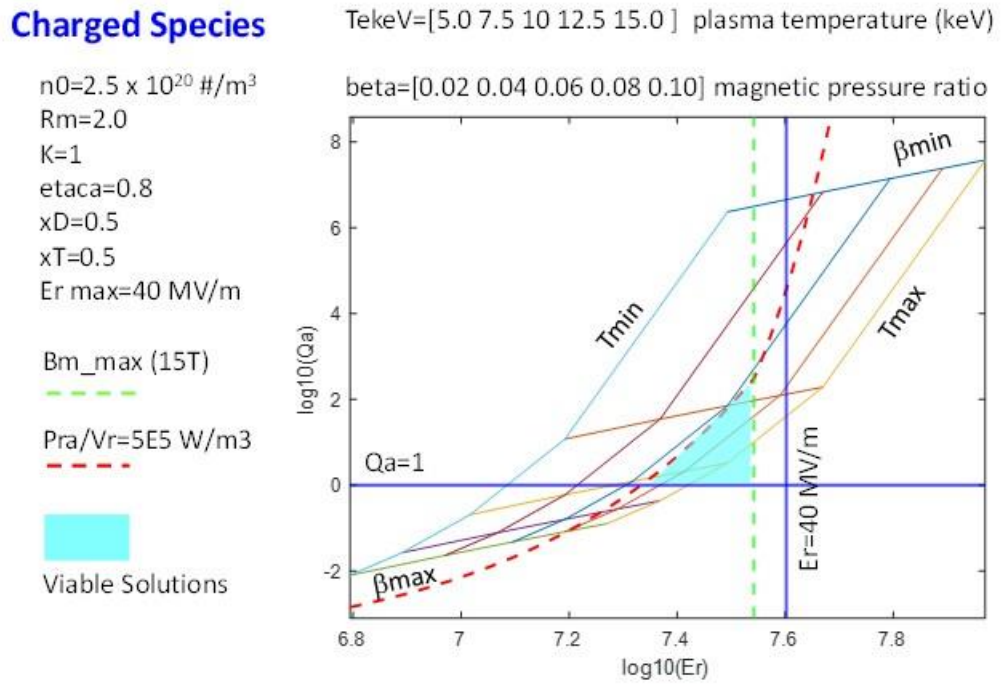

Figure 4-19 – Operability for charged species powering – n0=2.5 x 10^{20} #/m^3, Rm=2

The operational space is limited by the magnetic field strength limits of 15 T, and minimum $\bar{P}_r^{\alpha}$. Figure 4-19 indicates that this system can achieve Q^{α}up to $O(10^2)$. However, when the same system is run with a mirror ratio of 1.5 as shown in Figure 4-20, the operational space decreases substantially, and the maximum value of Q^{α} is reduced to less than $O(10^1)$. The lower mirror ratio results in a higher $B_{z\,max}$, and therefore lower β. The result is that the system curves shift to higher E_r per Equation (4.18), and the operational space becomes constrained by the 40 MV/m limit.

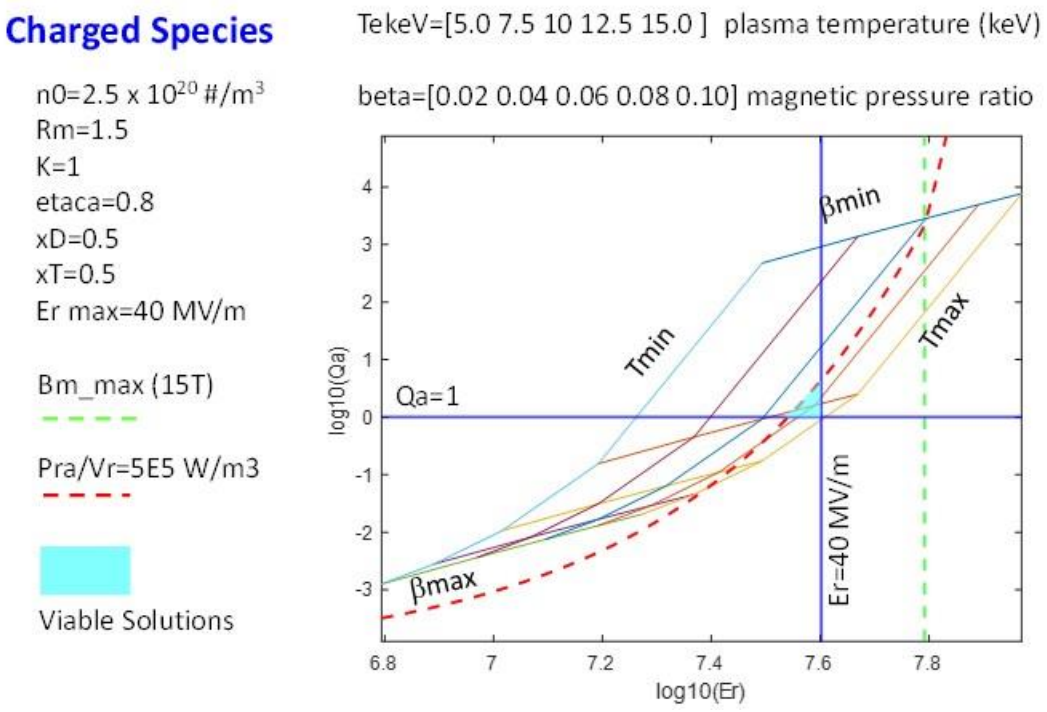

Figure 4-20 - Operability for charged species powering – n0=2.5 x 10^{20} #/m^3, Rm=1.5

Figure 4-21 is the same system as that shown in Figure 4-19, except the number density is doubled to 5×10^{20} #/m^3. In this case, the constraints for $B_{z\,max}$ and $\bar{P}_r^{\alpha}$ eliminate all operational space from the domain. This is consistent with results from Cases 7, 8, and 9, for which no viable solutions were observed for either neutron or charged species powered systems.

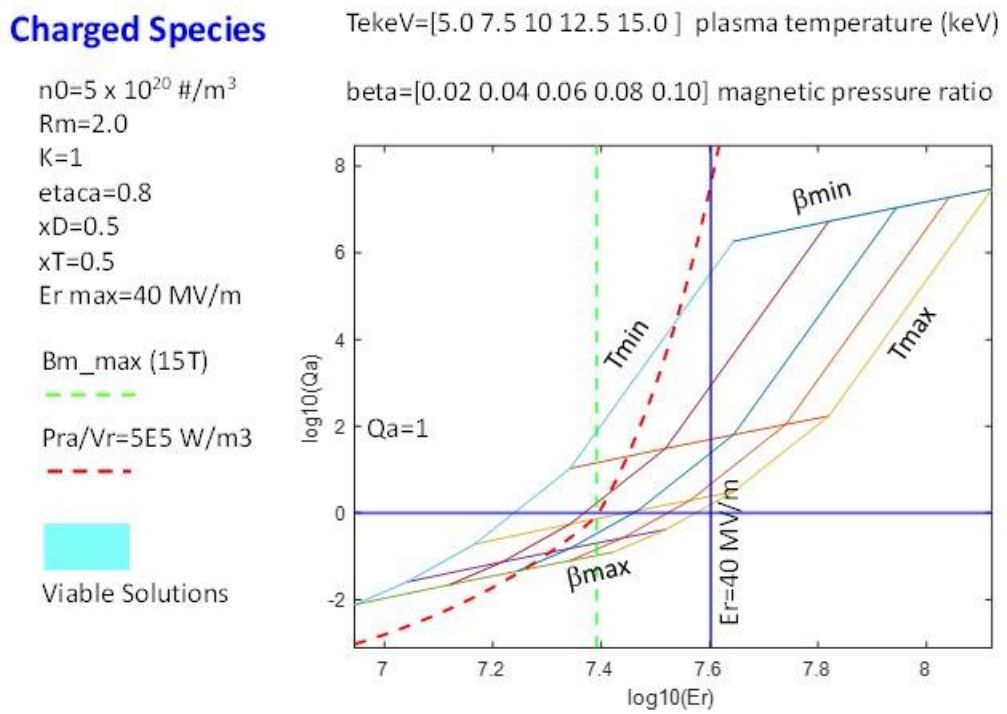

Figure 4-21 - Operability for charged species powering – n0=5 x 10^{20} #/m^3, Rm=2.0

Figures 4-22 and 4-23 for neutron powered systems show trends consistent with charged species powered systems. Q^n values shown account for notional conversion efficiency and blanket leakage factors. The results indicate that neutron powered reactors operate with lower electric fields than those powered by charged species. As with charged species, increasing the number density of the reactor tends to shift the system curves to higher electric fields, as shown for $n_0 = 5 \times 10^{20}$ #/m3 in Figure 4-23. The $B_{z\,max}$ limit becomes operative at the higher number density and reduces the operational space of the reactor.

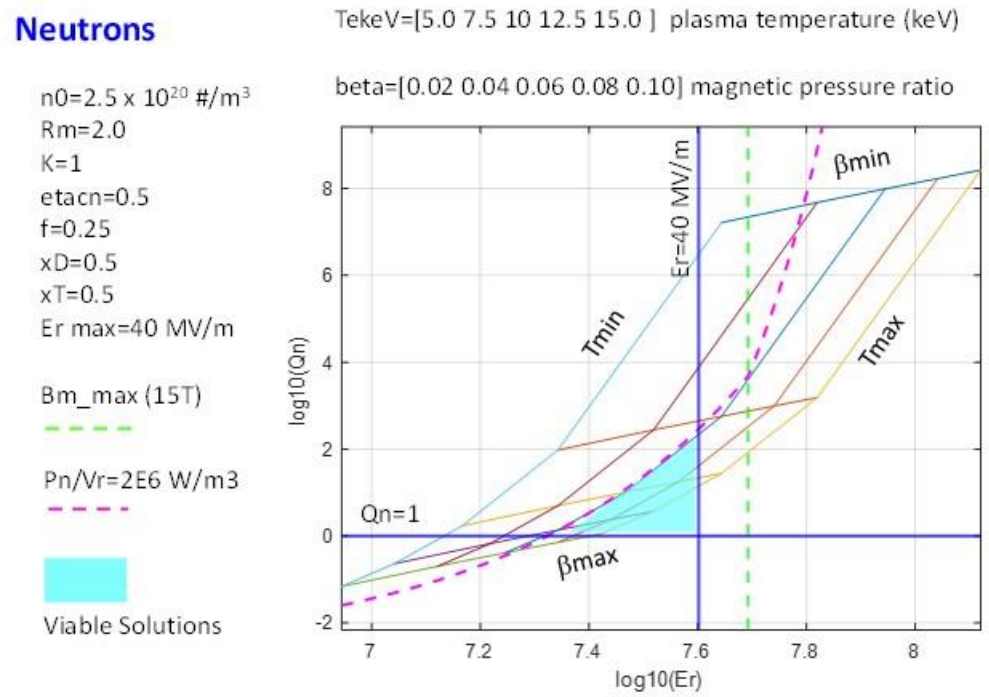

Figure 4-22 - Operability for neutron powering – n0=2.5 x 10^{20} #/m^3, Rm=2.0

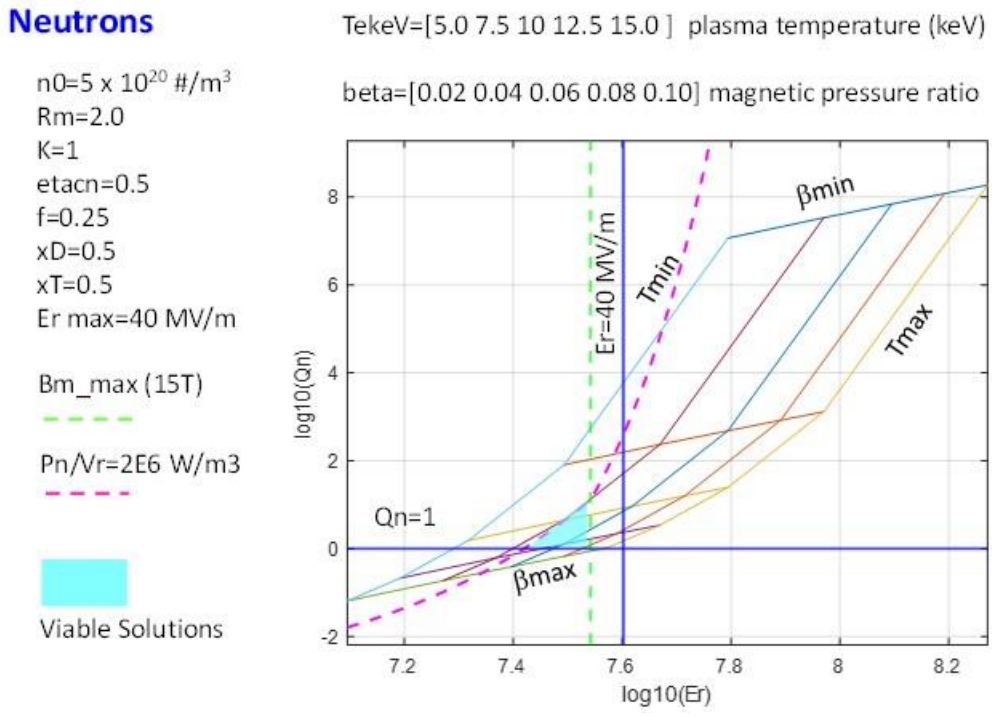

Figure 4-23 - Operability for neutron powering – n0=5 x 10^{20} #/m^3, Rm=2.0

The results presented are qualified by the following considerations. First, the curves in Figures 4-19 through 4-23 are constructed from Equations (3.26) and (3.27), which are approximations. Some fidelity was added by including the electrostatic terms in the calculation of the well potential Ξ_i, but the value for φ_0 is also an approximation. Nevertheless, the curves provide useful insights into constraints for reactor configurations in propulsion systems. One important idea is that the range of operation is a strong function of mirror ratio. Higher mirror ratios offer more access to operable space and higher Q^x, which should be of interest to terrestrial plants. Propulsion systems which require only that $Q^x \sim 1$ can operate in theory at lower mirror ratios. This in turn can reduce system mass, and promote higher specific jet power $\bar{P}_{J0}$, the power leaving the jet-side mirror per volume of burning plasma. The "nought" is included to differentiate this value from delivered jet power P_J. The latter accounts for losses in the propulsion system.

4.4 Reactor Performance and Model Configurations

4.4.1 Jet Power

Ideal jet power provided by the reactor, P_{J0}, is determined by the reactor power density and the loss cone factor resulting from the jet-side mirror ratio. Characteristics like Mach number and well potential affect jet-side mirror ratio, which means that jet power must be considered in balance with reactor operability. A solution from Case 6 was adapted to form a use case to evaluate this relationship over three levels of plasma temperature, as shown in Table 4-8. Values for n_0, K, and R_{mP} remain constant, while the value for β is traversed from 0.005 to 0.05.

Table 4-8 – Use case for DFD-CM performance assessment

Parameter	Units	Levels		
n0	#/m^3	2.5×10^{20}		
K		1		
RmP		1.5		
Te	keV	10	12.5	15
Ti	keV	10	12.5	15

Figure 4-24 is a plot of $\bar{P}_{J0}$ and Mach number in the reactor for the three plasma temperatures in Table 4-8. The curves indicate that jet power increases with plasma temperature, as would be expected. The maxima result from the behavior of the well potential, and they occur in the critical Mach region. From a performance standpoint, small changes in Mach number in the sub-critical branches of the curves, away from the critical region, can significantly affect jet power. In the critical region, the relative benefit of increasing Mach decreases. The sensitivity of jet power to Mach number below the critical Mach appears asymptotic. The well potential for these plasmas at varying β is shown in Figure 4-25. The minima exhibited in these curves result from the asymmetry in the power and jet-side mirror ratios.

The Mach number is related to the magnetic pressure ratio β through Equation (3.29b). Figure 4-26 is the same data from Figure 4-24 plotted against β. Jet power varies to a lesser extent over the range 0.02 to 0.04 for β and then drops off rapidly above 0.04. As β increases in the latter region, Mach number decreases, and so the jet-side mirror ratio must increase in order to maintain well potential for plasma confinement. With that increase in the jet-side mirror ratio, the loss cone decreases, and with it, the prompt and thermal species available for jet power.

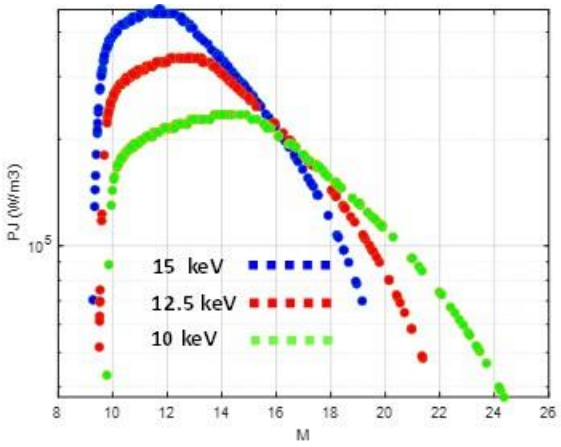

Figure 4-24 – Ideal jet power (PJ0) at varying Mach numbers for reactor operation

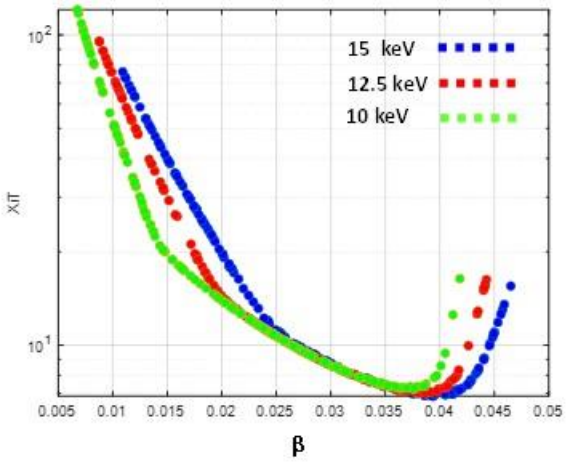

Figure 4-25 – Normalized well potential at varying β for reactor operation

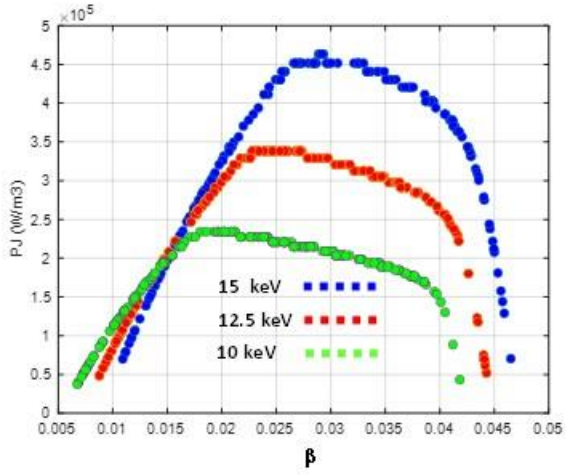

Figure 4-26 – Ideal jet power (PJ0) at varying β for reactor operation

4.4.2 Reactor Self-Powering

Figures 4-24 and 4-26 do not show constraints for Q and self-powering. Figures 4-27a and 4-27b are plots Q^{α} and Q^{n} at varying well potentials for the jet-side mirror for Case 0.

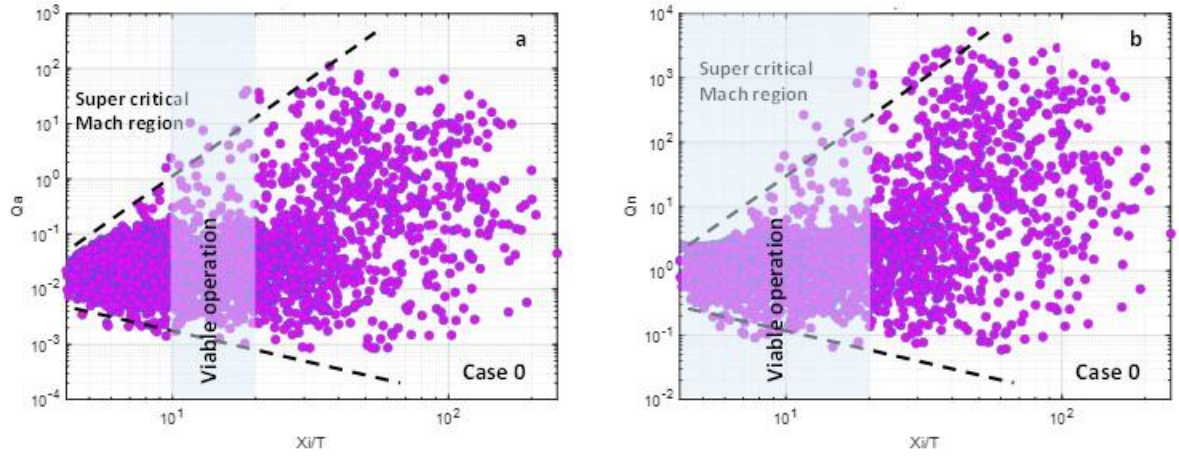

Figure 4-27 – Breakeven factors at varying well potential – Case 0

The light blue shading shows viable ranges of operation bounded by $Q\sim1$ and associated $(\Xi_i/k_BT_i)_J$. The upper bound for $(\Xi_i/k_BT_i)_J$ is taken from the range of values for viable solutions in Case 11. Figure 4-27 suggests that self-powered CM reactors will operate in the supercritical regions. $(\Xi_i/k_BT_i)_J\sim10$ appears to be a reasonable nominal value, based on these data, and from Figure 4-25, the corresponding nominal value for β would be 0.025.

Figures 4-28 and 4-29 are plots of Q^{α} and Q^{n}respectively at varying β for the Table 4-8 plasmas. The 12.5 keV and 15 keV curves are within the Case 11 domain, which has the highest density of viable solutions for self-powering reactors. Accordingly, these curves are good indicators of the β that is generally needed to operate in self-powering regimes. For self-powering with charged species, the lower temperature curves require low values of β, which in turn drive higher electric and magnetic fields. Although satisfactory jet power can be achieved at relatively higher β, the

Q^{α} constraint limits reactor operations to β less than 0.025. Higher temperature plasmas allow marginally larger β. By comparison, reactors self-powered by neutrons can operate at higher β with commensurately lower electric fields. As shown in Figure 4-28, Q^{α} begins to roll off above β in the range of 0.03 to 0.04. These considerations suggest a potential opportunity to optimize overall system performance for neutron self-powered reactors. Figure 4-29 also indicates that high values for Q^{n} are achievable, which will be of interest in terrestrial applications. These results are consistent with the analysis presented in Figures 4-19 through 4-23.

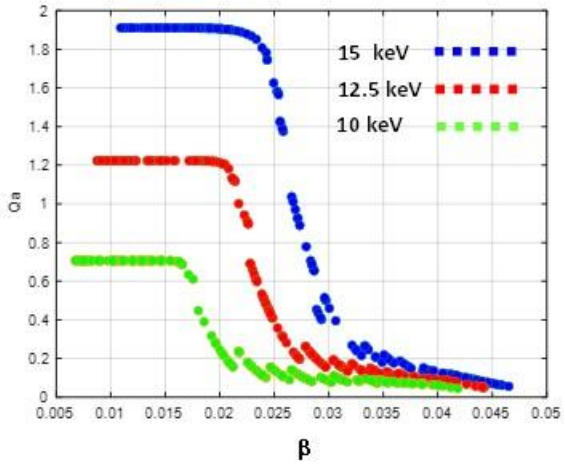

Figure 4-28 – Breakeven factor Q^{α} at varying β

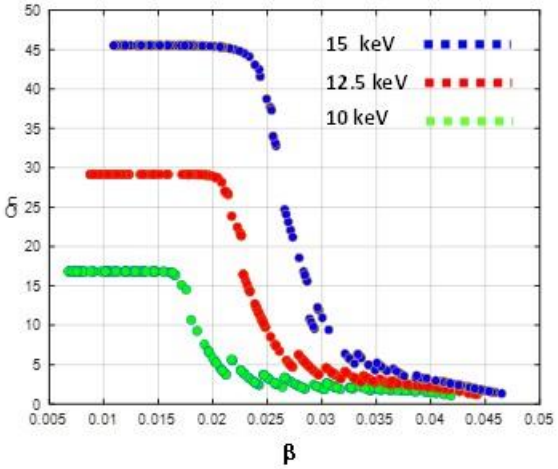

Figure 4-29 – Breakeven factor Q^{n} at varying β

4.4.3 Model Reactor Configurations

Table 4-9 provides performance and operation data on four model reactors grouped by charged species power density $\bar{P}_r^{\alpha}$ and by whether they are self-powered by charged species or neutrons (*C* or *N*). The two power levels are roughly 500 kW/m^3 and 1 MW/m^3 (*L* and *H*).

All of the model configurations operate in the super-critical region characterized by high Mach numbers and electric fields. They were extracted from Case 11. Case 11 solutions meeting requirements in Table 4-6 were isolated and then the solution with the lowest electric field strength was chosen. Input parameters were refined in some cases in order to round number density and temperature. The electric fields for all configurations exceed the target limit provided in Table 4-6. For the configurations self-powered by charged species (*CL* and *CH*), the electric fields were over twice the Table 4-6 values. The neutron self-powered configurations (*NL* and *NH*) were marginally higher. All other limits from Table 4-6 were met.

Note that Q^{α} is included for the neutron self-powered configurations, and vice versa. These values showed in light blue cells provide additional context to the respective solutions. In the case of the configurations self-powered by charged species, the values for Q^{n} indicate the need for mitigation and management of neutron radiation. Conversely, the values for Q^{α} for neutron self-powered configurations suggests that there would be little value in combining contributions of neutron and charged species.

Table 4-9 – Model reactor configurations

Parameter		Units	Model Reactors			
			CL	CH	NL	NH
Specification						
Number density	n0	#/m^3	$1.4x10^{20}$	$1.9x10^{20}$	$1.8x10^{20}$	$2.5x10^{20}$
Magnetic pressure ratio	β		0.02	0.021	0.03	0.04
Karman number	K		0.95	0.93	1	1
Electron temperature	Te	keV	14	14	11.3	12
Ion temperature	Ti	keV	14	14	11.3	12
Forward mirror ratio	RmP		1.4	1.5	1.5	1.5
Fueling	xD/xT		0.5/0.5	0.5/0.5	0.5/0.5	0.5/0.5
Performance						
Jet power	PJ/Vr	MW/m3	0.122	0.243	0.146	0.249
Jet side mirror ratio	RmJ		1.48	1.4	1.36	1.63
Power - charged species	Pr^{α}/Vr	MW/m3	0.543	1.000	0.582	1.271
Power - neutrons	Pr^{n}/Vr	MW/m3	2.188	4.029	2.345	5.120
Power conversion efficiency - charged species	ηc		0.8	0.8	0.8	0.8
Power conversion efficiency - neutrons	$(1-f)*F*\eta c$		0.5	0.5	0.5	0.5
Q - charged species	Q^{α}		1	1	0.083	0.084
Q - neutrons	Q^{n}		21.44	22.91	2	2
Operation						
Mach number	M		13.44	12.84	11.55	10.00
Electric field strength	Er	MV/m	87.64	95.2	56.29	52.83
Magnetic field - midplane	Bz	T	8.88	10.1	7.39	7.77
Bremsstrahlung radiation	PB/Vr	MW/m3	0.039	0.072	0.0582	0.116
Prompt species generation	ndot α	#/m3-s	9.70×10^{17}	1.79×10^{18}	1.04×10^{18}	2.27×10^{18}
Thermal species losses	ndot_th	#/m3-s	2.26×10^{16}	1.51×10^{17}	4.33×10^{18}	1.22×10^{19}
Fueling rate	ndot f	#/m3-s	8.92×10^{17}	1.74×10^{18}	5.27×10^{18}	1.40×10^{19}
Ion confinement time	τ	s	6194.7	1258.3	41.6	20.5

These model reactors provide a basis for DFD-CM propulsion system analysis developed in Chapters 5 and 6, mainly through the ξ^{θ} that results from indicated values of prompt and thermal flow rates. The power densities are used to estimate the volume of burning plasmas in the propulsion system cases.

One final observation relative to Table 4-9 concerns the ion confinement times. The values of τ_i for (*NL* and *NH*) configurations are comparable with near-term targets for CMFX as calculated by MCTrans++. However, those for (*CL* and *CH*) are one to two orders of magnitude higher.

References – Chapter 4

1. Chap, Andrew M., Sedwick, Raymond J., "One-Dimensional Semianalytical Model for Optimizing the Standing-Wave Direct Energy Converter," JOURNAL OF PROPULSION AND POWER Vol. 31, No. 5, September–October 2015
2. Catto, P.J., Bernstein, Ira B., "Collisional end losses from conventional tandem mirrors," Phys. Fluids 24 (10), October 1981
3. White, Roscoe, Hassam, Adil, and Brizard, Alain, "Centrifugal particle confinement in mirror geometry," Physics of Plasmas 25, 012514 (2018); doi: 10.1063/1.5003359
4. Abel, I.G., "MCTrans++ Reference Manual, version dated 21 August 2021
5. Bekefi, G., "Radiation Processes in Plasmas," New York, 1966, p95

5 The Propulsion System

5.1 System description

5.1.1 Overview

The propulsion system consists of the warm plasma and the magnetic nozzle. Its performance is determined by fusion species kinetic energies (prompt and thermal), and the propellant "bypass" flow ratio ξ^{β}, i.e., the ratio of propellant number rate (#/s) to the rate at which prompt fusion species arrive at the warm plasma, $\dot{n}^{\alpha} g_J V_r$. The corresponding value for fusion thermal species ξ^{θ} is the number rate of thermal fusion products arriving at the warm plasma normalized by that of the prompt species. At the same time, $\xi^{\theta} \approx \frac{1-g_J}{g_j}\left(\frac{f^{\alpha}}{\tau_{ii}}\right) n_0$, where f^{α} is the high-energy tail of the thermals in the reactor plasma, and τ_{ii} is the ion collision time. This expression is functionally equivalent to the loss of thermals calculated using Equations (3.18) and (3.19). Definitions for ξ^{β} and ξ^{θ} allow the power balance for the warm plasma to be expressed in terms of the prompt fusion product generation rate, and they fix the proportions in which fusion power is converted to thrust and exhaust velocity, i.e., specific impulse. The warm plasma, heated by the reactor products, flows through the magnetic nozzle and is accelerated by electrostatic forces to produce thrust. The electrostatic field is created by the segregation of charged species that results from the greater mobility of the electrons. This creates the current-free layer, or structure, similar to the sheath between a plasma and a physical wall. The current-free structure follows from the requirement that electron and ion fluxes must be equal as they leave the sheath. Based on this requirement, the resulting potential of the plasma at the nozzle throat can be represented by the plasma sheath Equation (1.16)

$$\phi = -\frac{k_B T_e}{2e}\left[1 + ln\left(\frac{m_i}{2\pi m_e}\right)\right]. \quad 1.16$$

The temperature T_e is the bulk electron temperature of the warm plasma. For potential ϕ in the warm plasma, the fluxes of the ions and electrons in the current free-structure are the same, consistent with a current-free layer. The ions are denser, but slower than the electrons. [Chen, 2006][LaFleur, 2015] Since jet power P_J is proportional to $e\phi$, jet power is a function of electron temperature in the warm plasma. Equation (1.16) can be used to relate the potential ϕ to the specific impulse, because $e\phi \approx \frac{1}{2}mU_x^2$. In a system with propulsion cycle efficiency η_J, ϕ and T_e will be lowered from ideal, so that exhaust velocity U_x is reduced from $U_{x\,ideal}$. Further, for $\dot{n}^\alpha V_r g_J E^\alpha$ power arriving from the reactor, the bypass ratio ξ^β fixes the mass flow rate leaving the system, i.e. $\dot{m} = \dot{n}^\alpha g_J V_r\left(m_\alpha + \xi^\theta m^\theta + \xi^\beta m^\beta\right)$. The system then delivers thrust and specific impulse as follows

$$F_t \approx \dot{n}^\alpha g_J V_r\left[\left(1 + \xi^\theta + \xi^\beta\right)\left(m^\alpha + \xi^\theta m^\theta + \xi^\beta m^\beta\right)\left(2\eta_J e\phi\right)\right]^{\frac{1}{2}}, \quad 5.1$$

and

$$I_{SP} \approx \frac{1}{g_0}\left[\frac{\left(1 + \xi^\theta + \xi^\beta\right)2\eta_J e\phi}{m^\alpha + \xi^\theta m^\theta + \xi^\beta m^\beta}\right]^{\frac{1}{2}}. \quad 5.2$$

The potential ϕ is obtained from Equation (1.16). Appendix B provides a derivation of Equations (5.1) and (5.2).

The cycle efficiency η_J has two components, the warm plasma efficiency η_w, and expansion efficiency, η_{exp}, so that $\eta_J = \eta_w \eta_{exp}$. η_w accounts for losses due to power deposition rates, propellant ionization and heating, and losses due to radiation, charge exchange and wall

interactions. η_w also includes η^α that accounts for the loss of fusion products that enter the warm plasma in the loss cone for the nozzle. This is discussed in Section 5.1.2.2. η_{exp} reflects effects due to polytropic cooling of ions and electrons between the warm plasma and the nozzle throat, loss of adiabaticity of the plasma during expansion, and losses due to cross-field transport of electrons in the expansion zone. Loss of adiabaticity is manifested in lower values of γ, the ratio of the specific heats, for plasma components. This limits plasma acceleration during expansion. Additionally, cross-field transport of electrons appears to be a necessary process to allow them to detach from the magnetic field along with the ions, which being heavier detach through inertial processes. However, such transport would be dissipative. Note that effects due to η_{exp} are modeled in the current effort as a reduced γ for electrons, and other loss mechanisms are not accounted for.

Figures 5-1 through 5-3 show solutions for Equations (1.16) and (5.1, 5.2), which represent the propulsion capacity of a simple 0D warm plasma model. The solutions are calculated for varying values of ξ^β. For each value of ξ^β, a range for cycle efficiency η_J is assumed. Jet power is calculated based on a derated electron temperature, i.e. $\eta_J T_{e0}$ and is also calculated based on losses for heating and ionization. It is assumed that $\xi^\theta = 0$. The model iterates η_J to find a value such that the two expressions for jet power are equal. Accordingly, the warm plasma electron temperature shown in Figure 5-1 accounts for losses due to propellant heating and ionization. Specific impulse is shown in Figure 5-2. To the first order, both T_e and I_{SP} are single valued functions of ξ^β. Reductions in I_{SP} result from losses related to propellant heating and ionization that are factored in through ξ^β, i.e. $P_{LOSS} \sim \dot{n}^\alpha g_J V_r \xi^\beta \left[\frac{3}{2} k_B (T_i + T_e) + e\phi_{ion}\right]$. By comparison, thrust is proportional to input power from the reactor, because of the dependence on mass flow

due to ξ^{β}. Figure 5-3 shows delivered thrust for reactor outputs of 100 kW, 500 kW, and 1000 kW.

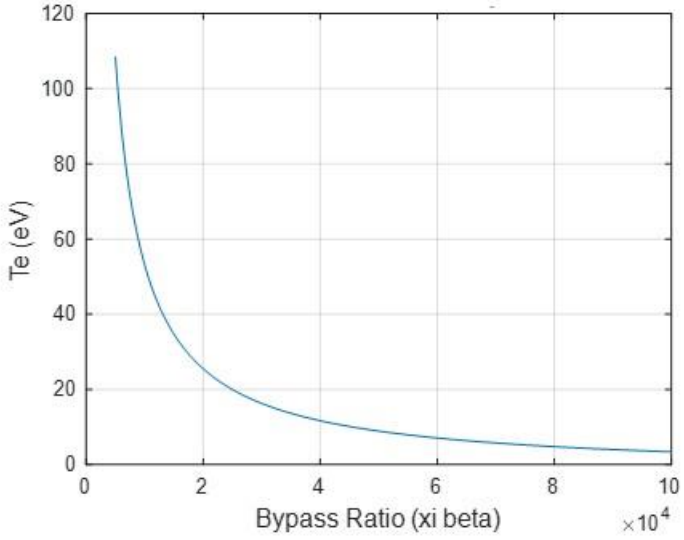

Figure 5-1 - Warm plasma electron temperature as function of bypass ratio

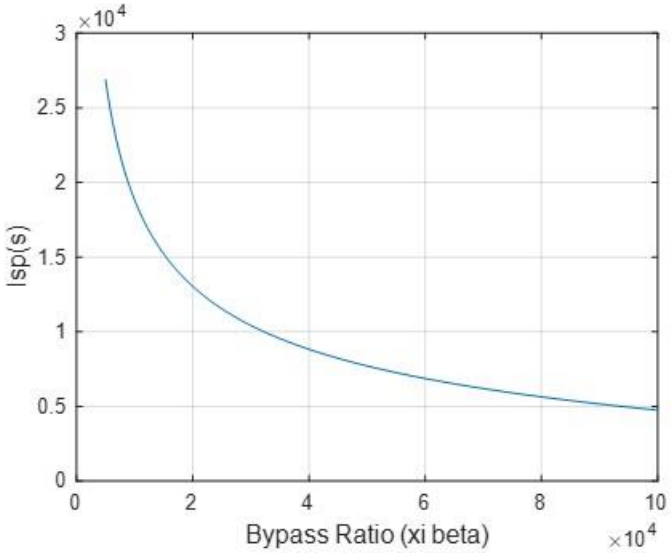

Figure 5-2 - Specific impulse as a function of bypass ratio

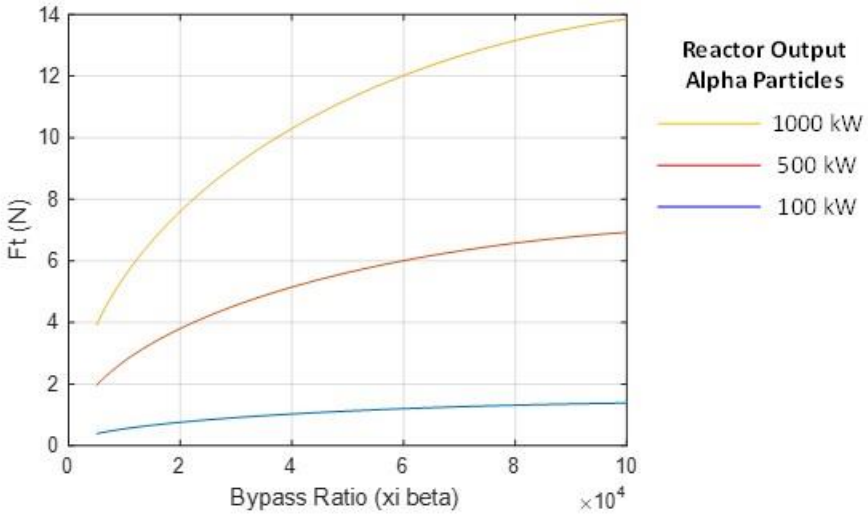

Figure 5-3 - Thrust as a function of bypass ratio

Equations (5.2) and (5.3) are based on the sheath model for plasma acceleration. At low values of ξ^{β}, less than 5000, the accuracy of these equations suffers, as monoenergetic alphas become the main channel for delivering jet power, and the sheath model is less applicable.

5.1.2 Reactor-Warm Plasma Interface

5.1.2.1 Traverse energy losses for thermal species

When thermal species depart the reactor, they take with them their potential energy, per Equation (3.16). This provides the energy necessary for them to traverse the well potential.

$$\overline{PV}_{\parallel} = \dot{n}_i(\Xi_i + Z_i\Xi_e). \qquad 3.16$$

The prompt species, alphas in the case of the D-T reaction, are not centrifugally confined because of their high-energy. Although they are born in the well, their traversal energy is negligible

compared with their birth energy. The thermal species, however, lose a non-negligible portion of their energy in traversing the well. Considering again the definitions for the well potential

$$\Xi_s = Z_i e\varphi - \frac{m_s}{2}\Omega^2 r^2, \tag{3.17}$$

it can be seen that the potential energy of a given ion species is a function of the square of its radius of azimuthal rotation. That radius is related to the magnetic field flux, so that the difference between potential energy at the mirror and the center of the well can be calculated based on conservation of flux. Ions traversing the flux surface from the center of the well to the mirror must give up potential energy in the amount

$$\Delta\Xi_i = Z_i e(\varphi_m - \varphi_0) - \frac{m_i}{2}\Omega^2(r_m^2 - r_0^2), \tag{5.3a}$$

where m and 0 indicate conditions at the mirror and center of the well, respectively. For electrons, $m_e \ll m_i$, and assuming quasi-neutrality

$$\Delta\Xi_e \approx -Z_i e(\varphi_m - \varphi_0). \tag{5.3b}$$

Summing the two equations, and noting that $r_m^2/r_0^2 \approx 1/R_m$ gives the energy lost in the traversal

$$\Delta\Xi_m = \frac{m_i}{2}\Omega^2 r_0^2\left(1 - \frac{1}{R_m}\right), \tag{5.3c}$$

The ions arrive at the mirror with the mechanical energy $E_m = \Xi_0 - \Delta\Xi_m$

$$E_m = \frac{m_i}{2}\Omega^2 r_0^2 - \frac{m_i}{2}\Omega^2 r_0^2\left(1 - \frac{1}{R_m}\right) = \frac{m_i\Omega^2 r_0^2}{2R_m}. \tag{5.3d}$$

Combining this mechanical energy with the thermal energy of the ions gives the total energy of the ions at the mirror. Noting that $m_i\Omega^2 r_0^2 = k_B T_e M^2$, the total energy of the thermal ions arriving at the warm plasma is

$$E_i^{\theta} = \left(\frac{3}{2} + \frac{M^2}{2\tau R_m}\right) k_B T_i, \qquad 5.3e$$

where $\tau = T_i/T_e$, introduced in Equation (3.50). Electrons arrive at the warm plasma with their usual thermal energy $\frac{3}{2} k_B T_e$.

5.1.2.2 Mirror losses for fusion products in the warm plasma

The fusion products leaving the reactor well will have a pitch angle $\theta = arccos\,(V_{\|0}/V_0)$ that is less than the critical pitch angle $\theta_c = arcsin\left(1/R_{mJ}\right)^{1/2}$, where R_{mJ} is the mirror ratio of the rjet-side mirror as seen from the reactor. Because of their high-energy, their transit time through the warm plasma is much shorter than collision times. For warm plasmas with a nozzle magnet, the fusion products within the loss cone for the nozzle will depart. The rest would reflect back into the warm plasma, the reflection times and thermalization times determining the number of reflections before they are thermalized. This assumes that their pitch angle is not such that they pass back into the reactor. The fraction of fusion products that do not depart the warm plasma – expressed in terms of an efficiency - may be estimated

$$\eta^{\alpha} = \frac{g_J - g_N}{g_J} \qquad 5.4$$

This equation relates the reactor loss cone g_J to g_N, the loss cone of the mirror at station *N*, the magnetic nozzle throat. A g_J of 0.5 suggests an isotropic population of alphas arriving from the reactor, while smaller values indicate lower pitch angles. Conversely, in order to retain any of the

alphas, the nozzle mirror ratio R_{mN} must be larger than R_{mJ}. If $R_{mN} = R_{mJ}$, then $g_N = g_J$, and $\eta^\alpha = 0$. These mirror ratios are defined for particles upstream of the respective mirrors. The jet-side mirror presents two mirror ratios, one to particles upstream in the reactor, which is R_{mJ}, and one to particles downstream in the warm plasma, which is designated R'_{mJ}. B_z for the reactor well is much larger than B_z in the warm plasma. As a result, the mirror ratio R'_{mJ} that the warm plasma sees relative to the reactor is larger than R_{mN}.

The relationship between g and R_m defined in Equations (3.30) for monoenergetic alphas is general, since the solution to the integral posed is dependent only upon θ_c and by extension, R_m. Accordingly, Equation (3.30b) is applicable to any arbitrary distribution, and so it can be used to calculate g_N for a Maxwellian warm plasma. Figure 5-4 shows alpha particle retention rate within the warm plasma as a function of R_{mJ} and R_N. Values for R_{mJ} are relatively low, given that the field strength in the reactor will be moderately high. For these values of R_{mJ}, field strengths for the reactor mirrors should remain within the mid-field strength (1-15 T) range. The field strength of the warm plasma will be relatively low, 1T or less, so that fairly high mirror ratios for the nozzle should be practical. These considerations suggest that values of η^α of 0.8 or higher are viable with fairly low nozzle magnet strengths. The relationship between alphas entering the warm plasma and those that contribute to propulsion is

$$\dot{N}_\theta^\alpha \approx \eta^\alpha g_J \dot{n}^\alpha V_r. \qquad 5.5$$

The quantity $\dot{N}_\theta^\alpha$ refers to alphas that leave the reactor and are thermalized in the warm plasma. Equation (5.5) assumes all fusion energy that does not depart immediately through the nozzle magnet is deposited in the warm plasma.

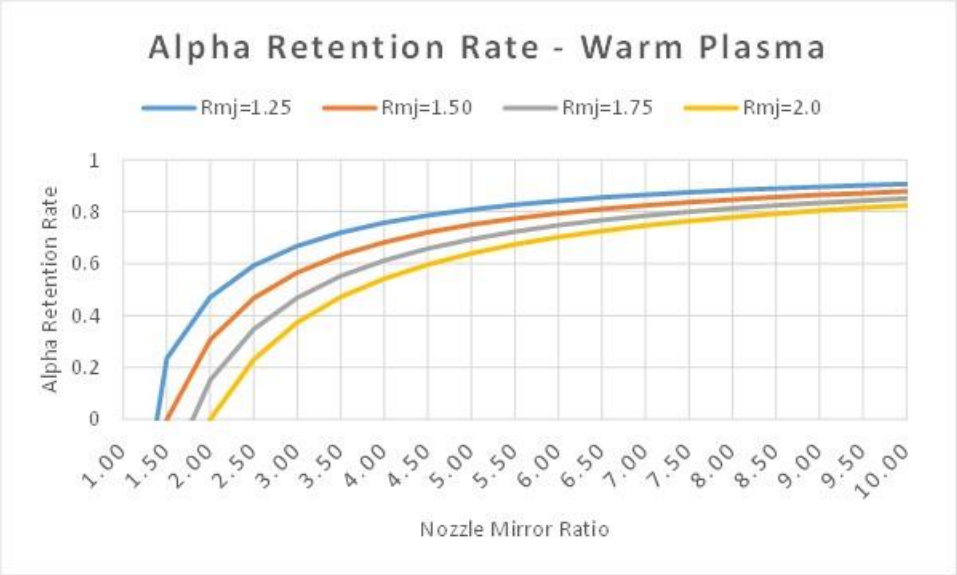

Figure 5-4 – Alpha retention rate in the warm plasma

5.1.2.3 Electrical coupling between the reactor and warm plasma

DFD-CM consists of the thermonuclear plasma in the reactor and the propulsion system's warm plasma. The magnets of the respective plasmas impose a field that is continuous within the plasmas and closes a magnetic circuit externally. Within reactor plasma, with its negatively biased central electrode, magnetic flux surfaces are equipotential giving rise to the iso-rotation law and the accompanying $E \times B$ drift.

While there is a common magnetic circuit for the two plasmas, the nature and extent of any electrical coupling is unclear. If the warm plasma is electrically isolated from the reactor well, its floating potential would be higher than that of the reactor. The flux must then exhibit Debye shielding in order to traverse the resulting electric field. However, effective Debye shielding in the flux implies that the flux is electrically conductive, so that the warm plasma might necessarily be electrically coupled to the reactor to some extent.

If the warm plasma and reactor are electrically coupled, then there must be an electric field in the warm plasma sufficient to support the electric field in the reactor, and in turn, the electric field in the warm plasma would likely impose a local $E \times B$ drift. One model for a coupled system is to constrain warm plasma properties so that its resistance supports the electric field in the reactor plasma. Based on classical transport, this would drive lower number densities but higher temperatures in the warm plasma. At the same time, the warm plasma would itself be centrifugally confined, with uncertain effects on propulsion performance. The question of electrical coupling between the reactor and warm plasma is important and will be pursued in the near future. Pending better understanding, the warm plasma is modeled in the current research as uncoupled from the reactor, which may be a reasonable approximation at higher (>20000 seconds) specific impulses.

5.1.3 Warm Plasma Thermodynamics

5.1.3.1 Alpha transport and energy deposition

Energy deposition in the warm plasma is intimately related to transport properties of the prompt alphas. The prompt alphas enter the warm plasma as a monoenergetic species with energy E^{α}. But transport relations necessary to calculate energy deposition are based on the assumption of a Maxwellian distribution. These considerations are accommodated by the quasi-Maxwellian, or "slowing down" distribution defined in [Helander, 2002][Mila-Estrada, 2006]: $T_s^{\alpha} = f(a)E^{\alpha}$, where a is the ratio of alpha cross-over velocity v_c to its birth velocity, i.e., $a = v_c/v_{\alpha}$. Given an alpha source S_0 $(\#/m^3 - s)$, the slowing down distribution is found by solving the steady-state Fokker-Planck equation, which results in

$$f_s(v) = \frac{S_0 \tau_s}{4\pi} \frac{H(v_\alpha - v)}{v_c^3 - v^3}. \quad 5.6$$

The slowing down time τ_s is defined [Mila-Estrada, 2006]

$$\tau_s = \frac{3}{16\sqrt{\pi}} \left(\frac{4\pi\varepsilon_0}{Z_\alpha^2 e^2} \right)^2 \frac{m_e m_\alpha v_e^3}{n_e ln\Lambda}, \quad 5.7$$

and the cross-over velocity for a D-T system is

$$v_c = \left(\frac{5 m_e \sqrt{\pi}}{4 m_\alpha} \right)^{1/3} v_e. \quad 5.8$$

Above v_c, energy losses in the alpha population are due mainly to alpha-electron collisions; below v_c, the losses are mostly due to alpha-ion collisions. [Helander, 2002] [Mila-Estrada, 2006] derive the slowing-down temperature as

$$k_B T_s^\alpha = \frac{2 I_4(a)}{3 I_2(a)} E^\alpha, \quad 5.9$$

where $I_2(a) = \frac{1}{3} ln \left(\frac{1+a^3}{a^3} \right)$, and

$$I_4(a) = \frac{1}{2} - a^2 \left\{ \frac{1}{6} ln \left(\frac{1 - a + a^2}{(1+a)^2} \right) + \frac{1}{\sqrt{3}} \left[arctan \left(\frac{2-a}{a\sqrt{3}} \right) + \frac{\pi}{6} \right] \right\}. \quad 5.10$$

I_2 and I_4 are integrals of the form $I_n(a) = \int_0^1 dx \frac{x^n}{a^3 + x^3}$, which [Mila-Estrada, 2006] uses to evaluate different moments of Equation (5.9). For the warm plasma, S_0 must be taken as the arrival rate of prompt alphas per unit volume of the warm plasma, so that in a 0D warm plasma, $S_0 \approx \dot{N}_\theta^\alpha / V_w$.

The slowing down distribution and associated quasi-Maxwellian temperature T_s^α allow for the calculation of transport properties for the alpha particles. Prompt alphas will be thermalized mainly by electrons at a rate proportional to their number density in the warm plasma, i.e., $\dot{S}^\alpha \approx n^\alpha \sum \frac{1}{\tau^{\alpha/s}}$ $(\#/m^3)$, where $\tau^{\alpha/e}$ is the controlling rate. Alphas will also be convected from the system as the warm plasma departs through the magnetic nozzle.

In order to characterize the steady state number density of alphas in the warm plasma, it is assumed that radial transport of alpha particles is negligible, so that the 0D conservation equation is

$$\frac{dn_s^\alpha}{dt} \approx \frac{\dot{N}_\theta^\alpha}{V_w} - \frac{u_z n_s^\alpha A_z}{V_w} - \frac{n_s^\alpha}{\tau^{\alpha/e}}. \tag{5.11}$$

The first term on the right-hand side of Equation (5.11) is the source term for alphas arriving from the reactor. The second term is the convective losses of alphas departing through the nozzle set by bulk convective u_Z and by A_Z, the axial area of the warm plasma. The third term is the loss rate due to thermalization of the slowed down alphas. $\tau^{\alpha/e}$ is normally much smaller than that of other species, so that the electrons in the warm plasma are the main channel for fusion power deposition. Accordingly, Equation (5.12) is presented as a simplified approximation useful for characterizing the steady-state value of n_{ss}^α $(\#/\mathrm{m}^3)$, which is of interest because the rate of energy deposition is $\dot{Q}_{DEP}^\alpha \approx n_{ss}^\alpha E^\alpha V_w/\tau^{\alpha/e}$. Setting the left-hand side of Equation (5.11) to zero

$$n_{ss}^\alpha = \frac{\dot{N}_\theta^\alpha}{u_z A_z + \frac{V_w}{\tau^{\alpha/e}}}. \tag{5.12}$$

Substituting Equation (5.12) into the expression for $\dot{Q}_{DEP}^\alpha$ allows for an approximation of the energy deposition by alphas. For $u_z A_z \ll V_w/\tau^{\alpha/e}$, $\lim_{t\to\infty} \dot{Q}_{DEP}^\alpha = \dot{N}_\theta^\alpha E^\alpha$. This means that in the

limit $t \to \infty$, the energy deposited in the warm plasma would be equal to that coming out of the reactor.

5.1.3.2 *Power balance in the warm plasma*

Figure 5-5 is a schematic of the power balance in the warm plasma. Fusion energy arrives in the warm plasma at the rate $\dot{n}^{\alpha} V_r g_J E^{\alpha} = \dot{N}_J^{\alpha} E^{\alpha}$, while the warm plasma is supplied by propellant at a rate $\dot{n}^{\beta} V_w$. In steady state, combined jet power and loss terms must equal the rate at which fusion power is deposited into the warm plasma. As discussed, in the limit of $t \to \infty$, $\dot{Q}_{DEP}^{\alpha} = \dot{Q}_{IN}$, however, the warm plasma experiences a finite residence time, so that fusion power deposition in practical systems may be less than $\dot{Q}_{IN}$. This limit would contribute to decreasing T_e. Some losses, like propellant heating and radiation losses, will be lower, because of the decreased electron temperature. The energy that is not deposited to the warm plasma departs the system through the nozzle via a high-energy channel $P_{JH} \approx Q_{IN}(f_w^{\alpha} + \eta^{\alpha})$, where to the first order, $f_w^{\alpha} = 1 - \frac{n^{\alpha} V_w}{\tau^{\alpha/e}} \frac{1}{\dot{N}_{\theta}^{\alpha}}$, and $\lim_{t \to \infty} f_w^{\alpha} = 0$.

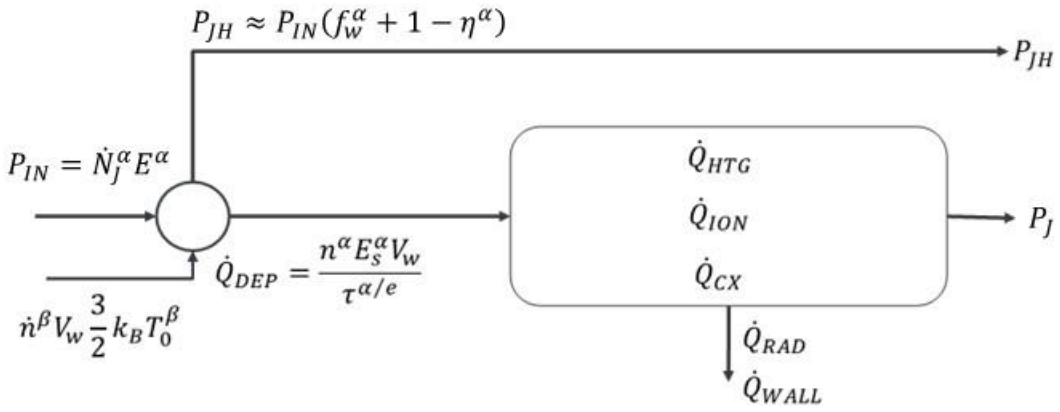

Figure 5-5 – Energy deposition in the warm plasma

Since the current-free structure downstream of the nozzle throat fixes the flow to the Bohm velocity, it functions analogously to a physical nozzle that limits the flow to the acoustic velocity. Assuming the number density of the propellant is much larger than that of other species, plasma leaves the warm plasma at the rate $\dot{m} \approx n^{\beta} m_{\beta} u_z A_z$, where u_z is a net velocity for transport of the $n^{\beta} m^{\beta}$ at the aft boundary of the warm plasma, and it is defined

$$u_z = e^{-0.5}(g_N / R_{mN}) \left(\frac{k_B T_e}{m^{\beta}} \right)^{1/2}. \tag{5.13}$$

As before, subscript N refers to conditions in the vicinity of the nozzle. Equation (5.13) is a form of the continuity equation. It requires that particles passing through the nozzle travel at the Bohm sheath velocity. The mirror ratio $R_{mN} = A_z / A_N$, and $n_N^{\beta} / n_w^{\beta} = e^{-0.5}$, as required by sheath theory. The loss cone factor g_N constrains particles passing through the nozzle to the population within the loss cone. The 1D warm plasma model assumes that particles from the bulk plasma replenish the loss cone at the rate at which they are scattered.

The combined jet power is nominally $P_J + P_{JH}$. P_J delivers the principal thrust at specific impulse reduced by losses in the warm plasma. P_{JH} would provide low thrust, but at specific impulses approaching $\sqrt{2E^{\alpha}/m_{\alpha}}/g_c$, depending on whether these high-energy alphas and accompanying electrons can detach from the diverging magnetic field of the nozzle. For purposes of the current research, it is assumed that the high-energy species do not detach from the magnetic field, and that they must be somehow recombined external to the flow path. Therefore, the high-energy species P_{JH} do not contribute to the jet power in this model.

5.1.3.3 *Propellant supply*

Neutral propellant is supplied to the warm plasma at the rate $\dot{S}^n = \xi^\beta \dot{n}^\alpha V_r \eta^\alpha$. The rate is assumed to be constant in time, and spatially is a function of the injection mode. The 1D model has three modes of neutral injection: 1) front end "top-hat" injection at the forward end of the warm plasma; 2) circumferential feed from the outer walls; and 3) neutral beam injection to the center of the plasma. Ionized propellant is generated at the rate $\dot{S}^\beta = n^e n^n \sigma_{ion}^n v_{th}^e$, where σ_{ion}^n is the Maxwellian-averaged ionization cross-section of the neutral species, and v_{th}^e is the thermal velocity of the bulk electrons. The respective rates of arrival of the neutrals and their ionization, along with related transport, results in a population of neutrals $n^n(t,r)$ and ionized propellant $n^\beta(t,r)$ within the warm plasma. The warm plasma loses energy mainly through ionization and heating of the incoming propellant. Ionization losses are $\dot{Q}_{ion} = \dot{S}^\beta E_{ion}$, and plasma heating losses are $\dot{Q}_{htg} = \dot{S}^\beta \frac{3}{2} k_B (T_e + T_{iw} - 2T_{n0})$, where T_e and T_{iw} are the bulk plasma electron and ion temperatures, while T_{n0} is the supply temperature of the neutrals, arbitrarily set to 0.5 eV. The model assumes pre-heating of the propellant prior to injection. Because of the relative rates of energy transfer among species, electrons are preferentially heated through interactions with incoming fusion products, but then pass much of their energy on to neutrals and ions.

5.1.4 The Warm Plasma Magnetic Field

5.1.4.1 *Constraints related to minimizing loss of alphas*

Equation (5.4) shows that the loss of alphas is related to the magnetic field strengths of both the jet-side mirror in the reactor and the nozzle magnet. This in turn affects the shape of the field between the two magnets, and therefore the shape and volume of the warm plasma. Figure 5-6 is

a schematic of the geometry of the warm plasma magnet system bisected at the midplane. The angle α and radius r describe the position of the magnet centroid relative to the center of the warm plasma. The dimensions $r0$ and $R0$ are the aperture radius and center position of the magnet relative to the centerline.

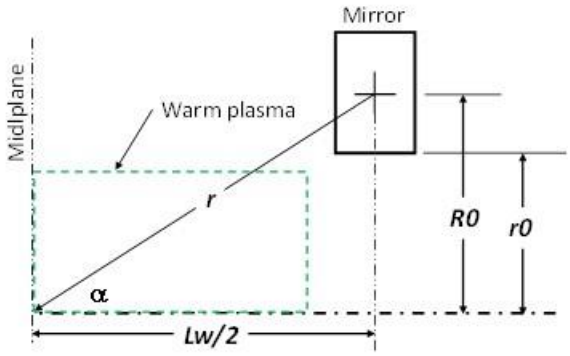

Figure 5-6 – Configuration of warm plasma magnetic field

Even though the field strengths of the respective magnets may differ, the geometrical elements of the two are the same, so there is symmetry in the calculation of the field. Accordingly, the magnetic field can be estimated by summing the respective fields calculated from the Biot-Savart law. For $\alpha = atan(R_0/z)$ and $r = R_0/sin\alpha$, with the origin at the center of the jet mirror, the magnetic field is

$$\mathrm{B} = \frac{\mu_0}{2}\frac{i_J R_{0J} sin\alpha_J}{r_J^2} + \frac{\mu_0}{2}\frac{i_N R_{0N} sin\alpha_N}{r_N^2} \qquad 5.14$$

At the center of the respective magnets, $\alpha = \pi/2$, and $\mathrm{B} = \mu_0 i/2R_0$, where i is the current in the magnet. Given $z = 0$ at the jet-side mirror, at any point along z, $\alpha_J = atan\left(R_{0J}/z\right)$; $\alpha_N = atan(R_{0N}/(z_N - z))$; $r_J = R_{0J}/\sin\alpha_J$; and $r_N = R_{0N}/\sin\alpha_N$. Figures 5.7 and 5.8 are representative magnetic fields that illustrate the relationship between magnetic field configuration

and η^{α}. Both have a common jet-side geometric configuration and B_{mJ} for both is 15 T. Figure 5-7a has a midfield magnetic field of 0.68 T and a nozzle field strength of 5 T. η^{α} for this configuration is 0.84. Figure 5-7b shows the maximum last closed flux surface is 1.96 m from the centerline.

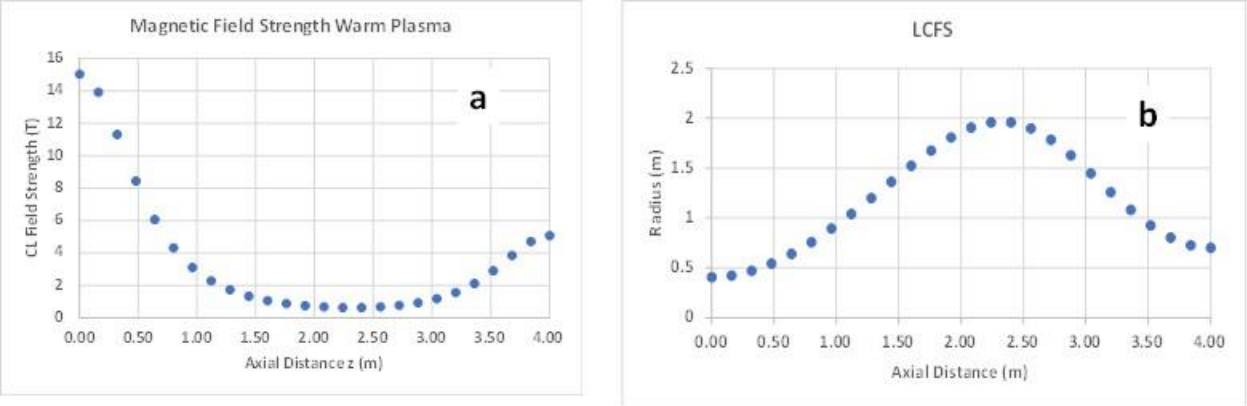

Figure 5-7 – Warm plasma magnetic field configuration 1, $\eta^{\alpha} = 0.84$

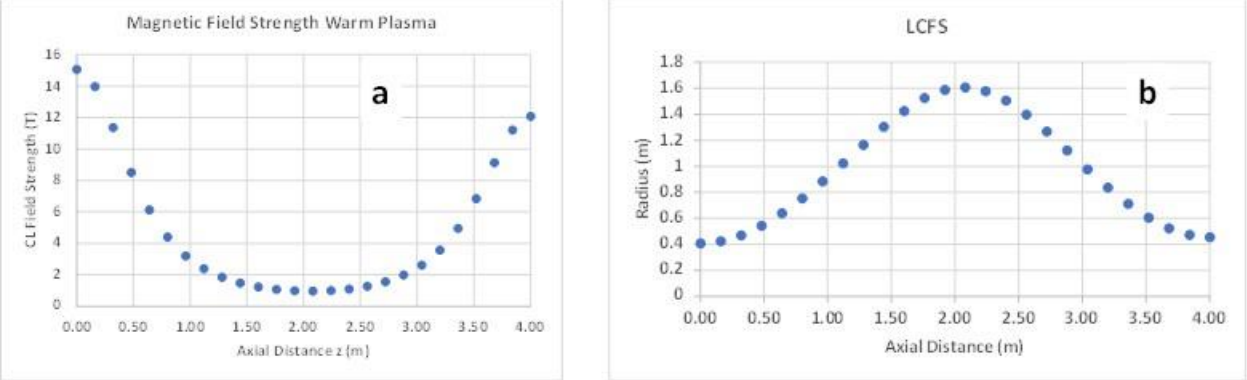

Figure 5-8 – Warm plasma magnetic field configuration 2, $\eta^{\alpha} = 0.9$

The magnetic field in Figure 5-8a differs from that in Figure 5-7a only in that the nozzle magnet is 12 T, which results in a lower g_J and higher η^{α} of 0.9. With the higher magnetic field, the last closed flux surface has the smaller radius of 1.6 m. The ability to obtain higher η^{α} is offset by the higher mirror ratio which reduces mass flow through the nozzle and specific thrust.

5.1.4.2 *The magnetic field and radial momentum transport*

The radial momentum flux in the warm plasma is

$$F^p = u_r p + P + \frac{B^2}{2\mu_0}, \tag{5.15}$$

where $p = \rho u_r$ is the bulk momentum. In a system where the evolution of $P(n,T)$ is known, because of specified rates of mass and energy deposition, also knowing B as a function of time would allow the calculation of radial momentum and velocity through the relation $\frac{\partial p}{\partial t} = \nabla \cdot F^p + \dot{p}$. A coupled solution to Faraday's law $\frac{\partial B}{\partial t} = -\nabla \times E$ provides a means to calculate B and therefore the rest of the system.

Given Ohm's law, $E + u \times B = J/\sigma_\perp$ for radial transport, and the diamagnetic current $J = \frac{B \times \nabla P}{B^2}$, the electric field can be expressed in terms of the pressure gradient

$$E = \frac{1}{\sigma_\perp}\frac{B \times \nabla P}{B^2} - u \times B. \tag{5.16a}$$

At the midplane, $B = B_z\hat{z}$, and $u = u_r\hat{r} + u_z\hat{z}$. Accordingly, Equation (5.16a) is evaluated

$$E = \left(\frac{1}{\sigma_\perp}\frac{\nabla_r P}{B_z} - u_r B_z\right)\hat{\theta}. \tag{5.16b}$$

Substituting Equation (5.16b) into Faraday's law provides the time derivative of the z-component of the magnetic field at the midplane

$$\frac{\partial B_z}{\partial t} = \left(\frac{1}{\sigma_\perp}\frac{\nabla P}{B_z^2} + u_r\right)\nabla_r B_z + \left(\frac{u_r}{r} + \nabla_r u_r\right)B_z - \frac{1}{\sigma_\perp B_z}\left(\frac{\nabla_r P}{r} + \nabla_r^2 P\right). \tag{5.16c}$$

Equation (5.16c) in conjunction with a time-marching scheme and the momentum equation provides solutions for p and u_r. In this formulation, B_z is the magnetic field internal to the plasma. For the restricted case where radial momentum transport is due only to B and $P(n,T)$, it might be expected that p and u_r are negligible. This is because in cylindrical systems, the terms $P + \frac{B^2}{2\mu_0}$ is equal to the external magnetic field B_{ext} and is practically constant. Therefore, with any change in P, there will be a concomitant change in B such that any net forces will be minimal and due primarily to transients. As will be discussed in Section 5.2, Equation (5.16c) was implemented in preliminary versions of the model with the observed result that the solution evolved an exceedingly small convective velocity u_r.

5.1.5 Plasma Acceleration and Expansion

5.1.5.1 Energy conservation along stream tubes

The factor $k_B T_{e1}/2e$ in Equation (1.16) represents the acceleration of the plasma analogous to that through the pre-sheath region of a normal sheath structure. [Chen, 2006] Figure 5-9 is a schematic of the flowpath between the warm plasma and the magnetic nozzle exit plane.

The warm plasma facing the nozzle is designated Station 1; the current-free structure and presheath downstream of the nozzle throat, Station N; and the exit plane of the nozzle, Station x. The state of the warm plasma can be calculated at any point along a stream tube using a quasi-1D energy equation.

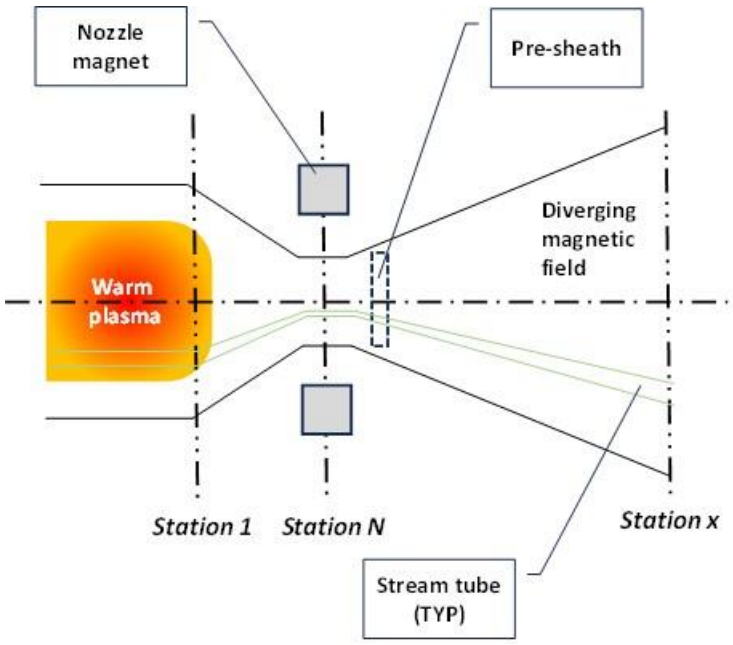

Figure 5-9 – Magnetic nozzle configuration

Based on this approach, there appears to be a relationship between the electron temperature in the warm plasma T_{e1} and its temperature at the sheath edge T_{eN}. At this point, the plasma has been accelerated to the Bohm velocity, and the number densities of the two species are both $n_1 exp(-1/2) \approx 0.6 n_1$. The energy equation for electrons along the stream tube between the warm plasma and the nozzle throat is

$$g = \frac{\gamma_e}{\gamma_e - 1}\frac{k_B}{m_e}T_{e1} = \frac{\gamma_e}{\gamma_e - 1}\frac{k_B}{m_e}T_{eN} + \frac{U_{Ne}^2}{2} - \frac{e\phi_N}{m_e}. \quad 5.17$$

Given $\frac{1}{2}U_N^2 \ll g$, and substituting $\phi_N = -k_B T_{e1}/2e$ allows for an expression shows that T_{eN}/T_{e1} is a constant for an ideal plasma

$$T_{eN} = \left(1 - \frac{\gamma - 1}{2\gamma}\right) T_{e1}. \quad 5.18$$

For γ=1.67, approximately 0.2 of the electron's energy is converted to energy in the electric field, so that T_{eN} can be estimated. At station *N*, the ion velocity is the Bohm velocity, corresponding to Mach 1 at the throat of a conventional nozzle.

5.1.5.2 Nozzle expansion

After acceleration through the current-free structure downstream of the nozzle throat, the plasma expands through the diverging section of the magnetic field. Returning to the notion of stream tubes, the two-fluid energy equations for 1D acceleration are

$$f = \frac{\gamma_i}{\gamma_i - 1}\frac{k_B}{m_i}T_{ix} + \frac{U_{ix}^2}{2} + \frac{e\phi_x}{m_i} \quad 5.19$$

$$g = \frac{\gamma_e}{\gamma_e - 1}\frac{k_B}{m_e}T_{ex} + \frac{U_{ex}^2}{2} - \frac{Z_i e\phi_x}{m_e} \quad 5.17$$

$$T_{ex} = T_{eN}\left(\frac{n_x}{n_N}\right)^{\gamma_{ex}-1} \quad 5.20a$$

$$T_{ix} = T_{iN}\left(\frac{n_x}{n_N}\right)^{\gamma-1} \quad 5.20b$$

In real systems, the value of γ_{ex} is less than 5/3, consistent with experimental observations of electron cooling in plasma expansion. [Zhang, *et al*, 2016][Lafleur, *et al*, 2015] Taking $\frac{1}{2}U_{ex}^2 \ll g$, ϕ_x is found directly from Equation (5.17). The value of T_{ix} is calculated assuming isentropic expansion. This model is similar to that provided in Equation (2.5b). [Ahedo and Merino, 2017]

Assuming quasi-neutrality, the system has five unknown quantities, $n_x, T_{ex}, T_{ix}, \phi_x$ and U_x, so a fifth equation, the continuity equation, is needed to solve it. Upstream of the nozzle throat, the conservation of magnetic flux provides a method for calculating flow area based on specified magnetic fields. Downstream of the throat, the flow does not necessarily follow the magnetic field. The relationship between the magnetic field and the flow field represents a strong second order

effect for propulsion systems. Experimental observations have shown that depending on the configuration of the magnetic field, the plume may expand more or less with the field, or it may be collimated, often with a characteristic divergence angle. [Deline, 2009][LaFleur, 2015][Olsen, 2015] For plasma expansion that is not frozen-in, the flow must depart from the magnetic field, so flux conservation cannot be used downstream of the nozzle throat.

[Deline, 2009] investigated the effects of downstream magnets with varying configurations of current direction and magnitude and showed that beam current was stronger farther downstream with more highly collimated fields. The VX-200 demonstrator described in [Olsen, 2015] includes a set of magnetic coils downstream of the throat magnet that are used to confine the plasma during the ion cyclotron heating (ICH) stage. These coils also appear to collimate the plasma beam.

Based on these considerations, the plasma expansion model assumes a constant divergence angle for the outer surface of the plasma plume. The flux area of the plume can then be calculated along the expansion axis, and the system of equations closed. This approximation is discussed in more depth in Section 5.1.6.2 with the benefit of context to be provided in the following sections.

5.1.6 Plume Detachment

5.1.6.1 Background

Magnetic nozzles will be an integral component of any plasma based propulsion systems, but their performance may be affected by the tendency of plasmas to remain attached to magnetic lines of force associated with the nozzle. According to Alfvén's frozen-in theorem, "in a fluid with infinite electric conductivity, the magnetic field is frozen into the fluid and has to move along with it."

[Alfvén, 1942] From a field perspective, this may be stated as $U \times {}^{B}/_{\mu_0} = 0$, that is, the velocity streamlines are coincident with magnetic field lines. From a particle perspective, it is manifested by the tendency of charged species to remain attached to magnetic field lines, i.e., magnetized. If frozen-in holds, theoretically magnetic nozzles could be incapable of generating thrust, so the question is of practical importance. While it appears that ion species in some experiments are in fact detaching, the fate of the electrons in those experiments is often less clear. Unless the electrons also detach, ambipolar forces will substantially reduce or eliminate the momentum of the escaping ions and reduce thrust.

5.1.6.2 The Physics of Plasma Expansion and Detachment

Section 2.2 provides a survey of research on plasma expansion and detachment from magnetic nozzles. Collectively, theory and observations presented in these papers do not provide a clear consensus on how plume detachment in magnetic nozzles may occur. The preponderance of experimental observations suggests that detachment does occur in some cases, and that each of the proposed mechanisms may play a role. It appears, for example, that an operative role for inertial forces in heavy ion detachment might be generally accepted. Work going back to [Kuriki and Okada, 1970] reports small Hall parameters for ion species in nozzle flows. At the same time, ion detachment is described similarly by several investigators from a phenomenological standpoint, i.e. the transition to super-Alfvénic flow is a consistent observation in both experimental and theoretical work. [Deline, *et al,* 2009] and [Ahedo and Merino, 2014 and 2017] provide criteria relevant for ion detachment that are motivated by kinematic or energy considerations, and which correlate spatially with the super-Alfvénic transition.

Electron detachment remains problematic. The theoretical treatments surveyed did not provide generally satisfactory explanations for electron detachment, and in some cases, did not address the matter at all. Nevertheless, several ideas were proposed that serve as partial explanations. The mechanisms proposed by [Olsen, *et al*, 2015] are especially cogent as they are stated in the context of particular experimental observations. The occurrence of high-frequency electric fields in the so-called anomalous transport region may be due to competing magnetic and ambipolar forces acting on the electrons. It appears likely that there is a degree of collimation in the applied magnetic field as a result of the internal plasma magnetic field. A similar observation was reported by [York, *et al*, 1992] and not in the context of demagnetization, but rather based on estimated values of the magnetic pressure ratio β along the nozzle. [Ahedo and Merino, 2014 and 2017] assert that demagnetization and the generation of propulsive forces are related. Whether effected by a CFDL or a large potential structure as reported by [Olsen, *et al*, 2015], the energy distribution of the electrons along the flow path clearly is important to their ability to demagnetize, and it would also affect the degree of any ambipolar acceleration. Both [Zhang, *et al*, 2016] and [Ahedo and Merino, 2017] discuss the high-energy tail of electron populations as being operative both in generating ambipolar forces, and also for ensuring zero-net current in the nozzle.

The plasma expansion model outlined in Section 5.1.5.2 includes the assumptions that the plasma expands polytropically, and that the plasma is confined to a collimated beam with a characteristic divergence angle. These two assumptions will now be discussed. Polytropic behavior may be the consequence of a self-consistent loss of adiabaticity during expansion. In the context of plume detachment, this loss is related to demagnetization, which is manifested by growth of the first magnetic invariant μ during expansion. One consequence of demagnetization of a particle is an increase in its Larmor radius

$$r_L = \frac{mv_\perp}{eB}. \qquad 5.21$$

Qualitatively, it can be seen that with decreasing B, r_L would tend to increase. At the same time, both $\omega_c = \frac{eB}{m}$ and $v_\perp$would tend to decrease. At some point, the system departs from conditions necessary for μ to remain invariant. As previously discussed in Chapter 2, [Ilin, *et al*, 2002], describe an increase in μ attendant with plume expansion. This increase was demonstrated in simulation.

For rapidly expanding B fields, the magnetic variant would rapidly increase in the z-direction. In some cases, however, the plasma flow might tend to follow the magnetic field lines, and it would not experience the increase in μ. Therefore, it would remain frozen-in even as it cooled. By contrast, in a collimated plasma, changes in B and μ would be relatively incremental, but the combined effects of plasma acceleration and cooling would tend to favor detachment. In practical systems, it may be necessary to augment the throat magnet with a shaping field. Anecdotally, of the four experiments discussed in Section 5.1.6.3, two in which detachment was likely observed, included solenoid stages. [Deline, 2009][Olsen, 2015] [York, 1992] was a theta-pinch device, which was self-collimating. The nozzle for case in which detachment likely did not occur [Takahashi, *et al*, 2016] consisted only of a throat magnet.

Equation (2.5a) relates the curvature of an ion's trajectory to its Hall parameter and the local Mach number. [Ahedo and Merino, 2017] The equation arises from solution of continuity and momentum equations assuming fully magnetized, isothermal electrons, and colder ions of varying degrees of magnetization. The results show plasma densities decrease less rapidly than the B-field

intensity, indicating detachment. In the far-field, $\kappa_i R \sim 1/M_\infty^2$ in radians, which for notional values of M_∞ of 4-6 would result in divergence angles in the range of 0.03 to 0.06 radians.

[Little and Choueiri, 2009] derive an expression for the divergence angle based on the MHD equations applied to a solenoid field. Assuming a collisionless plasma, so that $\sigma \to \infty$, the electric field is $E = -u \times B$. Applying coordinate and variable transformations, Faraday's law is cast as

$$B\frac{\partial \theta}{\partial \tau} = -cos\theta\left(\frac{\partial U_\perp B}{\partial z}\right)_\Phi - \frac{U_\perp B sin\theta}{r}. \qquad 5.22a$$

θ is the angle between the solenoid axis and the magnetic field lines at any location z. $U_\perp$ is the perpendicular component of U. Equation (5.22a) is further developed into the non-dimensional expression

$$\frac{\partial \theta_P}{\partial \tau} = -\left(\frac{2\Gamma^2\tau^2}{\bar{z}^3} + \frac{a}{\bar{z}}\right)\bar{U}_\perp^2 cos\theta_P. \qquad 5.22b$$

Γ is a function of plasma conditions at the magnetic throat, a is function of the magnetic field, and τ is dimensionless time. Equation (5.22) is integrated, and its limit for $(\tau \to \infty)$ and $(\bar{\bar{z}} \to \infty)$ provides a solution for θ_P in terms of $\bar{\bar{r}}_0$, the radius of the plasma at the throat normalized by the solenoid coil radius, and the magnetic pressure ratio at the throat β_0. The investigators describe this solution as assuming "that the plasma flow effectively stretches the magnetic field lines to infinity." For small β_0 and $\bar{\bar{r}}_{p0} \sim 0.5, \theta_P = 0.1\ radians$.

These two models provide comparable values for the plasma divergence angle, even though they are based on different understanding of the physics. The consistency among solutions, despite differing physical bases, suggests using a representative value for divergence angle in evaluating plasma expansion, with the range for θ_P.

There are both inertial processes involved in plasma expansion and detachment as well as processes arising from the interaction of plasma flow and the magnetic field. Proponents of the inertial detachment model observe that the flow must be super-Alfvénic to enable detachment. At the same time, those proposing stretching of field lines note the importance of the ratio of kinetic energy to magnetic energy in the flow. There is commonality in these two views that follows from the observation that flows in the trans- and super=Alfvénic regions will distort the magnetic field internal to the plasma. This is demonstrated by the observation that at any point along the expansion, momentum arising from the magnetic field external to the plasma must be offset by the momentum internal to the plasma, or for quasi-1D flow

$$\rho U_z^2 + P_z + \frac{B_{z\_int}^2}{2\mu_0} = \frac{B_{z\_ext}^2}{2\mu_0}. \tag{5.23}$$

Equation (5.23) follows from the expectation that hydrodynamic equilibrium is maintained at the outer boundary of the plume. It is a statement of 1D momentum equation where the pressure and dynamic terms are zero external to the plume. Since $P_z = \beta \frac{B_{zi}^2}{2\mu_0}$, and $U_z = KV_A$, Equation (5.23) can be rewritten

$$\frac{B_{z\_int}^2}{2\mu_0}(2K^2 + \beta + 1) = \frac{B_{z\_ext}^2}{2\mu_0}. \tag{5.24a}$$

The relationship between the internal and external fields then is

$$\frac{B_{z\_int}}{B_{z\_ext}} = \frac{1}{\sqrt{2K^2 + \beta + 1}}. \quad 5.24b$$

At small values of *K*, Equation (5.24b) is equivalent to the familiar relationship for β. At higher values of *K*, and especially at super-Alfvénic velocities where $K > 1$, Equation (5.24b) provides a first order estimate of the distortion of the magnetic field due to plasma flow.

5.1.6.3 Engineering relations for nozzle performance

A common method for engineering relations is to use experimental data to develop correlations based on relevant dimensionless groups. An early exploration of dimensionless groups relevant to plasmas is provided in [Beiser and Raab, 1961]. The approach requires sufficient data and, at a minimum, a rough physical model. For plasmas expanding through a magnetic field, the proposed model is based on the general mechanism suggested most clearly by [Olsen, *et al*, 2015]. The bulk behavior of the ions is captured in the momentum equation, Equation (5.25). Given the criticality of cross-field transport in demagnetization of the electrons, the generalized form of Ohm's Law, provided in Equation (5.26), would also appear operative. Assuming a quasi-neutral plasma, these two equations are coupled through the current density *J* and the magnetic field strength *B*.

$$\rho \frac{dU}{dt} = -\nabla p + \nabla \cdot \bar{\bar{\tau}} + J \times B + \rho_e E + F_{B,} \quad 5.25$$

$$\rho_e E + \nabla P_e = \rho_e \eta J + J \times B. \quad 5.26$$

There are twelve variables in Equations (5.30) and (5.31), some of them related to one another, others that may be neglected or eliminated. Assuming a stationary electric field, the current density *J* can be expressed by Ampere's Law as $J = \frac{1}{\mu_0} \nabla \times B$. Additionally, assuming the absence of body forces, and quasi-neutrality as the plasma expands through the nozzle, $F_B = 0$, and $\rho_e \sim 0$.

Applying these considerations to Equation (5.25) and expanding the substantial derivative on the left-hand side, Equation (5.25) can be expressed

$$\frac{\partial U}{\partial t} + (U \cdot \nabla)U = -\frac{\nabla p}{\rho} - \frac{1}{2\mu_0 \rho}\nabla B^2 + \nu \nabla^2 U. \qquad 5.27$$

Equation (5.26) is now considered based on the assumption of a fully ionized plasma, which is consistent with the application of an efficient propulsion system. For $J = \rho_e U$ and constant scalar conductivity $\sigma = 1/\eta$,

$$\vec{J} = \sigma\left[\vec{E} + \mu_0\left(\vec{U} \times \vec{H}\right) + \frac{1}{\rho_e}\vec{\nabla} P_e\right]. \qquad 5.28$$

Taking the curl of this expression, after [Cambel, 1963]

$$\nabla \times J = \sigma(\nabla \times E) + \sigma\mu_0[\nabla \times (U \times H)] + \frac{\sigma}{\rho_e}(\nabla \times \nabla P_e). \qquad 5.29$$

Recalling from Equation (5.26) that $\rho_e \sim 0$. While small, its value may be finite. However, $\nabla \times \nabla P_e$ is identically zero, so the last term drops out. Next, applying Ampere's Law to the left-hand side and Faraday's law to the first term on the right

$$\nabla \times \nabla \times H = -\sigma\mu_0 \frac{\partial H}{\partial t} + \sigma\mu_0[\nabla \times (U \times H)]. \qquad 5.30$$

The double curl on the left is expanded

$$\nabla \times \nabla \times H = \nabla(\nabla \cdot H) - \nabla^2 H. \qquad 5.31$$

Noting that the divergence of H is zero, and that $B = \mu_0 H$, Equation (5.31) can be expressed

$$\frac{\partial B}{\partial t} = \nabla \times (u \times B) + \nu_m \nabla^2 B \qquad 5.32$$

Equation (5.32) is the magnetic diffusion equation, and the preceding development is due to [Cambel, 1963]. The value ν_m is the magnetic diffusivity $\nu_m = \frac{1}{\mu_0 \sigma}$. In steady-state, for an infinitely conducting fluid, if the magnetic diffusion, or leakage, is zero, $u \times B$ must also be zero. This is the definition of frozen-in, i.e., velocity and magnetic field lines are identical. However, for finite σ, steady-state, $u \times B$ will be non-zero, indicating that velocity and magnetic field lines are diverging, and the system is departing from frozen-in.

Assuming an inviscid flow, the physical quantities contained in these two relations are therefore reduced to velocity, density, pressure, magnetic flux, conductivity, and length $[U, \rho, P, B, \sigma, L]$. The quantity L is obtained implicitly from the gradients. It would be useful to relate these quantities to the performance of the magnetic nozzle, so a seventh quantity of thrust F_t is added. These quantities and their respective dimensions are provided in Table 5-1.

Table 5-1 - Nozzle flow parameters and dimensions

Quantity	Dimensions
Ft	ml/θ^2
L	l
B	$m/\theta q$
ρ	m/l^3
U	l/θ
σ	$\theta q^2/ml^3$
p	$m/l\,\theta^2$

According to the Buckingham-π theorem, with seven quantities and four dimensions (m, l, θ, q), there should be three dimensionless groups, such that $\pi_1 = f(\pi_2, \pi_3)$. Defining π as

$$\pi = F_t^a L^b B^c \rho^d U^e \sigma^f P^g, \tag{5.33}$$

for which there is a matrix

	a	b	c	d	e	f	g
m	1	0	1	1	0	-1	1
l	1	1	0	-3	1	-3	-1
θ	-2	0	-1	0	-1	1	-2
q	0	0	-1	0	0	2	0

5.34

The columns represent exponents for the respective quantities, while the rows the constituent dimensions. The rows must sum to zero, so Equation (5.34) represents four equations. Since there are seven unknowns, it is necessary to assign three values with the constraint that the determinant of the matrix formed by the remaining columns is not zero. This condition ensures that the resulting dimensionless group is independent of the others. For π_1, the following set of exponents are assigned: $a = 1, f = g = 0$, which results in

$$\pi_1 = \frac{F_t}{\rho U^2 A}. \tag{5.35a}$$

This is thrust normalized by the momentum flux. Similarly, for π_2 $a = 0, f = 1, g = 0$ results in

$$\pi_2 = \frac{\sigma B^2 L}{\rho U}. \tag{5.35b}$$

The group π_2 is the interaction parameter, also called the Stuart number. Finally, for $a = f = 0, g = 1$,

$$\pi_3 = \frac{P}{\rho U^2}, \qquad 5.35c$$

which is the pressure coefficient N_P.

In principle, a relation of the form $\pi_1 = C\pi_1^m \pi_2^n$ could be derived with a sufficient amount of data. Such a relation would allow the estimation of nozzle performance as a function of the Stuart number and the pressure coefficient. However, it should be remembered that the definition of these groups follows from a basic assumption about the physics of detachment, that is, the ions detach inertially, and that electrons diffuse across magnetic field lines to follow the ions. The operative equation in this scenario is the magnetic diffusion equation, Equations (5.32). It is fair to point out that the mechanism suggested by [Deline, 2009] [Takahashi, 2017][Briezman, 2008], and others, i.e., stretching magnetic lines, would probably result in different dimensionless groups.

5.1.6.4 Plume detachment calculations

Observations provided in [Olsen, *et al*, 2015],[Deline, *et al*, 2009],[Takahashi, *et al*, 2016], and [York, *et al*, 1992] were analyzed with the purpose of exploring the use of the dimensionless groups as they relate to plume detachment, specifically the evaluation of St and N_P along the axis of expansion. [York, *et al*, 1992] and [Deline, *et al*, 2009] provide nozzle performance data for lighter ion species, while [Olsen, *et al*, 2015] and [Takahashi, *et al*, 2016] both experimented with argon. These datasets were chosen from among the references cited because they provided relatively complete data on state variables, velocity, and magnetic fields over the region of plasma expansion. Accordingly, the need to estimate missing data was minimized. In general, the principal calculations done in adapting these data were the adjustment of the z-dimension so that the nozzle

throat is the zero-station, and estimation of conditions at the nozzle throat. For number density and temperatures, this was done through a power law extrapolation from the downstream data, taking into consideration the relative shortness of the distance. The Bohm velocity was then assumed to estimate velocity in the vicinity of the throat. It should be noted that while [Olsen, *et al*, 2015] provided a robust dataset for normalized parameters along the centerline of expansion, the tabulated data for basic plasma properties in the plume did not allow for direct extraction of the normalizing parameters for specific shots. Given their extensive campaign of over 450 firings, this is understandable. In order to take advantage of their data, other works on similarly configured experiments by these investigators were consulted in order to derive a representative surrogate for a single shot, one that respected general system parameters documented in [Olsen, *et al*, 2015], as well as [Longmeir, *et al*, 2011] [Deline, *et al*, 2009]. Properties of the four plasmas at the magnetic throat are provided in Table 5-2; values in blue font indicate estimates.

Table 5-2 - Characterization of four experimental datasets

Reference	Plasma Heating	Plasma	L	B0	n0	Te0	Ti0
			m	T	#/m^3	eV	eV
Olsen, C.S., et al, 2015	Helicon +ICH	Ar	3.2	0.17	3.75×10^{18}	4.2	37.1
Deline, C.A., et al, 2009	Pulsed plasma washer gun	H	5	0.07	4.70×10^{18}	1.4	
Takahashi, et al, 2016	Helicon	Ar	0.3	0.26	1.90×10^{19}	3.5	
York, T.M., et al, 1992	theta-pinch	D	0.183	2.3	3.00×10^{22}	19	1.6

Figure 5-10 shows the Stuart number for the four datasets as a function of z/L where L is the length of the expansion zone for which data were collected. Figure 5-11 shows the pressure coefficient. It can be seen immediately that the Stuart number decreases by several orders of magnitude during

the expansion, indicative of a rapid decrease in magnetic flux density and conductivity. These changes overmatch any effect of the decreasing density in the plume. Since the Stuart number expresses the ratio of electromagnetic forces to dynamic forces, a reasonable inference is that the momentum forces of the plasma become large compared to the electromagnetic forces, consistent with plume detachment.

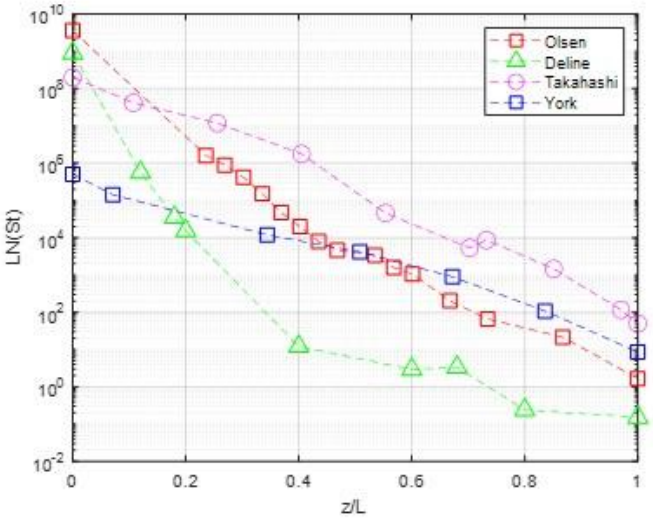

Figure 5-10– Stuart number vs. z/L for four experimental datasets

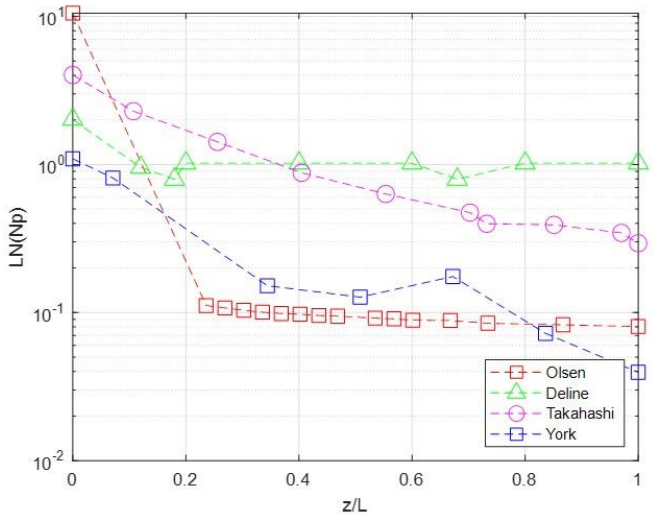

Figure 5-11 – Pressure coefficient for four experimental datasets

By contrast, the pressure coefficient decreases by roughly an order of magnitude for the datasets. The pressure coefficient expresses the ratio of static to dynamic pressure in the system. Given the small value of the static pressure to begin with, it is likely that the contribution of N_p to overall system performance would be secondary relative to that of *St*.

The data shown in Figures 5-10 and 5-11 must be qualified. The $z/L = 0$ station represents the nozzle throat, for which data was not explicitly provided by the respective investigators, but was estimated. Further, scalar values for B and σ were used to calculate St, and the scalar values can vary significantly from the respective vector or tensor components, especially during the initial expansion region. The perpendicular component of σ in a magnetic field, for example, is equal to $\frac{\sigma_0}{(\omega_{ce}\tau)^2}$, or the scalar conductivity divided by the square of the Hall parameter for electrons. Finally, the characteristic length used to calculate St does not correspond with the effective length of the nozzle, as might be the case in a physical de Laval nozzle. In the case of the data shown, it is generally the location where the investigators stopped taking data. However, this dimension is easy to apply and may at most affect the value of St by half an order of magnitude.

The Stuart number can be expressed in terms of the magnetic Reynolds number and the Cowling number.

$$St = Re_m Co = \mu_0 \sigma U L \cdot \frac{B^2}{\mu_0 \rho U^2} \tag{5.36}$$

It will be remembered that Deline suggested criteria for detachment at a value of $\beta_k > 1$, which is identical to saying the Cowling number must be less than unity, i.e., the flow has become super-Alfvénic. Figure 5-12 shows the Cowling number for these four datasets.

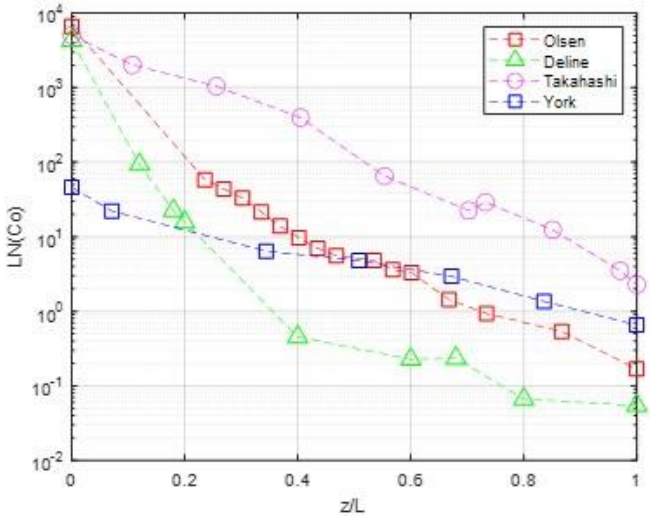

Figure 5-12 - Cowling number for four experimental datasets

Three of these datasets show the transition to super-Alfvénic velocities, while the fourth, Takahashi, is clearly trending toward that transition. It can be inferred that the ions in these experiments detached. As a physical quantity, the Cowling number is based on the ratio of the propagation speed of magnetic disturbances to that of the fluid flow. A low Cowling number is consistent with an increasing Larmor radius as ions expand upon weakening magnetic lines of force, a condition often cited as precursor to the ion's detachment due to inertial forces. However, the Cowling number criteria provides no insight into the fate of the electrons.

If the electrons are to detach, in the context of the proposed model, it is due to the ambipolar forces between the ions and the electrons that allows the electrons to diffuse across magnetic lines of force. This implies a sufficient rate of diffusion across the field lines, or more specifically, conductivity. Accordingly, the magnetic Reynolds number may provide relevant insight into the ability of the electrons to effect this diffusion. Noting again that $\nu_m = \frac{1}{\mu_0 \sigma}$, it can be seen that if

conductivity is infinite, as assumed in MHD, that ν_m will be zero, and that Re_m will be infinite, and the plasma will be frozen in. Conversely, a high, but finite conductivity implies a lower Re_m. Summarizing, if frozen-in holds, $\frac{\partial H}{\partial t} = 0$. If the magnetic fields are not frozen-in, $\frac{\partial H}{\partial t} < 0$, i.e., the magnetic field is diffusing or "leaking." These considerations are reflected in the integral of Equations (5.32) along z

$$\int \frac{\partial \vec{B}}{\partial t} dz = \left(\vec{U} \times \vec{B}\right) + \nu_m \nabla \vec{B} < 0, \qquad 5.37$$

from which the magnetic Reynolds number can be scaled. Assuming that scalar B decreases with z, Equation (5.37) leads to the approximation $UB - \nu_m B/z < 0$, and

$$\frac{UL}{\nu_m} = \sigma \mu_0 UL < 1. \qquad 5.38$$

Experimental values for the magnetic Reynolds number will be larger than one, even for systems that demonstrate detachment. Equation (5.38) represents the physics of an idealized one-dimensional plasma where only momentum and magnetic diffusion are accounted for. In real plasmas, there are also viscous and electrostatic forces, as well as three dimensional effects. Figure 5-13 shows the magnetic Reynolds number for the exemplar datasets.

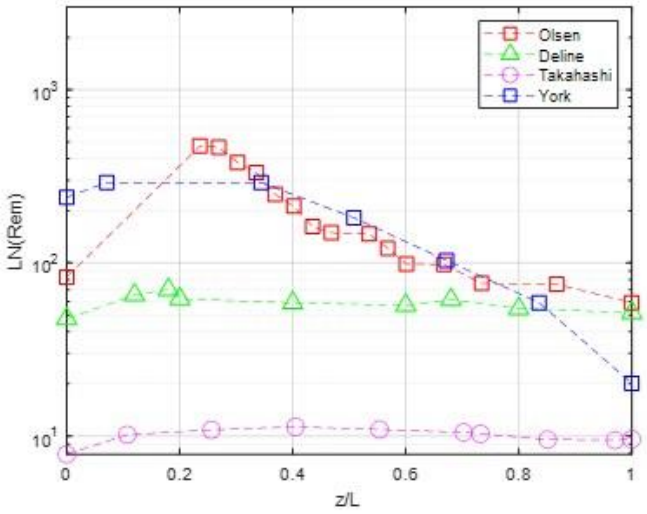

Figure 5-13 - Magnetic Reynolds number for four experimental datasets

The data in Figure 5-13 are presented with the same qualifications mentioned earlier with respect to the characteristic length and the use of scalar quantities. The use of scalar quantities is especially pertinent to the discussion of why Re_m is greater than unity in plasmas that appear to detach. Figure 5-14 shows the scalar conductivity σ_0 for the [Olsen, 2015] dataset, along with conductivity parallel $\sigma_\parallel$ and perpendicular $\sigma_\perp$ to the magnetic field lines. As the magnetic field lines bend outward with increasing z/L, the velocity component normal to the field lines increases, as $\sigma_\perp$ also increases. Since the Hall parameter also decreases along the axis of expansion, as shown in Figure 5-15, the perpendicular conductivity tends toward the scalar value. The Hall parameter in Figure 5-15 is for electron-ion collisions, which would be expected to contribute the most to electron diffusion, based on the net exchange of momentum. [Huba, 2013] A small Hall parameter for electrons is associated with electron detachment, as the cyclotron frequency tends toward the same order as the collision frequency. [Olsen, et al, 2015][Kuriki and Okada, 1970]

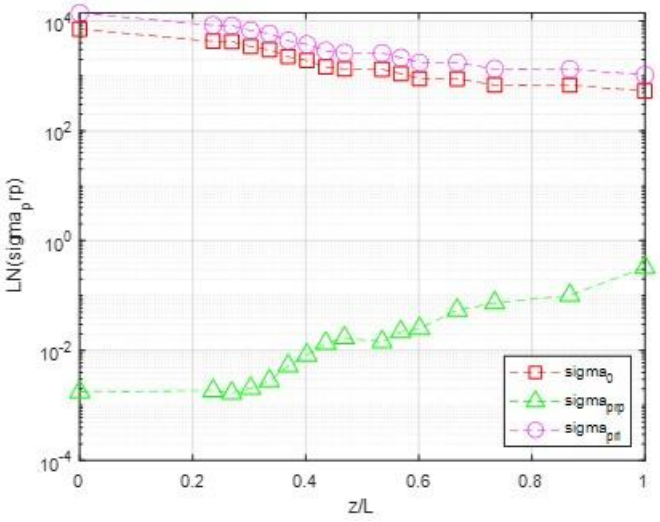

Figure 5-14 - Scalar and transverse conductivities for [Olsen, 2015]

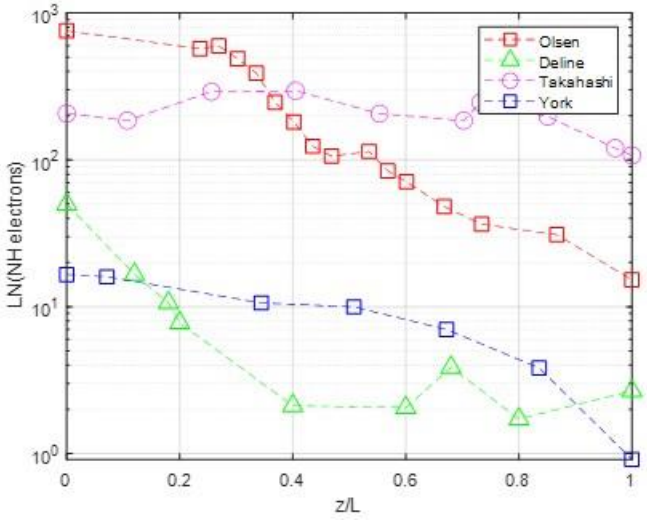

Figure 5-15 - Hall parameter for four experimental datasets

The Cowling number in each case is near unity, indicating ion detachment. The Hall parameter and magnetic Reynolds numbers for three of the datasets indicate electron detachment based on suggested reasoning previously discussed. The estimated Hall parameter for [Takahashi, *et al*, 2016] is much greater than that of the other datasets, even though the magnetic Reynolds number would appear low enough for detachment. It will be recalled that cross-field diffusion is dependent

upon the perpendicular component of the conductivity, and that $\sigma_\perp$ is reduced relative to σ_0 by the square of the Hall parameter. The results from [Takahashi, *et al*, 2016] therefore demonstrate the need for the Hall parameter as an adjunct to the magnetic Reynolds number as an indication of electron detachment.

5.1.6.5 Nozzle performance

Given $\frac{F_t}{\rho U^2 A}$ for π_1, it is possible that detachment can be characterized as performance, as opposed to simply, did the plume detach, or did it not. Charged species that do not detach, as well as kinetic energy loss associated with detachment, will both reduce thrust. One way to cast π_1 is an efficiency of delivered or estimated thrust relative to the maximum theoretical thrust, expressed as $\rho U^2 A$. Another possibility is to evaluate $\rho U^2 A$ at an upstream location, such as the nozzle throat. The resulting quantity would be analogous to the thrust coefficient defined for conventional rockets, $C_f = \frac{F_t}{p_c A_{th}}$. Substituting the expression for the Bohm velocity in for U, this "magnetic" thrust coefficient could be expressed as

$$C_{fm} = \frac{F_t}{\left(n_i k_B T_e A_p\right)_{th}} \tag{5.39}$$

The delivered thrust then is related to electron temperature near the throat, which in turn is related to the maximum theoretical plume energy $e\varphi$ where φ is determined from Equation (1.16).

Experimentally, ions appear to accelerate quickly in the region of the nozzle throat and then their velocity may remain constant through expansion and detachment. For example, both [Olsen, *et al*, 2015] and [Deline, *et al*, 2009] reported relatively constant ion velocities in the nozzle well before the detachment point. Curves from the two investigators' work are provided in Figures 5-16 and

5-17. Figure 5-16 shows ion velocity for the Ad Astra VX-200 thruster in both helicon and ICH modes. [Olsen, *et al*, 2015] Figure 5-17 shows ion velocity reported by [Deline, et al, 2009] for H+ and He+ plasmas. These data suggest a rapid, electrostatic acceleration within the nozzle throat region and then a slowly increasing velocity flow until detachment. Note that a low degree of acceleration in the diverging section of the nozzle would be consistent with a loss of adiabaticity in the sense of γ only slightly greater than unity. Practically speaking, the apparent lack of acceleration in the diverging section of the nozzle may be due to limits in axial measurements.

Conditions for detachment occur when B decreases to the point that ions can achieve an inertial detachment, while T_e decreases facilitating electron detachment. Number density must remain high enough to support a collisional plasma, though. Collectively, these factors contribute to an increase in magnetic moment and associated loss of adiabaticity discussed previously. [Illin, *et al*, 2002]

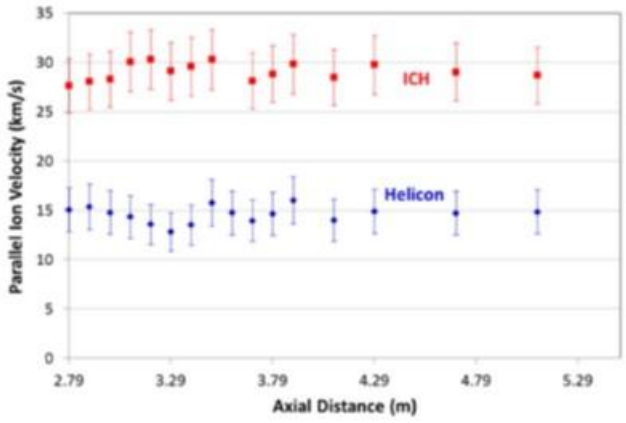

Figure 5-16 - Ion velocity for VX-200 thruster [Olsen, et al, 2015]

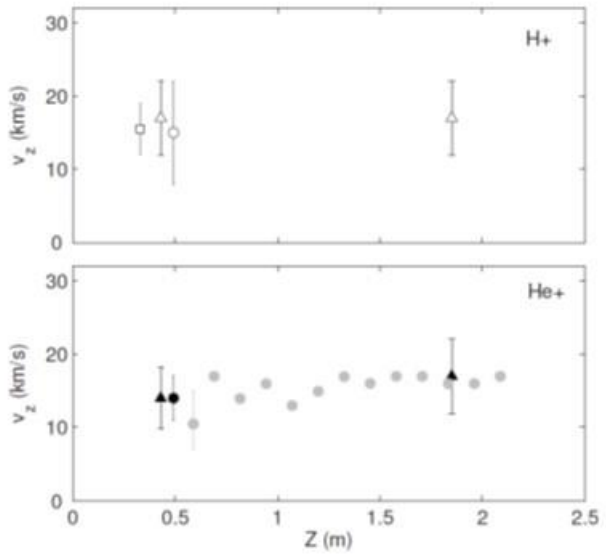

Figure 5-17 - Ion velocity – H+ and He+ [Deline, et al, 2009]

5.1.6.6 Provisional engineering criteria for plume detachment

The current analysis does not include sufficient data for a valid evaluation of C, m, and n in the relation $\pi_1 = C\pi_1^m \pi_2^n$, but it does provide an anecdotal basis for provisional engineering criteria for plume detachment. Table 5-3 summarizes key data presented in Figures 5-10 through 5-15 and provides the basis for provisional criteria for detachment given in Table 5-4.

Table 5-3 - Key plasma properties of four experimental plasmas at detachment

Investigator	z/L	B/B0	n/n0	Te/Te0	NHe	Co	Re_m	Remarks
Olsen, et al, 2015	0.667	0.027	0.022	0.239	48.1	1.436	98.1	ICH
Deline, et al 2009	0.4	0.004	0.005	1	2.12	0.454	58.8	Te as reported
Takahashi, et al, 2016	1	0.003	0.003	0.714	107	2.279	9.6	Detachment uncertain
York, et al, 1992	1	0.043	0.033	0.111	0.91	0.653	20.2	

Table 5-4 - Provisional criteria for plume detachment

Event	Criteria	Rationale
Ion detachment	Co ~ 1	Indicates super-Alfvenic velocities, as well as kinetic energy greater than magnetic energy
Electron detachment	$Re_m<10^2$	Observed values for Rem at Co=1 in experiments with probable plume detachment
	$NH_{ei}<10^0 \sim O(10^1)$	Larmor radius comparable with system characteristic lengths; cyclotron frequency comparable with collisional frequencies
Plume detachment	$St<10^2$	Given Co ~1, the Stuart number will be approximately the same as Re_m

If ion acceleration occurs only within the current-free layer downstream of the nozzle throat, the fact of constant ion velocity, cannot be taken as evidence of detachment. The plasma in this case does not expand in the sense that conventional rocket plumes expand in physical nozzles, with flow velocity increasing as a direct result of thermodynamic expansion. Rather, based on the assertion that ion acceleration is primarily electrostatic, and scales with T_e, the processes affecting detachment during expansion are those related to conductivity, the decrease in magnetic field strength and number density, as these collectively relate to the velocity. These considerations are captured in the local Stuart number. Conditions supporting detachment of ions and electrons are reflected in the Cowling number and magnetic Reynolds number, respectively, both components of the Stuart number. Ion detachment appears to occur at the transition to super-Alfvénic conditions, indicating $Co \sim 1$. Theoretically, electron detachment would occur at $Re_m < 1$, but based on the considerations and data presented in the current analysis, it is suggested provisionally that electrons may detach at $Re_m \sim O(10^2)$. In addition to the anecdotal data, the tensor character of conductivity also supports this evaluation. As shown in Figure 5-13, the perpendicular component of conductivity is much lower than the parallel component and scalar values. Since

diffusion across magnetic lines is more or less related to the perpendicular component, depending upon $U \times B$, it is likely that detachment can occur at relatively large values of Re_m as calculated from scalar conductivity. Instead of investigating the use of a tensor magnetic Reynolds number, the Hall parameter for electron-ion collisions NH_{e-i} is proposed as a criterion adjunct to Re_m. Both on theoretical grounds and observation [Kuriki and Okada, 1970], NH_{e-i} within an order of magnitude of unity appears consistent with requirements for electron detachment.

5.1.6.7 Evaluation of the criteria

In order to calculate St and N_P, knowledge of plasma conditions within the nozzle is necessary. Whether determined experimentally or analytically, obtaining state properties (n, T, B) is relatively straightforward. Estimating transport properties (σ, NH_{e-i}) is more complicated and involves some judgment. Additionally, the choice of characteristic length can be problematic, since there are few physical dimensions, e.g., aperture diameter of the throat magnet, and they may not be directly relevant.

For highly ionized plasmas, the scalar conductivity is obtained [Huba, 2013]

$$\sigma_0 = \frac{ne^2\tau_{ei}}{m_e}, \tag{5.40}$$

where τ_{ei} is calculated

$$\tau_{ei} = \frac{3(4\pi\varepsilon_0)^2\sqrt{m_e}(k_B T_e)^{3/2}}{4\sqrt{2\pi}nln\Lambda e^4}. \tag{5.41}$$

The data presented in Figures 5-9 through 5-14 are for highly ionized plasmas, for which Equations (5.40) and (5.41) are appropriate. For a plasma of arbitrary ionization, Spitzer's free path

conductivity may be used, in which case τ_{ei} is calculated as the ratio of mean free path to thermal velocity

$$\tau_{ei} = \frac{\lambda}{\left(\frac{8k_B T_e}{\pi m_e}\right)^{1/2}}, \tag{5.42}$$

where $\lambda = \frac{1}{\sum_j n_j Q_j}$ for j species – charged and neutrals – interacting with the electrons. [Cambel, 1963] State properties (n, T) must also be calculated for respective species in a plasma with arbitrary levels of ionization.

In order to evaluate the Hall parameter, the frequency of Coulomb collisions is needed. Taking the electron as the test particle and the ions as field particles, the collision rate for perpendicular collisions is

$$\nu_{\perp}^{e/i} = 2\left[\left(1 - 1/2x^{e/i}\right)\psi\left(x^{e/i}\right) + \psi'\left(x^{e/i}\right)\right]\nu_0^{e/i} \tag{5.43a}$$

$$\nu_0^{e/i} = \frac{e^4 ln\Lambda n_i}{4\pi\varepsilon_0^2 m_e^2 v_e^3} \tag{5.43b}$$

$$x^{e/i} = \frac{m_i v_e^2}{2k_B T_i} \tag{5.43c}$$

where ψ and ψ' are the error function and its derivative. [Huba, 2013] The parameter $x^{e/i} \gg 1$ for the systems in Figures (5-9)-(5-14), and so the expression in Equation (5.48a) involving ψ and ψ' reduces to unity, as suggested by [Olsen, 2015]. This will generally be the case with electron-ion

collisions, given the electrons' low mass and resulting thermal velocities for a given T_e. With the collision frequency obtained, the Hall parameter is calculated $NH_{e-i} = \omega_{ce}/\nu_{\perp}^{e/i}$.

In evaluating St and Re_m in Figures 5-9 and 5-12, the characteristic length is associated with their respective experiments, the maximum distance from the thruster exit for which they collected data. Although arbitrary, these lengths do reflect the far-field for respective nozzles, and they are consistent with the overall scale of the experiment. L for [Olsen, 2015] and [Deline, 2009] was on the order of meters, for example, while for [Takahashi, *et al*, 2016] and [York, 1992], it was on the order of centimeters. It would also be possible to take L as the location where $Co = 1$, which would provide a common physical basis for evaluating St and Re_m. And it would be possible to evaluate them based on the local value of z, as is sometimes done in engineering relations for aerodynamics and heat transfer. Each of these methods has merit, but for the current analysis, L based on the respective experimental scales appears sufficient to provide useful insights.

5.2 Propulsion System Modeling

5.2.1 Objectives

The warm plasma and propulsion model was developed with the following primary goals:

- Characterize realistic performance regimes for DFD-CM based on medium fidelity modeling
- Assess the propulsive performance of DFD-CM relative to specified ideal performance, i.e., propulsion efficiency
- Provide a better understanding of fusion energy deposition in the warm plasma

- Estimate effects of neutral propellant supply, heating, and ionization on propulsion performance
- Assess the effects of transport in the warm plasma on performance
- Assess the performance of the magnetic nozzle in DFD-CM, including the ability of the warm plasma to detach from the magnetic field

Additionally, there were the following secondary goals

- Assess the effects of reactor flux geometry
- Assess the effects of warm plasma geometry
- Assess the effects of propellant delivery methods

5.2.2 The Warm Plasma

The above considerations determined the fidelity of the model in terms of species and processes included, as well as configurations for the warm plasma that could be simulated. At the top level, it was necessary to include species for fusion products, the ionized propellant, the neutral propellant feed, the thermalized fusion products, and the bulk population of electrons. Mass conservation equations are solved for the collective species, so that their radial distributions can be calculated. Bulk plasma properties are then calculated from these data, and associated momentum and energy equations are solved.

5.2.2.1 System equations

The 1D radial model of the warm plasma expressed in conservative form is

$$\frac{\partial Q_s}{\partial t} = \nabla_r \cdot F_s^Q + S_s^Q, \tag{5.44}$$

where the quantities Q are $Q_n = \left[n^\alpha\ n^\beta\ n^\theta\ n^{DT\theta}\ n_e\ n_n\right]$ for continuity; $Q_p = [p_{iB}]$ for momentum; and $Q_k = \left[T^{iB}\ T^{eB}\ \right]$ for energy. The quantities F_s^Q are the flux terms for quantities Q and species s. Similarly, the quantities S_s^Q are respective source terms. The system includes six species for number density equations: prompt alphas (α), thermal ions from the reactor (θ), neutrals supplied as propellant (n), ionized propellant (β), and thermalized fusion products (DT_θ), and (n_e) the number density for bulk electrons is determined through quasi-neutrality. The momentum equation is solved for the bulk warm plasma ions. The energy equation is solved for bulk warm plasma ions and electrons. The result is a system of nine integral equations coupled through transport and source terms. The general form for source terms related to energy transfer is $\dot{S}_s^Q = Q_s(r)\sum_j \frac{1}{\tau_{sj}}$ where j are species which interact with species s through collisional processes. The flux terms represent the transport in the 1D radial direction. There are also source terms based on explicit collisional cross-sections, including ionization discussed in Section 5.1.3.3. Also included in this category is charge exchange.

For mass, momentum, and energy transport, the flux terms are

$$F_s^m = u_r n^s + D^s \frac{\partial n^s}{\partial r} \tag{5.45a}$$

$$F^p = u_r p + P + \frac{B^2}{2\mu_0} \tag{5.45b}$$

$$F_s^K = \left(u_r n^s + D^s \frac{\partial n^s}{\partial r}\right)\frac{3}{2}k_B T_s + \kappa_{\perp,s}\frac{\partial T_s}{\partial r} \tag{5.45c}$$

For Equation (5.45b), it will be recalled that $p = \rho u_r$, and so is the bulk momentum of the fluid. Consistent with the definitions of Q_s, terms for F_s^m are calculated for individual species, while F^p is calculated for the bulk plasma, and F_s^K is calculated for bulk plasma ions and electrons.

5.2.2.2 Transport properties

Source terms for continuity and the energy equation are both based on τ_{12} for energy, the rate of energy transfer from species 1 to 2 [Trubnikov, 1965].

$$\nu_{12} = n_2 \frac{q_1^2 q_2^2}{(4\pi\varepsilon_0)^2} \frac{8\pi}{m_1 m_2 V_1^3} ln\Lambda, \tag{5.46}$$

and $\tau_{12} = 1/\nu_{12}$. This rate applies to continuity as well as the energy balance because source terms reflect losses and gains of species due to thermalization processes. In the case of energy deposition of alphas, for example, energy arrives in the warm plasma at the rate of $\dot{S}^\alpha E^\alpha$. The quantity V_1 in Equation (5.46) is evaluated as the thermal velocity for any given test particle species 1. In the case of the prompt alphas, the thermal velocity is calculated using the slowing down temperature T_s^α, and for the thermal species from the reactor, T^θ.

The diffusion coefficients in Equations (5.45) are the ambipolar form described by [Chen, 1974]

$$D_A = \frac{\mu_i D_i + \mu_e D_e}{\mu_i + \mu_e}. \tag{5.47a}$$

Since $\mu_e \gg \mu_i$,

$$D_A = D_i + \frac{\mu_i D_e}{\mu_e}. \tag{5.47b}$$

Because of the Einstein relation $\mu = |q|D/k_B T$, for $T_e \approx T_i$, the ambipolar diffusion coefficient in Equation (5.52b) reduces to $D_A = 2D_i$, where $D_i \approx r_L^2/\tau_{ii}$. The use of the ambipolar diffusion

coefficient is an approximation based on the assumption that longitudinal transport is negligible. This assumption is appropriate for a long, cylindrical plasma. However, as shown in Section 5.1.4, this may not be the case with the warm plasma, so the use of the ambipolar diffusion coefficient may result in some loss of accuracy in the warm plasma solution.

Investigation identified no appropriate models for neutral diffusivity in partially ionized plasmas. One possible work around would be to apply relations for diffusivity within a neutral fluid, and to neglect the presence of charged species. In this model, an encounter between a neutral and charged particle would result in an ionization or a charge exchange. Otherwise, diffusion would occur only through neutral-neutral interactions. However, this approach requires assumptions on statistics of interactions with multiple charged species and about cross-sections for neutral interactions. Given the potential complexity of these considerations, a notional, constant value of 10 m^2/s was used in the model. This in the lower range of D_N in neutral fluids as calculated from [Bird, et al, 1960], and an order of magnitude larger than D_S for ions.

The thermal conductivities $(m^{-1}s^{-1})$ for transport across magnetic field lines are calculated using relations from [Braginskii, 1965] and [Huba, 2013]

$$\kappa_{\perp}^{i} = \frac{2n_i k_B T_i}{m_i \omega_{ci}^2 \tau_i}, \tag{5.48a}$$

$$\kappa_{\perp}^{e} = \frac{4.7 n_e k_B T_e}{m_e \omega_{ce}^2 \tau_e}. \tag{5.48b}$$

Coulomb logarithms $\lambda = ln\Lambda$ are calculated using relations from [Huba, 2013].

$$\lambda_{ee} = 23.5 - ln\left(n_e^{1/2} T_e^{-5/4}\right) - [10^{-5} + (lnT_e - 2)^2/16]^{1/2}, \quad 5.49a$$

$$\lambda_{ei} = 24 - ln\left(n_e^{1/2} T_e^{-1}\right), \quad 5.49b$$

$$\lambda_{ii'} = 23 - ln\left[\frac{ZZ'(\mu + \mu')}{\mu T_{i'} + \mu^i T_i}\left(\frac{n_i Z^2}{T_i} + \frac{n_{i'} Z'^2}{T_{i'}}\right)^{1/2}\right]. \quad 5.49c$$

Equations (5.49) are functionalized in the code with cgs units and temperatures in eV, per [Huba, 2013].

5.2.2.3 Simulation specification and initial conditions

Inputs to the warm plasma model include the power output of the reactor in terms of fluxes of prompt and thermal species. For a D-T reactor, the prompt species are monoenergetic and arrive at the warm plasma at 3.5 MeV. The thermal species carry in their $k_B T$ energy, as well as residual potential energy from the reactor well, as described in Equation (5.3e). The flux and energies have a radial spatial distribution in the reactor, which is an annulus reflective of the well configuration. The warm plasma model approximates this distribution as a sine function, whose form is derived in Appendix B. Other inputs from the reactor include the midplane magnetic field strength, the associated inner and outer radii of the burning plasma, and the jet-side mirror ratio in the reactor. These data are available from the 0D reactor model and are required to calculate corresponding values in the warm plasma based on conservation of magnetic flux.

Initial conditions for the solution are determined by setting Equation (5.44) equal to zero and solving for Q with source terms evaluated at initial state conditions. The latter follow from the specification of ideal jet power, specific impulse, and propellant, e.g., hydrogen. From specific

impulse, exhaust velocity follows, i.e., $U_e = g_0 I_{SP.}$ As discussed in Section 5.1.1, $e\phi = \frac{1}{2} m U_x^2$ for the ideal system, where m is the mass of the propellant particles. This relation, along with Equation (5.1) allows calculation of the initial warm plasma electron temperature $T_e(t_0, r)$. Knowing jet power and exhaust velocity allows calculation of mass flow rate from the engine, based on the definition of jet power $P_J = \frac{1}{2}\dot{m} U_e^2$. For the Bohm velocity calculated from $T_e(t_0, r)$ and a given nozzle area A_N, the mass flow rate is used to calculate the propellant number density at the nozzle throat. The bulk plasma number density then follows from sheath theory $n_{wp} = n_N e^{1/2}$. The nozzle throat diameter is determined by the reactor jet mirror field and the desired retention rate of prompt alphas, as discussed in Section 5.1.2.2.

5.2.3 Numerical Methods

5.2.3.1 Finite volume representation

The geometry of the warm plasma model is shown in Figure 5-18. The figure is an annulus that is one of n elements of a cylindrical plasma. The flux $\Gamma_{in}(r)$ is representative of any of the fluxes entering the control volume, e.g. propellant supply. The model also allows circumferential supply of the propellant, in which case, the flux enters through $A_{n+1/2}$ Entering power from the reactor is specified as a jet power P_{J0} based on prompt alphas and thermal species.

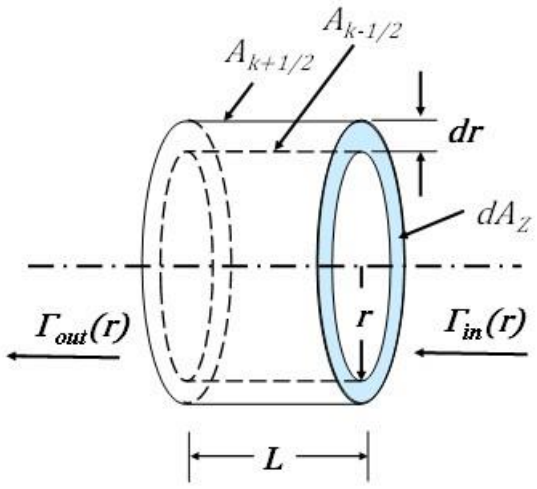

Figure 5-18 – Warm plasma model control volume V_k

Equations (5.44) and (5.45) are expressed in integral form as

$$\frac{d}{dt}\int_V Q_s dV = \oint_A n \cdot F_s^Q dA + \oint_V S_s^Q dV, \tag{5.50}$$

where the gradients of the fluxes in Equation (5.46) are expressed in terms of a surface integral by the divergence theorem. For $\vec{Q}_s$ expressed as a vector of length n over radius r, Equation (5.50) is

$$\frac{d}{dt}\overrightarrow{n_j} = \frac{1}{V_k}\left\{\frac{k+\frac{1}{2}}{k}F^m_{j,k-\frac{1}{2}}A_{k-\frac{1}{2}} - F^m_{j,k+\frac{1}{2}}A_{k+\frac{1}{2}}\right\} + S^m_{j,k}, k = 1{:}n \tag{5.51a}$$

$$\frac{d}{dt}(\overrightarrow{\rho u_r}) = \frac{1}{V_k}\left\{\frac{k+\frac{1}{2}}{k}F^p_{j,k-\frac{1}{2}}A_{k-\frac{1}{2}} - F^p_{j,k+\frac{1}{2}}A_{k+\frac{1}{2}}\right\} + S^p_{j,k}, k = 1{:}n \tag{5.51b}$$

$$\frac{d}{dt}\overrightarrow{T_j} = \frac{1}{n_{j,k}m_j C_{v,j}V_k}\left\{\frac{k+\frac{1}{2}}{k}F^K_{j,k-\frac{1}{2}}A_{k-\frac{1}{2}} - F^K_{j,k+\frac{1}{2}}A_{k+\frac{1}{2}}\right\} + S^K_{j,k}, k = 1{:}n \tag{5.51c}$$

The variables on the right-hand side of Equations (5.51) are calculated in the code as vectors based on $\vec{Q}_s$. The index j is the particular component of $\vec{Q}_s$, $n^{DT\theta}$, for example. Two flux terms are calculated for each control volume V_k, one at the inner surface, $f^Q_{j,k-\frac{1}{2}}$ based on $Q_{s,k-\frac{1}{2}} = \frac{1}{2}\left(Q_{s,k-1} + Q_{s,k}\right)$; and the second $f^Q_{j,k+\frac{1}{2}}$ based on $Q_{s,k+\frac{1}{2}} = \frac{1}{2}\left(Q_{s,k} + Q_{s,k+1}\right)$ at the outer surface. This operation results in a flux on either side of a given boundary, which will be slightly different. This discontinuity is resolved by flux splitting, $F^Q_{j,k-\frac{1}{2}} = \frac{1}{2}\left(f^{Q,inner}_{j,k-\frac{1}{2}} + f^{Q,outer}_{j,k-\frac{1}{2}}\right)$ for the inner boundary of V_k, and $F^Q_{j,k+\frac{1}{2}} = \frac{1}{2}\left(f^{Q,inner}_{j,k+\frac{1}{2}} + f^{Q,outer}_{j,k+\frac{1}{2}}\right)$ for the outer boundary. A Neumann boundary condition for each Q_s is imposed, such that $\left.\frac{\partial Q_s}{\partial r}\right|_{r=0} = 0$. In the finite volume representation, these boundary conditions are implemented by setting $F^{Q,inner}_{j,k-\frac{1}{2}}$ to zero at $k=1$. At the same time, for n control volumes, at the outer surface of V_k, where $k = n$, $F^{Q,inner}_{j,k+\frac{1}{2}}$ is approximated as $F^{Q,outer}_{j,k-\frac{1}{2}}$.

Section 5.1.4.2 discussed the effect of the magnetic field and pressure on radial transport. The relations for calculating ρu_r, including Equation (5.16c), were implemented in early versions of the code, and calculated values for u_r were on the order of 10^{-5} m/s over 10s of ms of run time. Extending this to typical run times of the 0D model in the 100s of ms, it is estimated that the model would not evolve convective velocities greater than 10^{-2} m/s for the cases evaluated. Physically, this follows from the hydrostatic relationship $P + \frac{B^2_{int}}{2\mu_0} = \frac{B^2_{ext}}{2\mu_0}$, where the latter is constant. Therefore, any local change in P resulting from changes to temperature and density is offset by a

change in B_{int}. As a result, hydrostatic forces that would impart momentum to the plasma are nil. At the same time, assuming pre-heating, the neutral propellant is introduced at 0.5 eV, with the associated acoustic velocity resulting from injections by small jets. It is assumed that the neutrals penetrate the warm plasma at the associated Bohm velocity, based on the jet penetrating into a near vacuum. As mentioned in Section 5.1.3.3, the injection temperature T_{n0} assumes some pre-heating of the propellant prior to injection. Therefore, propellant supply adds little momentum to the system because the mass flows are still minute. Given these considerations, and the computational expense of integrating Equation (5.51b), the value for ρu_r is set to zero in current versions of the 0D model. Transport within the 1D warm plasma model therefore results entirely from diffusive processes.

5.2.3.2 Time marching

The 1D warm plasma model uses the Adams-Bashford 3 (AB3) explicit solver to integrate Equations (5.51a and 5,51c).

$$u_{i+1} = u_i + \frac{h}{12}[23u'_i - 16u'_{i-1} + 5u'_{i-2}]. \tag{5.52}$$

The code solves the first three time steps with the Euler explicit method, while building the matrix $[u'_{j,i-r}]$. For six species of n^s, two temperatures T_e and T_i, and $r = -2, -1, 0$, $[u'_{j,i}]$ is a 3x8 matrix that is updated each time step to provide the values of u'_j needed to evaluate Equation (5.52).

The time step h is updated at each simulation iteration using a pseudo-velocity calculated from the previous time step solution vector $\vec{Q}_s$ and respective flux term $F^Q_{j,k+\frac{1}{2}}$.

$$\vec{U}_i^Q = \left| F^Q_{j,k+\frac{1}{2}} / Q_{i-1} \right|. \tag{5.53}$$

For mass conservation, $Q_{i-1} = n_{j,i-1}$; for the energy equation, $Q = \frac{3}{2}\left(n_{bulk,j} k_B T_j\right)_{i-1}$. The element of $\vec{U}_i^Q$ with the largest magnitude is used to calculate the time step based on a Courant relation $h = \frac{1}{2}\frac{dr}{U}$. As risk mitigation for each run, a maximum h, usually 10^{-6} seconds, is specified. At the same time, a minimum h is specified. This protects against early time stepping from driving the simulation to impractical values of h. By monitoring h during a simulation, the general health of the run can be assessed, based on whether h remains between the two limits.

5.2.4 Organization of the Code

The 1D warm plasma model and plasma expansion code are shown graphically in Figure 5-19 and the 1D warm plasma solver is shown graphically in Figure 5-20. Descriptions of individual elements are provided in Tables 5-5 and 5-6.

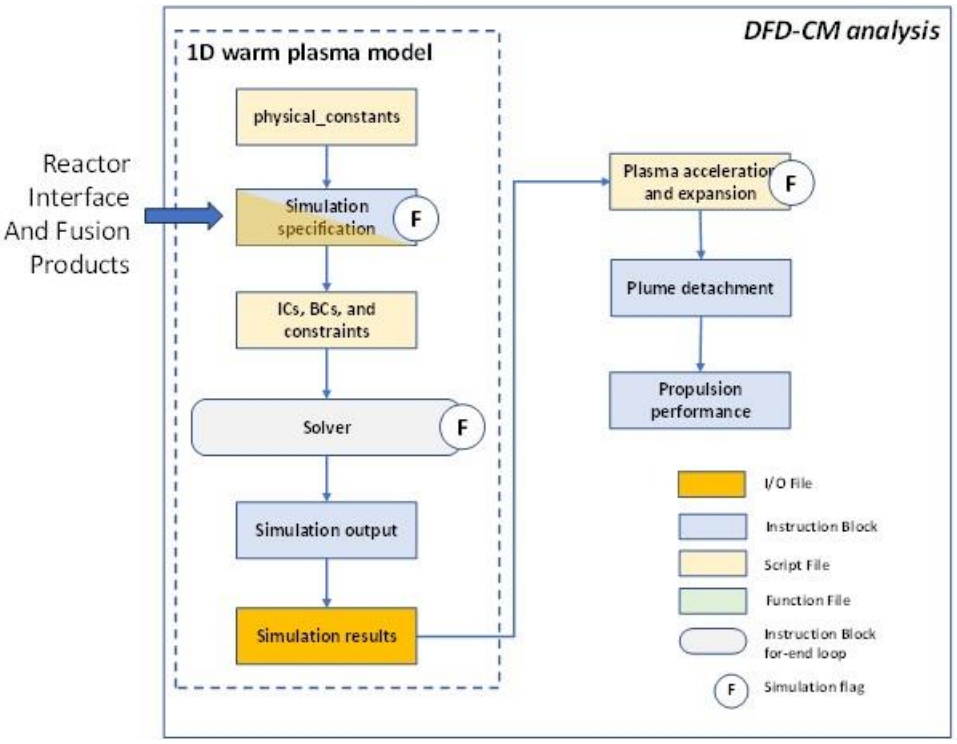

Figure 5-19 – DFD-CM simulation organization

Output from the 1D warm plasma is down-sampled and files with data for warm plasma geometry, simulation time, state properties, and propulsion performance are created. These files are then used as inputs to the plasma acceleration and expansion model. The output files do not include data on transport properties, as old values are discarded at each time step. However, it is possible to run the simulation and in the simulation environment to extract specific transport properties for the final time step. The 1D warm plasma code provides options for reactor flux modeling and propellant feed in the performance specification as discussed in Sections 5.1.3.3 and 5.2.2.3, which are implemented through flags in the code. The propulsion performance can be run with a parametric magnetic nozzle field or one based on a specified geometry using the Biot-Savart law. The propulsion model creates axial profile curves for state properties and other parameters, as well

as values at the exit plane, defined as the point at which $B_x/B_N = 0.001$. Other output includes C_F, integrated values for F_t, P_J and I_{SP}.

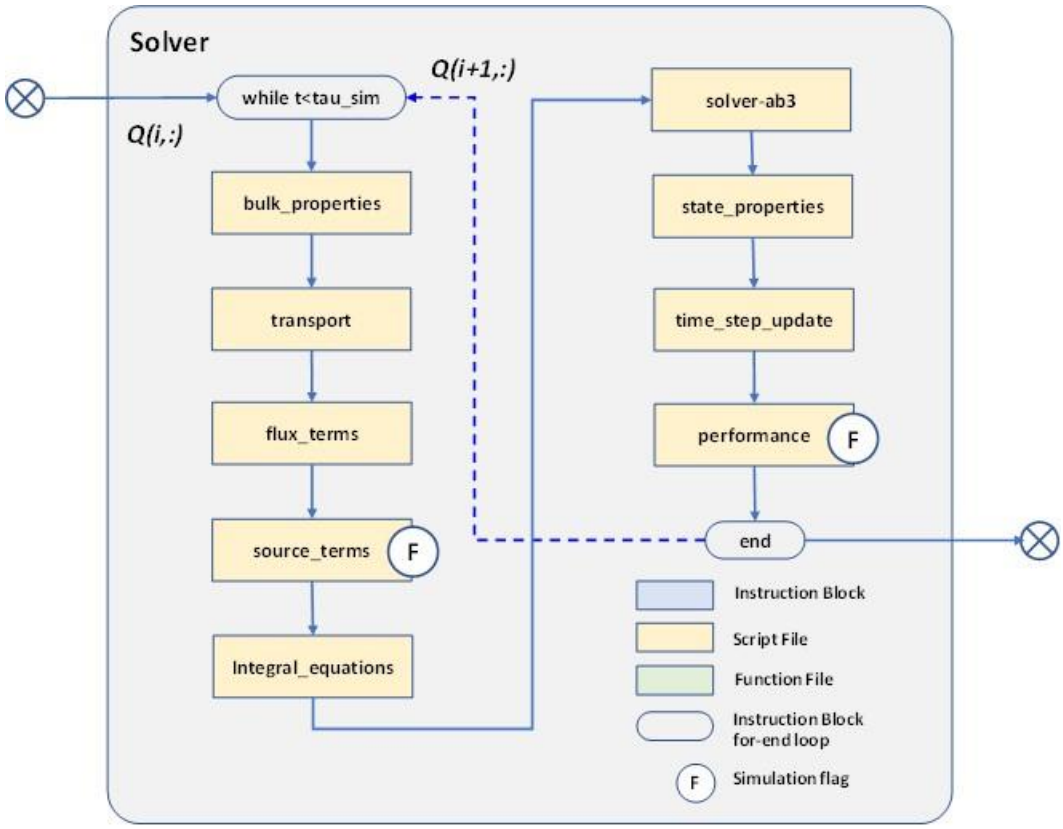

Figure 5-20 – Warm plasma model solver

Table 5-5 – Functional description of main code elements

Element	Type	Function	References
physical_constants	Script File	Defines physical constants	
Simulation specification	Script File	Specifies reactor conditions and output; desired Isp and Ft; warm plasma geometry; simulation parameters	
reactor interface	Script File	Allocates prompt and thermal species to radial distribution based on either "top hat" or psuedo-parabolic profiles	Section 5.2.2.3, Appendix B
Initial conditions	Script File	Based on simulation specification, solves steady state integral equations to generate initiate solution vectors for n^s, Te, Twi, P, p, u_r	Section 5.2.3
Solver	Script File	Solves Equations (5.51) for warm plasma in a while-for marching loop that terminates at specified simuation time	Sections 5.1, 5.2.2, 5.2.3
Plasma acceleration and expansion	Script File	Defines state conditions at magnetic nozzle throat based on warm plasma solution; calculates state and transport properties for annular regions in diverging section of nozzle	Sections 5.1.5, 5.1.6, 5.2.3, 5.3
Plume detachment	Script File	Calculates Co, Rem, St, B at nozzle exit plane and compares results with criteria for detachment	Section 5.1.6
Propulsion performance	Script File	Calculates delivered Ft, Isp, CF, cycle efficiency	Sections 5.1.1, 5.1.5, 5.1.6
Simulation output	Instruction Block	Reads simulation results to csv files	

Table 5-6 – Functional description of solver elements

Element	Type	Function	References
while-end loop	Script File		
transport	Script File	Transport properties as a function of T(r,t) and n(r,T)	Sections 5.2.2.2, 5.2.3
flux_terms	Script File	Mass, momentum, and energy fluxes over surfaces between annular CVs	Sections 5.2.2, 5.2.3
source_terms	Script File	1) Source terms for spatially discretized reactor fluxes and effluent to nozzle; 2) mass and energy deposition within CVs	Sections 5.2.2, 5.2.3
integral_equations	Script File	Time derivatives of form Equation (5.51) for Q[ns, p, Te, Twi]	Sections 5.2.2, 5.2.3.1
solver_ab3	Script File	Solves for Q[ns, p, Te, Twi] using AB3 solver	Section 5.2.3.2
state_properties	Script File	Pressure, density, specific heats for bulk plasma ion and electrons	Sections 5.2.2
time_step_update	Script File	Updates time step h based on flux values from current time step	Section 5.2.3.2
warm_plasma_performance	Script File	Power deposition, jet power, plasma heating, ionization power, etc., as function of time	Section 5.2.5

5.3 System Performance Calculations

5.3.1 Warm Plasma Performance

The integrated power arriving from the reactor P_{in} is found by multiplying the power fluxes for the prompt alphas and thermal species by the projected axial area of each V_k and then summing them. Other components of the power balance are found by multiplying the appropriate source terms by respective control volume V_k and then summing. Propellant heating losses are calculated

by multiplying the source term for ionization by $k_B \Delta T$ for both ions and electrons, given the specified supply temperature T_{n0} of 0.5 eV.

The warm plasma is approximated as a constant volume system, so that energy exchanges are calculated on the basis of internal energy. The approximation is appropriate as a standard control volume analysis, because the confinement time of the warm plasma is normally 2-3 orders of magnitude longer than energy deposition time scales. However, the axial losses to the nozzle are calculated on the basis of enthalpy. At the mirror throat, the pressure in the highly magnetized plasma is isotropic. As provided by [Helander, 2002], the pressure tensor is dependent upon the velocity components of the particles

$$\begin{pmatrix} P_{\parallel} \\ P_{\perp} \end{pmatrix} = \int m \begin{pmatrix} v_{\parallel}^2 \\ v_{\perp}^2 \end{pmatrix} f \, d^3 v. \tag{5.54}$$

For particles within the loss cone, the parallel component will dominate, so that the effective pressure will tend to be aligned along the magnetic lines of force and thus contribute to Pv work during expansion. Given the unit tensor $\bar{\bar{1}}$,

$$\begin{pmatrix} P_{\perp} & 0 & 0 \\ 0 & P_{\perp} & 0 \\ 0 & 0 & P_{\parallel} \end{pmatrix} = P_{\perp}\left(\bar{\bar{1}} - \hat{\boldsymbol{b}} \cdot \hat{\boldsymbol{b}}\right) + P_{\parallel} \hat{\boldsymbol{b}} \cdot \hat{\boldsymbol{b}}. \tag{5.55}$$

Based on these considerations, the enthalpy is taken as the proper basis for the flow leaving the warm plasma.

5.3.2 Propulsion Performance

Section 5.1.5 describes the system of equations used to calculate plasma acceleration and expansion. It is a simple energy balance model that can be closed analytically, unlike solutions

based on the momentum equation, which require numerical integration. The latter calculation is avoided by assuming a constant divergence angle for the plasma expansion. This simplification in fact provides information about the expansion that normally would arise from the momentum equation. However, it comes with the requirement that all the model elements are self-consistent. Specifically, the plasma potential from sheath equation described in Section 5.1.1 would over-predict performance if used in conjunction with the current propulsion model. More appropriate is the model proposed by [Ahedo and Merino, 2015] and [LaFleur, 2015] based on polytropic expansion

$$\frac{T_{ex}}{T_{eN}} = \left(\frac{n_{ex}}{n_{eN}}\right)^{\gamma_{ex}-1}, \tag{5.20}$$

and the specific energy imparted to the ions during expansion is $e\phi_{max}/m_i$, where

$$\frac{e\phi_{max}}{m_i} = \frac{\gamma}{\gamma-1}\frac{k_B T_{eN}}{m_i}\left[1-\left(\frac{n_{ex}}{n_{eN}}\right)^{\gamma_e-1}\right]. \tag{5.56a}$$

In the limit $n_{ex} \to 0$

$$e\phi_{max} = \frac{\gamma}{\gamma-1} k_B T_{eN}. \tag{5.56b}$$

Substituting Equation (5.19) into Equation (5.56b) allows calculation of $e\phi_{max}$ in terms of the warm plasma electron temperature T_{e0}

$$e\phi_{max} = \left(\frac{1}{2} + \frac{\gamma}{\gamma-1}\right) k_B T_{e0}. \tag{5.56c}$$

It should be noted that [Ahedo and Merino, 2015][LaFleur, 2015] take γ to be γ_{ex}, which may be less than 5/3 in practical systems. Equation (5.56c) provides an alternative basis for evaluating the system of equations used in the plasma expansion model.

As discussed in [LaFleur, 2015], experimental measurements show that the sheath equation tends to overpredict the plasma potential. Based on the present research, even the more conservative model provided in Equation (5.56c) may overpredict $|\phi_{max}|$, especially if γ_{ex} is less than 5/3. Therefore, in the propulsion model, the floating potential $\phi_f(z)$ is initially calculated assuming the potential of the warm plasma is zero. Then ϕ_{max} is evaluated at $z \gg z_x$, where z_x is the location of the exit plane defined as the point where $B/B_N = 0.001$. The value $|\phi_{max}|$ is then added to $\phi_f(z)$ As mentioned, this calculation assumes that the vacuum must be ground, so that the warm plasma will assume the value $\phi_p = |\phi_\infty| = |\phi_{max}|$.

5.4 Model Assessment

Preliminary assessment of the 1D warm plasma model and of the plasma expansion model was performed as shown in Table 5-7.

Table 5-7 – Propulsion model assessment

Model	Method of Evaluation
0D Warm Plasma	Comparison with hand calculations and conformance with conservation laws
1D Warm Plasma	Benchmarking with 0D Warm Plasma model; conformance with conservation laws
Propulsion Model	Comparison with hand calculations for 1D plasma acceleration and expansion; consistency and scaling of results with conservation laws

The 0D warm plasma model presented in Section 5.1 was written to provide early assessments of DFD-CM propulsion performance in advance of the 1D model. It is an iterative model which calculates system losses on the basis of a parametric efficiency. In addition to serving that function, it also provided solutions with which results of the 1D model can be compared. This is illustrated in Figure 5-21a, which shows the evolution of a 200 kW transient solution over 200 ms compared with the 0D prediction. Figure 5-21b shows the same comparison with the radial temperature distribution at 200 ms.

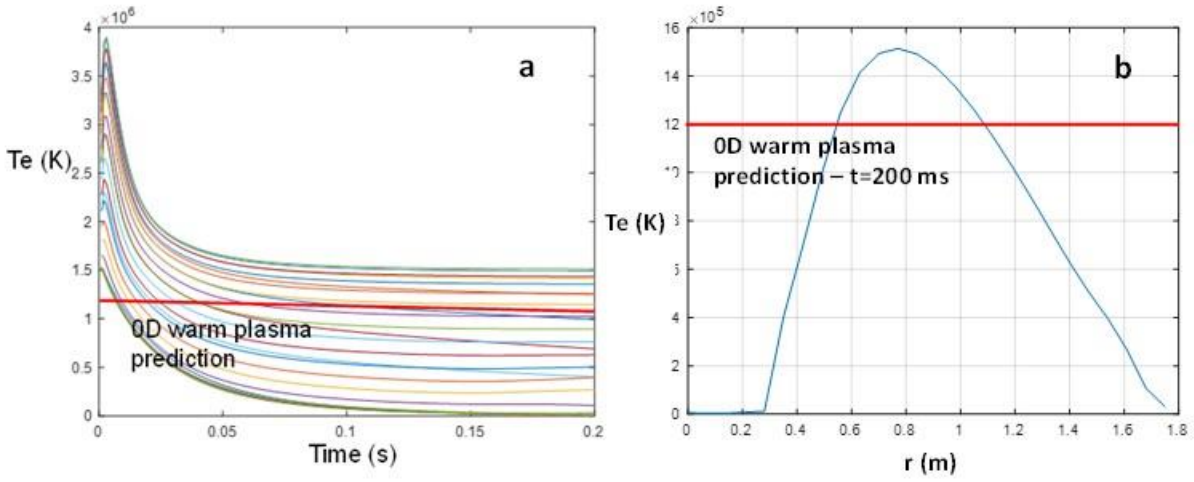

Figure 5-21 – Comparison of 0D and 1D warm plasma model results

The 1D model also has in inherent capability for assessing results. The power deposition that arises from transport calculations can be compared with the sum of system losses calculated by integrating sources terms over the warm plasma volume. This comparison is quantified as Q_{norm}, with typical values of ~ 1.07, which implies a 7 percent error. The evolution of the main components of the power balance for the same case as Figure (5-21) is shown in Figure (5-22). Figure (5-22) also illustrates the utility of risk reduction runs written into the preliminary analysis matrix. The divot in the ionization power curve was ultimately traced to a sign error in the wall losses that remained small up to 300 ms runs, but then ballooned in longer runs.

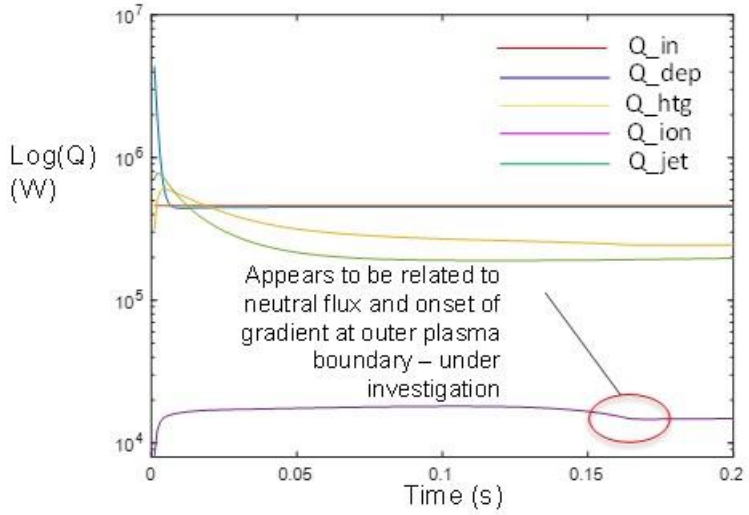

Figure 5-22 – Representative risk reduction run for 1D model

References – Chapter 5

1. Chen, Francis, "Physical mechanism of current-free double layers," Physics of Plasmas, 13, 034502 (2006)
2. LaFleur, T., et al, 2015, "Electron dynamics and ion acceleration in expanding-plasma thrusters," Plasma Sources Sci. Technol. 24 06513
3. Helander, Per, and Sigmar, Dieter, "Collisional Transport in Magnetized Plasmas," 2002
4. Mila-Estrada, C., Candy, J., Waltz, R.E., "Turbulent transport of alpha particles in reactor plasmas," Phys. Plasmas 12, 112303 (2006)
5. Zhang, Y., Charles, C., Boswell, R., "Thermodynamic Study on Plasma Expansion along a Divergent Magnetic Field," Physical Review Letters 116, 025001 (2016)
6. Merino, M., Ahedo, E., "Space Plasma Thrusters: Magnetic Nozzles for," Encyclopedia of Plasma Technology DOI 10.108/E-EPLT-120053936, 2017

7. Deline, C.A., Bengston, R.D., Breizman, B.N., Tushentsov, M.R., Jones, J.E., Chavers, D.G., Dobson, C.C., Schuettpelz, B.M., ”Plume detachment from a magnetic nozzle,” Physics of Plasmas 16, 033502 (2009)
8. Olsen, C.S., Ballenger, M.G., Carter, M.D., Chang-Diaz, F.R., Giambusso, M., Glover, T.W., Ilin, A.V., Squire, J.P., Longmier, B.W., Bering, E.A., Cloutier, P.A., “Investigation of Plasma Detachment From a Magnetic Nozzle in the Plume of the VX-200 Magnetoplasma Thruster,” IEEE Transactions on Plasma Science, Vol. 43, No.1, January 2015
9. Alfvén, H. (1942) “Existence of Electromagnetic-Hydrodynamic Waves. Nature,” 150, 405-406
10. Kuriki, Kyoichi and Okada, Osami, “Experimental Study of a Plasma Flow in a Magnetic Nozzle,” The Physics of Fluids, Volume 12, Number 9, September 1970
11. Merino, M., Ahedo, E., “Plasma detachment in a propulsive magnetic nozzle via ion demagnetization,” Plasma Sources Sci. Technol. 23 (2014) 032001
12. Ilin, A.V., Chang-Diaz, F.R., Squire, J.P., Tarditi, A.G., Breizman, B.N., Carter, M.D., ”Simulation of Plasma Detachment in VASIMR,” AIAA 2002-0346
13. York, T.M., Jacoby, B.A., Mikellides, P., “Plasma Flow Processes Within Magnetic Nozzle Configurations,” Journal of Propulsion and Power, Vol.8, No.5, Sept-Oct. 1992
14. Takahashi, K., Komuro, A., Ando, A., “Operating a magnetic nozzle helicon thruster with strong magnetic field,” Phys. Plasmas 23, 033505 (2016)
15. Little, J., and Choueiri, E., “Divergence pf a Propulsive Plasma Flow Expanding through a Magnetic Nozzle,” IEPEC-2009-260

16. Beiser, A., Raab, B., “Hydromagnetic and Plasma Scaling Laws,” The Physics of Fluids 4 177 (1961); doi. 10.1063/1.1724425
17. Cambel, Ali Bulent, “Plasma Physics and Magnetofluid-Mechanics,” 1963
18. Takahashi, K., Ando A., “Laboratory Observation of a Plasma-Flow-State Transition from Diverging to Stretching a Magnetic Nozzle,” Physical Review Letters 118, 225002 (2017)
19. Breizman, B.N., Tushentsov, M.R., Arefiev, A.V., “Magnetic nozzle and plasma detachment model for a steady-state flow,” Phys. Plasmas 15, 057103 (2008)
20. Longmier, B.W., et al, “Ambipolar ion acceleration in an expanding magnetic nozzle,” 2011 Plasma Sources Sci. Technol. 20 015007
21. Huba, J.D., Naval Research Laboratory Plasma Formulary, 2013
22. Trubnikov, B.A., “Particle Interactions in a Fully Ionized Plasma,” Rev. Plasma Physics I,p105 (1965)
23. Chen, F.F. “Introduction to Plasma Physics,” 1974
24. Bird, R.B., Stewart, W.E.., Lightfoot, E.N., “Transport Phenomena,” 1960
25. Braginskii, S.I., “Transport Processes in a Plasma,” Rev. Plasma Physics I, p205 (1965)
26. Merino, M., and Ahedo, E., “Influence of Electron and Ion Thermodynamics on the Magnetic Nozzle Plasma Expansion,” IEEE Transactions of Plasma Science, Vol 43, No.1, January 2015

6 DFD-CM System Performance

6.1 Technical Approach for End-to-End Analysis

6.1.1 Objectives

The main goal of the end-to-end analysis is to characterize the configuration and performance of a nominal 200 kW jet power, 15000 second specific impulse (delivered) DFD-CM propulsion system. This base case system would operate on hydrogen propellant and be able to send highly capable probes to the outer Solar system with mission durations of 3-5 years, and to the outer edge of the heliosphere in 25-30 years. Five such systems ganged together would deliver a megawatt of jet power for man rated missions to Mars, Jupiter and Saturn. Secondary objectives are: 1) characterize DFD-CM system performance relative to jet power and specific impulse; 2) estimate propulsion performance of concepts based on the model reactors derived in Chapter 4; 3) assess propulsion performance of lower field magnetic nozzles. Tertiary objectives are to assess the performance of selected excursions, including nitrogen propellant and alternate propellant loading schemes.

Results of the performance analysis include two efficiencies, both based on power of the fusion products arriving from the reactor, $P_{IN} = \dot{n}^{\alpha} g_J V_r \left[E^{\alpha} + \frac{3}{2} \xi^{\theta} k_B \left(T_i^{\theta} + T_e^{\theta} \right) \right]$. The warm plasma efficiency η_w, discussed in Section 5.1.1, is calculated from the power flux leaving the warm plasma, and the cycle efficiency η_J from delivered jet power. The two efficiencies are related through $\eta_J = \eta_w \eta_x$, where η_x is the expansion efficiency. In this model, expansion losses result mainly from setting $\gamma_e = 1.33$, and η_x is usually near unity.

6.1.2 Base Case Configuration

Tables 6-1 and 6-2, directly extracted from the input file of the 1D model, summarize characteristics of the reactor and warm plasma used in the base case, Case 1. The reactor is in class with the CH model reactor described in Chapter 4, including the thermal flux $\xi^{\theta} \approx 0.1$. The warm plasma is configured mainly around magnetic field constraints to minimize loss of prompt alphas through the nozzle. The constraints impose a high mirror ratio on the nozzle, which results in a nozzle magnet strength of 10.7 T.

The reactor flux arriving in the warm plasma is modeled on the annular dimensions of the reactor well, as indicated by flag_flux of 2. The propellant loading is a top hat distribution from the forward region of the warm plasma, as indicated by flag_prop of 2.

Table 6-1 - Baseline DFD-CM reactor configuration

Quantity	Symbol	Units	Value
ideal jet power	PJ0	kW	500
thermal flux ratio	ξ^{θ}		0.1
inner radius-plasma column	rir	m	0.1
outer radius-plasma column	ror	m	0.5
length of plasma column	Lr	m	2.7
jet mirror field strength	Bmr	T	13.14
field strength midplane	Bzr	T	8.88
jet side mirror ratio	RmJ		1.48
flux distribution function	flag_flux		2
number density	n0r	1E20/m^3	2
temperature	TeVr	keV	10
ion mass	miar	amu	2.5
ion charge state	Zir		1

Table 6-2- Baseline DFD-CM warm plasma configuration

Quantity	Symbol	Units	Value
ideal specific impulse	Isp0	seconds	30000
propellant ion mass	miba	amu	1.008
propellant ionization state	Zi		1
propellant ionization energy	e_ion	eV	13.595
propellant dissociation cross-section	sigma_d	m^2	1.00E-23
propellant supply	flag_prop		2
Outer radius of plasma column	ro	m	1.75
Length of plasma column	L	m	4
Field strength midplane	Bz	T	0.725
Nozzle mirror field strength	BN	T	10.708
Reactor flux efficiency	η_{flux}		0.92
Magnetic nozzle mirror ratio	RmN		14.769

Modeling of acceleration and expansion of the plasma includes specified values for beam divergence angle $\theta_P = 0.045$ radians, based on nominal Mach numbers in the far field; and $\gamma_e = 1.33$, based on representative values from the literature. Unless otherwise stated for a given case, these values are used throughout the analysis.

6.1.3 Methodology

Chapters 3 and 5 described the models developed to perform the DFD-CM system analysis. The resulting code base implemented in MATLAB is

- DFD-CM 0D Reactor Model (dfdcm_r5a)
- DFD-CM Propulsion Model
    - Warm Plasma Model (dfdcm_propulsion_r3) – includes Reactor-Propulsion Interface
    - Plasma Acceleration and Expansion Model (dfdcm_propulsion_performance_r2a)

The relationship among the models and the flow of data are shown in Figure 6-1. Cases for the warm plasma model were run on three instances of dfdcm_r3.m on the University of Maryland

Zaratan High Performance Computing Cluster (HPC). Data from the warm plasma model runs are down-sampled by a factor of 1000 in the output files, which are then used by the propulsion model.

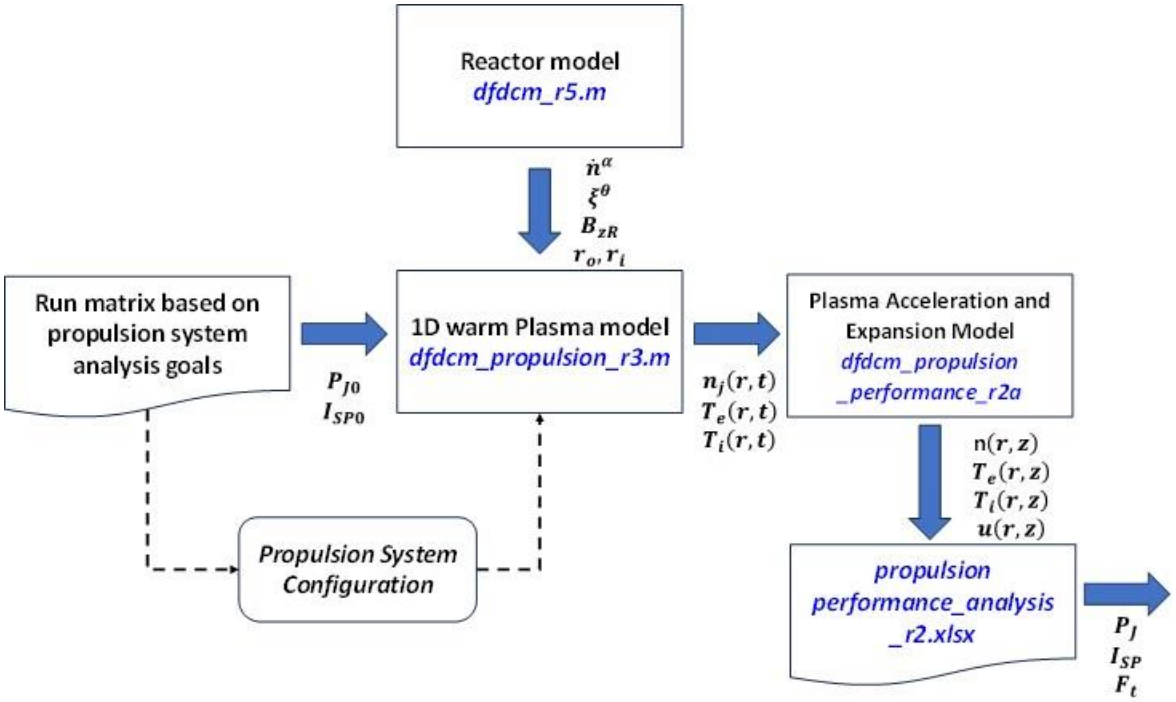

Figure 6-1 – Analytic process and data flow

Table 6-3 is the run matrix for the system performance analysis. The run matrix includes estimates for confinement time in the warm plasma. The confinement time for each annular control volume V_k is calculated $\tau_{conf\ k} = V_k/u_{zk}A_{zk}$, where u_{zk} is calculated from Equation (5.13). Confinement times for V_k vary within an order of magnitude for any given case, and the mean confinement time across all k is calculated for each time step. This quantity is a good metric for assessing the length of the simulation time relative to residual transient effects. Ideally, simulation times would be long enough to reach the steady-state solution, nominally 3-5 confinement times. However, runs were limited to 1-2 confinement times, in part because of wall time limits on Zaratan HPC, and in part

for reasons of practicality. Therefore, there is transient error in the results in addition to a base $O(\Delta x^2)$ discretization error.

Table 6-3 - Propulsion system performance run matrix

Case		Propulsion Performance					Run Time Analysis		
		Delivered (est)		Ideal		Rationale	tau_conf (Est)	tau_sim	
		PJ	Isp	PJ0	Isp0				
FN	Pri	kW	s	kW	s		ms	tau_conf	s
1	High	250	15000	500	30000	Base case for man-rated systems H2 propellant - high RmN	201.6	2	403.2
2, 2b, 2c, 2d	Med	250	15000	500	30000	N2 propellant - high BN; varyiing Zi=1-4	200	1	200
2a	Med	250	6250	500	12500	N2 propellant - high BN; Zi=1	200	1	200
3	Med	250	15000	500	25000	Circumferential propellant loading - baseline case 5	201.6	1	201.6
4	High	250	15000	500	30000	Assess effects of varying specific impulse on performance and operability	201.6	1	201.6
5	High	250	12500	500	25000		220.0	1	220
6	High	250	10000	500	20000		242.0	1	242
7	Med	250	7500	500	15000		268.9	0.8	215.1
8	High	125	12500	250	25000	Assess effects of varying jet power on performance and operability	242.0	1	242
9	High	250	12500	500	25000		242.0	1	242
10	High	375	12500	750	25000		242.0	1	242
11	Med	500	12500	1000	25000		242.0	0.8	193.6
12	Med	250	15000	500	25000	Assess effect of varying warm plasma volume	201.6	1	201.6
13	Low	250	15000	500	25000		201.6	1	201.6
14,15	Not Used								
16	Low	121.5	12500	243	25000	CH model reactor	302.4	1	302.4
17	Med	124.5	12500	249	25000	NH model reactor	302.4	1	302.4
18	Med	121.5	12500	249	25000	Assess effect of thermal PV carry into warm plasma - Case 17 baseline	302.4	1	302.4
19	Low	100	12500	500	25000	Lower BN	50.0	2	100
20	Med	100	6250	500	12500	Lower BN	100.0	1	100

As discussed in Section 5.4, the results of the code can be used to assess the transient error. The integrated power deposition rate is calculated based on the thermalization of the fusion products in the warm plasma, while the individual constituents of the balance, i.e. ionization losses, are

calculated from source terms in the warm plasma. In steady-state, these two quantities should be the same, so that any difference indicates that the solution is transient. Analysis of several cases shows that the difference, or error, drops significantly after one confinement time to a value ranging from 6 to 8 percent. Assuming a nominal discretization error of 0.5 percent, solutions are taken to be quasi-steady-state with nominal transient error. In general, higher specific impulse and lower jet power cases have smaller errors, while lower specific impulses and higher jet powers have larger ones. The largest source of transient error appears to be the number density of the ionized propellant, which must increase from initial conditions, while temperatures decrease. This behavior results from Equation (5.13), which limits flow from the warm plasma. For specified I_{SP0}, the resulting mass flow rate does not change for the run. As ion and electron temperatures decrease from initial values, the flow and number density of ions must increase to maintain conservation of energy. In most solutions, the number density of the propellant does not fully reach steady-state, even if temperatures do.

6.2 Results

6.2.1 Base Case

6.2.1.1 State properties

The simulation time for Case 1 was 400 ms, or 1.69 confinement times, for a mean confinement time of 237.8 ms over warm plasma radius *r*. The value $\bar{Q} = \sum Q_j / Q_{dep} = 1.065$, where Q_j are the respective losses in the warm plasma at the final time step. The solution is taken to be quasi-steady-state, and steady-state electron temperature and ion number density of the warm plasma are the principal determinants of delivered jet power. Figure 6-2 shows ion and electron temperature over the plasma radius of 1.75 m for Case 1. The profile results from the annular flux of power from prompt and thermal species arriving from the reactor. Figure 6-3 shows the number densities

of the respective ion species. Toward the center of the annulus where temperatures are highest, the flux of particles leaving the plasma is higher because of the relatively higher Bohm velocity downstream of the nozzle. As a result, number densities of the propellant and neutrals tend to be a bit higher near the centerline and the outer plasma surface. Otherwise, the profiles of the prompt alphas and thermal species, as well as that of the thermalized deuterium and tritium appear to track with the flux from the reactor.

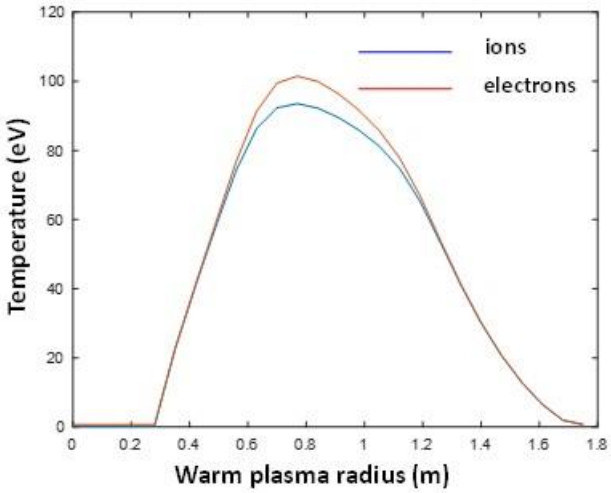

Figure 6-2 – Warm plasma temperature profile (eV) – Case 1

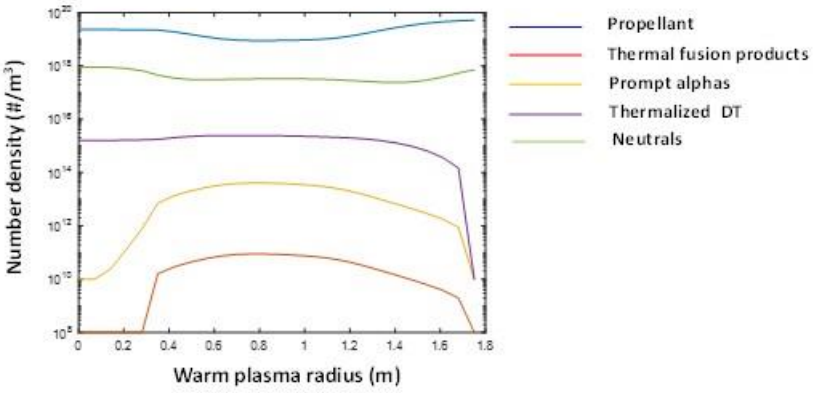

Figure 6-3 – Warm plasma number density profile (#/m^3) – Case 1

6.2.1.2 Transport

Electrons are the main channel by which fusion energy is deposited in the warm plasma. The electrons then transfer a portion of their energy to the propellant ions. This is essentially a two-step process, since other interactions do not greatly contribute to the energy transfer. Figure 6-4 shows the distribution of collision times for α–e, α–β, and e-β interactions. The α–β interaction times are very long, which is generally the case with other interactions. However, the α–e, and e-β interactions are rapid, $O(10^{-4}\ to\ 10^{-3})\ s$. As can be seen in Figure 6-2, electron and ion temperatures nearly in equilibrium. This is because of the scale of the interaction times. Early in the evolution of the transient simulation, $T_e \gg T_i$.

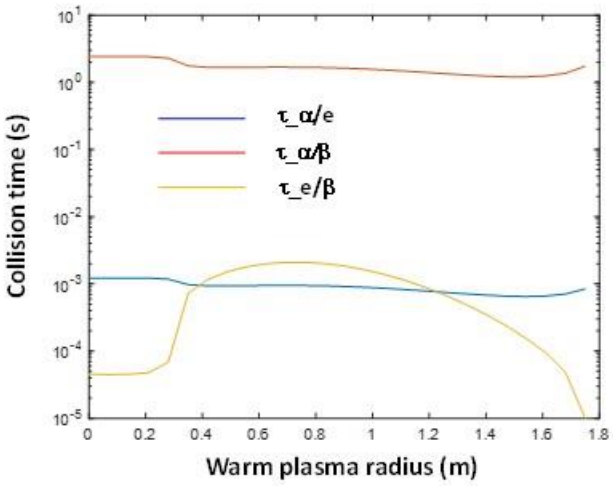

Figure 6-4 – Interaction times in warm plasma – Case 1

Diffusive transport follows from the number densities of the species and their respective ambipolar coefficients of diffusivity, shown for the ion species as a function of radius in the warm plasma in Figure 6-5. The prompt alphas display higher diffusivity despite their higher quasi-Maxwellian temperature. This is the result of their larger Larmor radii. The thermal species from the reactor

and thermalized D-T have very similar values for diffusion coefficients, because they are both modeled at having masses of 2.5 amu. Given that, their profiles are so close that they lie on top of each other. As discussed in Section 5.2.2.2, the diffusivity coefficient for the neutrals is taken to be constant $10\ m^2/s$. Figure 6-3 shows that at 1.68 confinement times, the density of propellant and neutrals are tending toward a relatively flat profile, the slight increase at the centerline and outer plasma notwithstanding. The prompt and thermal products arriving from the reactor are diffusing outward from the annulus, but appear to be thermalized and so contribute to the population of thermalized deuterium and tritium. The latter three species, being relatively low density, appear to be rapidly depleted at the outer plasma by wall losses.

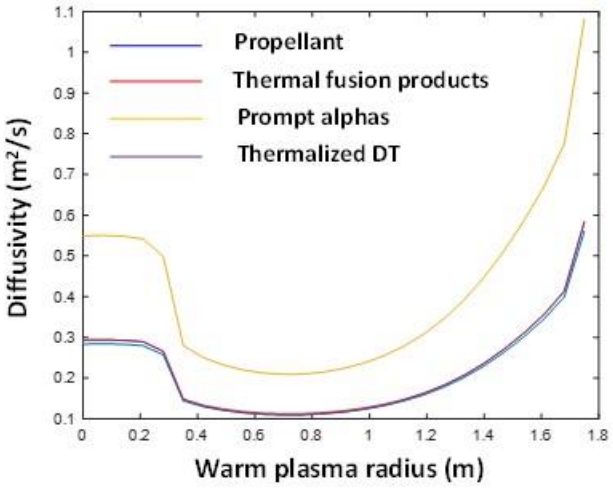

Figure 6-5 – Ambipolar diffusion coefficients in the warm plasma (m^2/s) – Case 1

Radial profiles for thermal conductivity for ions and electrons are shown in Figure 6-6. The thermal conductivity for the ions is much higher than that of the electrons. Since Figure 6-2 indicates that the ions and electrons are almost in thermal equilibrium, it can be inferred that energy deposition into the annulus of the warm plasma is much more rapid than heat conduction out of it.

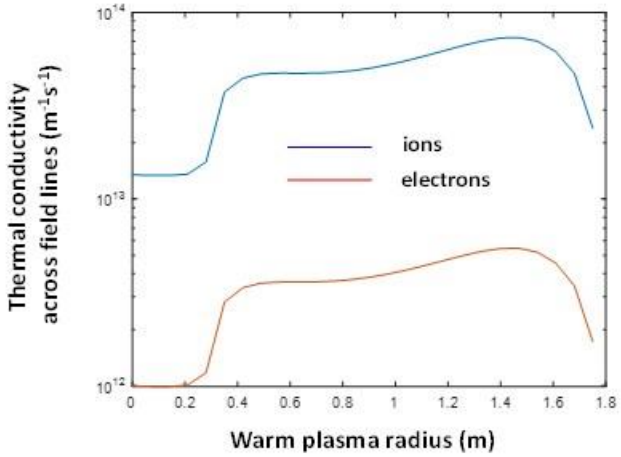

Figure 6-6 – Thermal conductivity of electrons and ions in the warm plasma ($m^{-1}s^{-1}$) – Case 1

The dynamics of neutrals in the warm plasma are illustrated in Figure 6-7 showing the time evolution of their number density over the warm plasma radius. The local peaks at all radii at about 150 ms indicate the maximum density of the neutrals prior to ionization and diffusive processes becoming dominant. The higher peaks are at the outer plasma where temperatures and electron velocities are lower. The propellant loading scheme is a constant, top-hat distribution from the front of the warm plasma. The radial distribution is bounded by the radius of the LGFS of the warm plasma, consistent with a square-well approximation. The propellant loading model is discussed in Appendix B. The local peaks at 150 ms appear as inflections in transient curves for heating and ionization losses.

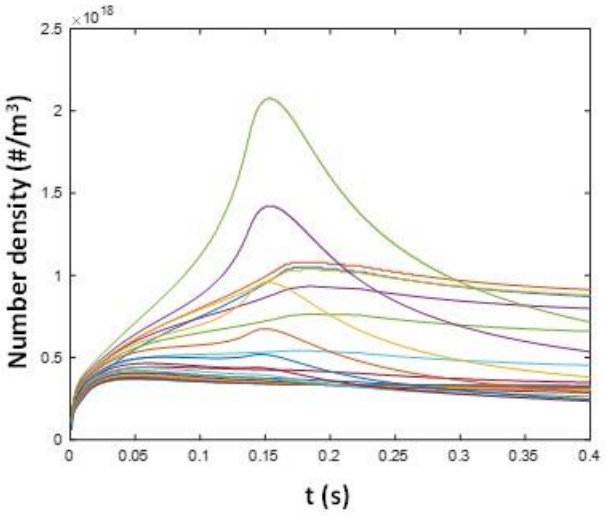

Figure 6-7 – Time evolution of neutrals in the warm plasma – Case 1

6.2.1.3 Propulsion performance

The largest losses in the warm plasma are from propellant ionization and heating, as shown in Table 6-4. At 400 ms confinement time, 452 kW are deposited into the warm plasma, as compared with 459.9 kW entering the warm plasma CV. In all, ~500 kW P_{IN} arrive from the reactor, but 40 kW are lost due to low pitch fusion products departing through the nozzle loss cone without interacting with the warm plasma. 32 kW are lost due to combination of wall losses, charge exchange, and radiation. The power flux leaving the warm plasma for the nozzle is 263 kW for a warm plasma efficiency of 0.526. Table 6-5 summarizes propulsion performance for Case 1. The state properties shown are along the center of the warm plasma annulus. The overall cycle efficiency is 0.491, given η_w and expansion efficiency of 0.93.

Table 6-4 – Warm plasma integrated power and loss stack up – Case 1

tau_sim	ms	400
tau_conf	ms	237.8
	norm	1.696
Q_in	kW	459.9
Q_dep	kW	453.6
Q_wall	kW	0.5
Q_cx	kW	20.2
Q_rad	kW	1.7
Q_ion	kW	19.4
Q_htg	kW	178.3
Q_jet_wp	kW	263.0
ηw		0.526
Q_norm		1.065

Table 6-5 - Propulsion performance – Case 1

Case	Ideal Performance		Warm Plasma		Delivered Performance				
	PJ0	Isp0	n^{β}	Te	Cf	Ft	Isp	PJ	η_J
	kW	s	$\#/m^3$	eV		N	s	kW	
1	500	30000	8.87×10^{18}	99.9	0.484	2.218	18828.8	245.37	0.491

Figure 6-8 shows plasma temperature for the annulus center along the expansion axis z. The zero position is the exit of the nozzle magnet. The lower rate of decrease for electron temperature is due to a specified $\gamma_{ex} = 1.33$, reflecting an assumed loss of adiabaticity in expansion. Figure 6-9 is the plasma floating potential for the annulus center along z. The warm plasma potential is 242.4 V which for a $T_e/2$ drop at the presheath results in a potential of 192.4 V in the vicinity of the nozzle mirror.

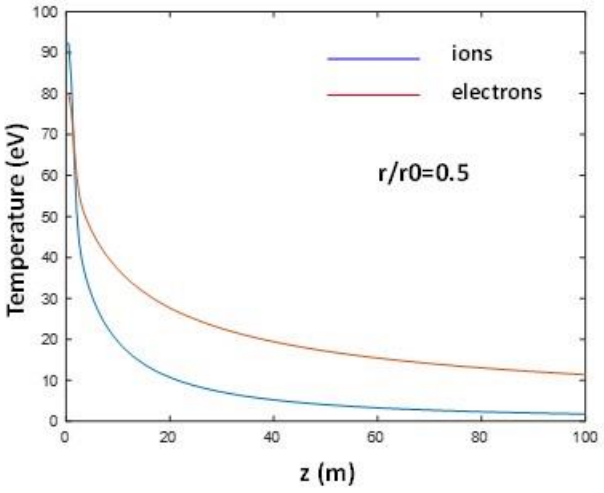

Figure 6-8 – Plasma temperature along axis of expansion – Case 1

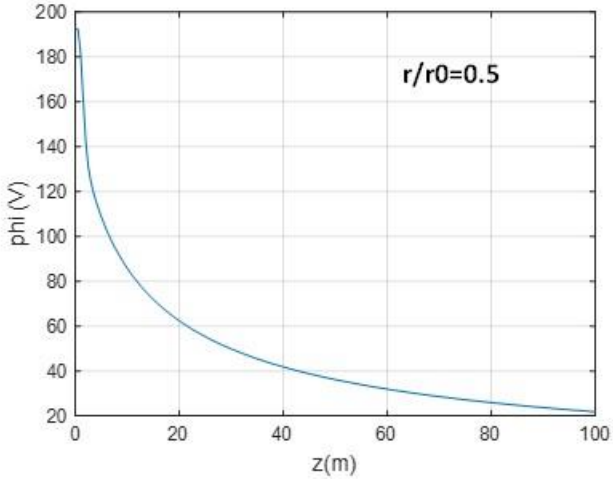

Figure 6-9 – Floating potential along expansion axis (V) – Case 1

Plasma velocity is shown in Figure 6-10. Figure 6-10a shows U_x for all stream tubes $U_x(\psi, z)$, while Figure 6-10b shows the radial distribution for $U_x(r)$ at nominal electron separation, $z = 70\ m$. The highest velocities are near the center of the annulus, and the lower velocities are near the centerline and outer plasma edge. The axial location for ion detachment is shown as the blue

line, indicated by a Cowling number on the center annulus of one, per Table 6-6. The red line is where the Hall parameter for electrons drops below 10 and so is within an order of magnitude of the ideal value of 1. While ion detachment is indicated, detachment of the electrons is less clear. The Hall parameter of a species indicates its degree of magnetization, and analysis suggests, on that count, electrons could be detaching. However, the magnetic Reynolds number remains well above 10^3, even in the far-field. Additionally, the location suggested by the Hall parameter is well downstream of that for ion detachment. It is uncertain whether these results follow from the relative coarseness of the analysis, or whether they reflect a valid, physical finding. If the latter, it is possible that electron temperatures of 100 eV in the warm plasma may be too high to allow electron detachment.

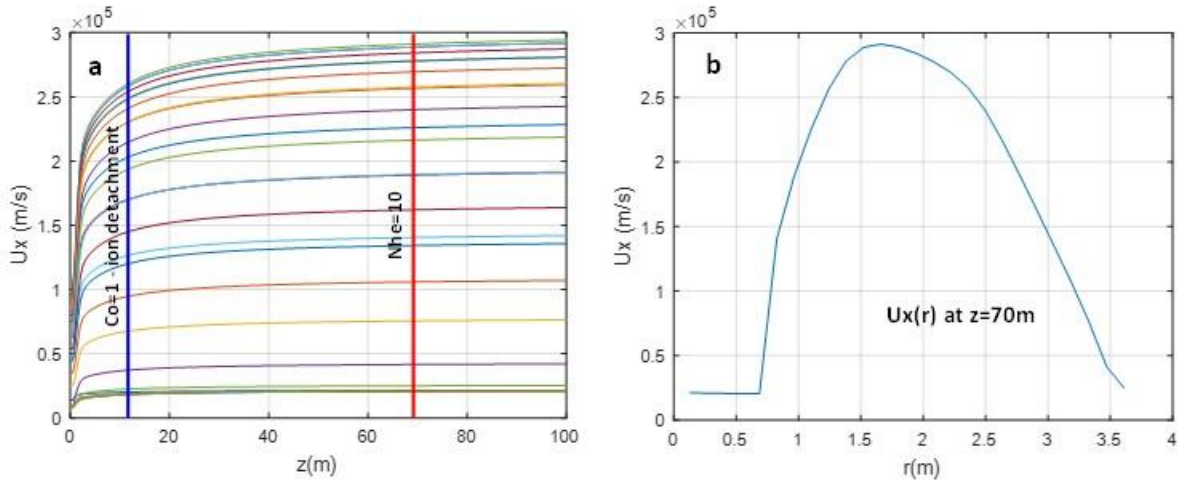

Figure 6-10 – Plasma velocity U_x – Case 1

Table 6-6 – Plasma detachment parameters – Case 1

Axial Location (z) Critical Mid-Chord Plasma Parameters		
Co=1	Rem=10^2	NH=10^1
m	m	m
13.07	NA	70.35

6.2.2 Sensitivities to Jet Power

Ideal jet power P_{J0} was varied from 250 kW to 1 MW while holding ideal specific impulse I_{SP0} constant at 25000 s. The results are summarized in Table 6-7. Plasma number density increased with jet power, but electron temperature did not vary significantly. Losses in the warm plasma scaled proportionally with ideal jet power, but overall warm plasma efficiency showed only slight sensitivity with nominal $\eta_w \sim 0.5$. Mean confinement times over the warm plasma radius ranged from 227 to 288 ms, increasing with jet power. Thrust coefficients, delivered specific impulse, and overall cycle efficiency showed little sensitivity to P_{J0}. At higher jet powers, the point at which the plasma reached the Cowling number of 1 is a little closer than in Case 1, but overall values for detachment parameters in Cases 8-10 were about the same as in Case 1. Cycle efficiencies improved nominally with increasing jet power, likely due to higher number densities and attendant improvements in transport. Note that Case 11 was run for shorter simulation time, because of wall time constraints, and the values for η_J, n^β, and C_f shown likely include larger transient errors.

Table 6-7 – Propulsion performance – Cases 8-11

Case	Ideal Performance		Warm Plasma		Delivered Performance				
	PJ0	Isp0	n^β	Te	Cf	Ft	Isp	PJ	η_J
	kW	s	#/m^3	eV		N	s	kW	
8	250	25000	7.80×10^{18}	67.2	0.806	1.192	16895.9	113.78	0.455
9	500	25000	1.60×10^{19}	66.2	0.807	2.407	17114.1	232.06	0.464
10	750	25000	2.46×10^{19}	65.8	0.810	3.663	17285.0	354.61	0.473
11	1000	25000	3.23×10^{19}	66.1	1.008	4.655	18086.7	461.52	0.461

6.2.3 Sensitivities to Specific Impulse

Specific impulse appears to be the primary determinant of both plasma temperature and number density. The propellant bypass ratio ξ^{β} scales inversely with specific impulse, so propellant flow is higher at lower specific impulses. At high specific impulse, number density is low and temperature is high, for a given jet power. These trends are shown in Table 6-8. Various runs indicate that there is a minimum specific impulse for the warm plasma, somewhere between 10000 and 15000 seconds. This contention is based on the observation that plasmas appeared to quench near the outer plasma at these specific impulses. The cycle efficiencies are essentially constant for Cases 4-6, but then drops for Case 7. This appears to be an artifact of the simulation. Case 7 is a low specific impulse, which is computationally expensive for the 1D warm plasma model. Accordingly, Case 7 was run for shorter simulation time, which appears to have resulted in a relatively large transient error possibly contributing to the lower cycle efficiency.

Table 6-8 – Propulsion performance – Cases 4-7

Case	Ideal Performance		Warm Plasma		Delivered Performance				
	PJ0	Isp0	n^{β}	Te	Cf	Ft	Isp	PJ	η_J
	kW	s	$\#/m^3$	eV		N	s	kW	
4	500	30000	8.85×10^{18}	99.5	0.771	1.976	20648.5	229.18	0.458
5	500	25000	1.69×10^{19}	66.3	0.857	2.363	17413.8	229.50	0.459
6	500	20000	3.28×10^{19}	41.6	0.965	2.949	14016.3	229.78	0.460
7	500	15000	7.54×10^{19}	23.0	1.473	3.484	11159.7	208.68	0.417

6.2.4 Model Reactors

Table 4-9 provides configurations for four model reactors extracted from the 0D reactor model. Most propulsion system cases summarized in Table 6-3, including Case 1, are in class with the CH

model reactor, but there are some differences in magnetic field or other characteristics. Case 16 and 17 are the model reactors, themselves, and characteristics are specified in the propulsion system analysis per Table 4-9. The ξ^{θ} for NH is 5.87. However, because ξ^{θ} much above 1 tends to drive longer wall times, for Case 17, it is set at 2. This change decreases estimated P_{J0} leaving the reactor from about 256 kW to 253 kW. Additionally, Cases 16 and 17 are run with smaller warm plasma volume (29 m^3 vs.38 m^3) consistent with smaller P_{J0} and desire for more compact systems.

The purpose of running Cases 16 and 17 is to show that the more detailed reactor models CH and NH support a viable propulsion system. At the same time, they provide a benchmark for other 250 kW P_{J0} class cases and show that despite some differences in configuration, the respective cases return consistent results. Table 6-9 summarizes Cases 16 and 17 along with Case 8 as a baseline. The higher nozzle mirror ratios in Cases 16 and 17 tend to confine the warm plasma more, so the propellant number densities are slightly higher. The smaller volume results in a lower confinement time. Overall, all the three systems provide very similar propulsion performance.

Table 6-9 – Model reactor characteristics

Case	Ideal Performance		Warm Plasma					Delivered Performance			
	PJ0	Isp0	BN	RmN	τ_conf	n^{β}	Te	Ft	Isp	PJ	η_J
	kW	s	T		ms	$\#/m^3$	eV	N	s	kW	
8	250	25000	10.71	14.769	226	7.80×10^{18}	67.2	1.19	16896	113.78	0.455
16	243	25000	7.915	13.126	124.6	5.32×10^{18}	71.9	1.121	17970	110.6	0.450
17	249	25000	10.63	16.77	139	9.69×10^{18}	64.6	1.129	18915	113.99	0.450

6.2.5 Alternate Warm Plasma Magnetic Field Configurations

The baseline magnetic field configuration from Case 1 is robust. It provides attractive performance for varying combinations of P_{J0} and I_{SP0}. In particular, it limits direct loss of fusion energy through the nozzle loss cone to 8 percent. However, the 10.71 T field in the nozzle magnet is a significant mass driver. A lower field nozzle would be advantageous for overall system mass, but at the expense of performance. Table 6-10 summarizes the characteristics and performance for two configurations based on a 5.21 T nozzle mirror, Case 19 with ideal I_{SP0} of 25000 s, and Case 20 with ideal I_{SP0} of 15000 s. The baseline is Case 5, with I_{SP0} of 25000 s and P_{J0} 500 kW. The outer plasma radius for Cases 19 and 20 is 2.25 m, vs.1.75 for the baseline case. Together with the lower B_N, this reduces η^{α} to 0.9 for both Cases 19 and 20, vs. 0.92 for the baseline.

Table 6-10 – Low nozzle mirror strength configurations

Case	Ideal Performance		Warm Plasma					Delivered Performance			
	PJ0	Isp0	BN	RmN	τ_conf	n^{β}	Te	Ft	Isp	PJ	η_J
	kW	s	T		ms	#/m^3	eV	N	s	kW	
5	500	25000	10.71	14.77	255.2	1.60×10^{19}	66.3	2.363	17414	229.5	0.459
19	500	25000	5.21	11.87	186.1	5.65×10^{18}	69.5	2.285	17125	219.7	0.439
20	500	15000	5.21	11.87	224.9	3.04×10^{19}	22.6	3.53	10574	204.6	0.409

For Case 19, propellant number density in the warm plasma is half that of Case 5. A slightly higher electron temperature and much shorter confinement time appear to offset the lower density, so that delivered jet power and cycle efficiency are only slightly less than the base case. For Case 20, with the much lower I_{SP0} of 15000 s, however, number density and thrust are higher than those of Case 5. The delivered specific impulse is only 10574 s. Note that Case 20 was run for 100 ms simulation time, which is less than one-half the confinement time, so that it is likely that Case 20 includes a relatively large transient error.

Early trials with lower B_N suggest there is a minimum operable nozzle mirror ratio. One preliminary case with an R_{mN} of about 6 demonstrated an extremely low confinement time and cycle efficiency of 10 percent. The low mirror ratio was allowing plasma to flow through the nozzle without sufficient heating. Cases 19 and 20 indicate that R_{mN} midway between 6 and the baseline case are viable. This potentially represents an important trade off in any practical design, specifically the mass associated a 50 percent reduction in field strength for the nozzle mirror vs. an 11 percent reduction in jet power.

6.2.6 Excursions

6.2.6.1 Propellant loading

All cases except Case 3 were run with top-hat, axial propellant loading from the front of the warm plasma. Case 3 is an excursion to evaluate circumferential loading. It is assumed that the neutrals enter at 0.5 eV, and that they penetrate the warm plasma at the associated Bohm velocity based on the expected behavior of a jet entering a new media. The code expresses penetration as a fraction of the radius, which then defines a region of propellant loading. Taking this fraction to be 0.1 results in a very high loading near the wall. In this case, diffusive processes do not transport the neutral and ionized propellant rapidly enough. Neither is radial momentum sufficient to fill the core plasma. Accordingly, the core plasma is less dense and heated to extremely high temperatures. This in turn tends to evacuate the core due to higher associated Bohm velocity downstream of the nozzle.

If the limiting time for penetration is taken to be on the order of a representative ion collision time, $O(10^{-2})$, the jet would traverse the entire radius. Case 3 assesses a situation between these two situations, with a specified penetration length of 0.67 of the warm plasma radius. Table 6-10 shows

the characteristics of the Case 3 configuration compared to Case 5. Figure 6-11 shows the radial distribution of number densities for respective species in the warm plasma.

Table 6-11 – Circumferential propellant loading – Case 3

Case	Ideal Performance		Warm Plasma			Delivered Performance			
	PJ0	Isp0	τ_conf	n^{β}	Te	Ft	Isp	PJ	η_J
	kW	s	ms	#/m^3	eV	N	s	kW	
5	500	25000	255.2	1.60×10^{19}	66.3	2.363	17414	229.5	0.459
3	500	25000	144.2	2.97×10^{17}	2881	1.744	14916	186.0	0.372

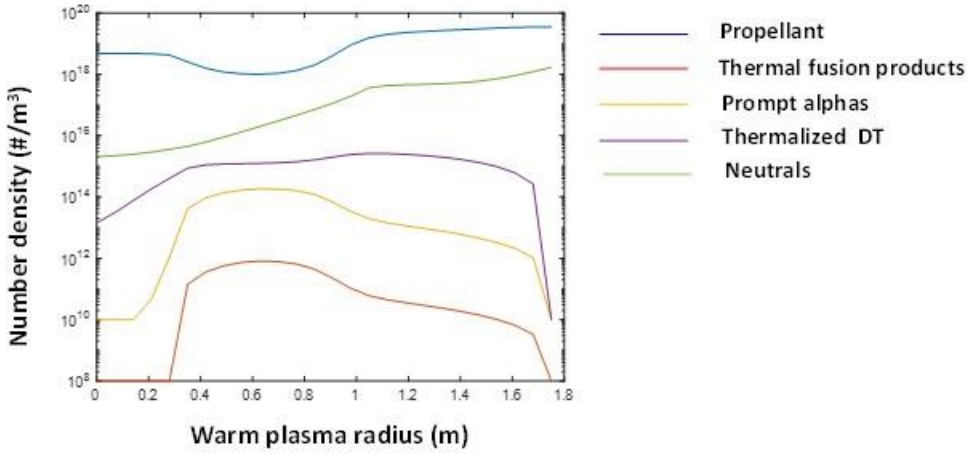

Figure 6-11 - Warm plasma number density profile (#/m^3) – Case 3

Table 6-11 shows that the number density of the propellant species at mid-radius is two orders of magnitude less than that of Case 5, while the electron temperature is much higher. The number density profiles in Figure 6-11 bear this out. It can be seen that neutral density decreases toward the centerline, a consequence of the circumferential fueling scheme. Similarly, the number density of the ionized propellant decreases toward the centerline. Even with the log scale in Figure 6-11, it can be seen that both species crowd the outer plasma. With the reduced number density at the

core of the plasma, power deposition from the fusion products heats the electrons and propellant to extremely high temperatures. As a result, the plasma experiences very high gradients in state properties and potential in the radial direction. Although the integrated jet power and thrust are comparable to the baseline Case 5, the cycle efficiency is 19 percent lower. It is uncertain whether these gradients would relax over time. The operative dynamic would be the rate of axial convection of particles leaving the warm plasma to their rate of radial diffusion into the core where they could interact with the fusion products. It appears then that a circumferentially loaded propellant would require more time to equilibrate. The results of Case 3 then provide some insight into potential issues with such a scheme, but probably do not provide a complete picture.

6.2.6.2 N2 propellant

Case 2 was run with the same ideal P_{J0} and I_{SP0} as Case 1, but with nitrogen propellant. The charge state of the ionized propellant was set to $Z_i = 1$ .The larger propellant mass had a major effect on the behavior and performance of the warm plasma and plasma expansion. For an ideal I_{SP0} of 30000 s and P_{J0} of 500 kW, the mass flow rate is 1.16×10^{-6} kg/s. For nitrogen, this results in a very low ξ^{β}, about 600. Transport is therefore highly constrained, with fusion power deposition going entirely to the electrons. This can be seen in Table 6-12. The number density of propellant species for Case 2 is an order of magnitude lower than that for Case 1, while the electron temperature for Case 2 is almost two orders of magnitude higher.

Case 2a was run with N2 propellant, 500 kW P_{J0}, and 12500 s I_{SP0}. As with Case 2, the propellant charge state was set to $Z_i = 1$. The lower specific impulse increases ξ^{β} to about 1400, still low compared to hydrogen systems. The Case 2a propellant number density is an order of magnitude higher than Case 2, but the electron temperature is much lower. The delivered specific impulse for

Case 2a is 9692 seconds with a thrust of 5.16 N. Overall, Case 2a delivers 34.5 percent more jet power than Case 2. With the relatively low values of ξ^{β}, losses due to ionization and charge exchange are lower than hydrogen systems. Even propellant heating is somewhat lower than hydrogen systems, because of the lower specific heat of the nitrogen propellant.

Based on the plasma temperatures in Cases 2 and 2a, it is likely that the charge state of the propellant will be greater than $Z_i = 1$. Therefore, Cases 2b-2d were run for $P_{J0} = 500\ kW$, $I_{SP0} = 30000\ s$ with parametric charge states 2,3 and 4. It can be seen that electron temperature and delivered specific impulse decreased with increasing charge state. For the specified P_{J0} and I_{SP0} in Cases 2b, 2c, and 2d, the mass flow rate and ξ^{β} are the same. However, with decreasing T_e, the Bohm velocity in the vicinity of the nozzle throat will be lower. This results in increasing propellant number density in the warm plasma. The increased charge state has a marked effect on delivered jet power and cycle efficiency. The power leaving the warm plasma is comparable with that of Cases 1 and 2, but more of that energy is being carried by the electrons. The ions remain cold, which lowers delivered thrust and jet power.

Table 6-12 – Propulsion performance for N2 propellant systems – Cases 2, 2b-2d, 2a

Case	Ideal Performance		Warm Plasma State			Delivered Performance			
	PJ0	Isp0	n^{β}	Te	Zi	Ft	Isp	PJ	η_J
	kW	s	$\#/m^3$	eV		N	s	kW	
1	500	30000	8.87×10^{18}	99.9	1	2.218	18828.8	245.37	0.491
2	500	30000	2.24×10^{17}	6537.0	1	1.875	19587	195.50	0.391
2a	500	12500	7.87×10^{18}	408.6	1	5.157	9692	262.91	0.525
2b	500	30000	6.74×10^{17}	1623.4	2	1.589	17995.6	149.09	0.298
2c	500	30000	1.03×10^{18}	1099.2	3	1.706	14961.8	135.26	0.270
2d	500	30000	1.53×10^{18}	873.7	4	1.872	13618.4	135.52	0.271

Figure 6-12 shows maximum ion and electron temperatures during plasma expansion for Cases 2 and 2a. Figure 6-13 shows the potential vs. z at $r/r_0 = 0.5$ for the two cases. The plasma potential for Case 2 is estimated at 4982 V, about half the sheath potential value of 9500 eV, so consistent with observations by [LaFleur, *et al*, 2015]. Given the potential of 4982 V, the theoretical specific impulse should be ~ 26000 s, compared with 19587 s predicted by the model. While hydrogen propellants demonstrate expansion efficiency of 0.97 to 0.99, Case 2 expansion efficiency is only 0.72. The overall cycle efficiency is 0.391, compared to ~0.5 for hydrogen systems. The low expansion efficiency might be the result of a situation analogous to under expansion in physical nozzles. As shown in Figure 6-13, the floating potential is above 500 V in the far field. Case 2a with the higher propellant loading has a higher nozzle efficiency of 0.9 and an overall cycle efficiency of 0.525. Again, this is suggestive of a Carnot-like limitation, as Case 2a has the lower floating potential of 100 V in the far field. Note that temperatures for Case 2 are shown on a logarithmic scale, given that the ions in this case are essentially unheated and cold. Cases 2b-2d with higher charge states demonstrated similarly high floating potentials in the far field, 271 V at $z = 100\ m$ for Case 02c, for example. The 1D warm plasma model does not have the capability to model multiple ionizations as successive events, or to estimate the charge state of the propellant for either transient or steady state solutions. The charge states for Cases 2b-2d were specified parametrically to provide insight into the likely performance of the warm plasma at higher charge states. Given the model's limitations, it was necessary to assume the specified charge state is achieved with s single $e - i$ collision, which certainly overpredicts the ionization rate. With these considerations in mind, it is suggested that Cases 2a and 2d represent the solutions most likely to be physically valid, based on assessment of charge states and electron temperatures.

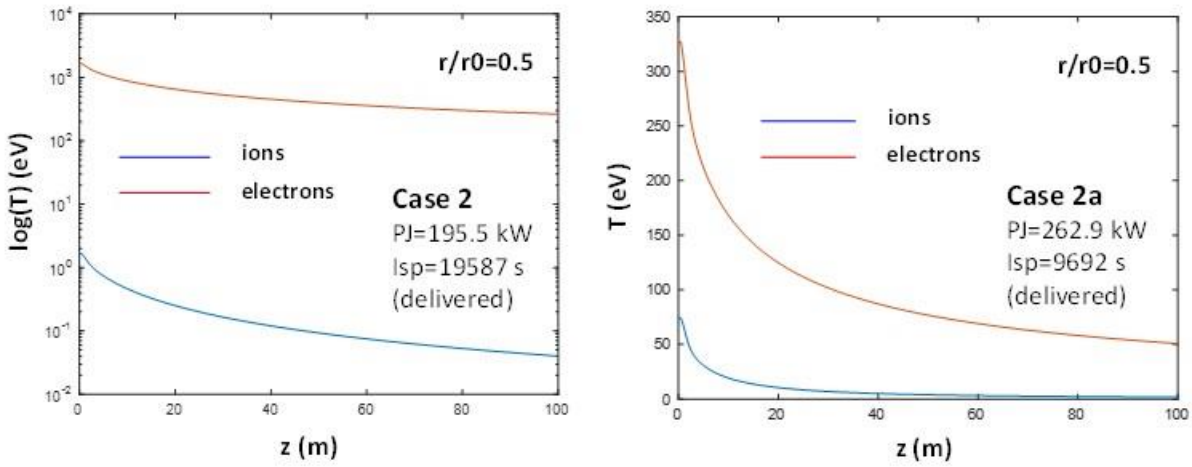

Figure 6-12 - Plasma temperatures for N2 propellant systems – Cases 2 and 2a

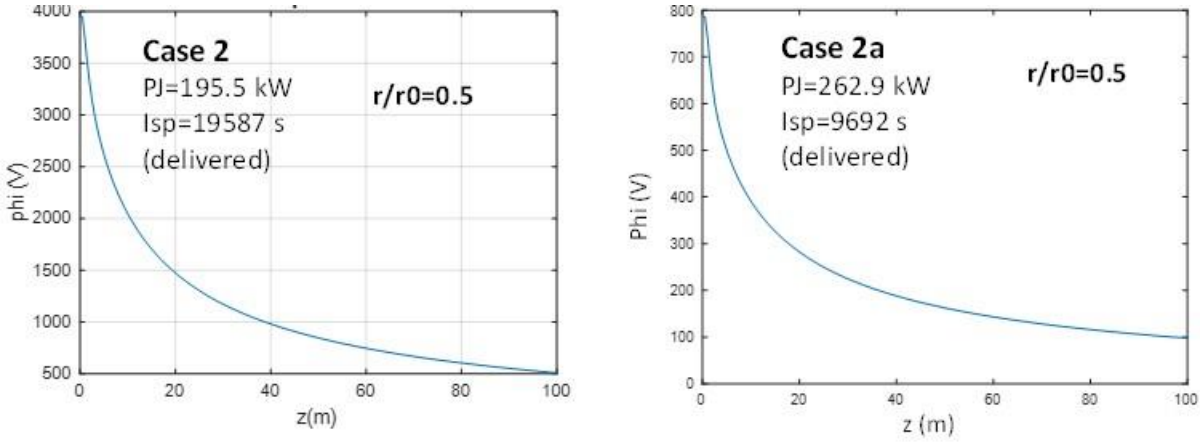

Figure 6-13 – Plasma potential for N2 propellant systems – Cases 2 and 2a

6.2.6.3 PV carry-in by reactor thermal species

Section 5.1.2.1 discusses the amount of potential energy (PV) thermal species could carry into the warm plasma. Equation (5.3e) says that ion energy $\frac{3}{2}k_B T_i$ could be augmented by another $\frac{M^2}{2Rm_N}k_B T_i$, which would be much larger. The cases run in this analysis have not included this

factor, because it has not been sufficiently validated. Additionally, most cases have been run with a low ξ^{θ}, about 0.1, which would tend to minimize the effect of the additional PV. (The low ξ^{θ} is reflective of model reactor CH, but it is also the case that higher values of ξ^{θ} are computationally very expensive.) The NH reactor has a ξ^{θ} of 5.67, but Case 17 runs the NH configuration at $\xi^{\theta} = 2$, in order to minimize wall time on the HPC. Case 17 was used as the baseline for Case 18, which assesses the impact of including residual PV in the fusion energy entering the warm plasma. The ideal jet power for Case 17 was 249 kW, and the ideal specific impulse was 25000 s.

Table 6-13 – Propulsion performance accounting for PV carry-in from reactor – Case 18

Case	Warm Plasma							Delivered Performance			
	Q_in	Q_dep	BN	RmN	τ_conf	n^{β}	Te	Ft	Isp	PJ	η_J
	kW	s	T		ms	#/m^3	eV	N	s	kW	
17	233.35	228.77	10.63	16.77	139	9.69 x 10^{18}	64.6	1.129	18915	113.99	0.450
18	281.45	228.79	10.63	16.77	139	9.69 x 10^{18}	68.2	1.129	18917	114.00	0.450

Table 6-13 is summary of performance for Cases 17 and 18. The main difference between the two cases is that power in from the reactor in Case 18 is approximately 21 percent higher than the baseline. That delta is due to accounting for the residual potential energy of the thermal species. With a $R_{mJ} = 1.63$, and residual power that scales with M^2, the residual potential energy of thermal ions is a significant fraction of power from the prompt alphas. While the power arriving from the reactor is higher, the power deposited in the warm plasma remains almost exactly the same, as do plasma state properties and propulsion performance. Collision times between thermal ions and bulk electrons are very short, even compared with those for prompt alphas and bulk electrons. The amount of energy transferred per interaction is still two orders of magnitude lower than that for the prompt alphas. It appears that the bulk electrons experience enhanced heating, but

with the relatively short confinement time of this configuration, the additional PV energy is not transferred to the ions effectively. At the same time, energy transfer from the thermal electrons is limited by relatively long interaction times, so they remain hot. Theoretically, the fusion products with high residual energy could contribute to the high-energy channel discussed in Section 5.1.3.2. Although this initial look at PV carry-in to the warm plasma is not encouraging, it should be remembered that this is a single case, likely with non-negligible transient error. Given these considerations, it remains possible that PV carry-in could increase delivered jet power by 10-20 percent and the idea warrants future investigation.

6.2.6.4 Warm plasma volume

Cases 12 and 13 were run to assess the effect of warm plasma volume on propulsion performance, and Table 6-14 summarizes the results of these cases along with a baseline in Case 5. I_{SP0} was 25000 seconds, and P_{J0} was 500 kW for all cases. Each case was run for 200 ms simulation time. The reduction in confinement time for the smaller volume is expected. Another difference between the baseline and the reduced volume cases is that heating losses and ionization losses are lower. For example, in Case 4, $Q\_htg = 191.5\,kW$, while for Case 12, $Q\_htg = 181.7\,kW$. The difference shows up in slightly higher Q_jet for Cases 12 and 13. It would have been expected that Q_dep would differ because of the smaller confinement times, however the results indicate that it does not change much. Overall performance does not appear to vary from baseline to test cases, however, it should be remembered that these are quasi-steady-state solutions and include transient error.

Table 6-14 – Propulsion performance with varying volumes of warm plasma – Cases 12 and 13

Case	Warm Plasma					Delivered Performance				
	Volume	τ_conf	Q_dep	n^{β}	Te	Cf	Ft	Isp	PJ	η_j
	m^3	ms	kW	$\#/m^3$	eV		N	s	kW	
5	38	255.2	456.3	1.60×10^{19}	66.3	0.857	2.363	17414	229.5	0.459
12	28.5	228.6	455.5	1.59×10^{19}	66.6	0.660	2.508	16572	237.5	0.475
13	23.8	192.2	454.8	1.58×10^{19}	67.0	0.583	2.575	16243	241.3	0.482

6.2.7 Electron Detachment Revisited

Plume detachment in DFD-CM for purposes of the current research is asserted on the basis of ion detachment, but that assertion remains provisional. More work is necessary to understand better electron detachment in regimes relevant to DFD-CM.

Data in Figure 6-10 and Table 6-6 for Case 1 are mixed with respect to plume detachment. On one hand, the plasma transitions to super-Alfvénic flow, an indication of ion inertial detachment, and the Hall parameter for electrons approaches unity, suggesting electron detachment. On the other hand, the magnetic Reynolds number is well above expected values for electron detachment, even in the far field. Additionally, the Hall parameter for detachment occurs well downstream from the point of super-Alfvénic transition. Across all cases evaluated, this is the general pattern. The plasma becomes super-Alfvénic within 20 m of the thruster exit, and NH becomes less than 10 at 50-80 m. For the experimental datasets evaluated in Section 5.1.6.4, the ion and electron detachment were much more proximate. This proximity is necessary for the mechanism proposed by [Olsen, *et al*, 2015], where ambipolar forces and cross-field diffusion of electrons enable detachment.

The detachment model derived in Section 5.1.6.3 is based on the momentum equation and the generalized Ohm's law, which account for much of the physics likely to be involved. Inclusion of other relations such as Coulomb's law and Gauss' law would have explicitly added the electric field to the quantities considered in the Buckingham-pi theorem analysis. Additionally, including the dissipative terms from the momentum equation may have evolved new groups like the magnetic Prandtl number ($\nu\mu_0\sigma$) or a magnetic corollary to the Schmidt number ($1/\mu_0\sigma D$), where ν is the dynamic viscosity. These quantities might have provided a more accurate model relative to mechanisms related to ambipolar forces and cross-field diffusion. In order to exploit this additional rigor, however, a higher fidelity expansion model would be necessary. For one thing, the current model assumes strict quasi-neutrality.

In addition to concerns about the relative fidelity of the model, there is also the matter that only four datasets were used in the analysis, and that their operational regimes are very different from DFD-CM. The higher DFD-CM specific impulses result in hotter, less dense plasmas. The higher temperatures result in conductivity 1-2 orders of magnitude larger than those in the experiments, and higher exhaust velocities directly impact the magnetic Reynolds number. The mean free paths of the fusion simulations were similarly much larger than those in the cited experiments

These observations suggest that the expanding warm plasmas may not be sufficiently collisional for optimal cross-field diffusion of electrons. This supposition is consistent with the plot of $log(n_e)$ vs. plasma temperature in Figure 6-14 for Case 1. The plot, adapted from [Araya and Girimaji, 2011] shows the regimes of operation for an expanding hydrogen-like plasma. In the electromagnetic regime, closest to the thruster exit, the Larmor radius of the ions is greater than the thruster characteristic length, but the electrons are still magnetized. In the electric region, the Larmor radius for both ions and electrons is larger than the thruster characteristic length.

According to [Araya and Girimaji, 2011], in the electric region, the plasma is not collisional, and the local electric forces are dominant over the magnetic field.

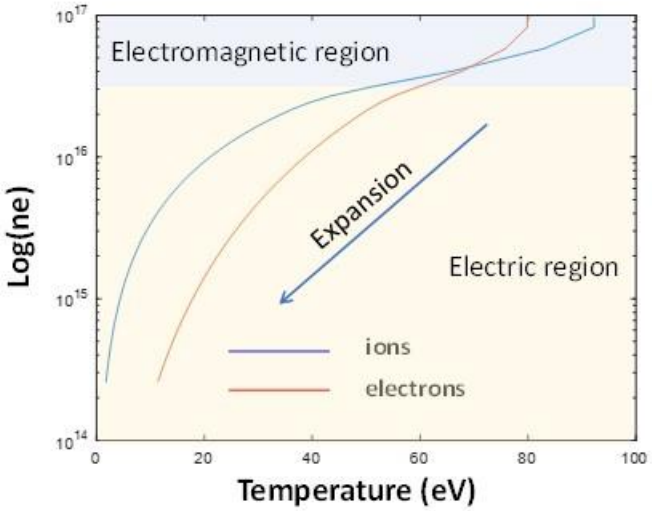

Figure 6-14 – Plasma flow regimes – Case 1

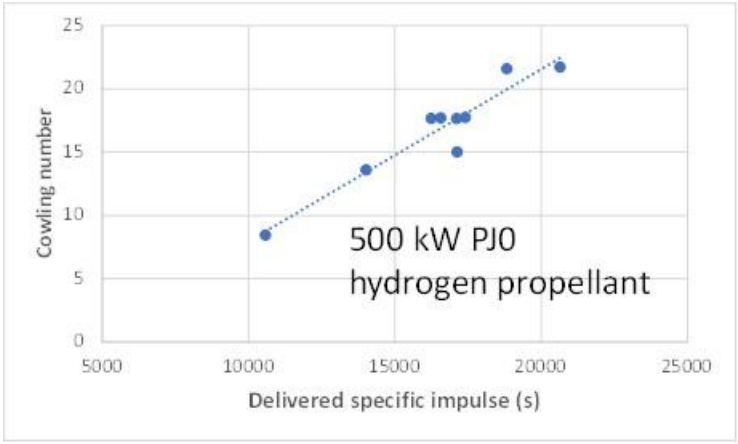

Figure 6-15 – Cowling number at nominal exit plane vs. delivered specific impulse

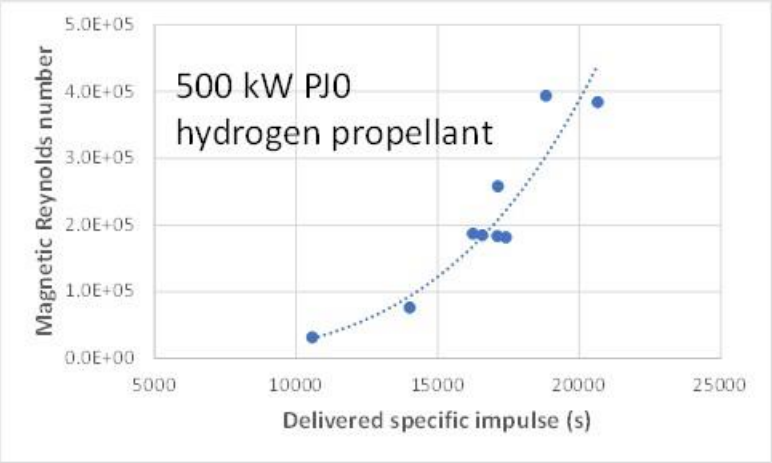

Figure 6-16 - Magnetic Reynolds number at nominal exit plane vs. delivered specific impulse

Figures 6-15 and 6-16 show plots of the Cowling and magnetic Reynolds numbers at the exit plane, nominally defined $B_{ext}(z)/B_N = 0.001$. For Case 1, this is about 9 m, which is representative of most other cases. These data suggest that plasmas operating above 5000 seconds specific impulse do not demonstrate detachment, at least prior to the nominal exit plane. However, all cases evaluated did achieve super-Alfvénic flows, usually at 15-20 m from the thruster exit, but downstream of the nominal exit plane. The magnetic Reynolds numbers remain well above 10^2, even in the very far field, $z{\sim}1000\ m$.

The issue is uncertainty of detachment of electrons as indicated by high magnetic Reynolds numbers. As discussed above, it is possible that the specific form magnetic Reynolds number is not complete. Continuing this line of thinking, the magnetic Reynolds number may not be an appropriate or complete indication of electron detachment. Its inclusion in this analysis follows from the Buckingham-π theorem which presupposed the relevant physics captured in the momentum equation and in Ohm's law. Derivation of the magnetic Reynolds number from

Equation (5.37) is based mainly on the basis of magnetic and flow field considerations, not from plasma collisionality in any explicit sense..

Overall, the model for electron detachment as presented in this work may not adequately reflect the physics underlying the interdependencies between ion and electron detachment. Specifically, the use of the magnetic Reynolds number to understand electron detachment in these regimes may be naïve and inadequate in addressing the aforementioned interdependencies. This dimensionless group apparently is relevant to the flow regimes of the experiments assessed, but the warm plasma regime as characterized in the current research is very different in terms of state properties and transport. Extending this line of thought even further, analysis involving dimensionless numbers can provide only limited insight into electron detachment.

References – Chapter 6

1. LaFleur, T., *et al*, 2015, "Electron dynamics and ion acceleration in expanding-plasma thrusters," Plasma Sources Sci. Technol. 24 06513
2. Olsen, C.S., Ballenger, M.G., Carter, M.D., Chang-Diaz, F.R., Giambusso, M., Glover, T.W., Ilin, A.V., Squire, J.P., Longmier, B.W., Bering, E.A., Cloutier, P.A., "Investigation of Plasma Detachment From a Magnetic Nozzle in the Plume of the VX-200 Magnetoplasma Thruster," IEEE Transactions on Plasma Science, Vol. 43, No.1, January 2015
3. Araya, Daniel B., Girimaji, Sharath, Carter, Mark D., Olsen, Christopher S., "Parameterization of magnetic nozzle flow physics for an in-space propulsion application," 42nd AIAA Plasmadynamics and Lasers Conferences, 27-30 June 2011 (AIAA 2011-4010)

7 Summary of Findings, Contributions, and Future Work

7.1 Summary of Findings

Direct fusion drive based on centrifugal mirror confinement (DFD-CM) using D-T fuel and hydrogen propellant appears thermodynamically feasible. A system capable of 200 kW jet power, 15000 s specific impulse (delivered) could operate at 49 percent cycle efficiency. One such system could power highly capable payloads for ambitious science missions or support asteroid mining operations. Ganging five systems would provide a megawatt of jet power and enable man-rated missions to the outer Solar system.

Analysis indicates the system can self-power, and would be relatively compact. For the 200 kW system, the volume of burning plasma in the CM fusion reactor is estimated to be on the order of 1 m^3, while the warm plasma volume could be as little as 30 m^3 (3m L, 1.75m r).

For propulsion applications, self-powering requires the DFD reactor operation at $M_\theta > 9$. This in turn requires electric fields ranging from 40-90 MV/m, and mirror strengths of 15T. DFD-CM self-powering with neutrons would operate at the low end of the range for electric fields, while those self-powering with charged species would operate at the upper end. These estimates assume power conversion efficiency 80 % for SWDEC based system; 50 % for neutron power.

The main losses in the propulsion system are due to heating and ionizing the propellant. These losses decrease with increasing specific impulse. Specific impulse for cases analyzed ranged from 10000 to 20000 seconds (delivered), while thrusts were between 2 and 5 N (delivered). There may be a minimum specific impulse between 10000 and 15000 seconds, where losses related to heating the plasma overmatch fusion power deposition resulting in localized quenching. The cycle

efficiencies for hydrogen propellant all fell within the approximate range of 0.4 to 0.5. Analysis indicates that cycle efficiency is primarily a function of delivered specific impulse, and that η_J falls off rapidly for specific impulse less than 10000 s. All of the cases in Table 6-3 were above 10000 s and so fell onto a flattening curve for cycle efficiency. The analysis is provided in Appendix B.

Systems with higher nozzle mirror ratios R_{mN} are generally robust. Case 1 R_{mN} was 14.8, and its field configuration was used in most other cases. However, high R_{mN} imposes a mass penalty. Lower nozzle mirror strengths and mirror ratios were assessed, with the result that R_{mN} in the 10-12 range appeared feasible, but with loss of performance. There appears to be a limit on how low $B_N$and R_{mN} can be, however, as one case with $R_{mN}\sim 6$ demonstrated a cycle efficiency of 10 percent. This reduction in cycle efficiency was associated with a much reduced confinement time in the warm plasma.

Several cases with nitrogen as a propellant were evaluated at varying charge states at ideal specific impulse 30000 s. At the high specific impulse, ξ^{β} was less than 1000 for nitrogen. By comparison, with hydrogen propellants, ξ^{β} is $O(10^4)$. With low propellant loading, almost all the fusion energy was transferred to the electrons. The result was that the warm plasma was essentially a hot electron gas, with cold ions and extremely high plasma potential. With increasing charge state, electron temperature and delivered jet power decreased. One N2 case with 15000 s ideal specific impulse and $Z_i = 1$ operated at much lower electron temperature and potential, but at higher thrust.

In all cases evaluated, ion detachment during plasma expansion appears likely, based on early onset of super-Alfvénic flows. Electron detachment appears less definitive in expansion, with $Re_m > 1000$, and Hall parameter for electrons reaching unity 30-40 m downstream from nominal

ion detachment. It is unclear whether these results follow from a shortcoming in model fidelity or whether they are reflective of the relatively high plasma temperature in the propulsion system.

Finally, it is again pointed out that this analysis assumes that reactor and warm plasma are electrically isolated from each other. The assumption is based on large $\xi^{\beta} > O(10^4)$, i.e. low particle density of fusion products in reactor flux for most cases. This is an area of research that deserves attention in the near term.

7.2 Contributions

This work has resulted in four contributions. To start, it is the first analysis of the end-to-end performance of direct fusion drive based on centrifugal mirror confinement of the burning plasma. It demonstrates that the concept is thermodynamically feasible with nominal cycle efficiencies of 50 percent based on fusion energy entering the propulsion system. The viability of the concept is indicated based on analysis showing the reactor is self-powering and that volumes of burning plasma are on the order of 1 m^3 for delivered jet power up to 500 kW.

The second contribution is characterization of CM fusion reactor performance and operability. A particular finding is that self-powering DFD-CM reactors in propulsion applications may need to operate at Mach numbers greater than 9. The 0D reactor simulation also identifies and describes a novel behavior of the reactor CM plasma, a critical Mach number characterized by a minimum jet-side mirror ratio. Adjunct to the critical Mach number finding is the observation in viable reactors, it tends to be the case that $R_{mJ} \approx R_{mP}$. Finally, with respect to reactor viability, the 0D model shows that operating regimes of self-powering CM fusion reactor are significantly constrained by

desirable operating parameters and nominal limits for magnetic and electric fields. The research provides initial insight into these constraints as a basis for future research and design.

The third contribution is the development and preliminary application of a set of engineering models of the reactor, warm plasma, and plasma acceleration and expansion. These models are considered moderate fidelity in that they account for first order effects, as well as salient second order effects. For example, the 0D CM reactor model allows the specification of different mirror ratios for jet-side and power-side mirrors. The 1D warm plasma model accounts for radial variation of transport properties. The research developed engineering relations based on experimental data from the literature to assess likelihood of plume detachment as the plasma expands in the diverging section of the magnetic nozzle. These relations were incorporated into the plasma acceleration and expansion model.

The fourth contribution is identifying the possibility that the burning plasma in the reactor and the warm plasma may be electrically coupled. The nature and implications of any coupling are uncertain, and the current research proceeds assuming that the coupling does not occur. However, the question indicates the need for further research.

The results of this research have been submitted for publication:

> Carson, J.L., and Sedwick, R.J., "Direct Fusion Drive based on Centrifugal Mirror Confinement," 2023, has been submitted to *Acta Astronautica*. The paper was presented at the 8th Interstellar Research Group Symposium held July 2023 in Montreal.

The following additional contributions to the literature are planned:

> "Propulsion performance of a direct fusion drive based on centrifugal mirror confinement;"

"Toward Engineering Relations for Predicting Performance and Plume Detachment in Magnetic Nozzles;"

"Dynamics of a centrifugally confined fusion plasma in space propulsion applications."

The latter three papers are planned for submission to the American Institute of Aeronautics and Astronautics *Journal of Propulsion and Pow*er.

7.3 Future Work

7.3.1 Planned Research

The current research was performed within a framework developed to focus SPPL efforts on DFD-CM. As a near-term follow-on to the research, three specific tasks will be performed..

Conduct balance of plant design analysis – Characterize technologies, mass properties, and performance of the balance of plant with priorities for powering the reactor, shielding, thermal management, system architectures, and performance for advanced fuels, e.g., D-He^3.

Incorporate a 1-D reactor model into the DFD-CM simulation – The CMFX team is developing the Maryland Numerical Transport Analyzer (MaNTA), which will be capable of simulating a 1D-radial reactor. The model will solve for state and transport properties, as well as electric field and velocity profile. This simulation would be used in conjunction with the 1D warm plasma and propulsion model to provide a higher fidelity estimate of the DFD-CM performance. These efforts may include porting the 1D warm plasma model to a more computationally efficient platform.

Develop preliminary design for warm plasma experiments – Results from this work will be coordinated with efforts by other SPPL team members and with the CMFX team to prepare preliminary design of experiments on operation of the warm plasma.

Successful completion of these tasks in combination with anticipated progress by the CMFX team would constitute achievement of Technology Readiness Level (TRL) of 3 for DCD-CM. The task on experiment design will inform efforts to obtain the resources for an experimental program.

7.3.2 Emergent Inquiries

The current research has identified specific shortfalls in our understanding of DFD-CM that merit further investigation in the near-term, including

- The lack of insight into the possibility of electrical coupling between the reactor well and the warm plasma, and of associated implications for system performance
- The need for better understanding of the detachment dynamics of electrons in high temperature plasma plumes
- The need for better understanding of multi-stage ionization for heavier propellant species in the warm plasma, and associated implications for transport and overall propulsion performance

Progress on these emergent research needs may affect the conduct of planned work previously described. Some of the emergent work may be accomplished by other members of the SPPL team.

7.3.3 Longer Term Goals

Research by SPPL on DFD-CM is intended to help realize a practical capability for direct fusion drive based on CM reactors and allied technologies. To that end, current SPPL efforts are being coordinated with those of our colleagues on the CMFX team.

The research presented in this dissertation and follow-on efforts outlined above reflect significant challenges in engineering and physics. Figure 7-1 provides a taxonomy of technology development needs for the overall system from the spacecraft perspective.

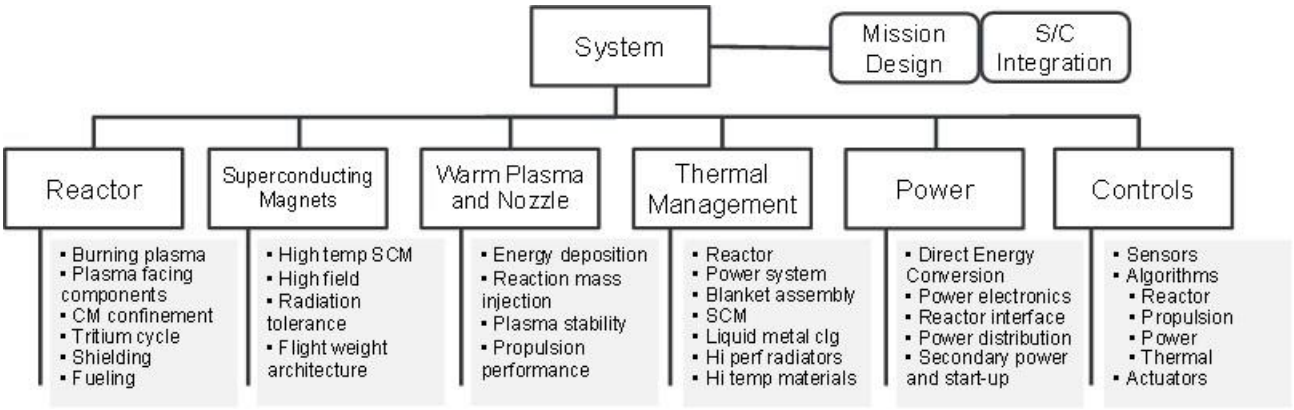

Figure 7-1 – DFD-CM technology taxonomy

The strategy to address these challenges in the longer term is to identify and to accomplish the scope that SPPL and the University of Maryland community are uniquely positioned to perform, and to leverage advances in other areas from external partners and from the fusion community in general. Figure 7-2 shows a model technology development program for DFD-CM from current state through the demonstration of a notional 150-kW jet power prototype. Planning includes continuing a mutually beneficial collaboration with the CMFX team. Note the near-term goal of TRL 3 and mid-term accomplishment of experiments supporting development of the warm plasma system.

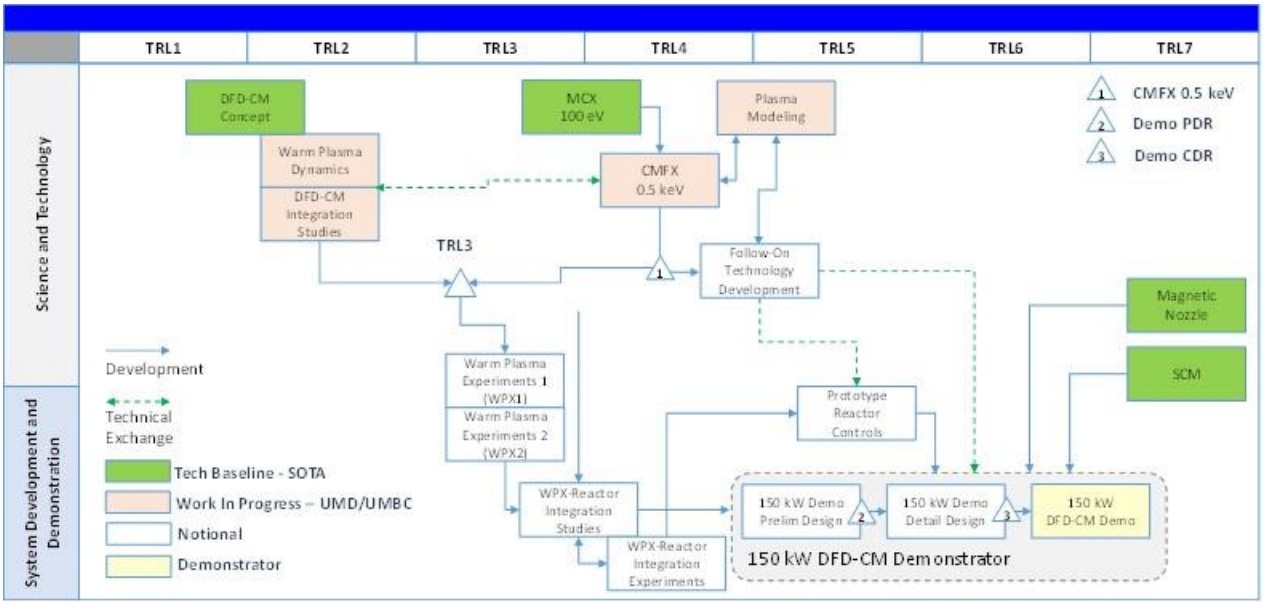

Figure 7-2 – DFD-CM model technology development

Appendix A – Glossary

Quantities

a	plasma column half-width (m)
a	ratio of alpha cross-over velocity to birth velocity
A	area (m^2)
B	magnetic field intensity (T)
Co	Cowling number
C_s	acoustic velocity (m/s)
C_V	specific heat, constant volume (J/kg-K)
C_P	specific heat, constant pressure (J/kg-K)
D	displacement vector (C/m^2)
D_s	diffusive coefficient of species s (m^2/s)
e	unit charge (C)
E	electric field (V/m)
E^{α}	energy of prompt alpha from D-T reaction (J)
f	distribution function
F	force (N)
F, G	expansion constants, potential equation – dimensionless
g	loss cone fraction
h	specific enthalpy (J/kg-K)
H	Magnetic intensity (A-turns/m), enthalpy (J), or Hamiltonian (J)
I	Magnetic moment ($A\text{-}m^2$)
I_n	moment integral of slowing down distribution, order n
IV_0	reactor power (W/m^3)
J	current density (A/m^2)
k_1	constant used to specify reactor well boundary conditions - Neumann
k_2	constant used to specify reactor well boundary conditions - Dirichlet
k_B	Boltzmann's constant (J/K)
K	Kármán number
$ln\Lambda$	Coulomb logarithm
L	length (m)
m_e	electron mass (kg)
mi	ion mass (kg)
M	Mach number
n	number density ($\#/m^3$)
$\dot{n}$	specific number flow rate ($\#/m^3\text{-s}$)
$\dot{N}$	number flow rate (#/s)
NH	Hall parameter
p	momentum (kg-m/s)
P	pressure (Pa)
P^{α}	alpha fusion power – reactor (W/m^3)
P^n	neutron fusion power – reactor (W/m^3)

P_B Bremsstrahlung losses – reactor (W/m^3)
P_C cyclotron radiation losses – reactor (W/m^3)
P_F fueling losses – reactor (W/m^3)
P_{IN} integrated power entering warm plasma (kW), also Q_{in}
P_J jet power – reactor (W/m^3)
P_{SH} shear losses – reactor (W/m^3)
P_{TH} thermal losses – reactor (W/m^3)
PV potential energy – reactor (W/m^3)
$Q_\perp$ heat conduction across magnetic field lines (W/m^3)
Q reactor power ratio, transport quantity, or heat rate (W)
Q_{cx} integrated charge exchange losses – warm plasma (kW)
Q_{dep} integrated power deposition – warm plasma (kW)
Q_{htg} integrated propellant heating losses – warm plasma (kW)
Q_{in} integrated power entering warm plasma (kW), also P_{IN}
Q_{ion} integrated ionization losses – warm plasma (kW)
Q_{rad} integrated radiation losses – warm plasma (kW)
r, R radius (m)
Re_m magnetic Reynolds number
R_{mJ} jet-side mirror ratio - reactor
R_{mN} nozzle mirror ratio – warm plasma
R_{mP} forward or power-side mirror ratio - reactor
r_L Larmor radius (m)
s specific entropy (J/kg-K)
S source term (quantity/m^3-s) or Poynting vector (W/m^2)
St Stuart number
t time (s)
T temperature (K or eV)
u velocity (m/s) or specific internal energy (J/kg)
U velocity (m/s) or internal energy (J)
v_c cross over velocity or critical ion velocity (m/s)
V volume (m^3)
V_A Alfvén velocity (m/s)
x_s partial pressure of species s
x, y auxiliary variables – described in text where used
Z_i charge state of ion
α angle (radians) or ionization fraction
β magnetic pressure ratio
γ ratio of specific heats
Γ flux (#/m^2-s) or magnetic field configuration integral (dimensionless)
ε_0 permittivity of free space (m^{-1}kg^{-1}s^{4}A^2)
η efficiency or resistivity (ohm-m)
θ angle (rad)
θ_P plasma beam divergence angle (rad)
κ heat transfer coefficient (1/m-s), or ratio of power-side losses to total well losses
κ_i curvature (rad/m)

λ_1, λ_2 roots of well potential expansion
μ_0 permeability of free space (N/A^2)
μ ion mass (amu), first magnetic invariant (J/T), or viscosity ($N\text{-}s/m^2$), or mobility (C-s/kg)
ν collision frequency (s^{-1})
ξ^s ratio of species s rate to prompt alpha rate
χ difference between centrifugal potentials at respective reactor mirrors
Ξ potential energy (J)
π dimensionless group or stress tensor (Pa)
ρ density (kg/m^3)
σ cross-section area (m^2), electrical conductivity (mho/m)
τ time interval (s), or ratio of temperatures T_i/T_e
φ_0 well offset potential (V)
ϕ_f floating potential (V)
ϕ_P plasma potential (V)
Φ magnetic flux (webers)
Φ_0 potential difference between reactor mirrors (V)
Ψ magnetic flux ($T\text{-}m^2$)
ω_{ce} cyclotron frequency, electrons (rad/s)
ω_{ci} cyclotron frequency, ions (rad/s)
Ω angular velocity (rad/s)
$\langle \sigma v \rangle$ thermonuclear reactivity ($\#/cm^3\text{-}s$)

Subscripts, superscripts, and indices

0 reference or initial value
B bulk plasma
e electron
i ion
$j \text{ or } s$ specified species or quantity
J jet or jet-side, cycle when used with η
mom momentum
n neutral
N mirror throat
P power-side
r reactor
w warm plasma
x exit plane
α alpha particle
β propellant
θ thermal species or azimuthal component

Appendix B – Selected Topics

Modeling the Reactor Flux into the Warm Plasma

This section describes how the reactor fluxes entering the warm plasma are calculated in the 1D warm plasma model. Consider a cylindrical warm plasma divided into concentric, annular control volumes such as the one shown in Figure B-1. Species *s* arrives at surface S at a flux rate $\Gamma(r)$.

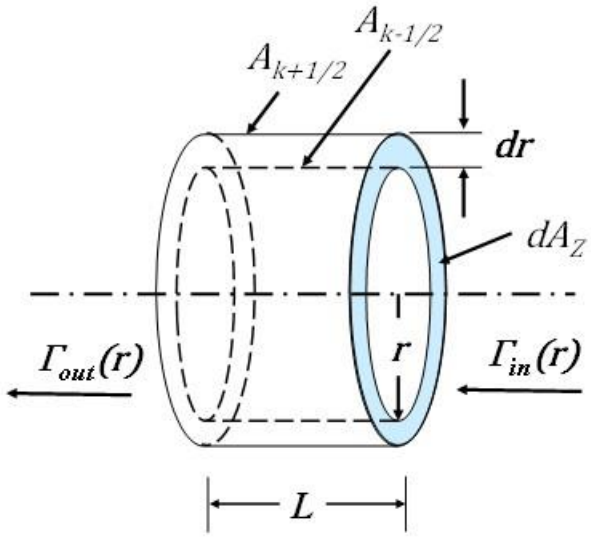

Figure B-1 – Warm plasma control volume

Top-hat distribution for reactor flux

For a species with rate $\dot{N}^s$ (#/s) express the arrival rate for the total control volume as a function of *r*, such that

$$\dot{N}^s = \int_{r_i}^{r_0} \int_0^{2\pi} \Gamma(r)\, r d\theta dr. \qquad \text{B.1}$$

Assuming a top hat profile, $\Gamma(r) = A$, a constant,

$$\dot{N}^s = 2\pi A \int_{r_i}^{r_0} r dr. \qquad \text{B.2}$$

Solving for A,

$$A = \frac{\dot{N}^s}{\pi(r_0^2 - r_i^2)}\ (\#/m^2 - s). \qquad \text{B.3}$$

The rate of arrival of species s (#/s) at any discretized control volume k is

$$\dot{N}_k^s = 2\pi A r_k \Delta r. \qquad \text{B.4a}$$

Expanding Equation (B.4a),

$$\dot{N}_k^s = \frac{2r_k \dot{N}^s \Delta r}{r_o^2 - r_i^2}. \qquad \text{B.4b}$$

Flux from annular reactor well

In order to model fusion products generated in a annulus in the reactor, it is more straightforward to specify $n^s(r)$ directly

$$n^s(r) = A sin\left[\left(\frac{r - r_i}{r_0 - r_i}\right)\pi\right]\Delta r. \qquad \text{B.5}$$

where Δr is the spatial discretization of the warm plasma model. In order to evaluate A, the relation is converted to a differential and integrated setting the result equal to the total integrated flux arriving from the reactor through the jet-side mirror.

$$A\int_{r_i}^{r_0} sin\left[\left(\frac{r-r_i}{r_0-r_i}\right)\pi\right]dr = \dot{N}_J^S. \qquad \text{B.6}$$

$\dot{N}_J^S$ is the integrated flux from the reactor. Setting $R = \left(\frac{r-r_i}{r_0-r_i}\right)$, then $dR = \frac{dr}{r_0-r_i}$ and $dr = (r_0 - r_i)dR$. Further, $R(r = r_i) = 0$, and $R(r = r_0) = 1$. Solving for A, and substituting into Equation (B-6)

$$\dot{n}_k^S(r) = \frac{\dot{N}_J^S\pi}{2(r_0-r_i)} sin\left[\left(\frac{r_k-r_i}{r_0-r_i}\right)\pi\right]\Delta r \qquad \text{B.7}$$

The Iso-Rotation Law

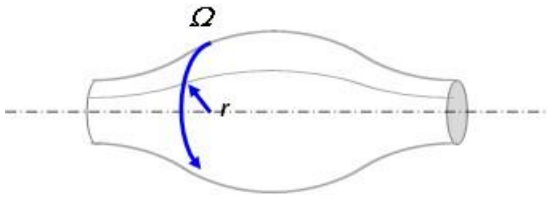

Figure B-2 – Axisymmetric magnetic flux surface

Angular velocity for a position vector r and azimuthal speed Ω:

$$u = r \times \Omega. \qquad \text{B.8}$$

The azimuthal velocity resulting from $E \times B$ drift is

$$u = \frac{E \times B}{B \cdot B}, \tag{B.9}$$

where

$$E \times B = \begin{vmatrix} \hat{r} & \hat{\theta} & \hat{z} \\ \dfrac{\partial \varphi}{\partial r} & 0 & \dfrac{\partial \varphi}{\partial z} \\ -\dfrac{1}{r}\dfrac{\partial \psi}{\partial z} & 0 & \dfrac{1}{r}\dfrac{\partial \psi}{\partial r} \end{vmatrix} = \frac{1}{r}\left(\frac{\partial \varphi}{\partial r}\frac{\partial \psi}{\partial r} + \frac{\partial \psi}{\partial z}\frac{\partial \varphi}{\partial z}\right)\widehat{\theta}, \tag{B.10}$$

and

$$B \cdot B = \frac{1}{r^2}\left[\left(\frac{\partial \psi}{\partial r}\right)^2 + \left(\frac{\partial \psi}{\partial z}\right)^2\right]. \tag{B.11}$$

For E and B with respective radial and axial components, the resulting drift is purely azimuthal, and so therefore is $r \times \Omega$ is

$$\mathrm{r}\Omega\hat{\theta} = \frac{\dfrac{1}{r}\left(\dfrac{\partial \varphi}{\partial r}\dfrac{\partial \psi}{\partial r} + \dfrac{\partial \psi}{\partial z}\dfrac{\partial \varphi}{\partial z}\right)\hat{\theta}}{\dfrac{1}{r^2}\left[\left(\dfrac{\partial \psi}{\partial r}\right)^2 + \left(\dfrac{\partial \psi}{\partial z}\right)^2\right]}. \tag{B.12}$$

Since all components are in the $\hat{\theta}$ direction,

$$\Omega = \frac{\left(\frac{\partial\varphi}{\partial r}\frac{\partial\psi}{\partial r} + \frac{\partial\psi}{\partial z}\frac{\partial\varphi}{\partial z}\right)}{\left(\frac{\partial\psi}{\partial r}\right)^2 + \left(\frac{\partial\psi}{\partial z}\right)^2}. \qquad \text{B.13}$$

Now assume a scaling of relative magnitudes of the factors and terms. Each flux surface will have a species density that is determined by the electric field and by Boltzmann's law, i.e., $n_e = n_0 exp\left(\frac{e\varphi}{k_B T_e}\right)$. The electrons are highly mobile and tend to distribute themselves evenly over the surface, so that each magnetic flux surface is equipotential. Given that the flux surfaces are equipotential, we know that the electric field lines must be normal to the flux surface, or

$$E \cdot B = -\frac{1}{r}\frac{\partial\varphi}{\partial r}\frac{\partial\psi}{\partial z} + \frac{1}{r}\frac{\partial\psi}{\partial z}\frac{\partial\varphi}{\partial z} = 0. \qquad \text{B.14}$$

Recognizing that

$$-\frac{1}{r}\frac{\partial\psi}{\partial z} = B_r,$$

and

$$\frac{1}{r}\frac{\partial\psi}{\partial r} = B_z,$$

it is possible to approximate the partials with respect to *z* in terms of partials with respect to *r*

$$\frac{\partial\varphi}{\partial z} = \frac{B_r}{B_z}\frac{\partial\varphi}{\partial r},$$

and

$$\frac{\partial\psi}{\partial z} = \frac{E_z}{E_r}\frac{\partial\psi}{\partial r}.$$

Substituting these into the expression for Ω

$$\Omega = \frac{\left(\frac{\partial\varphi}{\partial r}\frac{\partial\psi}{\partial r} + \frac{B_r}{B_z}\frac{\partial\varphi}{\partial r}\frac{E_z}{E_r}\frac{\partial\psi}{\partial r}\right)}{\left(\frac{\partial\psi}{\partial r}\right)^2 + \left(\frac{E_z}{E_r}\right)^2\left(\frac{\partial\psi}{\partial r}\right)^2},$$

and

$$\Omega = \frac{\frac{\partial\varphi}{\partial r}\frac{\partial\psi}{\partial r}\left(1 + \frac{B_r}{B_z}\frac{E_z}{E_r}\right)}{\left(\frac{\partial\psi}{\partial r}\right)^2\left[1 + \left(\frac{E_z}{E_r}\right)^2\right]}. \qquad \text{B.15}$$

For magnetic fields in centrifugal mirrors, $E_z \ll E_r$, and $B_r \ll B_z$. Given this scaling, and the expression (B-15), Ω is evaluated for a given flux surface as

$$\Omega = \left(\frac{\partial\varphi}{\partial r}\Big/\frac{\partial\psi}{\partial r}\right)_\psi = \left.\frac{d\varphi}{d\psi}\right|_\psi \qquad \text{B.16}$$

Remembering that potential φ is constant for any flux surface, $\left.\frac{d\varphi}{d\psi}\right|_\psi$ for two concentric flux surfaces in close proximity is also constant, and

$$\lim_{\psi_{2-}\to\psi_1} \frac{\varphi_{1-}\varphi_2}{\psi_{1-}\psi_2} = \frac{d\varphi}{d\psi} \sim constant \qquad \text{B.17}$$

Derivation of 0D Propulsion Equations

Equations (1.16) and (5.1, 5.2) provide a method for estimating propulsion performance based on the bypass ratio ξ^β and the warm plasma electron temperature T_e. This section shows how Equations (5.1) and (5.2) are derived. Starting with the sheath potential

$$\phi = -\frac{k_B T_e}{2e}\left[1 + ln\left(\frac{m_i}{2\pi m_e}\right)\right], \qquad 1.16$$

it can be seen that ϕ is proportional to T_e. Setting the kinetic energy of the ions equal to the electrostatic energy, $\frac{1}{2}m_i U_x^2 = \eta_J e\phi$, where η_J is the delivered efficiency of the propulsion system relative to the power deposition in the warm plasma. Note that propulsion efficiency is $\eta_J = \eta_w \eta_{exp}$, where η_w is the warm plasma efficiency defined in Section 5.1.1, and η_{exp} is the expansion efficiency which approaches unity for most cases, so that $\eta_J \approx \eta_w$. The velocity of the ions in the far field is $U_x = \left(2\eta_J e\phi/m_i\right)^{\frac{1}{2}}$. The ion mass is approximately that of the propellant species. It is expressed more exactly in terms of ξ^β and ξ^θ

$$m_i = \frac{m^\alpha + \xi^\theta m^\theta + \xi^\beta m^\beta}{1 + \xi^\theta + \xi^\beta}.$$

The specific impulse then is

$$I_{SP} = \frac{1}{g_0}\left[\frac{1 + \xi^\theta + \xi^\beta}{m^\alpha + \xi^\theta m^\theta + \xi^\beta m^\beta} 2\eta_J e\phi\right]^{\frac{1}{2}}. \qquad 5.2$$

The thrust is found $F_t = \dot{m} g_0 I_{SP}$, where

$$\dot{m} = \dot{n}^\alpha g_J V_r \left(1 + \xi^\theta + \xi^\beta\right) m_i,$$

so that

$$F_t = \dot{n}^\alpha g_J V_r \left(m^\alpha + \xi^\theta m^\theta + \xi^\beta m^\beta\right) g_0 I_{SP}.$$

This expression can be used with Equation (5.1) to arrive at the expression for thrust

$$F_t = \dot{n}^{\alpha} g_J V_r \left[\left(1 + \xi^{\theta} + \xi^{\beta}\right)\left(m^{\alpha} + \xi^{\theta} m^{\theta} + \xi^{\beta} m^{\beta}\right) 2\eta_J e\phi \right]^{\frac{1}{2}}. \qquad 5.1$$

General M-K-β Relation

The Mach and Kármán numbers of a plasma are related through the magnetic pressure ratio β. It is a useful relationship in characterizing the plasma. Equation(1.15) expresses the relation for a single-species plasma where ion and electron temperatures are the same, and the ion charge state is one. Equation (3.29b) provides the relationship for the slightly more general case of an arbitrary charge state Z_i. The following is the development of the general case for multiple species plasmas with arbitrary ionizations states, and where electrons and ions are different temperatures. Based on the definitions of M and K

$$u = MC_s = KV_A,$$

so that

$$M = K\frac{V_A}{C_s}. \qquad B.18$$

The acoustic speed is defined thermodynamically as the isentropic variation of pressure with density. It is the speed which an acoustic disturbance or wave passes through a media.

$$C_s = \left[\left(\frac{\partial P}{\partial \rho}\right)_s\right]^{\frac{1}{2}}. \qquad B.19$$

For perfect gas equation of state, the partial pressure of any component k is

$$P_k = n_{ik} k_B T_i + n_{ek} k_B T_e.$$

Defining $\tau_k = T_{ik}/T_{ek}$, the above can be expressed

$$P_k = \rho_k C_s^2 \tau_k + n_{ek} k_B T_e, \qquad \text{B.20}$$

Where $\rho_k = n_{ik} m_{ik}$ and the Bohm velocity $\left(\frac{k_B T_e}{m_{ik}}\right)^{\frac{1}{2}}$ is equal to the acoustic velocity of the ions. By Dalton's law, for j number of species k

$$P = \sum_j P_k = \sum_j (\rho_k C_s^2 \tau_k + n_{ek} k_B T_e). \qquad \text{B.21}$$

The mass fraction Y_k of each component k is

$$Y_k = \frac{n_{ik} m_{ik} V}{\sum (n_{ik} m_{ik}) V} = \frac{\rho_k}{\rho}.$$

From this relation, it can be seen that $\rho_k = \rho Y_k$. Substituting this into Equation B.21

$$P = \rho \sum_j Y_k C_s^2 \tau_k + \sum_j n_{ek} k_B T_{ek}. \qquad \text{B.22}$$

Equation (B.22) can be substituted into Equation (B.19) to obtain an expression for C_s in terms of C_{sk}. Since the electrons do not contribute to density, the second term is dropped from the differentiation and

$$C_s = \left\{ \sum_j Y_k C_s^2 \tau_k \right\}^{\frac{1}{2}} \qquad \text{B.23}$$

The differentiation must be carried out for constant entropy s, so that $du = -Pdv$, which results in the recovery of thermodynamic potential for pressure, $P = -\left(\frac{dU}{dV}\right)_s$. Accordingly, Equation (B.23) is self-consistent with the isentropic constraint of Equation (B.19).

The Alfvén velocity is defined $V_A = B\left(\frac{1}{\rho\mu_0}\right)^{\frac{1}{2}}$, so that Equation (B.18) can be expressed

$$M = K\left\{\left(\frac{B^2}{2\mu_0}\right)\frac{2}{\sum_j \rho_k C_{sk}^2 \tau_{sk}}\right\}^{\frac{1}{2}}.$$

Multiplying by $(P/P)^{\frac{1}{2}}$,

$$M = K\left\{\left(\frac{B^2}{2\mu_0 P}\right)\frac{2P}{\sum_j \rho_k C_{sk}^2 \tau_{sk}}\right\}^{\frac{1}{2}} = K\sqrt{\frac{1}{\beta}}\left\{\frac{2P}{\sum_j \rho_k C_{sk}^2 \tau_{sk}}\right\}^{\frac{1}{2}}.$$

The denominator in the curly brackets can be written $\sum n_{ik} k_B T_{ik}$ because of the definition of the Bohm velocity. Substituting this and Equation B.21 into the above allows

$$M = K\left(\frac{2}{\beta}\right)^{\frac{1}{2}}\left\{1 + \frac{\sum_j n_{ek} k_B T_{ek}}{\sum_j n_{ik} k_B T_{ik}}\right\}^{\frac{1}{2}}.$$

Finally, setting $n_{ik} = X_{ik} n_0$ and $n_{ek} = Z_i X_{ik} n_0$ results in

$$M = K\left(\frac{2}{\beta}\right)^{\frac{1}{2}}\left\{1 + \frac{\sum_j Z_i X_{ik} k_B T_{ek}}{\sum_j X_{ik} k_B T_{ik}}\right\}^{\frac{1}{2}}. \qquad \text{B.24a}$$

For $j = 1$ and $T_i = T_e$, Equation (B.24a) reduces to

$$M = K\left\{\frac{2(1+Z_i)}{\beta}\right\}^{\frac{1}{2}}. \qquad \text{B.24b}$$

For arbitrary $j = 1$ and $T_i = T_e = T$

$$M = K\left(\frac{2}{\beta}\right)^{\frac{1}{2}}\left\{1 + \sum_j X_{ik}Z_{ik}\right\}^{\frac{1}{2}}. \qquad \text{B.24c}$$

Viscous Term Approximation in 1D Reactor Plasma Model

The electric field at r_i in the 1D reactor plasma model is calculated from Ohm's law, and this quantity is then readily extended into the Taylor expansion for $\phi(r)$. However, there is no simple way to calculate $u''(r_i)$, since $u(r_i) = 0$ is specified as a no-slip boundary condition, and $u'(r_i)$ must be calculated iteratively to find a self-consistent value for the solution, per Equation (3.20c). Noting that the current density predicted by Ohm's law scales closely to the current density from viscous losses calculated in the 0D reactor, the Ohm's law value is used as a surrogate

$$u'' = -\frac{B_z J_2(r)}{\mu}, \qquad \text{B.25a}$$

and J_2 is calculated $J_2(r) = \sigma_\perp(E + u_\theta \times B_z)$. These two currents, again, are comparable in magnitude and much smaller than the current density induced by particle losses. Since $u_\theta \sim E/B_z$ at the midplane, $J_2 = 2\sigma_\perp u_\theta B_z$ and

$$u'' = -\frac{2\sigma_{\perp} u_{\theta} B_z^2}{\mu}. \qquad \text{B.25b}$$

Taking the definition of the Hartmann number, $Ha = BL\sqrt{\sigma/\mu}$, Equation (B.25b) can be expressed

$$u'' = -2\frac{u_{\theta}}{a^2} Ha^2. \qquad \text{B.25c}$$

The length scale a is the plasma annulus half-width. Equation (B.25c) provides a result consistent with a scaling estimate for the second derivative of u_{θ} at r_i without having to use $u_{\theta}(r_i)$ in the calculation, which would result in a non-physical value of zero. The approximation implies that $Ha^2 \sim 1$, which has physical implications that follow from the identity provided in [Cambel, 1963]

$$Ha^2 = CoRe_m Re. \qquad \text{B.25d}$$

In the reactor plasma, the Kármán number is near unity, to avoid distortion of the magnetic field, and since $K = 1/Co$, Equation (B.25d) requires that $Re = 1/Re_m$, which results in the constraint

$$(u_{\theta} a)^2 = \frac{\mu}{\rho \mu_0 \sigma_{\perp}} = \frac{\nu}{\nu_m} \gg 1. \qquad \text{B.25e}$$

For the highly magnetized plasma being analyzed, the dynamic viscosity ν is $O(10^{-4})\ m^2/s$, and the magnetic diffusivity ν_m is $O(10^{-13})\ m^2/s$, so the constraint is respected.

Analytic Relation for Cycle Efficiency

The cycle efficiency η_J was calculated for cases of interest in Chapter 6 by normalizing the estimated jet power by the input power post-simulation. A more direct, *a priori* method to estimate cycle efficiency would be useful. This section describes the development of an approximate method for calculating η_J. The cycle efficiency here is estimated from the main losses, heating and ionization, as well as from prompt alpha losses in the warm plasma described in Section 5.1.3. Other losses, e.g., radiation, are neglected.

$$\eta_J = 1 - \frac{Q_{htg} + Q_{ion} + P_{IN}(1-\eta^\alpha)}{P_{IN}}. \qquad \text{B.26}$$

Thermal and ionization rates are proportional to $\dot{N}^\beta$, which can be expressed as $\dot{N}^\beta = \dot{n}^\alpha \xi^\beta V_r$. Given $P_{IN} = \dot{n}^\alpha V_r E^\alpha$, and substituting expressions for thermal and ionization losses into Equation (B.26)

$$\eta_J = 1 - \left\{\tfrac{3}{2}\xi^\beta(1+\tau)\frac{k_B T_e}{E^\alpha} + \xi^\beta \frac{E_{ion}}{E^\alpha} + 1 - \eta^\alpha\right\}, \qquad \text{B.27}$$

where $\tau = T_i/T_e$, as usual. Equation (B.27) assumes $\dot{n}^\beta = \dot{S}^\beta$, which is a reasonable approximation, since in general, $n^n \ll n^\beta$. Taking the total differential of Equation (B.27)

$$d\eta_J = -\frac{\frac{3}{2}(1+\tau)k_B T_e}{E^\alpha} d\xi^\beta - \frac{E_{ion}}{E^\alpha} d\xi^\beta - \frac{\frac{3}{2}\xi^\beta(1+\tau)}{E^\alpha} d(k_B T_e) + \frac{\partial \eta_J}{\partial \eta^\alpha} d\eta^\alpha. \qquad \text{B.28}$$

From Section 5.1.1, $\eta_J = \eta_w \eta_{exp}$, where η_w is a function of warm plasma losses, including $(1-\eta^\alpha)$. However, for a given system, η^α is a function only of the magnetic field configuration, so that $d\eta^\alpha = 0$, and the last term in Equation (B.28) is dropped. Continuing the development,

$d(k_B T_e)$ can be expressed in terms of ξ^β. Assuming delivered energy per ion of $e\phi \approx \eta_J E^\alpha/\xi^\beta$ and applying the sheath Equation (1.16)

$$k_B T_e = \frac{2\eta_J E^\alpha}{\xi^\beta}\left[1 + ln\left(\frac{m_i}{2\pi m_e}\right)\right]^{-1}. \quad \text{B.29}$$

For H^+ the expression in the bracket is equal to 6.67 and Equation (B.29) can be approximated $k_B T_e \approx 0.3\eta_J E^\alpha/\xi^\beta$, and $d(k_B T_e) \approx -\left[0.3\eta_J E^\alpha/\left(\xi^\beta\right)^2\right] d\xi^\beta$. Substituting these expressions into Equation (B.28), the first and last terms on the RHS cancel out, and

$$d\eta_J = -\frac{E_{ion}}{E^\alpha} d\xi^\beta. \quad \text{B.30}$$

Equation (B.30) is noteworthy, because it says that cycle efficiency is dependent only on ionization energy and the bypass ratio ξ^β. This development follows from the apparent property, provisionally asserted, that

$$\frac{\partial}{\partial \xi^\beta} Q_{htg} d\xi^\beta = -\frac{\partial}{\partial (k_B T_e)} Q_{htg} d(k_B T_e). \quad \text{B.31}$$

The behavior described by Equation (B.31) is consistent with model results, in that electron temperature in the warm plasma decreases with increased propellant flow. The relation bears future study, but for now, continuing the current development it is possible to express Equation (B.30) in terms of delivered specific impulse. Returning to the energy delivered to the individual propellant ion, that quantity can also be expressed in terms of kinetic energy $\eta_J E^\alpha/\xi^\beta = \frac{1}{2} m^\beta g_c^2 I_{SP}^2$. Solving this for ξ^β, an expression for $d\xi^\beta$ can be written and substituted into Equation (B.30) with the result

$$d\eta_J = -\frac{2E_{ion}}{m^\beta g_c^2}\left(\frac{1}{I_{SP}^2}d\eta_J - \frac{2\eta_J}{I_{SP}^3}dI_{SP}\right). \quad \text{B.32}$$

Defining $\chi = 2E_{ion}/m^\beta g_c^2$ with units of s^2 and grouping terms,

$$\frac{\partial\eta_J}{\eta_J} = 2\chi\frac{dI_{SP}}{I_{SP}(\chi + I_{SP}^2)}. \quad \text{B.33}$$

Integrating Equation (B.33) provides an expression for η_J in terms of delivered specific impulse

$$\eta_J = expC_1\left(\frac{I_{SP}^2}{\chi + I_{SP}^2}\right), \quad \text{B.34}$$

where C_1 is a constant of integration.

Based on simple scaling from the range of delivered specific impulses in the warm plasma analysis plan, Equation (B.30) indicates that η_J would be expected to vary within a range of 10 percent over the cases evaluated. More strictly, η_J can be calculated using Equation (B.34). Analytically, in the limit $I_{SP} \to \infty, \eta_J = expC_1$. Taking $expC_1$ as an asymptotic limit for very large I_{SP}, in this regime, ξ^β is small and ionization losses negligible. The constant of integration can then be estimated by considering that $Q_{htg} \approx \frac{3}{2}V_r\dot{n}^\alpha(1 + \xi^\beta)k_B(T_i + T_e)$, because $T_i + T_e \gg 2T_{n0}$, where T_{n0} is the supply temperature of the propellant. To the first order, the expression for Q_{htg} is equal to that of Q_{jet}, and $P_{IN} = Q_{htg} + Q_{jet} = 2Q_{jet}$. This expression implies that in Equation B.34, $expC_1 \approx 0.5$. Figure B.1 shows the simulation results for H^+propellant from cases in Table 6-3 overlaid on the curve from Equation (B.34).

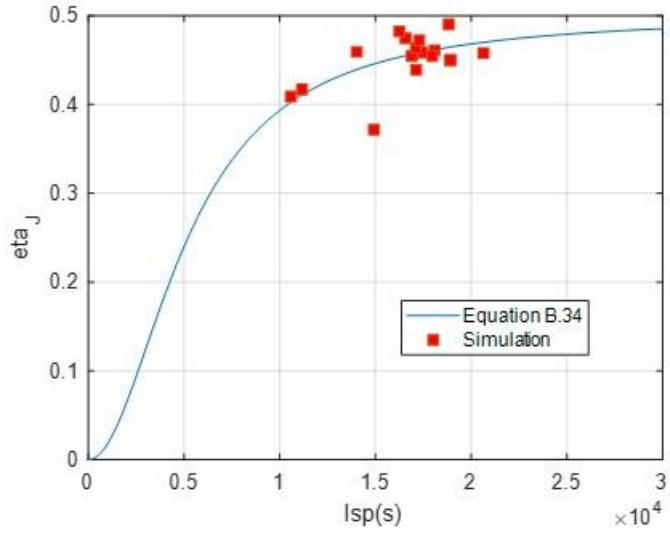

Fig. B-1 – Cycle efficiency vs. specific impulse, Equation B.34 and simulation

Figure B-1 shows that the analytic results are consistent with those from the simulation, and that η_J remains within a relatively narrow range for the H^+ systems evaluated. The low value of $\eta_J \sim 0.37$ at specific impulse of about 14000 s is Case 3, which in which the propellant loading was circumferential. Figure B-1 shows that η_J starts to drop rapidly below a specific impulse of 10000.

The pre-factor $expC_1$ was estimated by assuming it was a maximum, asymptotic value for cycle efficiency. However, Equation (B.29) is based on plasma acceleration calculated from the sheath equation, and as discussed in Section 5.1.1, the sheath equation model is not valid for specific impulses approaching the 3.5 MeV value of the prompt alphas. Therefore, the curve in Figure B.1 has a limit at some maximum specific impulse where the sheath model is no longer valid. The model is not appropriate for extremely high specific impulses where jet power is delivered primarily as monoenergetic alphas.

Bibliography

1. Abdrashitov, G.F., Beloborodov, V.I., Volosov, V.I., Kubarov, V.V., Popov, Y.S., Yuda, Y.S., "Hot Rotating Plasma in the PSP-2 Experiment," Nucl. Fusion 31 1275 1991
2. Abel, I.G., "MCTrans++ Reference Manual, version dated 21 August 2021
3. Abel, I.G., Plunk, G.G., Wang, E., Barnes, M., Cowley, S.C., Dorland, W., Schekochihin, A.A., "Multiscale gyrokinetics for rotating tokamak plasmas: fluctuations, transport and energy flows," Rep. Prog. Phys. 76 (2013) 116201 (69pp), doi:10.1088/0034-4885/76/11/116201
4. Alfvén, H. (1942) "Existence of Electromagnetic-Hydrodynamic Waves. Nature," 150, 405-406
5. Araya, Daniel B., Girimaji, Sharath, Carter, Mark D., Olsen, Christopher S., "Parameterization of magnetic nozzle flow physics for an in-space propulsion application," 42nd AIAA Plasmadynamics and Lasers Conferences, 27-30 June 2011 (AIAA 2011-4010)
6. Aydemir, A.Y., "Magnetohydrodynamic equilibrium and stability of rotating plasmas in a mirror geometry," Physics of Plasmas 11, 5065 (2004); doi: 10.1063/1.1799352
7. Baker, D.A., and Hammel, J.E., "Energy Measurements and Velocity Limiting Effects," The Physics of Fluids 4, 1549 (1961);doi:10.1063/1.1706313
8. Baker, D.A., Hammel, J.E., Ribe, F.L., "Rotating Plasma Experiments. I. Hydromagnetic Properties," The Physics of Fluids 4, 1534 (1961);doi:10.1063/1.1706312
9. Beiser, A., Raab, B., "Hydromagnetic and Plasma Scaling Laws," The Physics of Fluids 4 177 (1961); doi. 10.1063/1.1724425
10. Bekefi, G., "Radiation Processes in Plasmas," New York, 1966, p95

11. Bekhtenev, A.A., *et al*, “Problems of a thermonuclear reactor with a rotating plasma,” 1980 Nucl. Fusion 20 579
12. Bird, R.B., Stewart, W.E.., Lightfoot, E.N., “Transport Phenomena,” 1960
13. Braginskii, S.I., “Transport Processes in a Plasma,” Rev. Plasma Physics I, p205 (1965)
14. Breizman, B.N., Tushentsov, M.R., Arefiev, A.V., “Magnetic nozzle and plasma detachment model for a steady-state flow,” Phys. Plasmas 15, 057103 (2008)
15. Cambel, Ali Bulent, “Plasma Physics and Magnetofluid-Mechanics,” 1963
16. Catto, P.J., Bernstein, Ira B., “Collisional end losses from conventional tandem mirrors,” Phys. Fluids 24 (10), October 1981
17. Chap, Andrew M., Sedwick, Raymond J., “One-Dimensional Semianalytical Model for Optimizing the Standing-Wave Direct Energy Converter,” JOURNAL OF PROPULSION AND POWER Vol. 31, No. 5, September–October 2015
18. Chen, F.R., “Physical mechanism of current-free double layers,” Physics of Plasmas 13, 034502 (2006)
19. Chen, Francis F., “Introduction to Plasma Physics,” New York, 1974, p151
20. Clauser, T.M., “The Feasibility of Thermonuclear Propulsion,” 1958, Proceedings of the Conference on Extremely High Temperatures, John Wiley & Sons, Inc.
21. Deline, C.A., Bengston, R.D., Breizman, B.N., Tushentsov, M.R., Jones, J.E., Chavers, D.G., Dobson, C.C., Schuettpelz, B.M., ”Plume detachment from a magnetic nozzle,” Physics of Plasmas 16, 033502 (2009)
22. Ellis, R.F., A.B. Hassam, S. Messer and B.R. Osborn, “An experiment to test centrifugal confinement for fusion,” Physics of Plasmas, 8, 2057 (2001)

23. Ellis, R.F., Hassam, A.B., *et al*, 2012, "Final Technical Report 2012, The Maryland Centrifugal Experiment (MCX): Centrifugal Confinement and Velocity Shear Stabilization of Plasmas in Shaped Open Magnetic Systems," DOE Grant Number DEFG0200ER54605, 2012
24. Ghosh, J., Elton, R.C., Griem, H.R., Case, A., DeSilva, A.W., Ellis, R.F., Hassam, A., Lunsford, R., and Teodorescu, C., "Radially resolved measurements of plasma rotation and flow-velocity shear in the Maryland Centrifugal Experiment," Physics of Plasmas 13, 022503 (2006); doi: 10.1063/1.2167915
25. Ghosh, J., Elton, R.C., Griem, H.R., Case, A., Ellis, R., Hassam, A.B., Messer, S., and Teodorescu, C., "Spectroscopic measurements of plasma rotation and ion and neutral atom temperatures in the Maryland Centrifugal Experiment," Physics of Plasmas 11, 3813 (2004); doi: 10.1063/1.1765132
26. Hameiri, Eliezer, "The equilibrium and stability of rotating plasmas," The Physics of Fluids 26, 230 (1983); doi: 10.1063/1.864012
27. Helander, Per, and Sigmar, Dieter, "Collisional Transport in Magnetized Plasmas," 2002
28. Hooper, E.B., "Plasma Detachment from a Magnetic Nozzle," Journal of Propulsion and Power, Vol.9, No.5, Sept-Oct. 1993
29. Huang, Y., "Velocity Shear Stabilization of Centrifugally Confined Plasma," Physical Review Letters, Volume 87, Number 23, 3 December 2001
30. Huba, J.D., Naval Research Laboratory Plasma Formulary, 2013
31. Ilin, A.V., Chang-Diaz, F.R., Squire, J.P., Tarditi, A.G., Breizman, B.N., Carter, M.D., "Simulation of Plasma Detachment in VASIMR," AIAA 2002-0346
32. Kuriki, K., and Okada, O., "Experimental Study of a Plasma Flow in a Magnetic Nozzle," The Physics of Fluids, Volume 13, Number 9, September 1970

33. LaFleur, T., et al, 2015, “Electron dynamics and ion acceleration in expanding-plasma thrusters,” Plasma Sources Sci. Technol. 24 06513
34. Lehnert, B. “On the Possibilities of Plasmas Rotating at Supercritical Velocities,” 1974 Phys. Scr. 9 189
35. Lehnert, B., “On the Equilibrium and Stability of Rotating High-beta Plasmas,” Phys. Scr. 9 229, 1974
36. Little, J., and Choueiri, E., “Divergence pf a Propulsive Plasma Flow Expanding through a Magnetic Nozzle,” IEPEC-2009-260
37. Longmier, B.W., et al, “Ambipolar ion acceleration in an expanding magnetic nozzle,” 2011 Plasma Sources Sci. Technol. 20 015007
38. Merino, M., Ahedo, E., “Plasma detachment in a propulsive magnetic nozzle via ion demagnetization,” Plasma Sources Sci. Technol. 23 (2014) 032001
39. Merino, M., Ahedo, E., “Space Plasma Thrusters: Magnetic Nozzles for,” Encyclopedia of Plasma Technology DOI 10.108/E-EPLT-120053936, 2017
40. Merino, M., and Ahedo, E., “Influence of Electron and Ion Thermodynamics on the Magnetic Nozzle Plasma Expansion,” IEEE Transactions of Plasma Science, Vol 43, No.1, January 2015
41. Messer, S., Ellis, R., Case, A., Gupta, D., Hassam, A., Lunsford, R., and Teodorescu, C., “Observation of momentum confinement time scalings in a rotating plasma,” Physics of Plasmas 12, 062509 (2005); doi: 10.1063/1.1931981
42. Mila-Estrada, C., Candy, J., Waltz, R.E., “Turbulent transport of alpha particles in reactor plasmas,” Phys. Plasmas 12, 112303 (2006)
43. Olsen, C.S., Ballenger, M.G., Carter, M.D., Chang Diaz, F.R., Giambusso, M., Glover, T.W., Ilin, A.V., Squire, J.P., Longmier, B.W., Bering III, E.A., Cloutier, P.A., “Investigation of

Plasma Detachment From a Magnetic Nozzle in the Plume of the VX-200 Magnetoplasma Thruster," IEEE Transactions on Plasma Science, Vol 43, No. 1, January 2015

44. Osborn, B. R., Ellis, R. F., and Hassam, A. B., "Numerical simulation of the equilibrium and transport of a centrifugally confined plasma," Physics of Plasmas 10, 2389 (2003); doi: 10.1063/1.1571543
45. Pastukhov, V.P., Nucl Fusion 14 3, 1974
46. Personal communication with Dr. Adil Hassam, University of Maryland, June 2020
47. Reid, R.R., Romero-Talámas, C.A., Young, W.C., Ellis, R.F., and Hassam, A.B., "100 eV electron temperatures in the Maryland centrifugal experiment observed using electron Bernstein emission," Physics of Plasmas 21, 063305 (2014)
48. Romero-Talámas, C.A., Elton, R.C., Young, W.C., *et al*, "Isorotation and differential rotation in a magnetic mirror with imposed E×B rotation," Phys. Plasmas 19, 072501 (2012); doi:10.1063/1.4731729
49. Takahashi, K., Ando A., "Laboratory Observation of a Plasma-Flow-State Transition from Diverging to Stretching a Magnetic Nozzle," Physical Review Letters 118, 225002 (2017)
50. Takahashi, K., Komuro, A., Ando, A., "Operating a magnetic nozzle helicon thruster with strong magnetic field," Phys. Plasmas 23, 033505 (2016)
51. Teodorescu, C., Clary, R., Ellis, R.F., Hassam, A.B., Romero-Talámas, C.A., and Young, W.C., "Sub-Alfvénic velocity limits in magnetohydrodynamic rotating plasmas," Physics of Plasmas 17 052503 (2010)
52. Teodorescu, C., Clary, R.F., Ellis, A.B., Hassam, A.B., Lunsford, R., Uzun-Kaymak, I.., Young, W.C., "Experimental study on velocity limits of magnetized plasmas," Phys. Plasmas 15, 042504 (2008)

53. Teodorescu, C., Young, W.C., Swan, G.W.S., Ellis, R.F., Hassam, A.B., and Romero-Talámas, C.A., "Confinement of Plasma along Shaped Open Magnetic Fields from the Centrifugal Force of Supersonic Plasma Rotation," PRL 105, 085003 (2010) PHYSICAL REVIEW LETTERS, 20 August 2010
54. Trubnikov, B.A., "Particle Interactions in a Fully Ionized Plasma," Rev. Plasma Physics I,p105 (1965)
55. Uzun-Kaymak, I.U., Guzdar, P.N., Clary, R., Ellis, R.F., Hassam, A.B., and Teodorescu, C., "Analysis and modeling of edge fluctuations and transport mechanism in the Maryland Centrifugal Experiment," Physics of Plasmas 15, 112308 (2008)
56. White, Roscoe, Hassam, Adil, and Brizard, Alain, "Centrifugal particle confinement in mirror geometry," Physics of Plasmas 25, 012514 (2018); doi: 10.1063/1.5003359
57. York, T.M., Jacoby, B.A., Mikellides, P., "Plasma Flow Processes Within Magnetic Nozzle Configurations," Journal of Propulsion and Power, Vol.8, No.5, Sept-Oct. 1992
58. Young, W.C., Hassam, A.B., Romero-Talámas, C.A., Ellis R.F., and Teodorescu, C., "Diamagnetism of rotating plasma," Physics of Plasmas 18, 112505 (2011)
59. Zhang, Y., Charles, C., Boswell, R., "Thermodynamic Study on Plasma Expansion along a Divergent Magnetic Field," Physical Review Letters 116, 025001 (2016)